# Dynamics of UV-excited, protonated peptides in the gas phase

THÈSE N$^{O}$ 6399 (2014)

PRÉSENTÉE LE 17 OCTOBRE 2014

À LA FACULTÉ DES SCIENCES DE BASE
LABORATOIRE DE CHIMIE PHYSIQUE MOLÉCULAIRE
PROGRAMME DOCTORAL EN CHIMIE ET GÉNIE CHIMIQUE

ÉCOLE POLYTECHNIQUE FÉDÉRALE DE LAUSANNE

POUR L'OBTENTION DU GRADE DE DOCTEUR ÈS SCIENCES

PAR

Aleksandra ZABUGA

acceptée sur proposition du jury:

Dr S. Gerber, présidente du jury
Prof. T. Rizzo, directeur de thèse
Prof. C. Jouvet, rapporteur
Prof. J.-E. Moser, rapporteur
Prof. T. S. Zwier, rapporteur

ÉCOLE POLYTECHNIQUE
FÉDÉRALE DE LAUSANNE
Suisse
2014

Student: Dr. Einstein, aren't these the same questions as last year's final exam?

Dr. Einstein: Yes. But this year the answers are different.

– from the life of Albert Einstein

To my wonderful parents Vladimir and Natalia

# Abstract

The scope of this thesis is the electronically excited state dynamics of protonated peptides and their photofragmentation mechanism. UV radiation induces fragmentation of biological molecules and might cause various diseases, such as cataracts or skin cancer. The transition to the electronically excited states is the first step in the complex chain of photochemical reactions that lead to UV-induced photodamage. By performing experiments in the gas phase, one can separate the intrinsic photophysical properties of peptides from those involving solvent, potentially yielding insight into both.

The main part of this work presents evidence that following near-UV excitation of tyrosine or phenylalanine residues in gas-phase protonated peptides, some fraction of the molecules undergoes intersystem crossing to the triplet state. This pathway competes with direct dissociation from the excited electronic state and with dissociation from the electronic ground state subsequent to internal conversion. We employ UV-IR double-resonance photofragment spectroscopy to record conformer-specific vibrational spectra of cold peptides pre-excited to their $S_1$ electronic state. The absorption of tunable IR light by these electronically excited peptides leads to a drastic increase in fragmentation, selectively enhancing the loss of neutral phenylalanine or tyrosine side-chain. The recorded IR spectra evolve upon increasing the time delay between the UV and IR pulses, reflecting the dynamics of the intersystem crossing on a timescale of ~80 ns and <10 ns for phenylalanine- and tyrosine-containing peptides respectively. The IR spectra in 6 micron region reveal the absence of proton transfer during this time. Once in the triplet states, phenylalanine-containing peptides may live for more than 100 ms, unless they absorb IR photons and undergo dissociation by the loss of an aromatic side-chain. We discuss the mechanism of this fragmentation channel and its possible implications for photofragment spectroscopy and peptide photostability.

The second part describes conformer-dependent anharmonic coupling between fast and slow vibrations in an electronically excited protonated tri-peptide. By analyzing the infrared spectra of different vibrational levels of the $S_1$ electronic state and performing DFT calculations, we

identify the vibrational modes involved in the coupling, the nature of this coupling, and which conformational changes induce it.

The last part presents the combination of cold ion spectroscopy, $^{13}C$ isotopic labeling, and DFT calculations to determine coupling between different amide chromophores in a helical peptide. These results are used to assess the spectroscopic maps developed for protein structure elucidation in solution.

**Key words**: phenylalanine, tyrosine, triplet state, UV fragmentation, intersystem crossing, photostability, photodamage, photophysics, excited state, side-chain loss, gas phase, UV IR photofragment spectroscopy, anharmonic vibrational coupling, DFT calculations, isotopic labeling

# Résumé

Cette thèse à pour sujet d'étude la dynamique des états électroniques excités de peptides protonnés ainsi que leurs mécanismes de photofragmentation. Le rayonnement UV induit la fragmentation de molécules biologiques et peut provoquer différentes maladies comme la cataracte ou le cancer de la peau (mélanome). La transition vers des états électroniques excités est la prémière étape d'une chaine complexe de réactions photochimiques conduisant aux dommages induit par le rayonnement UV. Les expériences in-vacuo permettent d'isoler les biomolécules comme des peptides protonnés et de sonder les propriétés intrinsèques de leurs états excités.

Dans ce travail, nous montrons que suite à l'irradiation dans le proche UV du résidu tyrosine ou phénylalanine de peptides protonnés, une partie des molécules subit un croisement inter-système vers un état triplet. Ce chemin réactionnel est compétitif avec la dissociation directe de l'état électronique excité et la dissociation à l'état fondamental après conversion interne. Nous avons utilisés la spectroscopie de photofragmentation de double résonnance UV-IR pour enregistrer les spectres résolus en conformère de peptides refroidis et pré-excités à l'état électronique $S_1$. L'absorption en fonction de la fréquence IR de ces peptides excités électroniquement conduits à une augmentation importante de la fragmentation et de manière sélective, à une augmentation de la perte sous forme neutre de la chaine latérale phénylalanine ou tyrosine. Les spectres infrarouges enregistrés évoluent en fonction du délai entre le pulse UV et IR, et reflètent la dynamique de la conversion intersystème à l'échelle de temps de ~80 ns et <10 ns pour les peptides ayant une phénylalanine ou une tyrosine respectivement. Les spectres IR dans la région 6 micromètres révèlent l'absence de transfert de proton pendant cet évènement. Une fois dans un état triplet, les peptides contenant de la phénylalanine possèdent une durée de vie de plus de 100 ms, sauf s'ils absorbent des photons IR qui provoquent leur dissociation part perte d'une chaine aromatique latérale. Nous discutons le mécanisme de ce canal de fragmentation et les possibles implications en spectroscopie de photofragments et de la photostabilité de peptide.

La deuxième partie de la thèse décrit le couplage anharmonique dépendant du conformère entre les vibrations rapides et lentes dans l'état électronique excité d'un tripeptide protonné. L'analyse des spectres infrarouge de différents niveaux vibrationnels de l'état électronique $S_1$ et les calculs DFT nous ont permis d'identifier les modes normaux de vibration impliqués dans le couplage et de caractériser la nature de ce couplage ainsi que les changements de conformation impliqués.

La dernière partie présente la combinaison de la spectroscopie d'ion froid, le labelling isotopique $^{13}C$, et les calculs DFT pour sonder les couplages entre différents chromophores amide dans une hélice peptidique. Ces résultats ont été utilisés pour évaluer les cartographies spectrométriques développées pour l'élucidation des structures de protéine en solution.

**Mots clés :** phénylalanine, tyrosine, état triplet, fragmentation UV, conversion intersystème, photostabilité, photodommage, photophysique, état excité, chaine latérale, phase gazeuse, spectroscopie de photofragmentation UV-IR, couplage vibrationnel anharmonique, calculs DFT, labelling isotopique

# List of Abbreviations

| | |
|---|---|
| BBO | Beta Barium Borate |
| CID | Collision-Induced Dissociation |
| CRM | Charge Residue Model |
| DC | Direct Current |
| DFT | Density Functional Theory |
| 2D-IR | Two-Dimensional Infrared |
| DNA | Deoxyribonucleic Acid |
| ESI | Electrospray Ionization |
| IC | Internal Conversion |
| IEM | Ion Evaporation Model |
| IR | Infrared |
| IRLAPS | Infrared Laser Assisted Photofragment Spectroscopy |
| IRMPD | Infrared MultiPhoton Dissociation |
| IRMPE | Infrared MultiPhoton Excitation |
| ISC | Intersystem Crossing |
| IVR | Intramolecular Vibrational energy Redistribution |
| KTP | Potassium Titanyl Phosphate |
| MD | Molecular Dynamics |
| Nd:YAG | Neodymium-doped Yttrium Aluminium Garnet (laser) |
| NMR | Nuclear Magnetic Resonance |
| OPA | Optical Parametric Amplifier |
| OPO | Optical Parametric Oscillator |
| PES | Potential Energy Surface |
| RF | Radio Frequency |
| R2PI | Resonant Two-Photon Ionization |
| UV | Ultraviolet |

# Table of Contents

# Chapter 1

# Introduction

The biological function of proteins is closely related to their three-dimensional structure. The sequence of amino acids comprises the primary structure of a protein, and how they interact with one another determines the secondary structure (such as β- and γ-turns,[1] α-helices, β-sheets,[2] etc.). The way the secondary structures are packed in 3D space forms the tertriary structure, and changes of the tertiary structure are involved in different biological functions of the proteins. Many proteins assemble further into quaternary structure, which is the arrangement of protein subunits hold together by non-covalent interactions and disulfide bonds.

All proteins are built from 20 naturally occurring amino acids, some of which humans and animals synthesize in the series of biochemical reactions and some they can only obtain with food. Among these amino acids, five are responsible for UV light absorption: tryptophan, tyrosine, phenylalanine, histidine, and cysteine (*via the* cystine S–S bond). Irradiation by near-UV light can cause damage in the proteins by changing their structure and functionality. Understanding the photochemistry of electronically excited proteins is essential to mitigating the harmful effects of UV radiation on the functions proteins play in living organisms.

Hydrogen bonding with water and surrounding molecules can change the intrinsic structure of biomolecules. While it is important to know the structure of biomolecules in their native environment in cells, it is difficult to model molecular interactions. To help to improve theoretical methods, many researchers investigate molecules in the gas phase, where they can remove the solvent. This allows one to separate the problem into two parts: first modeling the structure of the biomolecule in the absence of solvent, and then adding water molecules one after another to see how the structure would change.[3] In this work we mainly focus on the photophysics of phenylalanine-containing peptides. Though the amino acid phenylalanine absorbs UV radiation less strongly than tryptophan or tyrosine, the relative abundance of phenylalanine in proteins is higher.[4, 5] Interestingly, phenylalanine is one of a few essential amino acids that cannot be synthesized in the human body. A special enzyme, phenylalanine

hydroxylase, converts the excess of phenylalanine obtained with food to tyrosine and the lack of this enzyme causes serious mental retardation.[6]

## 1.1 UV photodamage in biology

Ultraviolet light coming from the sun is divided into three categories, based on its distinct biological effects: UVA (320-400 nm), UVB (280-320 nm), and UVC (200-280 nm).[7] UVC light is mainly blocked by ozone in the Earth's atmosphere, and thus only a small portion of it reaches the surface. UVA and UVB light penetrate the Earth's atmosphere in amounts that are sufficient to affect biological species. UVB radiation is the most dangerous, because it is absorbed into the skin and causes photochemical reactions that can eventually lead to skin cancer. UVA comprises most of the UV radiation coming from the sun and it is less harmful, causing aging and wrinkling of the skin.[7]

Skin prevents further penetration of the UV light into the organism by tanning and thickening. In recent years, with the ozone layer degradation, UVA exposure has become more severe and the melanoma cancer rate has increased.[8] UV irradiation can cause damage in both DNA and proteins. Proteins comprise approximately 68% of the dry matter of the cell and are the primary targets of photo-oxidative damage.[9] For example, the absorption of UV light by eye lens proteins causes cataracts[10] – if lens proteins are exposed to UV light, they change their color to yellowish brown and stop transmitting visible light.[11]

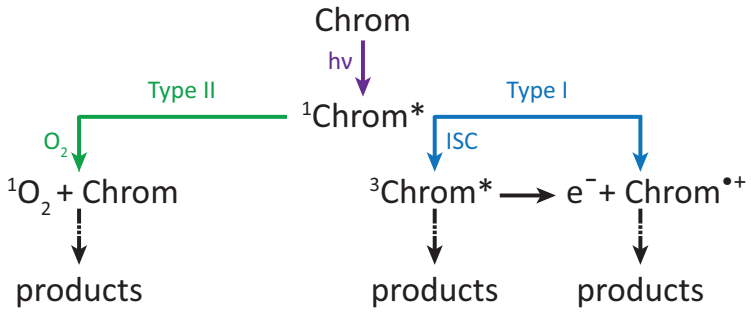


Figure 1.1 The pathways leading to photodegradation in proteins. Chrom stands for the UV chromophore, ISC stands for the intersystem crossing.

There are two ways of photo-oxidative damage of proteins. The UV light can cause direct protein damage through the formation of photoproducts (Type I) or indirectly through the

production of reactive oxygen species (Type II).[11-13] The first steps that lead to the photodegradation of proteins are summarized in Figure 1.1.

Let's first consider the photodegradation pathway of Type I. In proteins the main UV chromophores are the side chains of the amino acids tryptophan (Trp), tyrosine (Tyr), phenylalanine (Phe), histidine (His), and cysteine (Cys)/cystine.[13] In water, the tryptophan side-chain absorbs between 280-305 nm, while for tyrosine this occurs at 260-290 nm, at 240-270 nm for phenylalanine, and at 250-300 nm for the cystine -S-S- bond. Histidine absorbs in the deeper UV (200-220 nm) and has a very low absorption cross section.[14] Initially, the absorption of UV light by these chromophores promotes the molecules to an electronically excited singlet state. From here the molecule can fluoresce, undergo internal conversion (IC) to the ground state, dissociate (if the singlet state is dissociative) or undergo intersystem crossing (ISC) to the triplet state. These processes are schematically depicted in Figure 1.2.

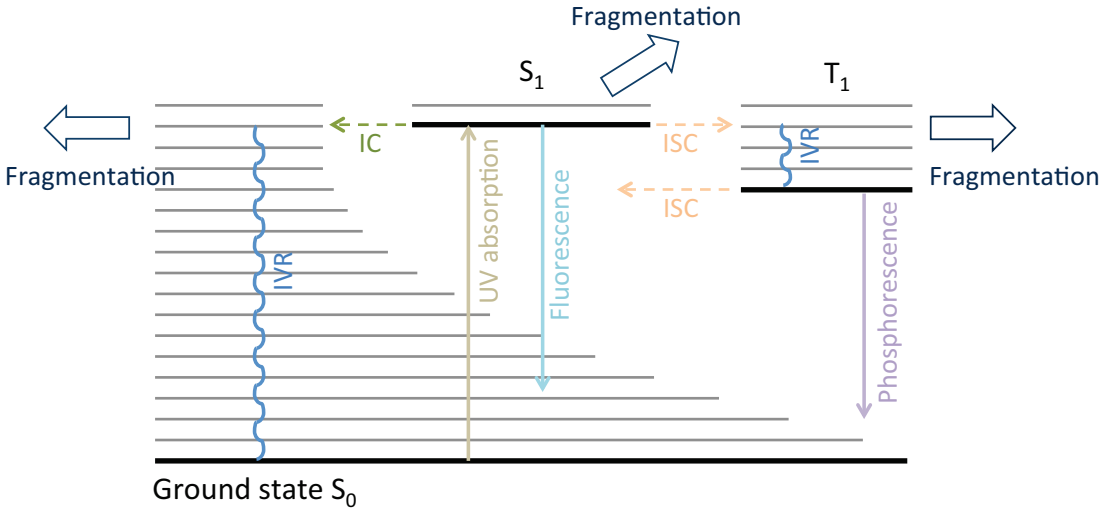


Figure 1.2 A Jablonski diagram indicating the electronic ground state ($S_0$), the first excited singlet state ($S_1$), and the first triplet state ($T_1$). IC – internal conversion, ISC – intersystem crossing, IVR – intramolecular vibrational redistribution.

In proteins containing several chromophores (for example, phenylalanine, tyrosine, and tryptophan) energy can be rapidly transferred from the singlet states of the higher energy chromophores (Phe and Tyr) to those with lower energy (Trp).[15] The efficiency of the energy transfer, however, depends on the proximity of chromophores and their relative orientation.[15] A change in protein conformation can alter the sites of the energy transfer and the final formation of reactive radicals. Pigault and Gerard showed that the fluorescence yield depends on whether tryptophan residues are buried inside the protein or exposed to the aqueous media.[16]

Bent and Hayon summarized the photodegradation pathways of tryptophan, tyrosine, and phenyalanine amino acids, and small peptides containing these chromophores in solution.[17-19] If the energy of the photon is not enough to cause photoionization, almost all UV-induced photodegradation processes are linked to the formation of reactive long-living triplet states.[11, 13] In the case of phenylalanine all type I photodegradation reactions occur *via* the triplet state as a precursor, even electron ejection.[17] The quantum yield of triplet state formation depends on the excitation wavelength, and at 248 nm it is 0.21, 0.50, and 0.40 for tryptophan, tyrosine, and phenylalanine, respectively.[20] These species can undergo energy transfer or react chemically with other molecules in solution. For example, triplet states of tyrosine and tryptophan readily undergo electron transfer with cysteine residues to produce the radical cysteine anion and the corresponding cations.[21-23] Triplet-triplet energy transfer also takes place between various chromophores, and like singlet-singlet energy transfer depends on their relative positions and orientations.[24] In the presence of oxygen, triplet states of aromatic amino acids can undergo electron transfer to form the superoxide anion radical ($O_2^{\bullet -}$) and a radical cation. The radical cation rapidly deprotonates to form a neutral radical, which then undergoes further reactions. In the case of the phenylalanine triplet state, this reaction competes with direct photodissociation to form a benzyl radical (phenylalanine side-chain radical) and a radical backbone (Figure 1.3).[17] The yield of benzyl radical formation from the triplet state shows strong temperature dependence, being higher at lower temperatures.[17]

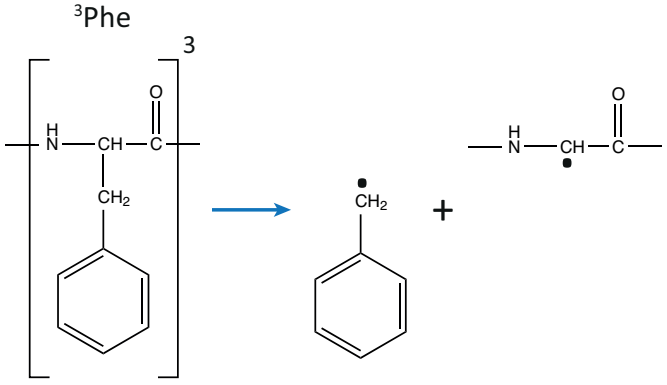


Figure 1.3 The direct photodissociation of phenylalanine containing peptides from the triplet state following UV excitation.

The photodegradation pathway of Type II involves the indirect photo-oxidation of proteins through the formation of the singlet electronic state of oxygen. The first excited singlet state of molecular oxygen is only 94 kJ/mol higher in energy than its ground triplet state. It can be

produced *via* energy transfer from the electronically excited triplet state of the chromophore. Singlet oxygen is very reactive and it interacts with different parts of proteins *via* physical quenching or various chemical reactions, resulting in protein fragmentation.[9, 11]

## 1.2 UV photofragmentation in the gas phase – photostability vs. photodamage

While researchers largely agree that triplet states play an essential role in the UV photodegradation of proteins in solution, several scientists investigating UV-excited peptides with phenylalanine, tyrosine, and tryptophan chromophores in the gas phase consider proteins intrinsically photostable.[25-29] Their photostability results from fast relaxation mechanisms that bring proteins from the excited state to the ground state before any photoreactions can occur. Fluorescence is one of the processes responsible for photostability, but in aromatic amino acids it comprises only a few percent of the total decay of the excited electronic state. The extremely low quantum yield of fluorescence (0.2 for tryptophan, 0.14 for tyrosine, 0.04 for phenylalanine in water pH 7[30]) indicates the presence of other non-radiative processes that lead to deactivation of the first electronically excited state. *Ab initio* calculations performed for aromatic chromophores and small peptides demonstrate the existence of ultrafast electron driven proton transfer, which through a series of conical intersections leads to vibrationally excited ground state molecules.[26, 27, 31-35] When in solution, instead of fragmentation, the molecule in a vibrationally excited ground state efficiently dissipates its energy in collisions with surrounding molecules, providing the basis for photostability. However, this deactivation mechanism is specific to conformations with a gamma turn, because it requires a hydrogen bond between NH and CO along which the hydrogen atom can transfer.

Mons and co-workers experimentally observed three conformers of N-acetylphenylalaninylamide (NAPA), using resonant, one-color, two photon ionization (R2PI) in a supersonic jet.[36] While two of those conformers (A and C) had lifetimes of 62 ns and 42 ns, the fluorescence from the other conformer (B) was not detected, implying that there are fast non-radiative decay processes taking place to shorten the lifetime.[36] The authors suggested that a strong NH - π-cloud interaction in conformer B enhances intersystem crossing, similar to what Zwier and co-workers observed in benzene-HCl and toluene-HCl.[37] The picosecond R2PI pump-probe experiments revealed 1.5 ns lifetime for conformer B of NAPA.[25] Malis et al. suggested that this lifetime is too short to be due to ISC and that other fast non-radiative decay processes

involving excitation and concomitant deplanarization of the peptide bonds take place.[25] They also indicate that these mechanisms might be more universal in UV-excited phenylalanine-containing peptides than the one proposed previously.[26]

Based on the same collaborative work between experimentalists and computational chemists,[25] Domcke and Sobolewski made an attempt to propose that the photostability mechanism in proteins might be related to their folding.[28] They suggest that short lifetime of the folded conformer B of NATA is due to the fast relaxation to the ground state that involves hydrogen atom transfer along the hydrogen bond of the gamma turn.[28] However, in amide-N-methylated derivative of NAPA (NAPMA) the excited lifetime of the folded conformer B is 48 ns[38] in contrast with the excited state lifetime of the folded conformer B of NAPA 1.5 ns.[25] Though both of these conformers have a hydrogen bond along which the hydrogen transfer can occur, it happens slower.

These mechanisms imply that peptides should be photostable. In solution after fast relaxation to the ground state the electronic energy converts to vibrational energy and dissipated to the surrounding environment. However, in the absence of collisions, for example in molecular beam experiments, the excess of the vibrational energy in the ground state would lead to fragmentation. Jouvet and co-workers extensively studied the photodissociation pathways of aromatic amino acids and small peptides.[34, 39-45] In small tyrosine-containing peptides it was shown that fragments identified with internal conversion and dissociation on the ground electronic potential energy surface dominate after electronic excitation.[44] The loss of tyrosine side-chain was attributed to the fragmentation from the electronically excited charge transfer state, which first involves the charge transfer to CO followed by proton transfer from $NH_3$ group.[44, 45] Tseng et al. proposes a different mechanism for the side-chain loss from phenylalanine chromophores based on the measurement of the kinetic energy of photofragments.[46] Upon excitation of small phenylalanine chromophore derivatives with 248 nm light, the authors observed fast and slow components in the translational energy distribution for the benzyl radical fragment (phenylalanine side-chain radical). The fast component in the translational energy distribution is due to fragmentation from the triplet state with an exit barrier, and the slow component results from fragmentation on the ground electronic state, populated either after direct internal conversion from the excited electronic state or by sequential intersystem crossing from the triplet state back to the ground electronic state. They observed that as the size of the backbone increases, the slow component becomes more abundant, indicating that internal conversion starts to play an increasing role.[46] However, this might change for other systems,

because different conformations have different excited electronic state lifetimes[36, 47] and hence might exhibit a different interplay between the internal conversion and intersystem crossing.

Usually, the rate of the intersystem crossing in the absence of heavy atoms is slow. In contrast with this common belief, Cogan et al. calculated that for simple organic molecules (ethylene, benzene, toluene, and pyrrole) at the $S_1/S_0$ conical intersection, there exists a triplet state degenerate with the two singlet states.[48] They also discovered that spin orbit coupling is large at the conical intersection, which results in fast and efficient intersystem crossing.[48] The results of the calculations showed that toluene (the precursor for phenylalanine amino acid side-chain) may dissociate *via* the triplet state to form benzyl radical,[48] consistent with the gas phase experiments performed by Dietz et al.[49] Even in those cases when triplet state yields are low, they might be very important players in dissociation. In the presence of collisions, the vibrationally excited ground state molecules formed after internal conversion can be stabilized below the dissociation barrier; whereas repulsive triplet states might dissociate more efficiently, increasing the photofragmentation yield. Recently, enhanced intersystem crossing between $S_1$ –$T_2$ with the subsequent internal conversion to $T_1$ was found in benzene, and it seems that this might be a universal mechanism for other aromatic compounds.[50]

DNA is considered to be photostable because of the access to conical intersections.[51-57] However, recent discoveries of the singlet $n\pi^*$ state opens the doorway to the intersystem crossing pathway to the long living triplet state.[58] Hare et al. recorded the infrared spectrum of the first triplet state of thymine and thymidine DNA bases.[59] Gonzalez and co-workers reported for the first time an excited-state dynamical study of a DNA nucleobase cytosine including singlet and triplet states and showed that intersystem crossing competes with internal conversion on the femtosecond timescale.[60] In order to probe triplet states in pump-probe laser experiments, the energy of the probe photon should be adjusted to ionize the molecules in the triplet state. For this reason intersystem crossing might be not detected in fast dynamics of molecules in some femtosecond experiments.[50]

In this work we would like to establish which mechanisms are responsible for the UV fragmentation of phenylalanine- and tyrosine- containing peptides of a larger size than those studied so far, and to understand whether triplet states indeed play an important role in the photophysical processes.

## 1.3 UV photofragmentation in mass spectrometry

For large biomolecules it becomes difficult to achieve high fragmentation yields using traditional mass spectrometric approaches. New analytical methods have developed to overcome this problem, and UV photofragmentation is the one of them. Ly and Julian use chemical modification of tyrosine to iodo-tyrosine with subsequent UV photofragmentation to achieve site-specific radical formation through the loss of iodine.[61] The other way would be to attach non-covalent chromophores such as crown-ether based adducts[62, 63] or to use 266 nm light to cleave disulfide bonds.[64] Brodbelt and co-workers uses UV photodissociation for the structural characterization of proteins and lipids.[65-70] Dugourd and co-workers combines UV photodissociation with subsequent collisional activation to increase sequence coverage for various tyrosine containing peptides.[71] UV photofragmentation is now used in mass spectrometry as a tool to get complementary fragments to other techniques such as collision-induced dissociation[72, 73] (CID), electron capture dissociation,[74] electron transfer dissociation,[75, 76] and surface induced dissociation.[77] While these methods start to be implemented, the mechanisms of photofragmentation are still under investigation. Dugourd and co-workers observe the appearance of fragments that are complementary to CID, such as side-chain loss, that they attribute to direct dissociation from electronically excited states or a fast cleavage from the ground state before intramolecular vibrational redistribution (IVR) takes place.[78] In small tyrosine-containing peptides at room temperature no tyrosine side-chain loss fragment was observed upon 266 nm excitation[29], in contrast with significant tyrosine side-chain loss fragmentation observed for the most stable conformations upon 284 nm excitation at 10 K.[79] In a review article, Reilly attributes the origin of non-statistical fragments (a- and x- ions) to the direct fragmentation from the excited electronic state.[80] More detailed understanding of the UV fragmentation mechanism might help investigators predict the specific fragmentation sites in a protein, and, potentially, even identify 3D motifs by the relative abundance of those photofragments at different laser wavelengths.

## 1.4 UV photofragmentation in spectroscopy

We mentioned above that the three-dimensional structure of proteins determines its activity and function. Nuclear magnetic resonance (NMR) and X-ray crystallography are currently the most widespread experimental techniques to disentangle the structures of biomolecules.

However, the modeling of proteins in condensed phases requires extensive computational power and accurate theoretical methods. *Ab initio* calculations are very time consuming, and as a result they are limited to the systems of a small size. Computational chemists develop new theoretical methods to model 3D structures of biomolecules, but all of those methods need validation by experiment. Experiments on isolated biomolecules simplify the comparison with theory. They allow to test theory in a step-by-step manner – first improving theoretical methods for bare biomolecules and then adding interaction with the solvent. An example of how gas phase spectroscopy tests new theoretical approach for protein modeling is discussed in Chapter 5.

The combination of electrospray ionization and ion traps has boosted the investigation of biomolecular ions in the gas phase. In living cells many proteins exist in ionic forms that make the study of protonated species more biologically relevant than that of their neutral analogs.[81] Moreover, mass selection in quadrupole mass filters allows one to isolate ions of interest from the decomposition products present in solution prior to investigation. Infrared spectra provide a set of vibrational frequencies that by comparison with calculations can validate the theoretical approaches. The history of different spectroscopic methods applied to gas phase ions as well as neutrals is well covered in several review papers and books.[82-85] Jockusch and co-workers employed fluorescence spectroscopy to determine polyproline peptide conformations in a quadrupole ion trap mass spectrometer.[86] However, due to the low density of the ions in the trap, direct absorption or fluorescence spectroscopy is extremely challenging. For this reason, many researchers use action spectroscopy, in which the consequences of the photon absorption (for example, photofragments) rather then the photons are detected. First introduced by Lee and co-workers[87] and further applied to neutral biomolecules,[88-93] IR-UV photofragment spectroscopy combined with cryogenic cooling provides conformer-specific and highly resolved vibrational spectra of protonated biomolecules in the gas phase.[3, 79, 94-98]

Nagornova et al. recorded highly resolved vibrational spectra of a cyclic decapeptide gramicidin S for four lowest energy conformations.[97, 98] These spectra served as a benchmark to determine the intrinsic structure of gramicidin S and helped to assess currently available computational methods.[97-99] Later, the authors recorded electronic and vibrational spectra of stepwise-solvated gramicidin S, bridging the gap between the gas phase and solution phase structures.[3]

As the size of biomolecules increases, the UV photofragmentation yield drops. The addition of a $CO_2$ laser excitation after UV excitation had been demonstrated to enhance aromatic side-chain loss photofragment intensity by several orders of magnitude and allowed recording highly

resolved conformer-specific spectra of a 17 amino-acid peptide.[100] Papadopoulos et al. used the same approach to record electronic spectra of bradykinin[96] and a protein as large as ubiquitin (76 amino acids).[101] However, the mechanism of the $CO_2$ laser-assisted UV-induced fragmentation, extensively studied by Guidi et al.,[102] remains unclear and is the primary topic of this thesis.

In this work we would like to establish the mechanisms that drive the fragmentation of protonated peptides upon UV excitation of aromatic residues. We are also interested in the structural changes that the peptides adopt in the electronically excited states. We discussed above the important roles of the long-living triplet states in UV photodamage of biomolecules in solution, and we would like to see whether triplet states are sufficiently populated to cause specific fragmentation in the gas phase. Understanding the photofragmentation mechanism would help us to establish the class and size of biomolecules that can be studied by means of photofragment spectroscopy.

## 1.5 Outline

This thesis is organized as follows.

In Chapter 2 we present the experimental apparatus built in our laboratory for the investigation of cold, biomolecular ions and the spectroscopic techniques to record conformer-specific spectra of biomolecules in their ground and excited electronic state. We also describe theoretical methods that we apply to determine the structure of the small protonated peptides.

Chapter 3 is the main chapter of the thesis, and it focuses on the UV fragmentation mechanism of protonated phenyalanine- and tyrosine- containing peptides. We employ UV-IR double resonance photofragment spectroscopy to follow the deactivation dynamics of the UV excited helical peptide. We measure the lifetime of the UV excited conformations and provide the fragmentation model that explains the formation of the side-chain loss photofragment.

In Chapter 4 we present conformer-selective infrared spectra of a tri-peptide AcFAK-$H^+$ in its ground and electronically excited state. For one of the conformations we observe Franck Condon like progressions in the vibrational spectrum upon UV excitation to different vibrational levels of the first electronically excited state. We attribute these progressions to the coupling between an NH stretch vibration and a low frequency mode in the molecule. In this chapter we provide theoretical explanation for the spectral intensities of combination bands and suggest the conformational change that causes this type of coupling.

Chapter 5 describes a joint project with a theoretical group of Prof. Skinner. We show how cold ion spectroscopy in combination with $^{13}C$ isotopic labeling helps to assess newly developed spectroscopic maps for modeling protein structures in solution.

Chapter 6 summarizes the results and possible applications of the current work.

# References


[1] G. D. Rose, L. M. Gierasch, and J. A. Smith, Adv. Protein Chem. **37**, 1 (1985).

[2] C. I. Brändén and J. Tooze, *Introduction to Protein Structure* (Garland Pub., 1999).

[3] N. S. Nagornova, T. R. Rizzo, and O. V. Boyarkin, Science **336**, 320 (2012).

[4] J. L. King and T. H. Jukes, Science **164**, 788 (1969).

[5] H.-D. Belitz, W. Grosch, and P. Schieberle, *Food Chemistry* (Springer, 2009).

[6] D. Puri, *Textbook of Medical Biochemistry* (Elsevier India, 2006).

[7] Y. Matsumura and H. N. Ananthaswamy, Toxicol. Appl. Pharm. **195**, 298 (2004).

[8] H. M. Gloster and D. G. Brodland, Dermatol. Surg. **22**, 217 (1996).

[9] M. J. Davies, BBA-Proteins Proteom. **1703**, 93 (2005).

[10] J. Longstreth, F. R. de Gruijl, M. L. Kripke, S. Abseck, F. Arnold, H. I. Slaper, G. Velders, Y. Takizawa, and J. C. van der Leun, J. Photochem. Photobiol. B **46**, 20 (1998).

[11] M. J. Davies and R. J. W. Truscott, J. Photochem. Photobiol. B **63**, 114 (2001).

[12] O. Blokhina, E. Virolainen, and K. V. Fagerstedt, Ann. Bot.-London **91**, 179 (2003).

[13] B. A. Kerwin and R. L. Remmele, J. Pharm. Sci. **96**, 1468 (2007).

[14] D. S. Caswell and T. G. Spiro, J. Am. Chem. Soc. **108**, 6470 (1986).

[15] W. R. L. J. B. Alexander Ross, Kenneth W. Rousslang, Hermann R. Wyssbrod, in *Topics in Fluorescence Spectroscopy*, edited by J. R. Lakowicz (Kluwer Academic Publishers, 2002), Vol. 3, p. 13.

[16] C. Pigault and D. Gerard, Photochem. Photobiol. **40**, 291 (1984).

[17] D. V. Bent and E. Hayon, J. Am. Chem. Soc. **97**, 2606 (1975).

[18] D. V. Bent and E. Hayon, J. Am. Chem. Soc. **97**, 2599 (1975).

[19] D. V. Bent and E. Hayon, J. Am. Chem. Soc. **97**, 2612 (1975).

[20] D. N. Nikogosyan and H. Gorner, J. Photochem. Photobiol. B **13**, 219 (1992).

[21] D. Creed, Photochem. Photobiol. **39**, 537 (1984).

[22] D. Creed, Photochem. Photobiol. **39**, 563 (1984).

[23] D. Creed, Photochem. Photobiol. **39**, 577 (1984).

[24] W. R. L. J. B. Alexander Ross, Kenneth W. Rousslang, Hermann R. Wyssbrod, in *Topics in Fluorescence Spectroscopy*, edited by J. R. Lakowicz (Kluwer Academic Publishers, 2002), Vol. 3, p. 16.

[25] M. Malis, Y. Loquais, E. Gloaguen, H. S. Biswal, F. Piuzzi, B. Tardivel, V. Brenner, M. Broquier, C. Jouvet, M. Mons, N. Doslic, and I. Ljubic, J. Am. Chem. Soc. **134**, 20340 (2012).

[26] D. Shemesh, A. L. Sobolewski, and W. Domcke, J. Am. Chem. Soc. **131**, 1374 (2009).

[27] A. L. Sobolewski and W. Domcke, ChemPhysChem **7**, 561 (2006).

[28] W. Domcke and A. L. Sobolewski, Nature chemistry **5**, 257 (2013).

[29] G. Aravind, B. Klaerke, J. Rajput, Y. Toker, L. H. Andersen, A. V. Bochenkova, R. Antoine, J. Lemoine, A. Racaud, and P. Dugourd, J. Chem. Phys. **136** (2012).

[30] R. V. Bensasson, E. J. Land, and T. G. Truscott, *Flash photolysis and pulse radiolysis: contributions to the chemistry of biology and medicine* (Pergamon, 1983).

[31] D. Shemesh and W. Domcke, ChemPhysChem **12**, 1833 (2011).

[32] D. Shemesh, C. Haettig, and W. Domcke, Chem. Phys. Lett. **482**, 38 (2009).

[33] A. L. Sobolewski, W. Domcke, C. Dedonder-Lardeux, and C. Jouvet, Phys. Chem. Chem. Phys. **4**, 1093 (2002).

[34] G. Gregoire, C. Jouvet, C. Dedonder, and A. L. Sobolewski, J. Am. Chem. Soc. **129**, 6223 (2007).

[35] D. Shemesh, A. L. Sobolewski, and W. Domcke, Phys. Chem. Chem. Phys. **12**, 4899 (2010).

[36] W. Chin, M. Mons, J. P. Dognon, R. Mirasol, G. Chass, I. Dimicoli, F. Piuzzi, P. Butz, B. Tardivel, I. Compagnon, G. von Helden, and G. Meijer, J. Phys. Chem. A **109**, 5281 (2005).

[37] A. J. Gotch and T. S. Zwier, J. Chem. Phys. **93**, 6977 (1990).

[38] M. Malis, Y. Loquais, E. Gloaguen, C. Jouvet, V. Brenner, M. Mons, I. Ljubic, and N. Doslic, Phys. Chem. Chem. Phys. **16**, 2285 (2014).

[39] V. Lepere, B. Lucas, M. Barat, J. A. Fayeton, V. J. Picard, C. Jouvet, P. Carcabal, I. Nielsen, C. Dedonder-Lardeux, G. Gregoire, and A. Fujii, J. Chem. Phys. **127**, 134313 (2007).

[40] H. Kang, C. Jouvet, C. Dedonder-Lardeux, S. Martrenchard, G. Gregoire, C. Desfrancois, J. P. Schermann, M. Barat, and J. A. Fayeton, Phys. Chem. Chem. Phys. **7**, 394 (2005).

[41] B. Lucas, M. Barat, J. A. Fayeton, M. Perot, C. Jouvet, G. Gregoire, and S. B. Nielsen, J. Chem. Phys. **128**, 164302 (2008).

[42] U. Kadhane, M. Perot, B. Lucas, M. Barat, J. A. Fayeton, C. Jouvet, A. Ehlerding, M. B. S. Kirketerp, S. B. Nielsen, J. A. Wyer, and H. Zettergren, Chem. Phys. Lett. **480**, 57 (2009).

[43] M. Perot, B. Lucas, M. Barat, J. A. Fayeton, and C. Jouvet, J. Phys. Chem. A **114**, 3147 (2010).

[44] C. Dehon, S. Soorkia, M. Pedrazzani, C. Jouvet, M. Barat, J. A. Fayeton, and B. Lucas, Phys. Chem. Chem. Phys. **15**, 8779 (2013).

[45] S. S. Kumar, B. Lucas, S. Soorkia, M. Barat, and J. A. Fayeton, Phys. Chem. Chem. Phys. **14**, 10225 (2012).

[46] C. M. Tseng, M. F. Lin, Y. L. Yang, Y. C. Ho, C. K. Ni, and J. L. Chang, Phys. Chem. Chem. Phys. **12**, 4989 (2010).

[47] T. Hashimoto, Y. Takasu, Y. Yamada, and T. Ebata, Chem. Phys. Lett. **421**, 227 (2006).

[48] S. Cogan, Y. Haas, and S. Zilberg, J. Photochem. Photobiol. A **190**, 200 (2007).

[49] T. G. Dietz, M. A. Duncan, and R. E. Smalley, J. Chem. Phys. **76**, 1227 (1982).

[50] D. S. N. Parker, R. S. Minns, T. J. Penfold, G. A. Worth, and H. H. Fielding, Chem. Phys. Lett. **469**, 43 (2009).

[51] I. Vaya, T. Gustavsson, F.-A. Miannay, T. Douki, and D. Markovitsi, J. Am. Chem. Soc. **132**, 11834 (2010).

[52] S. Ullrich, T. Schultz, M. Z. Zgierski, and A. Stolow, Phys. Chem. Chem. Phys. **6**, 2796 (2004).

[53] J. Peon and A. H. Zewail, Chem. Phys. Lett. **348**, 255 (2001).

[54] J. M. L. Pecourt, J. Peon, and B. Kohler, J. Am. Chem. Soc. **122**, 9348 (2000).

[55] C. Canuel, M. Mons, F. Piuzzi, B. Tardivel, I. Dimicoli, and M. Elhanine, J. Chem. Phys. **122** (2005).

[56] H. Kang, K. T. Lee, B. Jung, Y. J. Ko, and S. K. Kim, J. Am. Chem. Soc. **124**, 12958 (2002).

[57] C. E. Crespo-Hernandez, B. Cohen, P. M. Hare, and B. Kohler, Chem. Rev. **104**, 1977 (2004).

[58] P. M. Hare, C. E. Crespo-Hernandez, and B. Kohler, Proc. Natl. Acad. Sci. U.S.A. **104**, 435 (2007).

[59] P. M. Hare, C. T. Middleton, K. I. Mertel, J. M. Herbert, and B. Kohler, Chem. Phys. **347**, 383 (2008).

[60] M. Richter, P. Marquetand, J. González-Vázquez, I. Sola, and L. González, J. Phys. Chem. Lett. **3**, 3090 (2012).

[61] T. Ly and R. R. Julian, J. Am. Chem. Soc. **130**, 351 (2008).

[62] G. K. Yeh, Q. Y. Sun, C. Meneses, and R. R. Julian, J. Am. Soc. Mass. Spectr. **20**, 385 (2009).

[63] J. J. Wilson, G. J. Kirkovits, J. L. Sessler, and J. S. Brodbelt, J. Am. Soc. Mass. Spectr. **19**, 257 (2008).

[64] A. Agarwal, J. K. Diedrich, and R. R. Julian, Anal. Chem. **83**, 6455 (2011).

[65] M. W. Gardner and J. S. Brodbelt, Anal. Chem. **81**, 4864 (2009).

[66] B. J. Ko and J. S. Brodbelt, J. Am. Soc. Mass. Spectr. **22**, 49 (2011).

[67] J. A. Madsen, T. W. Cullen, M. S. Trent, and J. S. Brodbelt, Anal. Chem. **83**, 5107 (2011).

[68] J. A. Madsen, R. R. Cheng, T. S. Kaoud, K. N. Dalby, D. E. Makarov, and J. S. Brodbelt, Chem.-Eur. J. **18**, 5374 (2012).

[69] J. P. O'Brien, J. M. Pruet, and J. S. Brodbelt, Anal. Chem. **85**, 7391 (2013).

[70] S. A. Robotham, C. Kluwe, J. R. Cannon, A. Ellington, and J. S. Brodbelt, Anal. Chem. **85**, 9832 (2013).

[71] L. Joly, R. Antoine, M. Broyer, P. Dugourd, and J. Lemoine, J. Mass Spectrom. **42**, 818 (2007).

[72] J. M. Wells and S. A. McLuckey, in *Biological Mass Spectrometry*, edited by A. L. Burlingame (Elsevier Inc., 2005), Vol. 402, p. 148.

[73] J. Laskin and J. H. Futrell, Mass Spectrom. Rev. **22**, 158 (2003).

[74] R. A. Zubarev, N. L. Kelleher, and F. W. McLafferty, J. Am. Chem. Soc. **120**, 3265 (1998).

[75] J. Wiesner, T. Premsler, and A. Sickmann, Proteomics **8**, 4466 (2008).

[76] L. M. Mikesh, B. Ueberheide, A. Chi, J. J. Coon, J. E. P. Syka, J. Shabanowitz, and D. F. Hunt, BBA-Proteins Proteom. **1764**, 1811 (2006).

[77] V. Grill, J. Shen, C. Evans, and R. G. Cooks, Rev. Sci. Instrum. **72**, 3149 (2001).

[78] T. Tabarin, R. Antoine, M. Broyer, and P. Dugourd, Rapid Commun. Mass Spectrom. **19**, 2883 (2005).

[79] J. A. Stearns, M. Guidi, O. V. Boyarkin, and T. R. Rizzo, J. Chem. Phys. **127** (2007).

[80] J. P. Reilly, Mass Spectrom. Rev. **28**, 425 (2009).

[81] J. M. Berg, J. L. Tymoczko, and L. Stryer, *Biochemistry* (W. H. Freeman, 2007).

[82] T. R. Rizzo, J. A. Stearns, and O. V. Boyarkin, Int. Rev. Phys. Chem. **28**, 481 (2009).

[83] J.-P. Schermann, *Spectroscopy and Modelling of Biomolecular Building Blocks* (Elsevier, 2008).

[84] N. C. Polfer and J. Oomens, Mass Spectrom. Rev. **28**, 468 (2009).

[85] A. B. Wolk, C. M. Leavitt, E. Garand, and M. A. Johnson, Accounts Chem. Res. **47**, 202 (2014).

[86] F. O. Talbot, A. Rullo, H. Yao, and R. A. Jockusch, J. Am. Chem. Soc. **132**, 16156 (2010).

[87] R. H. Page, Y. R. Shen, and Y. T. Lee, J. Chem. Phys. **88**, 4621 (1988).

[88] J. R. Carney, F. C. Hagemeister, and T. S. Zwier, J. Chem. Phys. **108**, 3379 (1998).

[89] J. R. Carney and T. S. Zwier, J. Phys. Chem. A **104**, 8677 (2000).

[90] M. Mons, I. Dimicoli, F. Piuzzi, B. Tardivel, and M. Elhanine, J. Phys. Chem. A **106**, 5088 (2002).

[91] P. Carcabal, R. T. Kroemer, L. C. Snoek, J. P. Simons, J. M. Bakker, I. Compagnon, G. Meijer, and G. von Helden, Phys. Chem. Chem. Phys. **6**, 4546 (2004).

[92] R. A. Jockusch, R. T. Kroemer, F. O. Talbot, L. C. Snoek, P. Carcabal, J. P. Simons, M. Havenith, J. M. Bakker, I. Compagnon, G. Meijer, and G. von Helden, J. Am. Chem. Soc. **126**, 5709 (2004).

[93] C. Unterberg, A. Jansen, and M. Gerhards, J. Chem. Phys. **113**, 7945 (2000).

[94] J. A. Stearns, S. Mercier, C. Seaiby, M. Guidi, O. V. Boyarkin, and T. R. Rizzo, J. Am. Chem. Soc. **129**, 11814 (2007).

[95] J. A. Stearns, C. Seaiby, O. V. Boyarkin, and T. R. Rizzo, Phys. Chem. Chem. Phys. **11**, 125 (2009).

[96] G. Papadopoulos, A. Svendsen, O. V. Boyarkin, and T. R. Rizzo, Faraday Discuss. **150**, 243 (2011).

[97] N. S. Nagornova, M. Guglielmi, M. Doemer, I. Tavernelli, U. Rothlisberger, T. R. Rizzo, and O. V. Boyarkin, Angew. Chem., Int. Ed. **50**, 5383 (2011).

[98] N. S. Nagornova, T. R. Rizzo, and O. V. Boyarkin, J. Am. Chem. Soc. **132**, 4040 (2010).

[99] M. Doemer, M. Guglielmi, P. Athri, N. S. Nagornova, T. R. Rizzo, O. V. Boyarkin, I. Tavernelli, and U. Rothlisberger, Int. J. Quantum Chem. **113**, 808 (2013).

[100] M. Guidi, U. J. Lorenz, G. Papadopoulos, O. V. Boyarkin, and T. R. Rizzo, J. Phys. Chem. A **113**, 797 (2009).

[101] G. Papadopoulos, Ph. D. thesis, EPFL, Lausanne, 2012.

[102] M. Guidi, Ph. D. thesis, EPFL, Lausanne, 2010.

# Chapter 2

# Experimental and Theoretical Approach

This chapter presents the experimental and theoretical approach used to perform the work described in this thesis. It begins with a short overview of the tandem mass spectrometer and an explanation of the basic working principles of some of its essential elements. We then introduce the sample preparation procedure and electrospray ionization technique, followed by a description of the laser setups and spectroscopic techniques used to record different types of spectra. Finally, we discuss the computational methods used to calculate the ground state conformations of AcFAK-$H^+$ and those of the triplet states of $AcFA_5K$-$H^+$.

## 2.1 Experimental apparatus

### 2.1.1 Overview of the tandem mass spectrometer

We conduct all of the experiments in a tandem mass spectrometer, previously designed and built in our laboratory.[1] The experimental apparatus is comprised of several elements, schematically presented in Figure 2.1.

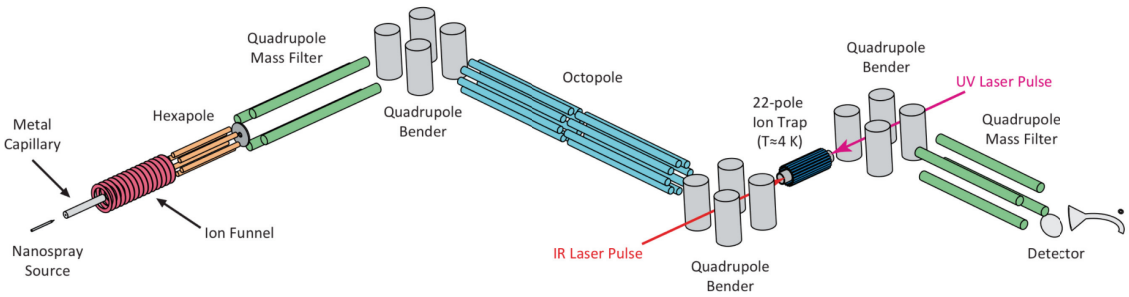


Figure 2.1 Schematic representation of the home-built tandem mass spectrometer.

We produce protonated peptides using a nano-electrospray ionization (ESI) source. The desolvated cations enter vacuum through a metal capillary maintained at a low positive potential. An ion funnel after the metal capillary focuses the initially divergent stream of ions through an orifice, and an RF hexapole guides them into the first quadrupole mass filter, where we select parent ions of a particular m/z ratio. The parent ions turn 90 degrees in a first electrostatic quadrupole bender and enter a linear, RF octopole trap. Helium gas continuously leaks into the octopole, resulting in a pressure of $5 \cdot 10^{-5}$ mbar to pre-trap the ions. After accumulation in the octopole for 80 ms, we release a 20 ms packet of ions and send it through a second electrostatic quadrupole bender and a set of deceleration lenses into a 22-pole ion trap that is cooled to 4 K. The injected ions cool by collisions with He gas, which is pulsed into the trap and given time to equilibrate with the trap housing before the ions arrive. Alternatively, we can pre-trap the ions in the hexapole and use the octopole as an ion guide, in which case we don't leak helium into the octopole section of the instrument. Because of the higher pressure in the hexapole ion trap, the ions thermalize faster, and we can release a shorter ion packet (few hundreds of μs) than when pre-trapping in the octopole.

Focused UV and IR laser beams counter-propagate inside the 22-pole ion trap and interrogate the cold parent ions. A fraction of the molecules that absorb a UV photon dissociate, and the charged fragments along with the parent ions are released from the trap by lowering the exit lens potential. The ions pass through a stack of lenses and a third electrostatic bender into a second quadrupole mass filter, where we select the fragments of a particular m/z ratio and detect them with a channeltron detector.

There are three types of experiments performed on this apparatus. (1) Irradiating the ions with the UV laser and collecting the photofragments with the second quadrupole mass filter as a function of the laser wavenumber produces an electronic photofragment spectrum, which reflects the electronic absorption band. (2) Fixing the UV laser wavelength on a peak that corresponds to a particular conformer and detecting with the second quadrupole mass filter the change in a particular dissociation fragment, while scanning the infrared laser, generates a conformer-specific infrared spectrum. (3) Fixing the wavelength of the lasers and scanning the last quadrupole mass filter yields a photofragment mass spectrum, which contains information on the fragmentation mechanism.

The time sequence of a typical two lasers experiment is schematically depicted in Figure 2.2. The experimental cycle of pulsing the He into the cold trap, filling it with ions, firing the UV laser, emptying the trap and counting the ions is repeated at 10 Hz (i.e. 100 ms cycle time), but

the second (IR) laser is fired with half this frequency. In this way we record two signals: fragmentation caused by the one laser and fragmentation caused by both lasers. This allows us to normalize the spectra to the long terms fluctuations in the parent ion signal.

The instrument has several differential pumping stages to allow the pressure in the section of the 22-pole ion trap to be $< 2 \cdot 10^{-9}$ mbar in the absence of helium buffer gas, which is injected for cooling. This is essential to prevent the freezing of nitrogen and atmospheric water onto the rods of the trap after it cools down to 4 K. By changing the helium pulse duration (250 – 400 μs) we could vary the average pressure in the 22-pole ion trap for different sets of experiments between $5 \cdot 10^{-6} – 1 \cdot 10^{-5}$ mbar.

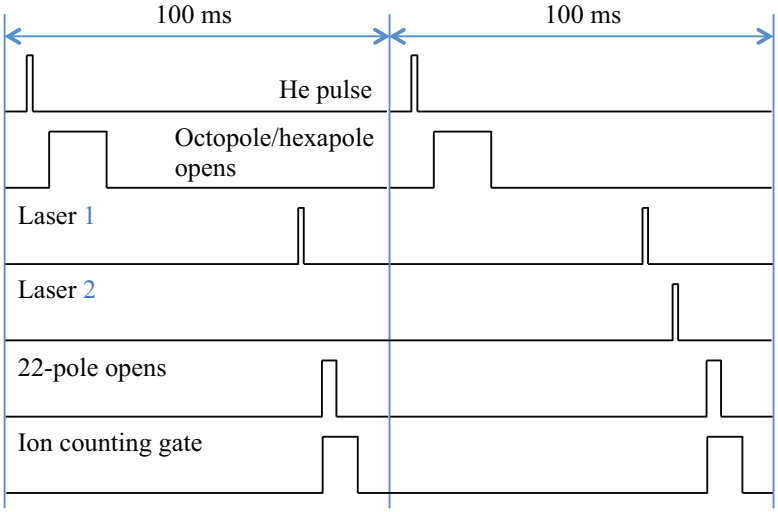


Figure 2.2 Timing of a typical experiment. The pulses represent the timing for the labeled events. The duration of each event varies in different experiments.

## 2.1.2 Sample preparation and electrospray ionization

The peptides $AcFA_5K$, $AcA_5FK$, $AcYA_5K$, and all $^{13}C$ and $^{15}N$ isotopically labeled samples were synthesized by Catherine Servis from the University of Lausanne using solid phase Fmoc chemistry on an Applied Biosystems 433 A synthesizer and purified by high-performance liquid chromatography to a minimum purity of 80% percent. For the synthesis of the singly and doubly $^{13}C$ isotopically labeled $AcFA_5K$ we purchased L-alanine-1-13C, N-FMOC, 99% $^{13}C$ from CortecNet. The peptide AcFAK was purchased from Centic Biotec with 95 % purity.

We dissolve each solid sample in 50:50:0.1 percent water-methanol-acetic acid to obtain 0.1 mM concentration. Sonication in an ultrasonic bath for 10 minutes accelerates its dissolution

without sample degradation as long as special care is taken to avoid a rise of temperature. The prepared solutions are stored in the freezer at -20 °C for later use.

A nano-electrospray ionization (ESI) source (Proxeon, ES070, Odense, Denmark) introduces peptides into the gas phase. The emitter used in the source is metalized borosilicate needle with an inner diameter 1 μm, which is initially sealed. We insert it into a 0.5 mL Eppendorf reservoir filled with the analyte solution and close the volume. The closed volume can be slightly pressurized with nitrogen gas, which helps the liquid fill the needle when its tip is cut. Application of a high positive voltage (1 kV) initiates electrospray ionization (ESI). Protonated peptides emerge into the gas phase from this source even without any pressure. One of the main advantages of nano-ESI over a conventional ESI sources is a low flow rate (20-50 nl/min), which decreases the consumption of expensive analytes.

ESI is a soft ionization method that allows the transfer of large biomolecules from solution into the gas phase without decomposition.[2] The use of ESI as an ion source for studies of macromolecules was first introduced by Dole in 1968[3] and further developed by Fenn and coworkers,[4-6] for which Fenn received a share in Nobel Prize in Chemistry in 2002. The schematic representation of the ESI process[7] is depicted in Figure 2.3. When high voltage is applied between the needle tip and the metal capillary, the liquid with analyte is oxidized and forms a Taylor cone.[5] Depending on the polarity of the applied voltage, either negatively or positively charged droplets are emitted from this cone and driven towards the capillary.

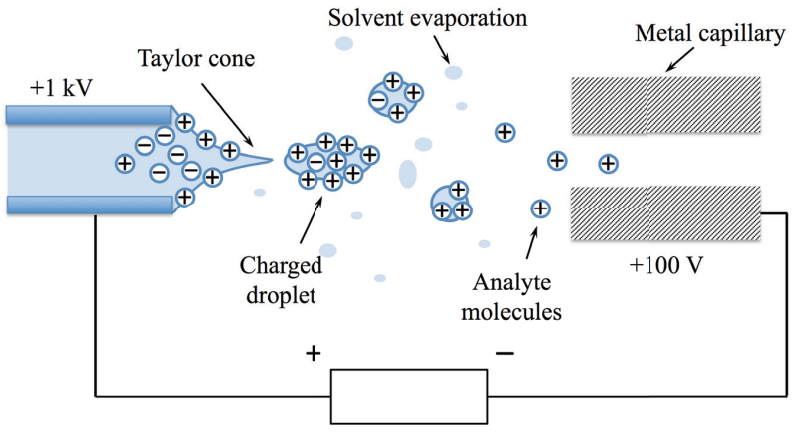


Figure 2.3 Schematic representation of the ESI process.

There are two main mechanisms that are used to explain the release of single analyte ions from these charged droplets:[8] the charge residue model (CRM)[3] and the ion evaporation model

(IEM).[9, 10] According to the CRM, neutral solvent evaporates from the charged droplets due to collisions with the surrounding gas, decreasing the size of the droplets. When Coulombic repulsion of the charge at the surface of the droplet exceeds the surface tension, the droplet divides into smaller droplets. The CRM proposes that this process continues up to the point when the charged molecules are completely desolvated. The IEM proposes that once the field on the droplet surface is sufficiently high the free energy of the ions in the droplet is higher than what they would be in vacuum and they spontaneously evaporate into the gas phase. There are still debates regarding which model is correct, but it is likely that both of them might take place during the ESI process, depending on the droplet size regime.[8, 11]

## 2.1.3 Ion traps and guides

### 2.1.3.1 Ion funnel

The ESI source works at atmospheric pressure. To limit the gas flow into the first vacuum chamber of the mass spectrometer, which is maintained at pressure ~2 mbar, the ions pass through a metal capillary with inner diameter of 0.5 mm. The ion beam exits the metal capillary as a slight jet expansion due to the presence of the background gas and a pressure difference.

In high vacuum ion motion can be manipulated precisely using conventional ion optics, however, at the elevated pressures (~2 mbar) that typically occur at the entrance of mass spectrometers, the motion of the ions is dominated by collisions with the background gas. Ion funnels are radio frequency devices that serve to focus the divergent ion beams coming from the ESI source to increase their transmission into the mass spectrometer.[12] The first design of an ion funnel was introduced by Shaffer et al.[13] It was a stacked ring radio-frequency ion guide similar to the one described by Gerlich,[14] but with ring electrodes gradually decreasing in diameter that allowed the focusing of the spatially dispersed ions. The effective potential creates a near field free region over most of the volume and increases steeply near the electrodes that confines the ions in the radial direction. The addition of a DC potential gradient later implemented by Shaffer et al[15] allows more efficient extraction of the ions from the funnel exit. The design of the ion funnel in our instrument follows the one of Smith and co-workers[16, 17] and is described in detail elsewhere. [1, 18]

### 2.1.3.2 Quadrupole mass analyzers

We use linear, RF quadrupoles as mass filters during a typical experiment: the first quadrupole selects the m/z of the parent ions out of all those entering the mass spectrometer from solution, and the second transmits photofragments with a selected m/z. Each RF quadrupole consists of four parallel rods, with opposing rods being electrically connected. Between each connected pair of rods a voltage of opposing polarity is applied ±(U−VcosΩt), where U is the DC voltage, V is the amplitude and Ω is the frequency of the RF field. This creates a radial potential that confines the ions in the x-y plane. The trajectories of the ions inside the quadrupole can be described with a special case of the Mathieu differential equations. For a given ratio U/V only the ions of a particular m/z within the small stability region will have stable trajectories and will be transmitted through the quadrupole in the z-direction. By linearly scanning the applied voltages while keeping the U/V ratio fixed (scanning line on the stability diagram), one can continuously scan quadrupole for a range of m/z values and record a mass spectrum.

### 2.1.3.3 Higher order multipoles for ion guiding and trapping

In quadrupoles the x and y motion of the ions can be decoupled, which allows them to be used as mass analyzers. In higher order multipoles this decoupling is no longer possible, but the axial motion of the ions can be nevertheless described by an effective potential,[11, 14]

$$U_{eff}(r) = \frac{n^2 z^2 V^2}{4m\Omega^2 {r_0}^2}\left(\frac{r}{r_0}\right)^{2n-2}$$

where 2n is the number of rods, z is the charge of the ion, m is the ion mass, V is the amplitude of the RF field, Ω is the frequency of the RF field, r is the radial distance from the axial center of the multipole, and $r_0$ is the inscribed radius for the rods. We use RF hexapoles (2n=6) and octopoles for guiding ions through the various sectors of our machine. In combination with DC potentials on end-cap electrodes, we can also use these devices as traps for storing ions.

The key element in the experimental apparatus of Figure 2.1 is the cold, 22-pole ion trap, which we used to cool the molecules and hence simplify their spectra. To fully exploit RF ion traps for cooling molecules, one has to consider the details of ion motion in the presence of a cold buffer gas. The motion of the ions consists of a smooth trajectory modulated by the wiggling motion at the RF frequency as the ions approach the electrodes.[14] If an ion has a collision with the buffer gas during these fast oscillations, its kinetic energy can be converted to internal energy of the ions, resulting in so-called RF heating. For a higher number of rods, the

effective radial potential will be flatter and the region of wiggling motion where the RF heating takes place will be smaller. Gerlich was the first to design a cryogenically cooled 22-pole ion trap to study small ions of astrophysical importance at low temperatures.[14, 19] Inspired by these experiments, Rizzo and co-workers coupled an ESI source with a cryogenically cooled 22-pole ion trap to record conformer specific infrared spectra of cold biological molecules.[20] While temperatures of 10 – 12 K were achieved,[1, 20, 21] the radial distribution of the ions in the 22-pole trap is spread due to its shallow effective radial potential. Moreover, the DC field from endcap electrodes confining the ions in the axial direction can penetrate inside the trap and push the ions off axis, creating an ion cloud with a dip on the axis.[22, 23] This is a disadvantage of the 22-pole ion trap, particularly for multiple-laser experiments, where several laser beams have to overlap with each other and with the ion cloud.

Recently, Oleg Aseev in our laboratory has designed and built an octopole ion trap, which we use in place of our 22-pole ion trap. Boyarkin and Kopysov have shown that vibrational cooling of YA-$H^+$ (m/z=253) in an octopole ion trap of a similar design is as efficient as in a cold 22-pole.[24] RF heating scales up with decreasing the mass ratio between ions and buffer gas and thus is not so important for ions of high mass.[25] The advantage of the cold octopole over the 22-pole is that due to a steeper radial effective potential well the ions are confined closer to the center axis of the trap and hence overlap better with the laser beams. Some of the latest experiments described in this thesis were performed in the cryogenically cooled octopole, as explained later in the text.

### 2.1.4 Ion detection

Batey has summarized different ion detectors used in quadrupole mass spectrometers.[26] In our tandem mass spectrometer we detect ions with a channeltron electron multiplier (DeTech, 402-A-H). The device consists of a hollow curved cylinder covered on the inside with a lead glass, which is specially processed to yield an efficient secondary electrons emitting layer. Its operation principal is similar to the one described by Goodrich and Wiley.[27] By applying high voltage between the opposite ends of the cylinder (entrance ~ -2 kV, exit grounded), we create a gradient of the potential. The positively charged ions hit the conversion dynode held at -5 kV, resulting in the emission of secondary electrons that accelerate towards the entrance of the channel electron multiplier held at lower potential. When those electrons hit the inner surface of the cylinder they generate more secondary electrons with the transverse velocity component. The transverse motion of the emitted electrons is combined with the longitudinal acceleration along the field

gradient. The electrons strike the inner walls of the cylinder in zigzag manner, generating more secondary electrons while moving towards the exit electrode. The current from the exit electrode is further amplified in a fast counting preamplifier (50000 counts per ms) and is detected as a pulse. Because of the fast response time of the channeltron detector, separate pulses of the current corresponding to the single ions arriving at the detector can be counted within the time specified by the ion counting gate (Figure 2.2). However, at high ion count rates saturation effects start to play a role, which makes it difficult to compare the absolute amounts of parent and fragment ions in one mass spectrum (See ref.[18] for details).

## 2.1.5 Laser setups

### 2.1.5.1 Generation of ultraviolet light

We produce ultraviolet light by doubling the visible output of a Nd:YAG (Neodymium-doped yttrium aluminium garnet) pumped tunable dye laser. Different dyes used in the lasers cover different regions of the electronic spectrum. A Lambda Physik tunable dye laser (Scanmate 2E) is pumped with the third harmonic (355 nm) of the Nd:YAG fundamental (1064 nm) and used with dyes that generate light below 560 nm. A Lumonics tunable dye laser (HD-500) is pumped with the second harmonic (532 nm) of the Nd:YAG fundamental and used to produce light of longer wavelengths. The output radiation from the visible dye laser passes through a BBO (Beta Barium Borate) crystal and partially converts into the UV light through second harmonic generation. The BBO crystal is mounted inside an autotracking device (Inrad, Autotracker III) that automatically rotates the crystal to fulfill the phase matching conditions as the wavelength of the visible laser changes. To compensate for the walk of the beam due to the rotation of the BBO crystal, a fused silica compensator is used. After the laser beam exits the Autotracker III, we cut most of the remaining visible radiation with an optical filter (Thorlabs, FGUV5S) and then further separate the UV beam by reflecting it from a dichroic mirror. We use a telescope composed from two UV lenses with variable distance (fused silica, 2:1 reduction factor) to reduce the size of the UV beam and slightly focus it inside the 22-pole ion trap (to a diameter of ~1 mm). The typical output UV power is 1–2 mJ/pulse. The pulse duration is ~5 ns and the line width is ~0.07 $cm^{-1}$ for both Lumonics and Lambda Physik dye lasers as measured by wavelength meter (HighFinesse, WS-6).

When recording the UV spectra, we also record the power of the UV light for every laser shot by directing the reflection from the $BaF_2$ entrance window of the machine into a pyroelectric detector connected to the digital oscilloscope.

### 2.1.5.2 Generation of infrared light in 3 micron and 6 micron region

To generate infrared light in the NH stretch region (3 micron) we use a tunable infrared optical parametric oscillator/amplifier (IR OPO/OPA) (LaserVision) pumped by the fundamental from a Nd:YAG laser. The schematic layout of the optical system is presented in Figure 2.4. A beamsplitter (1) divides the horizontally polarized 1064 nm pump beam into two – one pumps the OPO stage, and the other propagates into the OPA stage. The former passes through the half-wave plate (2) that changes its polarization to vertical before it is doubled in frequency in a Potassium Titanyl Phosphate (KTP) crystal (3) to pump the OPO stage with 532 nm vertically polarized light. The latter propagates through the half-wave plate (4) that also changes its polarization to vertical. The relative position between the grating (5), the tuning mirror (6) and the back mirror (7) determines the cavity length of the oscillator. For each wavelength, the angle of the other non-linear KTP crystal (8) is adjusted to ensure an efficient difference frequency mixing. The resulting idler wave is vertically polarized, and the signal wave is horizontally polarized, which is determined by the type II phase matching of the KTP crystal. Both waves from the OPO stage pass through the half-wave plate (9) to change their polarization. This is done for safety reasons, so that all the crystals of the OPA stage are rotated in the horizontal plane for phase matching conditions. The horizontally polarized idler wave from the OPO stage selected with the silicon plate (10) serves as a signal wave when combining with the 1064 nm pump beam from the OPA stage (11). The signal and pump beams co-propagate through four Potassium Titanyle Arsenate (KTA) crystals (12) for difference frequency mixing. Following the OPA stage, a dichroic mirror (13) removes the residual 1064 nm pump wave from the combined output. A Brewster plate polarizer (14) separates the vertically polarized idler wave from the IR OPO/OPA output, which is tunable in the mid-infrared region 2600–4000 $cm^{-1}$ with the spectral resolution ~1.5 $cm^{-1}$. The output power of the idler beam is 5–12 mJ/pulse, and we can attenuate it by rotating the half-wave plate (4) before the OPA stage. A periscope made of two gold mirrors inverts again the polarization of the idler beam. The horizontally polarized IR laser light enters the machine through a $BaF_2$ window placed at the Brewster angle. A 50 cm lens focuses the infrared beam inside the 22-pole ion trap for better overlap with the UV beam, propagating from the opposite side of the machine (Figure 2.1).

To generate IR laser light in the Amide I and II regions (6 micron) we add a Silver Gallium Selenide ($AgGaSe_2$) crystal 50 cm away from the output of the IR OPO/OPA. The Brewster plate polarizer is removed to allow difference frequency mixing of the signal and idler beams coming from the IR OPO/OPA into the crystal. The resulting laser light is tunable in the region

1300–2000 $cm^{-1}$ with an output power of 1–2 mJ/pulse and spectral resolution ~2 $cm^{-1}$. A ZnSe filter, placed just after the $AgGaSe_2$ crystal, removes the remaining idler and signal beams from the IR OPO/OPA output. We use the same optical scheme to guide the vertically polarized far-infrared laser light into the machine as for the mid-infrared light, but adjust the position of the lens, because the refractive index decreases with increasing wavelength.

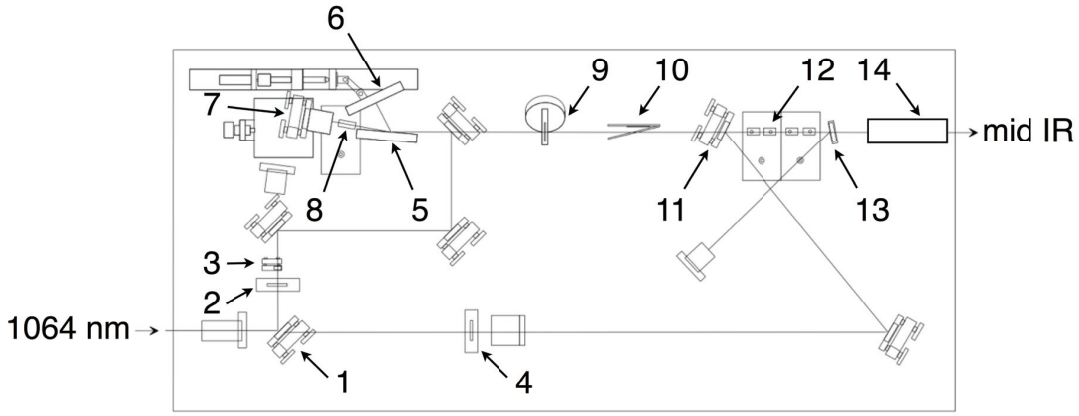


Figure 2.4 The schematic layout of IR OPO/OPA. Adapted from LaserVision manual.

A silicon plate at Brewster angle, which transmits IR radiation and reflects UV, protects the gold mirrors from the UV irradiation coming from the opposite side of the machine. We record the infrared laser power every laser shot by guiding the remaining infrared reflection from the silicon plate onto the pyroelectric detector .

### 2.1.5.3 Generation of infrared light in 10 micron region

We produce light in the 10 micron region with a Transversely Excited Atmospheric (TEA) $CO_2$ laser (PIC, model SP-7000[28]). The $CO_2$ laser works under the atmospheric pressure, and is energized by a high voltage electrical discharge in a gas mixture of 20% $CO_2$, 20% $N_2$, and 60% He. It is not continuously tunable and can generate light only at the frequencies of the rovibrational lines of the $CO_2$ molecule. Because we use the $CO_2$ laser for multiphoton excitation and do not need to scan its wavelength, we replaced the grating with a mirror for easier alignment of the cavity. The typical output power is ~350 mJ/pulse. The time profile of the pulse consists of a leading spike of ~50 ns duration caused by the radiation of the $CO_2$ molecules directly excited by the discharge and a tail of ~5 μsec caused by the radiation of the $CO_2$ molecules excited through collisional transfer from the $N_2$ molecules. The laser delivers 80% of

its power within the first 100 ns. A 100 cm ZnSe lens focuses the divergent output beam, which enters the machine from the same side as the mid- or far-infrared laser light.

## 2.2 Spectroscopic schemes

### 2.2.1 UV photofragment spectroscopy

We record a UV photofragmentation excitation spectrum by monitoring the amount of photofragments at a particular m/z as a function of the UV laser wavenumber (Figure 2.5). The fragmentation happens directly or indirectly from the electronically excited state or after the internal conversion to the ground state, revealing different types of photofragments. The exact mechanism of the UV fragmentation is a topic of the current thesis and will be discussed in detail in the next chapter. Cryogenic cooling allows us to obtain sharp transitions in the UV spectrum, some of which correspond to vibronic progressions and some are due to the existence of different conformers.

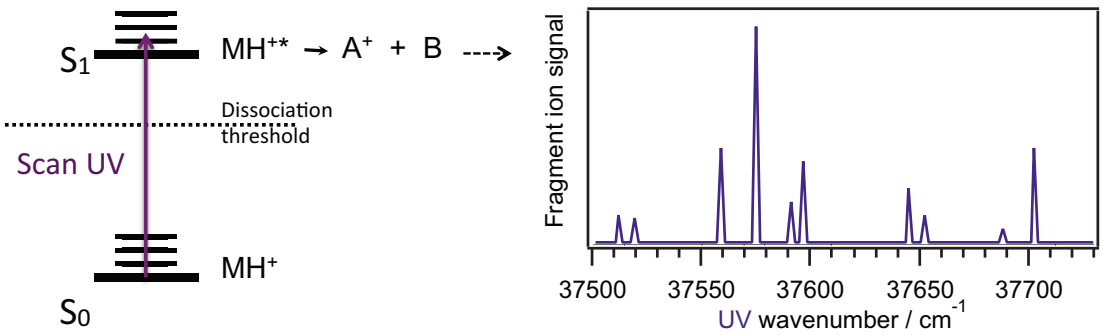


Figure 2.5 The schematic representation of UV photofragment spectroscopy.

### 2.2.2 IR-UV double resonance spectroscopy

IR-UV double resonance spectroscopy allows recording conformer specific infrared spectra of molecules in their ground electronic state (Figure 2.6). In this case, we fix the UV laser on one peak in the electronic spectrum associated with a particular conformer and introduce the IR OPO light ~150 ns earlier. If the frequency of the IR OPO coincides with the vibrational transition of this conformer in the grounds state, the UV fragmentation signal decreases because of the difference in UV absorption between molecules in the ground and vibrationally excited states.[29]

We record an infrared spectrum by monitoring the difference in the UV photofragmentation with and without the IR OPO as a function of the infrared wavenumber.

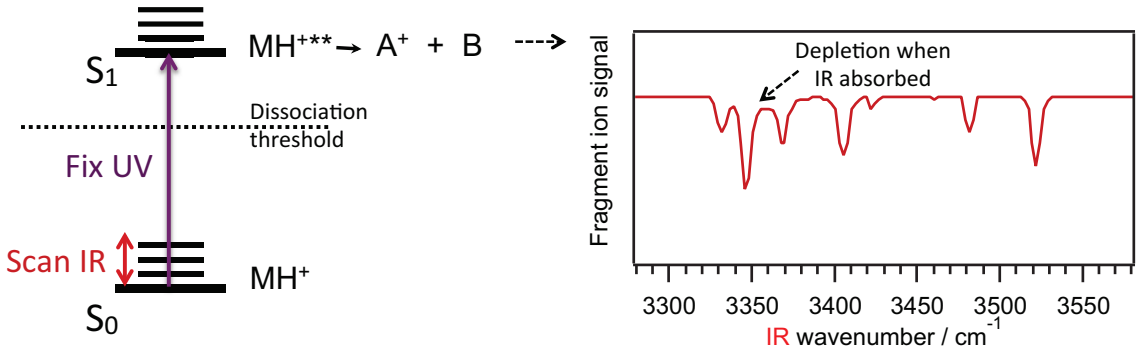


Figure 2.6 The schematic representation of IR-UV double resonance photofragment spectroscopy.

## 2.2.3 Infrared laser assisted photofragment spectroscopy (IRLAPS)

Because the photofragmentation yield following UV excitation is low, the Infrared Laser Assisted Photofragment Spectroscopy (IRLAPS) technique can be applied to enhance it, as illustrated in Figure 2.7. This method was previously used to record high vibrational overtone spectra of small neutral molecules[30-34] and then developed in our group to increase the photofragmentation efficiency of large biomolecular ions.[35, 36] After UV excitation of protonated peptides, an intense $CO_2$ laser pulse further energizes the ions *via* infrared multiphoton excitation (IRMPE), which greatly enhances the photofragmentation yield. The mechanism of the IRLAPS technique applied to large biomolecules is further discussed in Chapter 3.

## 2.2.4 UV-IR double resonance spectroscopy

The fact that infrared excitation enhances fragmentation of molecules promoted to the excited electronic state allows us to record infrared spectra of the electronically excited species by replacing the $CO_2$ laser with a continuously tunable, infrared optical parametric oscillator/amplifier. As illustrated schematically in Figure 2.8, the absorption of one or more IR photons in resonance with vibrational transitions of the electronically excited molecule can be detected as an increase of fragmentation yield. Because the UV laser can excite a single conformer of the molecule, conformer-specific IR spectra of the electronically excited species can be recorded, provided that the lifetime of the electronically excited state is longer than the

delay between pump and probe laser pulses. To be sure that the molecules are still in the $S_1$ state,the IR OPO probes the molecules 5 ns after the UV excitation, the shortest delay possible with our nanosecond lasers. By gradually increasing the delay between the UV laser and the IR OPO, we can monitor the deactivation dynamics, provided that the molecules that absorb infrared light fragment more efficiently than those that absorb only the UV photon.

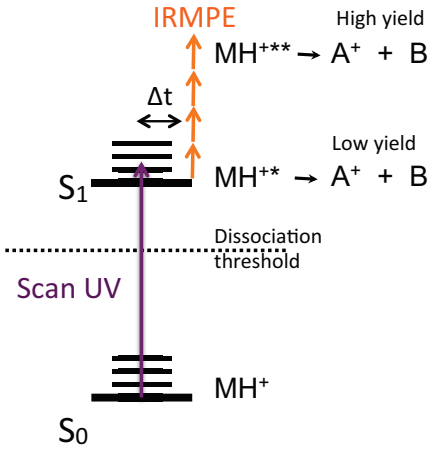


Figure 2.7 The schematic representation of the infrared laser assisted photofragment spectroscopy (IRLAPS).

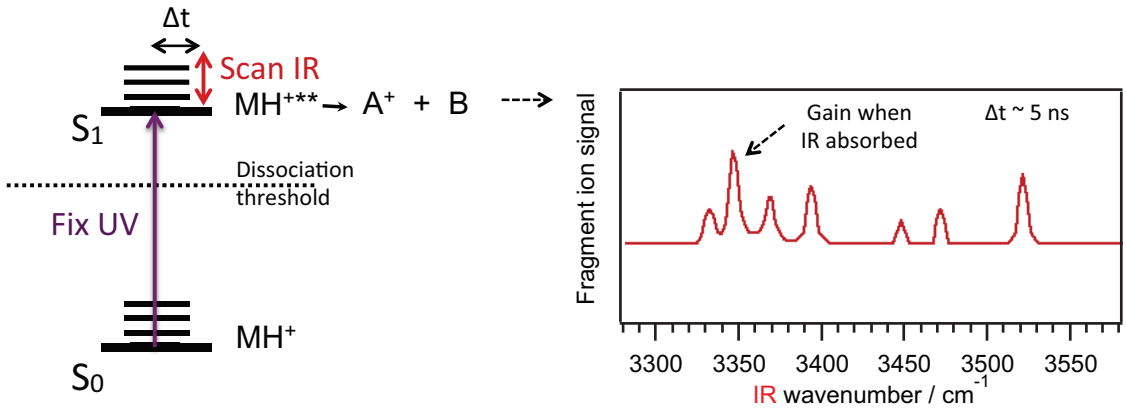


Figure 2.8 The schematic representation of UV-IR double resonance photofragment spectroscopy.

This approach is similar to that used by Huber and co-workers to study the electronically excited states of propynal[37] and that applied by Dian et al. for measuring IR spectra in excited states of indole and its derivatives.[38] Ebata and co-workers used analogous method to record infrared spectra of the electronically excited phenol-water clusters,[39] benzene and toluene,[40] and neutral aniline,[41] produced in supersonic jet expansion. In general, the quantum yield of fluorescence from the vibronic levels of $S_1$ state is much smaller than that from the zero-point

level, which allows one to record the IR spectrum by detecting a dip in fluorescence upon IR excitation.[37] The other detection method demonstrated by Matsumoto et al.[42] for hydrogen-bonded clusters of 2-naphthol involves the predissociation of the weakly bound clusters after the IR excitation. If the energy of the IR pulse following the electronic excitation is higher than the hydrogen bonding energy of the cluster, it dissociates into photofragments. Then one can monitor the background-free fluorescence from the photofragments to record the IR spectra of $S_1$ state of the clusters. In our case we record conformer-selective vibrational spectra of electronically excited molecules by detecting an increase in photofragment yield subsequent to IR absorption. The detailed explanation why this method of detection works for phenylalanine- and tyrosine- containing peptides will be also discussed in Chapter 3.

## 2.3 Computational methods

### 2.3.1 Calculation of AcFAK-$H^+$ ground state structures

The approach used in this thesis to determine the lowest energy structures of AcFAK-$H^+$ molecules is based on the comparison of experimental conformer-specific infrared spectra with calculated infrared spectra. In principle, for a system containing N nuclei and n electrons, the binding arising from the repulsive and attracting quantum interactions between the charges can be described by a total wavefunction through the exact solution of the Schrödinger equation. However, in general, the Schrödinger equation cannot be solved exactly and several approximation methods exist. By selecting a proper method and a basis set in a quantum mechanical software packages, one can usually obtain relatively good results for small molecules.

Because pure quantum mechanical methods are very time consuming, we use a combination of classical mechanics and quantum mechanical calculations. In classical mechanics the molecules are simply represented as atoms connected with each other by the set of springs acting as the chemical forces. These forces can be modeled with parameterized force fields. We use a Monte Carlo method to randomly explore the potential energy surface (PES) and determine the initial geometries for further optimization with a more precise density functional theory (DFT) method, based on an approximate solution of the Schrödinger equation.

#### 2.3.1.1 Method I

For the initial conformational search we carried out Monte Carlo simulations in the Conflex program[43] with the Merck molecular force field (MMFF94s)[44, 45] and the upper limit energy value of 1 kcal/mol. We found 60 conformations, some of which had different rotations of the aromatic side-chain and hydrogen-bonding patterns. To eliminate redundant conformations DFT calculations were performed at the B3LYP[46-48]/6-31+G** level of theory with the loose optimization criteria using Gaussian 09 program.[49] The optimized structures with the similar energies and torsion angles were grouped into families. For the most stable conformations out of 10 different families we re-optimized the structures in Gaussian09 removing the loose optimization criteria and calculated the vibrational frequencies. The total energies are corrected for zero-point energies using unscaled harmonic frequencies. For comparison to the measured infrared spectra, the calculated vibrational frequencies are scaled by factors of 0.987 and 0.952 in the hydride stretch and fingerprint regions of the vibrational spectra, respectively. Different levels of theory require different scale factors to account for anharmonicity effects, which have been discussed in the work of Bouteiller et al.[50]

#### 2.3.1.2 Extension of method I

Since the geometry optimization and frequency calculation with the traditional density functional B3LYP [46] did not provide a satisfactory match with experiment, we started exploring other theoretical methods. Hohenstein et al. showed that the empirical exchange correlation functionals, M05-2X and M06-2X, better describe noncovalent interactions than the traditional density functionals without dispersion correlation.[51] In a molecule such as AcFAK-$H^+$, the NH-π interaction plays an important role and has to be carefully taken into account. Four lowest energy structures after the geometry optimization at the B3LYP[46]/6-31+G** density functional level of theory were geometry-re-optimized at the M05-2X[47, 52]/6-31G** density functional level of theory with tight convergence criteria and an ultrafine grid. Rothlisberger and co-workers performed an extensive assessment of computational methods,[53] and the M05-2X level of theory yielded highly reliable geometries and vibrational spectra of gas-phase bare and micro-solvated tryptophan and gas-phase doubly protonated gramicidin S.[54] Buchanan et al. also confirmed the excellent reproduction of the vibrational frequencies and infrared intensities using this level of theory for various α-peptides, β-peptides, α/β-peptides and γ-peptides.[55] For the geometries optimized using M05-2X functional, we calculated the harmonic vibrational frequencies using B3LYP/6-31G** density functional level of theory (the approach is similar to the one used in

ref. [54]). The resulting frequencies were scaled by a factor 0.94 and 0.955 in the hydride stretch and fingerprint regions of the vibrational spectra, respectively, for the comparison with the experiment.

#### 2.3.1.3 Method II

We repeated the conformational search in Macro Model[56] using the optimized potentials for liquid simulations (OPLS) force field[57-59] with the following parameters of the search: mixed torsional/low-mode sampling, intermediate, 50000 steps, 1000 steps per rotatable bond, and 50 kJ/mol energy window. The Monte Carlo search generated 13578 structures, 785 different structures in the specified energy window. The lowest energy structure was found 21 times. We re-optimized the geometries of 60 lowest energy structures using M05-2X/6-31G** density functional level of theory. All the structures with the chromophore-charge interaction appeared to be more then 20 kJ/mol higher in energy then the other structures, for which the lysine $NH_3^+$ group interacts with the carbonyls. For the lowest energy structures, in which the lysine $NH_3^+$ group forms three hydrogen bonds with C=Os and the position of the chromophore differs only by the rotation around $C_\alpha$-$C_\beta$ bond (the justification to choose only those structures is dictated by the constraints discussed in Chapter 4), the geometry was re-optimized and the vibrational frequencies were calculated using M05-2X/6-31++G** density functional level of theory with tight convergence criteria and an ultrafine grid. The harmonic frequencies were scaled by 0.937 and 0.959 in the hydride stretch and fingerprint regions of the vibrational spectra, respectively.

### 2.3.2 Calculation of $AcFA_5K\text{-}H^+$ lowest triplet state structures

Stearns et al. previously reported the geometries for the four lowest energy conformations of $AcFA_5K\text{-}H^+$, calculated using DFT B3LYP/6-31G** in Gaussian 03.[60] We changed the spin multiplicity and utilized these geometries as an input structure for the full geometry optimization and harmonic frequency analysis of the conformations in the triplet state using the unrestricted hybrid density functional DFT-UB3LYP method[46-48] with a 6-31G** basis set in Gaussian 09.[49] The calculations are unrestricted in that the states with spin up and down for each orbital can be treated using independently constructed spatial wave functions. The resulting harmonic frequencies are scaled by the same factor 0.952 that was used to scale the frequencies of the ground state structures and the energies are zero-point energy corrected.

# References


[1] A. Svendsen, U. J. Lorenz, O. V. Boyarkin, and T. R. Rizzo, Rev. Sci. Instrum. **81** (2010).

[2] J. B. Fenn, M. Mann, C. K. Meng, S. F. Wong, and C. M. Whitehouse, Science **246**, 64 (1989).

[3] M. Dole, L. L. Mack, and R. L. Hines, J. Chem. Phys. **49**, 2240 (1968).

[4] J. B. Fenn, J. Biomol. Tech. **13** (2002).

[5] M. Yamashita and J. B. Fenn, J. Phys. Chem. **88**, 4451 (1984).

[6] M. Yamashita and J. B. Fenn, J. Phys. Chem. **88**, 4671 (1984).

[7] N. B. Cech and C. G. Enke, Mass Spectrom. Rev. **20**, 362 (2001).

[8] P. Kebarle and M. Peschke, Anal. Chim. Acta **406**, 11 (2000).

[9] J. V. Iribarne and B. A. Thomson, J. Chem. Phys. **64**, 2287 (1976).

[10] B. A. Thomson and J. V. Iribarne, J. Chem. Phys. **71**, 4451 (1979).

[11] J.-P. Schermann, *Spectroscopy and Modelling of Biomolecular Building Blocks* (Elsevier, 2008).

[12] R. T. Kelly, A. V. Tolmachev, J. S. Page, K. Tang, and R. D. Smith, Mass Spectrom. Rev. **29**, 294 (2010).

[13] S. A. Shaffer, K. Q. Tang, G. A. Anderson, D. C. Prior, H. R. Udseth, and R. D. Smith, Rapid Commun. Mass Spectrom. **11**, 1813 (1997).

[14] D. Gerlich, Adv. Chem. Phys. **82**, 1 (1992).

[15] S. A. Shaffer, A. Tolmachev, D. C. Prior, G. A. Anderson, H. R. Udseth, and R. D. Smith, Anal. Chem. **71**, 2957 (1999).

[16] T. Kim, K. Q. Tang, H. R. Udseth, and R. D. Smith, Anal. Chem. **73**, 4162 (2001).

[17] T. Kim, A. V. Tolmachev, R. Harkewicz, D. C. Prior, G. Anderson, H. R. Udseth, R. D. Smith, T. H. Bailey, S. Rakov, and J. H. Futrell, Anal. Chem. **72**, 2247 (2000).

[18] U. Lorenz, Ph. D. thesis, EPFL, Lausanne, 2011.

[19] D. Gerlich, Phys. Scripta **T59**, 256 (1995).

[20] O. V. Boyarkin, S. R. Mercier, A. Kamariotis, and T. R. Rizzo, J. Am. Chem. Soc. **128**, 2816 (2006).

[21] J. G. Redwine, Z. A. Davis, N. L. Burke, R. A. Oglesbee, S. A. McLuckey, and T. S. Zwier, Int. J. Mass Spec. **348**, 9 (2013).

[22] S. Trippel, J. Mikosch, R. Berhane, R. Otto, M. Weidemueller, and R. Wester, Physical Review Letters **97** (2006).

[23] O. Asvany and S. Schlemmer, Int. J. Mass Spec. **279**, 147 (2009).

[24] O. V. Boyarkin and V. Kopysov, Rev. Sci. Instrum. **85** (2014).

[25] D. Gerlich and S. Horning, Chem. Rev. **92**, 1509 (1992).

[26] J. H. Batey, Vacuum **101**, 410 (2014).

[27] G. W. Goodrich and W. C. Wiley, Rev. Sci. Instrum. **33**, 761 (1962).

[28] Physics Instrumentation Center, Troitsk, Russia, http://www.lasersys.ru.

[29] N. S. Nagornova, T. R. Rizzo, and O. V. Boyarkin, Angew. Chem., Int. Ed. **52**, 6002 (2013).

[30] O. V. Boyarkin, R. D. F. Settle, and T. R. Rizzo, PhysChemChemPhys **99**, 504 (1995).

[31] L. Lubich, O. V. Boyarkin, R. D. F. Settle, D. S. Perry, and T. R. Rizzo, Faraday Discuss. **102**, 167 (1995).

[32] O. V. Boyarkin and T. R. Rizzo, J. Chem. Phys. **105**, 6285 (1996).

[33] O. V. Boyarkin, L. Lubich, R. D. F. Settle, D. S. Perry, and T. R. Rizzo, J. Chem. Phys. **107**, 8409 (1997).

[34] J. Makowe, O. V. Boyarkin, and T. R. Rizzo, J. Phys. Chem. A **104**, 11505 (2000).

[35] M. Guidi, U. J. Lorenz, G. Papadopoulos, O. V. Boyarkin, and T. R. Rizzo, J. Phys. Chem. A **113**, 797 (2009).

[36] M. Guidi, Ph. D. thesis, EPFL, Lausanne, 2010.

[37] T. Walther, H. Bitto, T. K. Minton, and J. R. Huber, Chem. Phys. Lett. **231**, 64 (1994).

[38] B. C. Dian, A. Longarte, and T. S. Zwier, J. Chem. Phys. **118**, 2696 (2003).

[39] T. Ebata, N. Mizuochi, T. Watanabe, and N. Mikami, J. Phys. Chem. **100**, 546 (1996).

[40] C. Minejima, T. Ebata, and N. Mikami, Phys. Chem. Chem. Phys. **4**, 1537 (2002).

[41] T. Ebata, C. Minejima, and N. Mikami, J. Phys. Chem. A **106**, 11070 (2002).

[42] Y. Matsumoto, T. Ebata, and N. Mikami, J. Phys. Chem. A **105**, 5727 (2001).

[43] Conflex, version 7, http://www.conflex.us.

[44] T. A. Halgren, J. Comput. Chem. **20**, 730 (1999).

[45] T. A. Halgren, J. Comput. Chem. **17**, 490 (1996).

[46] A. D. Becke, J. Chem. Phys. **98**, 5648 (1993).

[47] C. T. Lee, W. T. Yang, and R. G. Parr, Phys. Rev. B **37**, 785 (1988).

[48] A. D. Becke, Phys. Rev. A **38**, 3098 (1988).

[49] M. J. Frisch, G. W. Trucks, H. B. Schlegel, G. E. Scuseria, M. A. Robb, J. R. Cheeseman, G. Scalmani, V. Barone, B. Mennucci, G. A. Petersson, H. Nakatsuji, M. Caricato, X. Li, H. P. Hratchian, A. F. Izmaylov, J. Bloino, G. Zheng, J. L. Sonnenberg, M. Hada, M. Ehara, K. Toyota, R. Fukuda, J. Hasegawa, M. Ishida, T. Nakajima, Y. Honda, O. Kitao, H. Nakai, T. Vreven, J. A. Montgomery, J. E. Peralta, F. Ogliaro, M. Bearpark, J. J. Heyd, E. Brothers, K. N. Kudin, V. N. Staroverov, R. Kobayashi, J. Normand, K. Raghavachari, A. Rendell, J. C. Burant, S. S. Iyengar, J. Tomasi, M. Cossi, N. Rega, J. M. Millam, M. Klene, J. E. Knox, J. B. Cross, V. Bakken, C. Adamo, J. Jaramillo, R. Gomperts, R. E. Stratmann, O. Yazyev, A. J. Austin, R. Cammi, C. Pomelli, J. W. Ochterski, R. L. Martin, K. Morokuma, V. G. Zakrzewski, G. A. Voth, P. Salvador, J. J. Dannenberg, S. Dapprich, A. D. Daniels, Farkas, J. B. Foresman, J. V. Ortiz, J. Cioslowski, and D. J. Fox, *Gaussian 09, Revision B.01* (Gaussian, Inc., Wallingford CT, 2009).

[50] Y. Bouteiller, J. C. Gillet, G. Gregoire, and J. P. Schermann, J. Phys. Chem. A **112**, 11656 (2008).

[51] E. G. Hohenstein, S. T. Chill, and C. D. Sherrill, J. Chem. Theory Comput. **4**, 1996 (2008).

[52] Y. Zhao, N. E. Schultz, and D. G. Truhlar, J. Chem. Theory Comput. **2**, 364 (2006).

[53] M. Doemer, M. Guglielmi, P. Athri, N. S. Nagornova, T. R. Rizzo, O. V. Boyarkin, I. Tavernelli, and U. Rothlisberger, Int. J. Quantum Chem. **113**, 808 (2013).

[54] N. S. Nagornova, M. Guglielmi, M. Doemer, I. Tavernelli, U. Rothlisberger, T. R. Rizzo, and O. V. Boyarkin, Angew. Chem., Int. Ed. **50**, 5383 (2011).

[55] E. G. Buchanan, W. H. James, S. H. Choi, L. Guo, S. H. Gellman, C. W. Müller, and T. S. Zwier, J. Chem. Phys. **137** (2012).

[56] MacroModel, version 10.3, (Schrödinger, LLC, New York, 2014).

[57] G. Kaminski, E. M. Duffy, T. Matsui, and W. L. Jorgensen, J. Phys. Chem. **98**, 13077 (1994).

[58] W. L. Jorgensen, J. D. Madura, and C. J. Swenson, J. Am. Chem. Soc. **106**, 6638 (1984).

[59] W. L. Jorgensen, D. S. Maxwell, and J. TiradoRives, J. Am. Chem. Soc. **118**, 11225 (1996).

[60] J. A. Stearns, C. Seaiby, O. V. Boyarkin, and T. R. Rizzo, Phys. Chem. Chem. Phys. **11**, 125 (2009).

# Chapter 3

# Fragmentation mechanism of UV-excited, protonated peptides in the gas-phase

In this chapter we describe our study of the fragmentation dynamics of phenylalanine- and tyrosine-containing protonated peptides upon UV excitation. We seek to understand, among other things, the reasons for the rupture of $C_\alpha$-$C_\beta$ bond of the aromatic amino acids, which seems to occur somewhat generally in protonated peptides. Using the molecules $AcFA_5K$-$H^+$, AcFAK-$H^+$, $AcA_5FK$-$H^+$ and $AcYA_5K$-$H^+$ as examples, we develop a spectroscopic technique that allows monitoring the time evolution of the infrared spectra after UV excitation. We propose a fragmentation model involving intersystem crossing to the triplet state, which is dissociative along the $C_\alpha$-$C_\beta$ bond with an exit barrier, and present experimental evidence that seems to verify it. In the end we discuss alternative models based on the fragmentation mechanisms proposed earlier for protonated aromatic amino-acids and other small peptides.

## 3.1 Introduction

Exposure to near-UV radiation leads to various diseases such as cataracts and skin cancer,[1, 2] and since peptides and proteins comprise 68% of the dry matter of cells they are likely targets for photodamage.[3] Photodegradation can occur either directly upon UV absorption or through a series of intra- and intermolecular energy transfer processes. The dynamics of photo-excited peptides begin when an aromatic amino acid (e.g. tryptophan, tyrosine, or phenylalanine) absorbs UV light, producing an electronically excited state of the molecule. The excited molecule may then relax through processes such as fluorescence, internal conversion to the ground state, intersystem crossing to the triplet state with subsequent phosphorescence, or dissociation. These intramolecular processes will be in competition with intermolecular processes involving solvent, such as electronic quenching and vibrational energy transfer. By performing experiments in the gas phase, one can separate the intrinsic photophysical properties

of peptides from those involving solvent, potentially yielding insight into both. In order to more fully understand how UV absorption ultimately leads to fragmentation, we thus investigate the photofragmentation dynamics of gas-phase peptides.

There are a number of previous gas-phase studies that attempt to elucidate the photofragmentation pathways of protein chromophores. Jouvet and co-workers extensively studied the photodissociation mechanism of protonated aromatic amino acids and small peptides in the gas phase.[4-11] While in small tyrosine-containing peptides the b- and y-ions associated with dissociation from the ground electronic state after internal conversion seem to dominate,[10] the loss of the tyrosine side-chain, which results from non-statistical fragmentation, is also observed.[10] This fragmentation channel was attributed to fast (< 20 ns) dissociation from the electronically excited charge transfer state, which first involves electron transfer to CO followed by proton transfer from the $NH_3^+$ group.[10, 11] Although this mechanism addresses the photophysics of amino acids and small peptides when the charge site is in close proximity to the chromophore, it is not clear whether or not this would still happen in larger systems where the two partners are further separated. In larger protonated systems the fragmentation mechanism might more closely resemble that of neutral analogs.

Sobolewski, Domcke and co-workers propose that internal conversion is the main radiationless deactivation pathway in neutral aromatic amino acids and small peptides through an electron-driven proton transfer mechanism.[12-15] Shemesh and Domcke showed that the short excited-state lifetimes for certain conformations of the capped dipeptides Ac-L-Phe-Xxx-$NH_2$ (Xxx=L-Ala, D-Ala, aminoisobutyric acid) are due to proton transfer along the $\gamma$-turn.[16] After being excited to the $\pi\pi^*$ state of the chromophore, the molecules relax to a low-lying locally excited dark state of the backbone, $^1$LE, that has a small barrier to the conical intersection with the charge transfer state, $^1$CT. The charge transfer state in turn has a conical intersection with the ground state, $S_0$, resulting in a fast internal conversion. Recent studies of Malis *et al.* also attributed the non-radiative relaxation of the short-lived conformer of N-acetylphenylalaninylamide (NAPA) to internal conversion to the ground state.[17, 18] Partially based on these experimental results, Domcke and Sobolewski explain the photostability of folded proteins by ultrafast deactivation of the electronically excited state *via* a charge transfer mechanism followed by internal conversion to the ground state.[19] A major goal of the current work is to understand if internal conversion is a general mechanism for the deactivation of electronically excited aromatic chromophores in larger biological molecules or whether there are alternative pathways that play an important role.

One example of an alternative pathway is found in the work of Tseng *et al.* who proposed a different mechanism of UV photofragmentation for neutral phenylalanine analogs that involves intersystem crossing to the triplet state.[20] However, in the same paper they suggest that as the backbone size increases, internal conversion successfully competes with intersystem crossing and becomes the major dissociation channel. It is likely that the dissociation mechanism for phenylalanine-containing peptides depends on the interaction of the aromatic ring with the other parts of the biomolecule (and hence its conformation), which is something that Tseng *et al.* were not able to investigate.[20] In a similar study, Lin *et al.* showed that for various neutral tryptophan chromophores internal conversion starts to play a major role in the dissociation process as the size of the molecules increases, and dissociation from excited states is completely quenched.[21] These studies imply that triplet states only play a role in gas-phase photodissociation when the molecule is small.

We find it intriguing that triplet states are not more widely used to explain gas-phase photofragmentation in light of the fact that they are ubiquitous in solution phase biology. For example, many protein-containing solutions phosphoresce subsequent to UV excitation.[22] If the protein possesses several aromatic residues the fluorescence and phosphorescence is dominated by tryptophan, owing to its superior absorption and emission characteristics. Kwiram and Ross reviewed the application of optically detected magnetic resonance, which is based on the emission from the triplet states, to study the dynamics of biological molecules.[23] Most proteins exhibit phosphoresce not only at low temperatures but also at room temperature in solution.[24] In the absence of molecular oxygen, which can efficiently quench phosphorescence, the triplet lifetimes of tryptophan-containing proteins are in the millisecond range.[25] Strambini et al. ruled out the possibility that the ms-long phosphorescence for aqueous indoles (indole, N-acetyl-L-tryptophanamide (NATA), tryptophan-glycine-glycine tripeptide and the protein ribonuclease $T_1$) might come from the recombination of photoproducts and attributed the lifetime of at least 5 ms to the triplet state formed entirely through the intersystem crossing.[26] There's some uncertainty in the lifetimes of the triplet state of indole and derivatives ranging from tens of microseconds to several milliseconds however.[27] In proteins that do not possess tryptophan residues, tyrosine phosphorescence prevails. Rousslang and collaborators have examined phenol, tyrosine and a number of related compounds in glass at 77K and determined that the phosphorescence decays are biexponential.[28] The longer living component is about 3 s and it comprised about 98 % of the decay. Phenylalanine phosphorescence is generally not observed in proteins due to its low yield,[23] yet electronically excited phenylalanine is also likely to produce triplet species in solution.[29] The relative abundance of phenylalanine in proteins is higher than

either tyrosine or tryptophan[30, 31] and it is important to understand how UV excitation of this amino acid influences the photophysics of a peptide or protein. One of the goals of this study is to understand the role that triplet states play in the photophysics of phenylalanine- and tyrosine-containing peptides in the gas phase.

A second motivation for this work is to determine what the limiting factors may be in extending UV photofragment spectroscopy to larger biomolecular ions. Infrared-UV double-resonance photofragment spectroscopy is a powerful method, which in combination with buffer-gas cooling, provides conformer-selective IR spectra of small peptides.[32, 33] Together with theoretical calculations, this approach has allowed structural determination of gas-phase peptides as large gramicidin S.[34, 35] Apart from the challenges in quantum chemical calculations for large systems, there are experimental challenges in extending these techniques to larger molecules. If upon absorption of a UV photon fragmentation occurs *via* internal conversion to the ground state, the dissociation process should be statistical, and the rate would decrease drastically with an increase in the number of the vibrational degrees of freedom,[36, 37] leading to low fragmentation yields on the timescale of a typical experiment. One contrary example can be found in the work of Nagornova et al., who successfully applied IR-UV photofragment spectroscopy to record a vibrational spectrum of cytochrome-c.[37] We would like to understand whether this is just a special case or if photofragment spectroscopy is generally applicable to larger biomolecular ions.

To pursue such a study, we chose the peptide $AcFA_5K\text{-}H^+$, which has been extensively investigated in our laboratory.[33, 38, 39] The UV photofragment excitation spectrum of this molecule, obtained by collecting the UV-induced photofragments as a function of the UV wavenumber in a cold 22-pole ion trap, reveals sharp transitions (see Figure 3.1). Stearns et al. applied conformer-selective IR-UV double resonance spectroscopy to assign the UV transitions to different conformations, denoted as A, B, C and D.[33] Nitrogen-15 isotopic substitution confirmed the assignment of the IR spectroscopic bands and validated DFT calculations of the conformer geometries. The four major conformations of $AcFA_5K\text{-}H^+$ in the gas phase were found to possess helical structures with relatively minor differences between them.

In this work we try to understand the photophysics of electronically excited phenylalanine and tyrosine chromophore containing peptides, isolated in the gas phase. Figure 3.2 depicts schematic structures of the molecules discussed in this chapter. We present conformer-specific IR spectra of the electronically excited $AcFA_5K\text{-}H^+$ and the evolution of these spectra in time. We also compare the photophysics of $AcFA_5K\text{-}H^+$ with the tyrosine-containing molecule,

$AcYA_5K\text{-}H^+$. We then establish the size dependence and the effect of the charge proximity to the chromophore by recording the time evolution of the electronically excited spectra of $AcFAK\text{-}H^+$ and $AcA_5FK\text{-}H^+$. Based on these data we propose a mechanism for the photodissociation of these peptides that involves the population of triplet states.

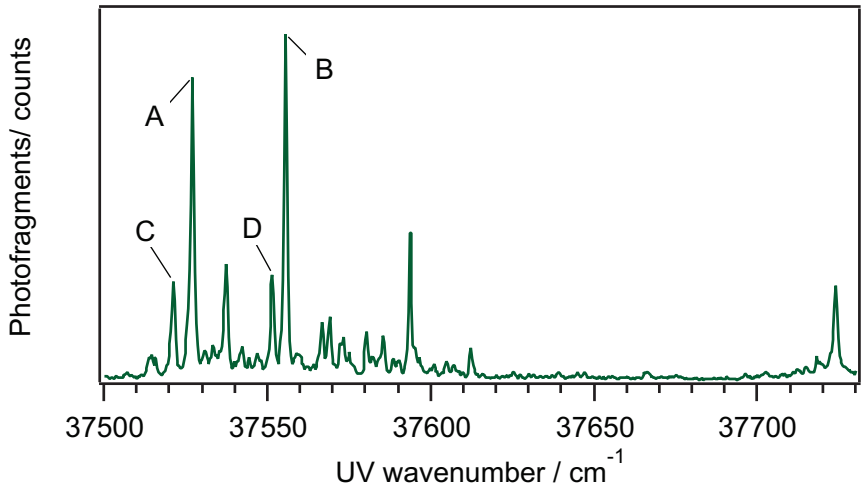


Figure 3.1. The UV photofragmentation spectrum of $AcFA_5K\text{-}H^+$, recorded monitoring the phenylalanine side-chain loss fragment as the function of UV wavenumber.[33] The letters label the band origins for the four conformers.

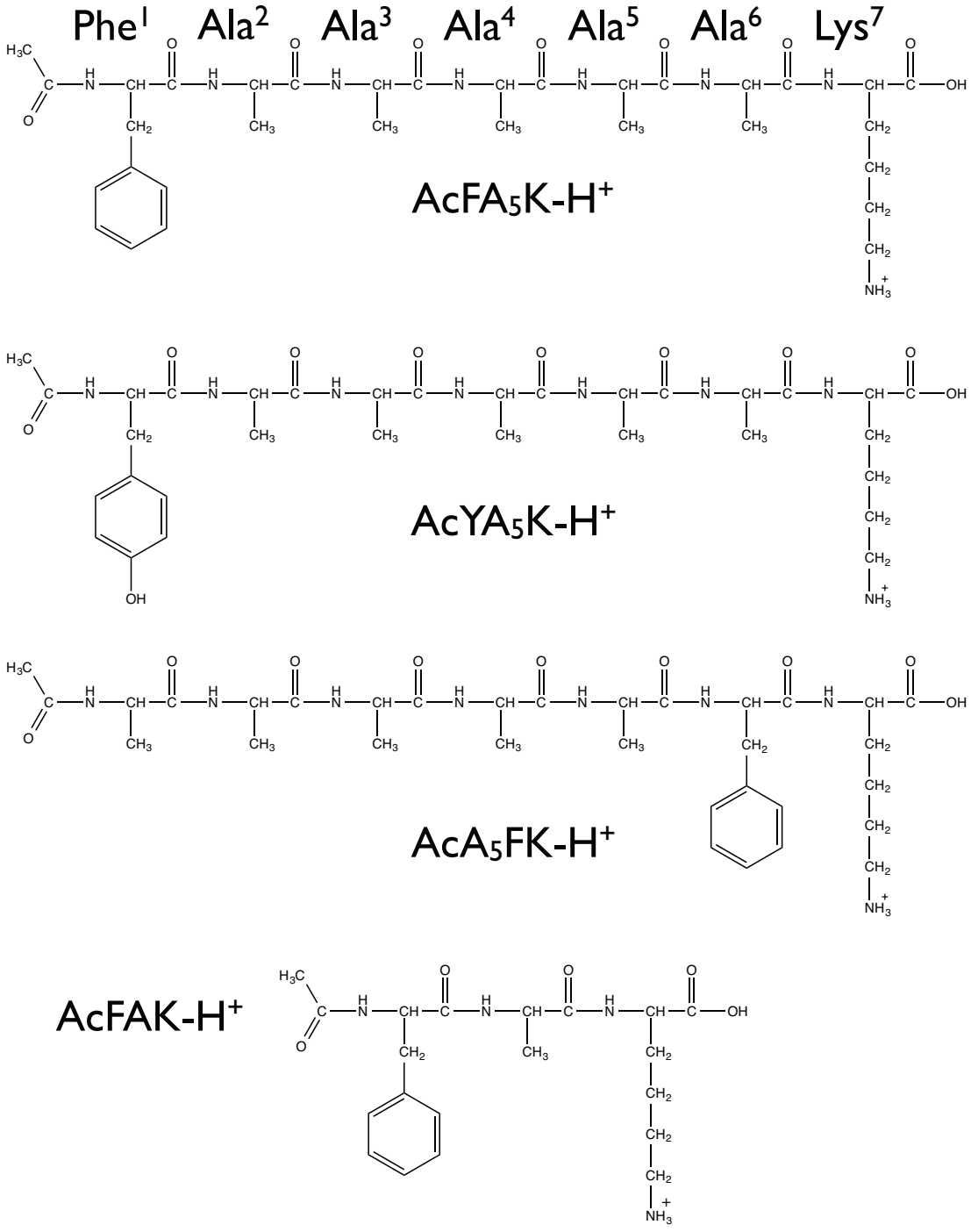


Figure 3.2. The schematic structures of the phenylalanine- ($AcFA_5K\text{-}H^+$, $AcA_5FK\text{-}H^+$, $AcFAK\text{-}H^+$) and tyrosine- ($AcYA_5K\text{-}H^+$) containing molecules studied in this chapter. We label the amino acids with numbers starting from N terminus.

## 3.2 Photofragmentation channels

Mass spectra displaying the photofragmentation patterns for $AcFA_5K\text{-}H^+$ are shown in Figure 3.3. These spectra are similar to the ones recorded by Guidi (although the relative photofragment intensities are different because of a different wavelength of the $CO_2$ laser).[40] The bottom trace (a) shows the mass spectrum of $AcFA_5K\text{-}H^+$ obtained without photoexcitation. In this case, we observe only a single peak at m/z 692, which corresponds to the parent ion mass, and we highlight the fact that there are no collision induced dissociation (CID) fragments under the experimental conditions. When the $CO_2$ laser alone irradiates the ions (2b), we observe $b_n$ and $y_n$ fragments, which reflects fragmentation of the molecules in the electronic ground state *via* infrared multiphoton dissociation (IRMPD). This is not surprising, as such fragments are commonly observed in IRMPD experiments performed with free-electron lasers[41] and in CID experiments.[42] If we irradiate the molecules with a UV laser instead of a $CO_2$ laser, one might expect a similar fragmentation pattern if the energy ultimately undergoes internal conversion to vibrational degrees of freedom. However, UV excitation produces several new photofragments (see Figure 3.3c) in addition to the species identified in Figure 3.3b as products of statistical dissociation from the ground state. This result suggests that these new fragments are produced through an alternative mechanism initiated by UV excitation. Interestingly, if the $CO_2$ laser irradiates the ions 1.2 μs after the UV laser, all photofragments are greatly enhanced, but the photofragment at m/z 601 is enhanced much more than most of the other fragments (see Figure 3.3e). This new species corresponds to phenylalanine side-chain loss produced by cleavage of the $C_\alpha$-$C_\beta$ bond, which is not the weakest bond in the ground state molecules. Similar photofragmentation patterns including the preferential loss of the side-chain were reported for several peptides[40, 43-45] and likely for the small protein ubiquitin,[46] suggesting that this behavior may be a general property of the UV chromophore instead of being unique to this particular chemical system.

The photofragmentation patterns mentioned above led us to believe that the $CO_2$ laser facilitates direct fragmentation from the excited electronic state first prepared by the UV laser, as it was first proposed in ref [44]. To test this hypothesis, the timing between the UV and $CO_2$ lasers was changed from 1.2 μs to 66 ms and the mass spectra were recorded. Remarkably, even with a delay of 66 ms between the two laser pulses, the loss of side-chain is still preferentially enhanced by the $CO_2$ laser, as shown in Figure 3.3d. Since the lifetime of the $S_1$ state for phenylalanine is typically ~70 ns,[47] we can dismiss the possibility of IR fragmentation directly from the $S_1$ state

or from a charge transfer state[10, 11] as the dominant dissociation pathway. We also note that no new photofragments were detected upon increasing the delay between the two lasers, indicating that the dissociation mechanism remains constant over this time.

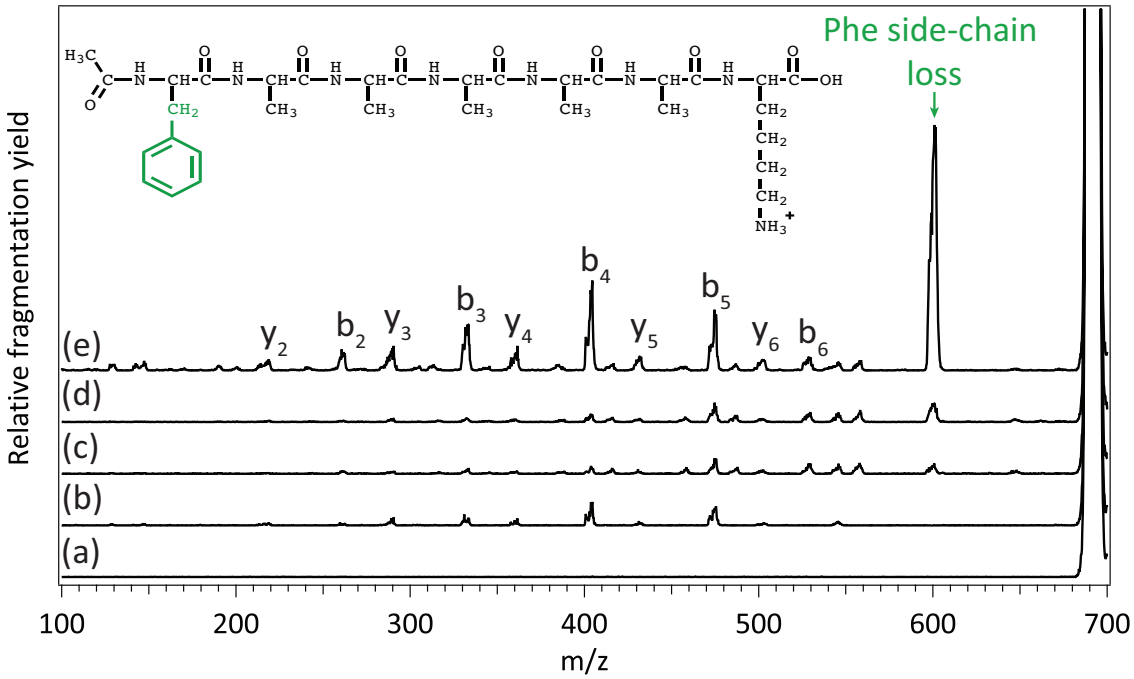


Figure 3.3. Mass spectra revealing the fragmentation patterns of $AcFA_5K\text{-}H^+$ upon irradiation with (a) no laser, (b) the $CO_2$ laser, and (c) the UV laser fixed at the band origin of conformer B (37555.3 $cm^{-1}$). Plots (d) and (e) highlight the largely non-statistical photofragmentation patterns that arise when the UV excitation is followed by the $CO_2$ laser at time delays of (d) 66 ms and (e) 1.2 μs. The primary structure of $AcFA_5K\text{-}H^+$ is shown in the inset.

## 3.3 Proposition of a dissociation model involving the triplet state

It is clear from the data presented above that UV excitation of the phenylalanine chromophore can produce a stable species, which, upon vibrational excitation, dissociates to produce fragments that are different than those observed using IRMPD alone. This suggests that a portion of the electronically excited molecules does not undergo internal conversion to the ground electronic state but rather forms a long-lived intermediate state. Since we have already eliminated the possibility of dissociating directly from the $S_1$ state, the simplest explanation is

that an intermediate triplet species is formed, as illustrated in Figure 3.4. In this model, UV excitation initially promotes the system to the first electronically excited state $S_1$. At this point, the molecule can either undergo internal conversion to the ground state, giving rise to $b_n$ and $y_n$ fragments, or it can experience intersystem crossing to a triplet state, which as explained below, has an exit barrier to $C_\alpha$-$C_\beta$ dissociation. In the latter case, a molecule that undergoes intersystem crossing to the triplet state may or may not have enough energy to dissociate. During the time it resides in a triplet state, the molecule can also experience collisions with residual helium in the cold ion trap, which may lower its vibrational energy below the dissociation threshold. In this case, the molecule will be trapped in the triplet state until sufficient energy is added to the system through infrared excitation, for example.

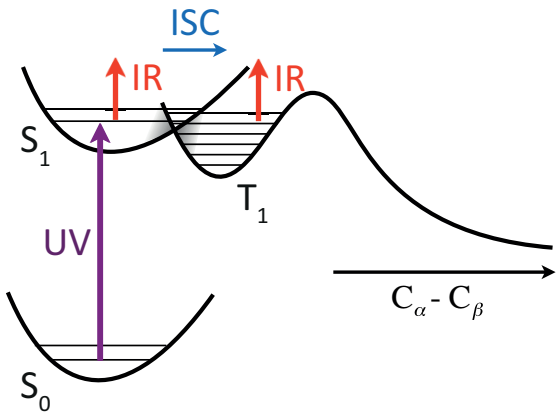


Figure 3.4. The model we use to explain the non-statistical photofragmentation patterns in phenylalanine- and tyrosine-containing peptides. A key feature of the model is a triplet state with a barrier to $C_\alpha$-$C_\beta$ bond dissociation. ISC stands for $S_1$-$T_1$ intersystem crossing.

Before presenting our data to support this model of photofragmentation, it is important to realize that there is a strong precedent in the literature for invoking triplet states to explain gas-phase chemistry of UV chromophores including phenylalanine and its derivatives. In one such report, Huang *et al.* performed molecular beam experiments on the simplest analogs of the phenylalanine chromophore: ethylbenzene and *n*-propylbenzene.[48] Photoexcitation at 284 nm was used to fragment the molecules, and the translational energy distributions of the fragments were measured. In both cases, photoexcitation resulted in C-C bond cleavage (analogous side-chain loss in $AcFA_5K$-$H^+$) and also the production of two distinct components in the translational energy distributions. This was explained by attributing the slow component of the distribution to dissociation after internal conversion to the ground state and the fast component to dissociation from a triplet state with an exit barrier. Interestingly, both ethylbenzene and *n*-propylbenzene

favor dissociation *via* the triplet state as evidenced by the fast component composing 75% and 80% of the fragment distribution for the two species, respectively.

In a subsequent study, Tseng *et al.* used a multi-mass ion imaging technique in a molecular beam to investigate the photodissociation mechanism of larger molecules containing a phenylalanine chromophore such as phenylethylamine, *N*-methyl-phenylethylamine, and *N*-acetyl phenylalanine methyl ester.[20] Again, photoexcitation at 248 nm predominantly produces fragments *via* cleavage of the $C_\alpha$-$C_\beta$ bond, and the translational energy distributions once again contain a fast component and a slow component. *Ab initio* calculations showed that the first triplet state is dissociative along $C_\alpha$-$C_\beta$ bond with an exit barrier of ~30 kcal/mol, and thus dissociation from the triplet state is the logical explanation for the fast component. However, as the size of the molecule is increased, the contribution of the fast component in the translational energy distribution decreases, indicating that internal conversion begins to dominate.

In another paper, the same authors showed that in phenol, *p*-methylphenol, *p*-ethylphenol the main photodissociation channel at 248 nm is H atom abstraction from the repulsive $\pi\sigma^*$ state.[49] However, as the density of states increases, for example due to the low frequency vibrational modes such as torsion of the side-chain in *p*-(2-aminoethyl)phenol, internal conversion and intersystem crossing quenches dissociation from the $\pi\sigma^*$ state, and the main photodissociation channel becomes $C_\alpha$-$C_\beta$ bond rupture. The authors attribute the fast component in the translational energy distribution to dissociation from the triplet surface with an exit barrier and the slow component to dissociation after internal conversion.

These results, along with our photofragmentation data presented in Figure 3.3, strongly imply that $C_\alpha$-$C_\beta$ cleavage is inherent to phenylalanine- and tyrosine-based UV chromophores. In order to fully characterize the intermediate state formed in our experiments after UV excitation, we employ a photofragmentation-detected analog of the approach used by Zwier and coworkers[50, 51] and Ebata and coworkers[52-54] for neutral molecules. Figure 2.8 illustrates one such scheme in which the UV laser is fixed on a resonant transition of the molecule and the infrared OPO is tuned throughout the mid-infrared. Interestingly, as the IR OPO is tuned through the resonant transitions of UV-excited $AcFA_5K\text{-}H^+$, we observe the enhancement of the photofragment associated with the loss of the phenylalanine side-chain (Figure 3.5). We emphasize that we only observe the enhancement of this particular photofragment, which is in sharp contrast to the situation encountered when the $CO_2$ laser is fired after UV excitation, which enhances all photofragments (see Figure 3.3d-e). This should not be completely unexpected, however, since the $CO_2$ laser has a much higher fluence than the infrared OPO and is likely to produce

photofragments through IRMPD of ground state molecules. As the delay between the UV laser and the IR OPO is increased, the relative enhancement of the photofragment steadily decreases, but the photofragmentation pattern remains the same.

The fact that we can induce fragmentation with the IR OPO in a wavelength-dependent manner allows us to acquire IR spectra for electronically excited species, which can provide valuable information on the structure of the molecule in the $S_1$ state. Most importantly, however, we can monitor how the spectrum, and hence the structure, changes as a function of time after the UV absorption by changing the delay between the UV pump and the IR probe.

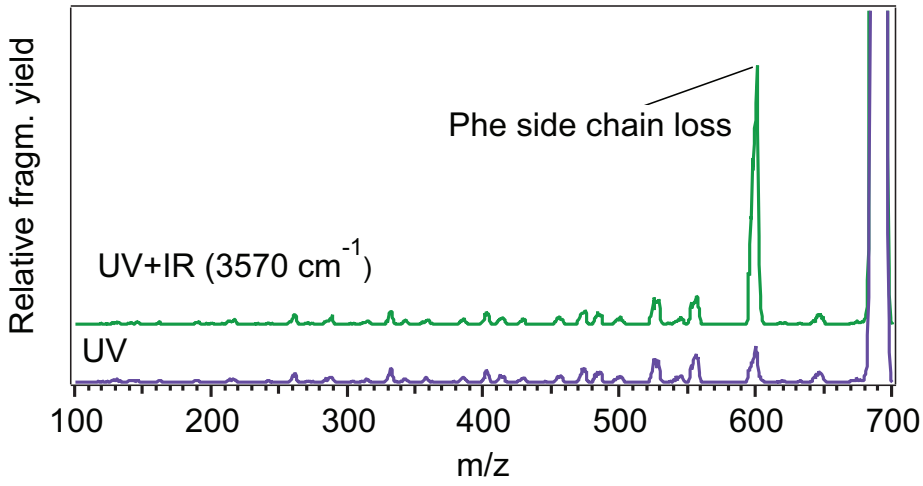


Figure 3.5. Photofragment mass spectrum of $AcFA_5K\text{-}H^+$ upon UV excitation (lower trace) and upon UV excitation followed by the IR OPO (upper trace). The UV laser is fixed at the band origin of conformer B (37555.3 $cm^{-1}$). The IR OPO fires 600 ns after the UV laser and is tuned to 3570 $cm^{-1}$, which corresponds to the COO-H stretch vibration. The power of the IR OPO is ~5 mJ/pulse, the power of the UV laser is ~2.6 mJ/pulse.

## 3.4 Evidence from transient IR spectra

### 3.4.1 Infrared spectra of the $S_1$ state of $AcFA_5K\text{-}H^+$

When the delay between the UV laser and IR OPO is ~5 ns, which is the shortest delay possible without overlapping the pulses, we measure sharp IR bands of the molecules in an electronically excited state. These spectra are shown in color in Figure 3.6 for the four conformers previously identified.[33] The peaks are plotted as positive-going because resonant IR

absorption produces a gain in the photofragment signal. The ground state spectra identified in an earlier report[33] have also been reproduced here for comparison (see the black negative-going spectra). Since most of the transitions in the ground state spectra were definitively assigned using $^{15}N$ isotopic substitution, we can determine which parts of the molecule are affected by UV excitation of the aromatic chromophore by comparing peak positions to those in the ground state. As can be seen in Figure 3.6, the excited-state spectra closely resemble those from the ground state with the exception of the oscillators nearest the chromophore, which are shifted to the red. This effect is clearly seen in the phenylalanine NH stretch ($Phe^1$) of conformer B, which is located at 3404 $cm^{-1}$ in the ground electronic state spectrum but shifts to 3369 $cm^{-1}$ in the excited electronic state. This makes intuitive sense, however, if one considers the close proximity of the phenylalanine NH to the π-cloud of the phenyl ring (see Figure 3.29). A red-shift is also observed for the first alanine ($Ala^2$) NH stretching vibration in conformers A and C, although these shifts are not as pronounced. Interestingly, this transition does not appear perturbed in the spectra obtained for conformers B and D, implying that the $Ala^2$ NH is positioned further from the chromophore than in the case of conformers A and C. The fact that no other transitions measured in this spectral region shift upon UV absorption, suggest that the initial UV excitation is local to the chromophore.

### 3.4.2 Comparison with the tyrosine chromophore: infrared spectra of the $S_1$ state of $AcYA_5K\text{-}H^+$

Having demonstrated that UV excitation is local to phenylalanine in $AcFA_5K\text{-}H^+$, we would now like to exchange phenylalanine for tyrosine (*i.e.* $AcYA_5K\text{-}H^+$) to determine the extent to which this behavior depends on the chomophore. The ground state spectra for the four conformers of this molecule have been reported previously[40] and are almost identical to those containing phenylalanine. The only difference between the two species is an additional OH group that gives rise to an OH stretch band with a characteristic wavenumber in the spectral region 3642-3660 $cm^{-1}$.[55]

For comparison we have chosen the most abundant conformer B, for which the tyrosine NH stretch appears at 3400 $cm^{-1}$ and the tyrosine OH stretch falls at 3649 $cm^{-1}$ in the ground state infrared spectrum (Figure 3.8). Just as in the case with the phenylalanine-containing peptide, absorption of infrared radiation from the IR OPO ~5 ns after UV excitation predominantly enhances cleavage of the $C_\alpha\text{-}C_\beta$ bond in $AcYA_5K\text{-}H^+$ (Figure 3.7). Scanning the IR OPO wavenumber reveals a sharp spectrum in the excited electronic state that again closely resembles

the ground state spectrum but with a red shift of vibrations nearest to the UV chromophore (Figure 3.8). Upon UV activation, the OH stretching wavenumber shifts to the red by 34 $cm^{-1}$ and now occurs at 3615 $cm^{-1}$ (Figure 3.8). Analogous to the case of $AcFA_5K\text{-}H^+$, the tyrosine NH stretching wavenumber also decreases upon UV excitation and occurs at 3386 $cm^{-1}$, which is 14 $cm^{-1}$ red-shifted (Figure 3.8). Ebata et al. reported a 76 $cm^{-1}$ red shift of the OH frequency upon $S_0$-$S_1$ transition in neutral phenol[53] based on the comparison with the earlier work of Bist and co-workers.[56] We observe more modest shift in $AcYA_5K\text{-}H^+$, perhaps because the tyrosine NH also interacts with the aromatic π-cloud.

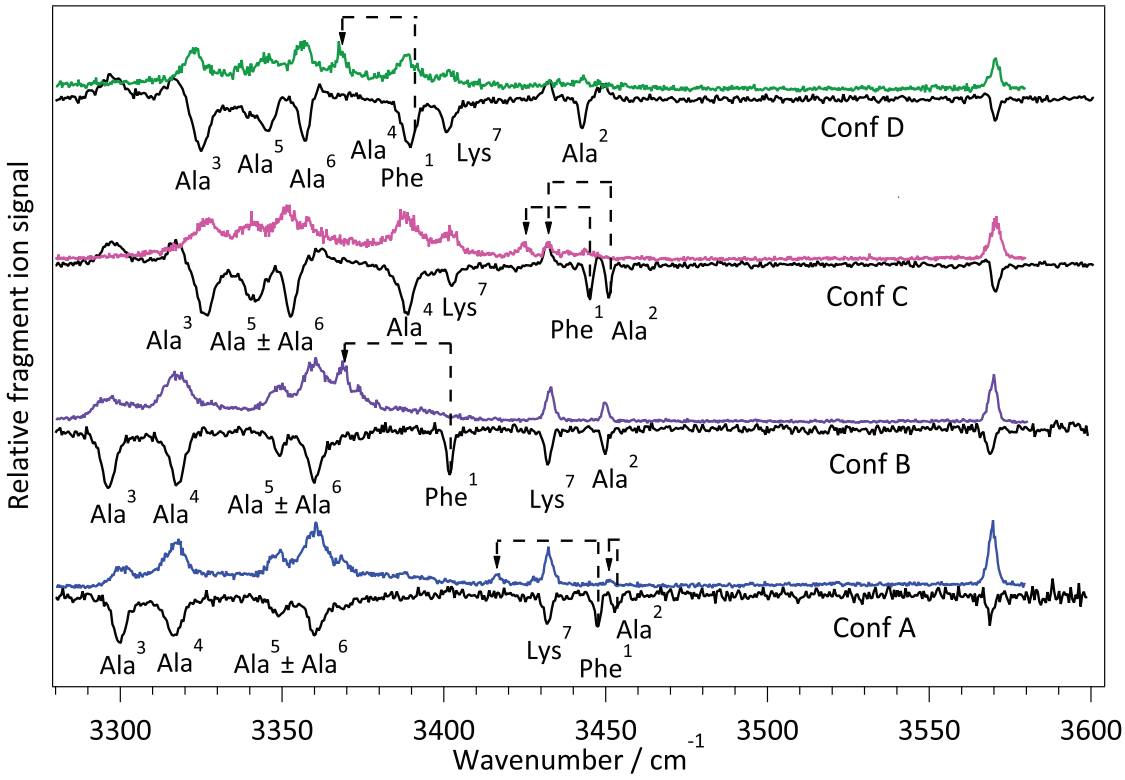


Figure 3.6. Plots comparing the ground-state[33] (negative-going) and electronically excited state (positive-going) infrared spectra for four different conformers of $AcFA_5K\text{-}H^+$. The UV-excited state spectra were recorded by fixing the UV laser on the band origin of each conformer and then probing the species with the IR OPO ~5 ns after the UV excitation.

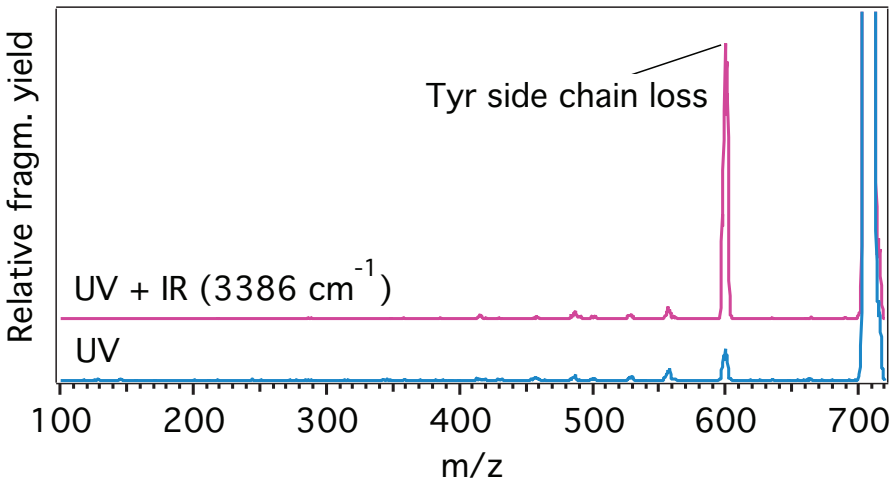


Figure 3.7. Photofragment mass spectrum of $AcYA_5K\text{-}H^+$ upon UV excitation (lower trace) and upon UV excitation followed by the IR OPO (upper trace). The UV laser is fixed at the band origin of conformer B (35406.4 $cm^{-1}$). The IR OPO fires ~5 ns after the UV laser and is tuned to 3386 $cm^{-1}$. The power of the IR OPO is ~7 mJ/pulse, the power of the UV laser is ~1.3 mJ/pulse.

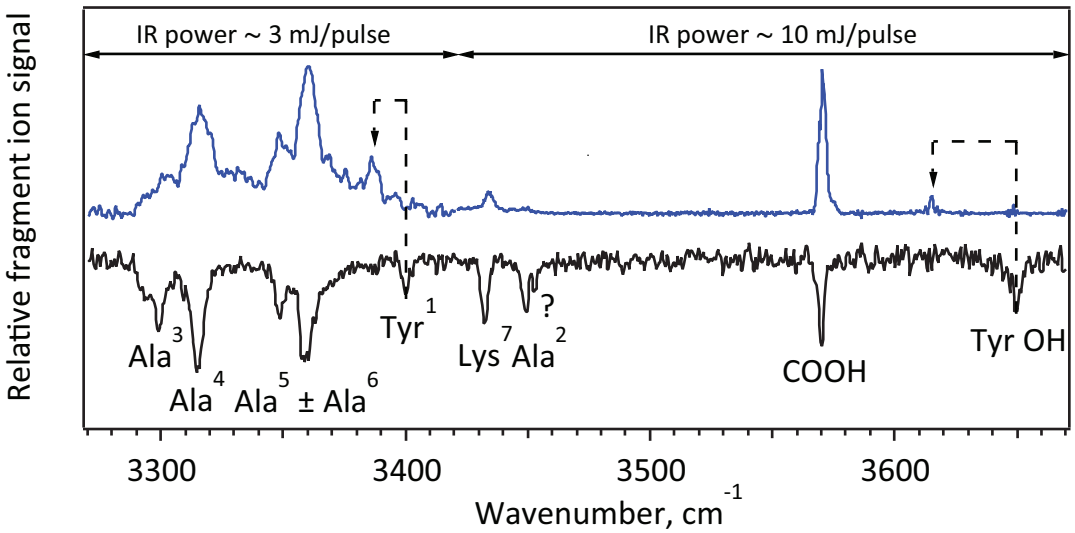


Figure 3.8. Comparison of the ground state[40] (negative-going, in black) and electronically excited state (positive-going, in blue) infrared spectra for conformer B of $AcYA_5K\text{-}H^+$. The UV-excited state spectrum was recorded by fixing the UV laser on the band origin of conformer B (35406.4 $cm^{-1}$) and then probing the species with the IR OPO ~5 ns after the UV excitation. To avoid the saturation of the NH-stretches the IR power in the spectral region 3270–3420 $cm^{-1}$ is reduced to ~3 mJ/pulse. The relative intensities of $Ala^2$ and $Lys^7$ NH stretches compared with the other NH stretches are lower in the spectrum of the electronically excited state than in the ground state. For these bands to become clearly visible in the IR spectrum of the electronically excited state the IR power is increased to ~10 mJ/pulse.

### 3.4.3 Time evolution of transient IR spectra of $AcFA_5K\text{-}H^+$

Having characterized the excited-state vibrational frequencies immediately following UV absorption, we now turn our attention to the time evolution of the activated species by varying the time delay between the UV and IR OPO laser pulses. If we first consider the phenylalanine-containing species ($AcFA_5K\text{-}H^+$), we indeed observe a change in the spectrum when the delay between the two lasers is longer than 5 ns. Figure 3.9 shows the evolution of the IR spectrum of conformer B as the delay between the pump and probe lasers is increased. On the timescale of 300 ns the spectra broaden and a new spectroscopic band appears at 3391 $cm^{-1}$. The fact that the lines broaden indicates that a portion of the energy acquired from the absorption of a UV photon has been deposited into vibrational degrees of freedom. Furthermore, this internal energy increase is sufficient to induce isomerization of the molecules, as evidenced by the formation of a new spectroscopic feature. This poses the question of how much energy is required to induce such an effect.

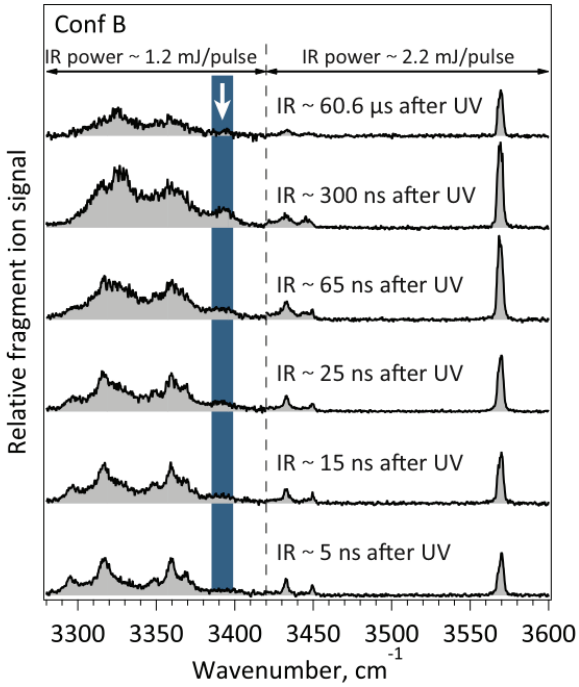


Figure 3.9. Infrared spectra of electronically excited $AcFA_5K\text{-}H^+$ (conformer B) depicting how the species evolves in time. The UV laser is fixed at the band origin of conformer B (37555.3 $cm^{-1}$), while the infrared OPO probes the electronically excited species at the indicated time delays. We adjust the infrared OPO power as shown to maximize the total fragmentation yield while avoiding spectral saturation. All spectra are normalized for laser power.

We can begin to address this question by repeating the UV-IR experiment for each of the different conformers of $AcFA_5K\text{-}H^+$. Infrared spectra obtained with the time delay between the UV laser and the IR OPO fixed to 300 ns are shown in Figure 3.10. Even though we begin with four different IR spectra at short delay between the UV and IR pulses (see Figure 3.6), on a 300 ns timescale the sharp features present in the spectra broaden and shift in such a way that all conformers yield essentially the same IR spectrum. The fact that COO-H stretch only broadens to 4.4 $cm^{-1}$ compared to the width of 3.0 $cm^{-1}$ for the cold, ground state molecules confirms that the UV excited molecules we observe don't undergo internal conversion to the ground state, which would deposit the entire photon energy into vibrational degrees of freedom. Instead, it suggests that these molecules remain on an electronically excited surface with only a small portion of the original photon energy as vibrational energy, but an amount that is high enough to cause isomerization between the conformers.

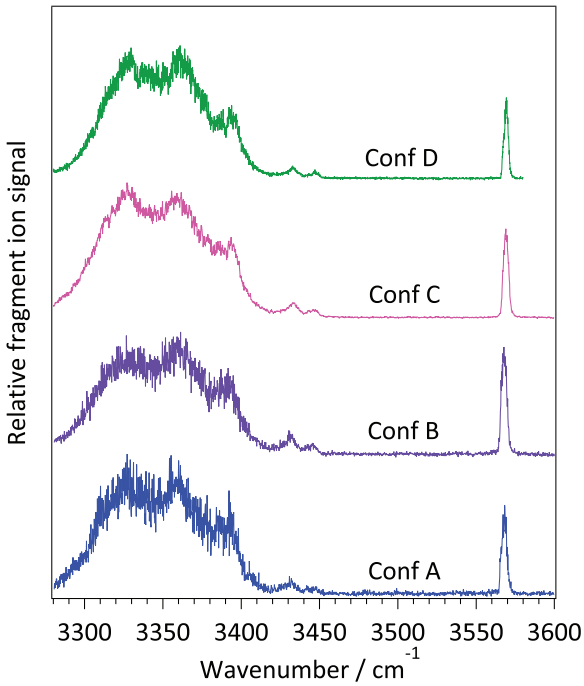


Figure 3.10. Infrared spectra of electronically excited $AcFA_5K\text{-}H^+$, acquired by selecting each of the four conformers with the UV pump laser, and probing with the IR OPO ~300 ns later. On this timescale, the initial spectra evolve to yield nearly identical spectra.

### 3.4.4 Time evolution of transient IR spectra of AcFAK-$H^+$. $^{15}N$ isotopic substitution on phenylalanine

We observe similar time evolution of transient IR spectra in a smaller molecule, AcFAK-$H^+$, the schematic structure of which is presented in Figure 3.2. Irradiation of the UV pre-excited molecules with the IR OPO greatly enhances the side-chain loss fragmentation channel as in the case of $AcFA_5K$-$H^+$ (Figure 3.11).

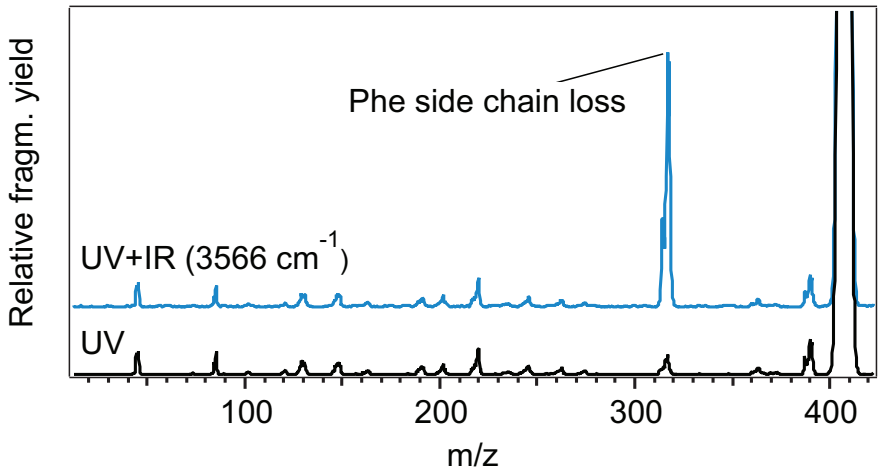


Figure 3.11. Photofragment mass spectrum of AcFAK-$H^+$ upon UV excitation (lower trace) and upon UV excitation followed by the IR OPO (upper trace). The UV laser is fixed at the band origin of conformer A (37484.0 $cm^{-1}$), see UV spectrum in Figure 4.1. The IR OPO fires 31 μs after the UV laser and is tuned to 3566 $cm^{-1}$, which corresponds to the COOH stretch vibration. The power of the IR OPO is ~4.4 mJ/pulse, the power of the UV laser is ~1.4 mJ/pulse.

We identify the two most abundant conformers (A and B) of AcFAK-$H^+$ and show their calculated ground state structures in Figure 4.7. In both structures the ammonium of the lysine side-chain interacts with the carbonyls. These structures differ mainly by the rotation of the phenyl ring around the $C_\alpha$-$C_\beta$ bond. The infrared spectra for both conformers in the first excited electronic state are presented in the bottom of Figure 3.12. They differ primarily by the position of the phenylalanine NH stretch vibration, labeled as F. The additional bands in the $S_1$ infrared spectrum of conformer A, labeled as F' in Figure 3.12, are combination bands that are analyzed in Chapter 4.

When we probe the UV pre-excited molecules with the IR OPO at delays longer than 5 ns, the initially sharp features become broader and a new spectroscopic band appears at 3397 $cm^{-1}$

(Figure 3.12). As in the case of $AcFA_5K\text{-}H^+$, at approximately 300 ns after UV excitation both conformers yield almost identical infrared spectra. The new spectrum consists of four peaks at 3397 $cm^{-1}$, 3418 $cm^{-1}$, 3439 $cm^{-1}$, and 3448 $cm^{-1}$, each having a width of 8-10 $cm^{-1}$. One might argue that these spectra are the superposition of the ground state spectra of conformers A and B (Figure 4.2). However, that would imply that in the infrared spectrum obtained 300 ns after UV excitation the infrared transitions at 3397 $cm^{-1}$ and 3439 $cm^{-1}$ both correspond to the phenylalanine NH stretch vibrations of conformers B and A respectively.

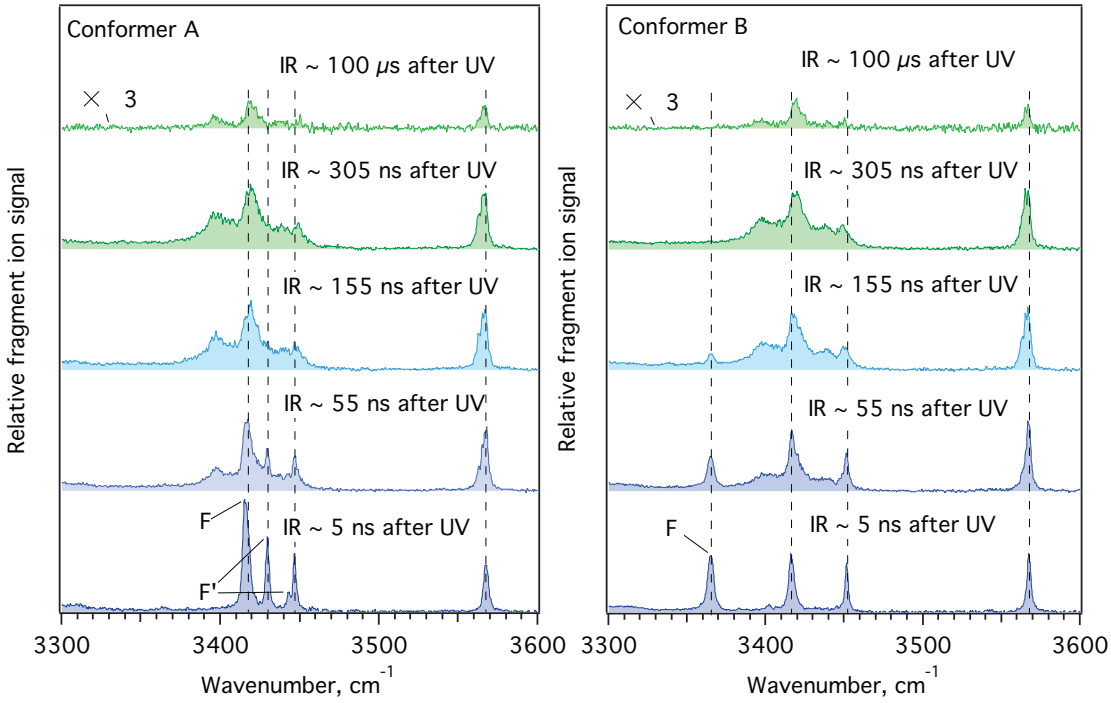


Figure 3.12 IR spectra of the UV excited conformer A (left) and conformer B (right) of $AcFAK\text{-}H^+$ at different delays between the UV and the IR OPO. The UV laser wavenumber is fixed at 37484.0 $cm^{-1}$ and 37532.2 $cm^{-1}$ for conformer A and B respectively. The IR power is ~2.4 mJ/pulse. F labels the position of the phenylalanine NH stretch in the $S_1$ state, F' labels the positions of the phenylalanine combination bands discussed in detail in Chapter 4. Vertical dashed lines we draw for easier comparison of the spectra.

To check this hypothesis, we performed $^{15}N$ isotopic substitution on the phenylalanine amino acid. Upon making this substitution, all spectroscopic bands corresponding to phenylalanine NH stretch should shift to the red compared with their positions in the infrared spectrum of the unlabeled peptide. Figure 3.13 presents the infrared spectrum, recorded ~300 ns after the UV excitation of $^{15}N$ isotopically labeled (b) and unlabeled $AcFAK\text{-}H^+$ (a). Only one band at 3397 $cm^{-1}$ shifts and thus corresponds to the phenylalanine NH stretch. The other band at 3439 $cm^{-1}$

does not change its position, contradicting the suggestion that this spectrum might arise from the superposition of the ground state spectra for conformers A and B. This result, together with relatively narrow (8-10 $cm^{-1}$) spectral width of the transitions, suggests that if there are several isomers buried under the spectrum in Figure 3.13a, these isomers should adopt similar structures. It also supports hypothesis of a molecule staying in the electronically excited state with a small amount of vibrational energy deposited in the internal degrees of freedom.

If the evolution of the spectra that we observe in Figure 3.12 reflects the intersystem crossing of the molecule from $S_1$ state to the triplet state, we also observe a very interesting phenomena of excited state hydrogen bond strengthening and weakening upon $S_1$-$T_1$ intersystem crossing for different conformers. In the $S_1$ state of conformer A the phenylalanine NH stretch (3415 $cm^{-1}$) is blue-shifted compared to its position in the triplet state (3397 $cm^{-1}$), and in the $S_1$ state of conformer B the phenylalanine NH stretch (3365 $cm^{-1}$) is red-shifted compared to its position in the triplet state (3397 $cm^{-1}$).

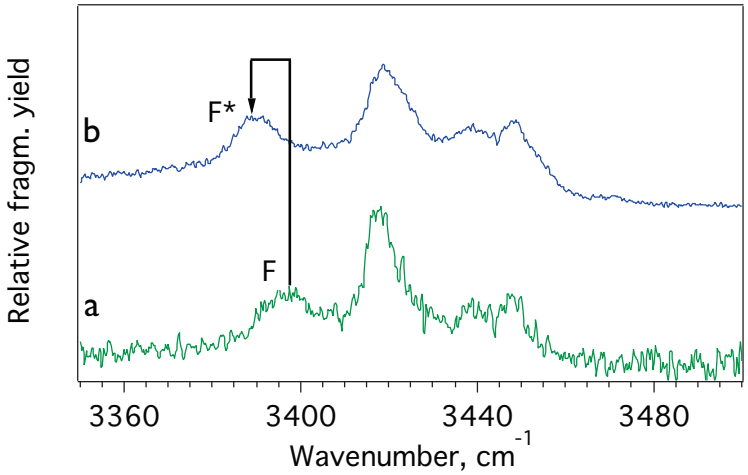


Figure 3.13 a) IR spectrum of conformer A of AcFAK-$H^+$ 300 ns after the UV excitation (37484.0 $cm^{-1}$). b) IR spectrum of conformer A of AcF*AK-$H^+$ 300 ns after the UV excitation (37484.0 $cm^{-1}$), where F* is $^{15}N$ isotopically labeled phenylalanine amino acid.

## 3.4.5 Time evolution of transient IR spectra of $AcYA_5K$-$H^+$

The same time delay experiment was performed on the tyrosine-containing peptide $AcYA_5K$-$H^+$ to determine the extent to which the UV chromophore influences this process. Qualitatively, we observe similar behavior. The initially sharp features become broader as the delay between the two lasers is increased (Figure 3.14). The major difference, however, is that

this broadening occurs on the ~30 ns timescale as opposed to the ~300 ns timescale required for the phenylalanine-containing compounds (Figure 3.9 and Figure 3.12).

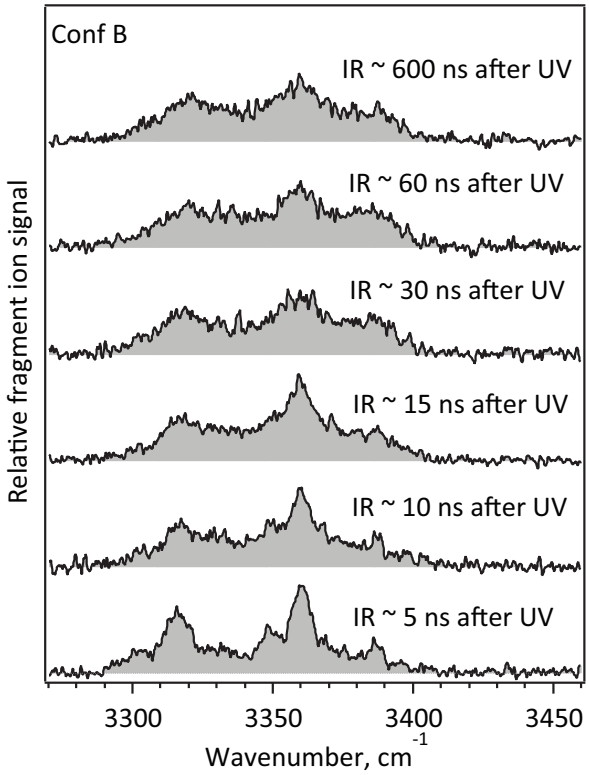


Figure 3.14. Infrared spectra of electronically excited $AcYA_5K\text{-}H^+$ depicting how the species evolves in time. The UV laser is fixed at the band origin of conformer B (35406.4 $cm^{-1}$), while the infrared OPO probes the electronically excited species at the indicated time delays. The average IR power in this spectral region is ~3 mJ/pulse.

## 3.4.6 Simplified kinetic model for the time evolution of singlet and triplet states. Comparison between $AcFA_5K\text{-}H^+$ and $AcYA_5K\text{-}H^+$

Up to this point, we have presented IR spectra for UV-excited $AcFA_5K\text{-}H^+$, $AcFAK\text{-}H^+$, and $AcYA_5K\text{-}H^+$, obtained by scanning the infrared laser at several fixed time intervals between the UV and IR excitation pulses. These spectra provide us with structural information on the UV-excited molecules at different points in time. We now explore how the total photofragmentation yield varies as a function of the time delay between the UV laser and the IR OPO when both lasers remain at fixed frequencies, which should reveal the time evolution of the different

electronically excited states involved in the process. To gather such information, we perform parallel experiments on $AcFA_5K\text{-}H^+$ and $AcYA_5K\text{-}H^+$, where the UV laser is fixed on the band origin of conformer B in both cases. We then fix the IR OPO to an infrared transition that only appears after UV excitation (3391 $cm^{-1}$ for $AcFA_5K\text{-}H^+$ and 3386 $cm^{-1}$ for $AcYA_5K\text{-}H^+$) and record the increase in photofragmentation yield as a function of the time delay between the two lasers. In both cases, we observe an initially steep increase in the photofragmentation enhancement followed by a slower decay as shown in Figure 3.15.

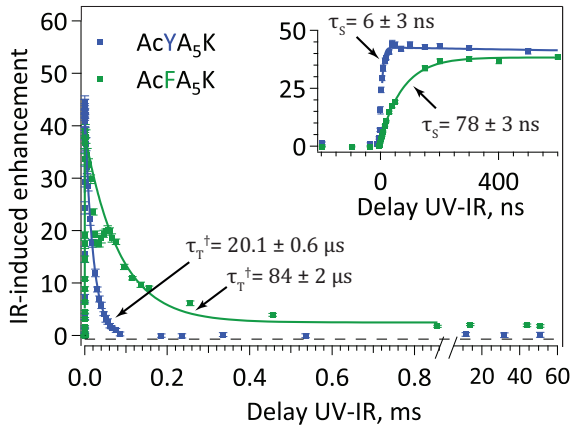


Figure 3.15 Infrared-induced enhancement of the chromophore side-chain loss fragment intensity for $AcFA_5K\text{-}H^+$ (green) and $AcYA_5K\text{-}H^+$ (blue) as a function of the UV-IR time delay, recorded in the 22-pole ion trap. The UV laser is fixed on the band origin of conformer B while the infrared OPO is fixed at 3391 and 3386 $cm^{-1}$ for $AcFA_5K\text{-}H^+$ and $AcYA_5K\text{-}H^+$, respectively. We use the maximum infrared power available of 12 mJ/pulse to maximize photofragmentation. The total IR-induced enhancement for $AcYA_5K\text{-}H^+$ is multiplied by a factor of 3 for comparison reasons. The initial rise and decay are fit with Eqn. (3.5) to produce the $S_1$ and $T_1$ time constants. The fit does not include the points responsible for the dip between 30 and 60 µs, as described in the text. The inset shows the initial rise of the signal and its exponential fit.

The curve for $AcFA_5KH^+$ also includes a dip in the signal around 0.3 ms caused by the translational motion of the ions inside the trap.[40] This dip reflects an initial decrease in the ion density probed by the IR beam followed by a partial recurrence. The timescale of this damped oscillatory ion motion provides a measure of the time it takes for the initially excited ions to redistribute over the trapped volume. Any further decay after this time should reflect the lifetime of the excited molecules. In principle, these oscillations should be dependent on the shape of the effective trapping potential, as this will influence the total field free volume available to the ions. We have recently verified this by replacing the 22-pole ion trap, which has a large trapping

volume relative to the probed volume, with an octopole in which the ion cloud is confined within the probe beam. In this case we record a curve that lacks the dip at 0.3 ms (see Figure 3.16), but has a similar long-time decay. In Figure 3.17 we present the same experiments on $AcFA_5K\text{-}H^+$ and $AcYA_5K\text{-}H^+$ as in Figure 3.15, performed in the new cold octopole ion trap. These curves provide more accurate measure of the lifetimes of the excited molecules, because they lack the oscillatory motion of the ions. We will use the data from Figure 3.17 in the analysis that follows.

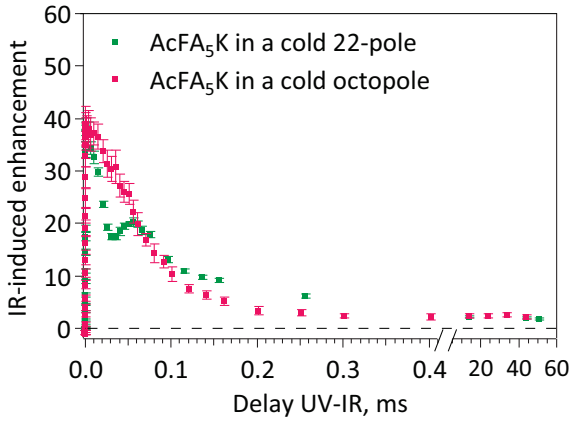


Figure 3.16 Infrared-induced enhancement of the chromophore side-chain loss fragment intensity for $AcFA_5K\text{-}H^+$ as a function of the UV-IR time delay, recorded in the 22-pole ion trap (red) and in the cold octopole ion trap (green). The UV laser is fixed on the band origin of conformer B while the infrared OPO is fixed at 3391 $cm^{-1}$. We used 12 mJ/pulse of IR power in the 22-pole trap and 8 mJ/pulse in the octopole trap. The total IR-induced enhancement for $AcFA_5K\text{-}H^+$ in octopole ion trap is multiplied by a factor of 3.4 for comparison reasons.

The photofragmentation enhancement behavior introduced in Figures 3.15-3.17 can be understood by considering a simplified kinetic model, in which we assume that a triplet species is formed before dissociation along the $C_\alpha$-$C_\beta$ bond as proposed in Figure 3.4. With this in mind, the kinetic model can be written as,

$$\begin{array}{ccccc} & & \xrightarrow{k_{ISC}} & & \xrightarrow{k_T} \\ [S_1] & & & [T_1^\dagger] & & (\text{Fragments; } [S_0]) \\ k_r+k_{IC} \downarrow & & & & \\ [S_0] & & & & \end{array} \qquad (3.1)$$

,

where $k_r$, $k_{IC}$, $k_{ISC}$, and $k_T$ are the rate constants for $S_1$ radiative decay, $S_1$ internal conversion to vibrationally excited ground state ($S_0^\dagger$), $S_1$ intersystem crossing to vibrationally excited triplet state ($T_1^\dagger$), and $T_1^\dagger$ total decay through fragmentation, collisional cooling, intersystem crossing

to $S_0^\dagger$, phosphorescence, and initial movement of the ions out of the probe beam. Using this model, the populations in the singlet [$S_1$] and vibrationally excited triplet state [$T_1^\dagger$] can be expressed as

$$\frac{d[S_1]}{dt} = -(k_r + k_{IC} + k_{ISC})[S_1] = -k_S[S_1] \quad (3.2)$$

$$\frac{d[T_1^\dagger]}{dt} = k_{ISC}[S_1] - k_T[T_1^\dagger] \quad (3.3)$$

where $k_s$ is the total singlet state decay rate. The integration of (3.2) provides the population of $S_1$ as a function of time after UV excitation and yields,

$$[S_1] = [S_1]_0 exp^{-k_S t} \quad (3.4)$$

where $[S_1]_0$ is the initial population in $S_1$ immediately after UV absorption. Substituting the solution given by Eqn. (3.4) into Eqn. (3.3) and integrating we find the population of $T_1^\dagger$:

$$[T_1^\dagger] = \frac{[S_1]_0 k_{ISC}}{k_T - k_S}(exp^{-k_S t} - exp^{-k_T t}) \quad (3.5)$$

The first exponential includes the rate constant for the decay of the $S_1$ species ($k_s$), while the second includes the rate constant for the decay of $T_1^\dagger$ ($k_T$). We use Eqn. (3.5) to fit the experimental photofragmentation enhancement data (as shown in Figure 3.15 and Figure 3.17).

While our simplified kinetic model describes well the initial rise and decay of the $T_1^\dagger$ population, it works less well in the case of $AcFA_5K\text{-}H^+$ for times greater than ~ 800 μs. We still observe the enhancement of the side-chain loss fragment, but it does not measurably decay after this time. Our treatment assumes that the deactivation rate $k_T$ is constant in time, which allows us to integrate the Eqn. (3.3). This assumption will not strictly be true, because as molecules in $T_1^\dagger$ begin to cool in collisions with the residual helium gas in the 22-pole ion trap, we would expect $k_T$ to decrease. The vibrational energy dependence of triplet lifetimes in alkylbenzenes was explored by Lohmannsroben *et al.,* who measured a linear decrease in lifetime upon changing the excess vibrational energy from 9300 to 10800 $cm^{-1}$ under collision free conditions in the gas phase. [57] By comparing these lifetimes with the measurements at low temperatures in condensed phases, the authors conclude that the triplet decay rate decreases by several orders of magnitude, going from $10^3$–$10^4$ $s^{-1}$ at room temperature to $10^{-1}$–10 $s^{-1}$ at low temperatures (20 K).[57] In $AcFA_5K\text{-}H^+$ at the delay times > 800 μs, population in $T_1^\dagger$ has most likely been quenched to its vibrational ground state where the lifetime should be considerably longer than that of the

vibrationally excited triplet state. As a result, we measure an average deactivation rate ($k_T$) with contributions from triplet species having a distribution of internal energies. Since the triplet lifetime of the cooled ions is likely to be much longer than the timescale of our experiment we cannot easily measure it. Thus, in the case of $AcFA_5K\text{-}H^+$ we added a constant to Eqn. (3.5) to compensate for the long time behavior in the fit.

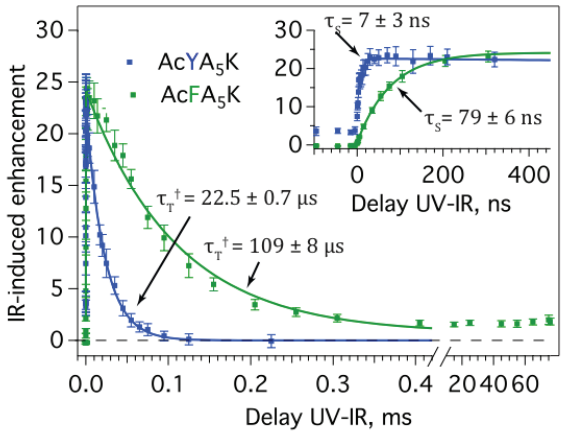


Figure 3.17 Infrared-induced enhancement of the chromophore side-chain loss fragment intensity for $AcFA_5K\text{-}H^+$ (green) and $AcYA_5K\text{-}H^+$ (blue) as a function of the UV-IR time delay, recorded in the cold octopole ion trap. The UV laser is fixed on the band origin of conformer B while the infrared OPO is fixed at 3391 and 3389 $cm^{-1}$ for $AcFA_5K\text{-}H^+$ and $AcYA_5K\text{-}H^+$, respectively. We use the maximum infrared power available of 14 mJ/pulse to maximize photofragmentation. The total IR-induced enhancement for $AcYA_5K\text{-}H^+$ is multiplied by a factor of 5.8 for comparison reasons. The initial rise and decay are fit with Eqn. (3.5) to extract the $S_1$ and $T_1$ time constants. The inset shows the initial rise of the signal and its exponential fit.

The fit parameters that arise from our simplified kinetic model provide the rate constants $k_S$ and $k_T$, and hence the lifetime of $S_1$ ($\tau_S$) and the average lifetime of $T_1^\dagger$ ($\tau_T$) :

$$\tau_S = \frac{1}{k_S};\ \tau_T = \frac{1}{k_T} \qquad (3.6)$$

This gives $S_1$ lifetimes of 79 ± 6 ns and 7 ± 3 ns for $AcFA_5K\text{-}H^+$ and $AcYA_5K\text{-}H^+$, respectively (Figure 3.17). These are the timescales on which the spectra presented in Figure 3.9 and Figure 3.14 evolve, where the initially sharp spectra broaden until all conformers yield the same final IR spectrum. In a similar manner, we determine the average triplet lifetimes to be ~100 µs and ~20 µs for $AcFA_5K\text{-}H^+$ and $AcYA_5K\text{-}H^+$, respectively (using the fit data from Figure 3.17).

The lifetimes we determine for $S_1$ are consistent with those reported for neutral Tyr and Phe analogs in previous gas-phase studies. Martinez et al. determined that the fluorescence lifetimes of tyrosine analogs in supersonic jet expansion experiments were less than 10 ns.[47] Sur and Johnson estimated the singlet state lifetime of phenol (the smallest analog of tyrosine) to be 2 ns for the bare molecule and 20 ns when stabilized by hydrogen bond formation with a single water molecule.[58] Other studies confirm the lifetime of ~2 ns for phenol and substitutes.[59, 60] These values are in good agreement with the 7 ± 3 ns lifetime we report above for $AcYA_5K\text{-}H^+$. In a similar manner, the 79 ± 6 ns lifetime we determine for $AcFA_5K\text{-}H^+$ is consistent with those reported in the literature for analogous systems. Hickman et al. measured the lifetime of the first electronically excited state of toluene (the smallest analog of phenylalanine) in supersonic jet expansion experiments to be 86 ns.[61] In similar experiments, Martinez and coworkers reported lifetimes for several analogs to be in the range of 65–74 ns.[47] Hashimoto et al. took the experiments one step further and showed that the $S_1$ lifetime of neutral L-phenylalanine is conformer dependent and ranges from 29 to 87 ns.[62] The authors give two possible explanations for this variation in lifetimes. The first involves conformer-selective intersystem crossing to a triplet state, while the second invokes a proton transfer reaction between the carboxylic and amino groups.[62] Additional experiments show that the lifetimes for the $S_1$ state of neutral phenylalanine range between 19.6–118 ns for different conformations.[63] The $NH_2$ – π-electron interaction seems to increase the non-radiative decay rate, shortening the lifetime of the $S_1$ state and decreasing the fluorescence quantum yield. To explore this idea further, Malis et al. measured conformer-specific $S_1$ lifetimes of the model system N-acetylphenylalaninylamide.[17] They report the lifetime to be 70 ns for the extended conformer, while the folded species have lifetimes of 35 ns and 1.5 ns.[17] In this work, we report only the $S_1$ lifetime for Conformer B of $AcFA_5K\text{-}H^+$ due to the difficulty of the experiment. However, we note that this value is consistent with a free phenylalanine chromophore, indicating that the ring does not strongly participate in non-covalent interactions.

In contrast to the $S_1$ lifetimes, the average vibrationally activated triplet lifetimes of ~100 and ~20 μs that we report above for $AcFA_5K\text{-}H^+$ and $AcYA_5K\text{-}H^+$, respectively, are much longer that those reported in the literature for the corresponding isolated chromophores. For example, Dietz *et al.* measured triplet lifetimes of 3 μs for the neutral phenylalanine analog toluene [64] and 300 ns for the neutral tyrosine analog phenol.[58] A significant difference between these gas-phase experiments and the current work is the size of the molecules. Our protonated peptides have many more vibrational degrees of freedom, and for the same amount of vibrational energy above the dissociation threshold would require more time to dissociate. This effect is caused by a

kinetic shift,[65, 66] which is the excess energy required to observe detectable dissociation within a certain experimental timeframe. A slower dissociation rate would extend the measured lifetimes in our experiment. Moreover, during the time required for the dissociation, the molecules in our experiment might experience several collisions with residual cold helium that decrease the unimolecular decay rate and increase the $T_1$ lifetime.

Collisional cooling also explains the long time behavior (> 1 ms) of $AcFA_5K\text{-}H^+$ where the infrared photofragmentation enhancement becomes constant within the observable time window of our 10 Hz experiment (see Figure 3.15 or Figure 3.17). We test the validity of this assumption by estimating the collision frequency using basic conductance calculations and assuming molecular flow. In the experiment, a small copper box encloses the ion trap and has a total conductance of 1.7 l/s when using helium at 10 K. A turbo molecular pump evacuates the chamber containing the ion trap at a rated pumping speed of 600 l/s for helium, which typically achieves a measured working pressure of $10^{-5}$ mbar. After correcting for the ion gauge's decreased sensitivity to helium, these parameters result in an estimated average pressure inside the ion trap of 2 x $10^{-2}$ mbar,[67] which corresponds to an average helium density at 10 K to be ~$10^{16}$ $cm^{-3}$ with a collision frequency of 1–10 collisions/μsec.[68] Under these conditions we expect complete cooling of the molecules within a few milliseconds, and this could extend the $T_1$ lifetime of $AcFA_5K\text{-}H^+$ to more than the 100 ms timescale of our experiment.

## 3.4.7 Effect of additional vibrational excitation on the lifetime of the singlet and triplet states in $AcFA_5K\text{-}H^+$

We decide to check whether excess vibrational energy on the triplet surface results in a decrease in the triplet state lifetime of $AcFA_5K\text{-}H^+$. The UV laser excites conformer B to either the band origin of the $S_1$ state or to the one of its vibronic levels, lying 531.1 $cm^{-1}$, 1460.1 $cm^{-1}$, or 2425.5 $cm^{-1}$ above the band origin (Figure 3.18). The UV transition $B_0$ (37555.3 $cm^{-1}$) is the band origin, and upon its excitation the molecules have zero vibrational energy in the $S_1$ state. In benzene the 0-0 transition is symmetry forbidden, but in the phenylalanine this transition is allowed, because the symmetry breaks when the alanyl group is added to the aromatic ring.[69] Another electronic transition $B_1$ at 38086.4 $cm^{-1}$ (531.1 $cm^{-1}$ to the blue from $B_0$) is probably due to in-plane bending vibration of the aromatic ring.[70] UV transition labeled as $B_2$ (39015.4 $cm^{-1}$, 1460 $cm^{-1}$ to the blue from $B_0$) might correspond to a skeletal stretching vibration of the aromatic ring, and $B_3$ (39980.8 $cm^{-1}$, 2425.5 $cm^{-1}$ to the blue from $B_0$) can be a combination of several lower frequency skeletal vibrations of the aromatic ring.

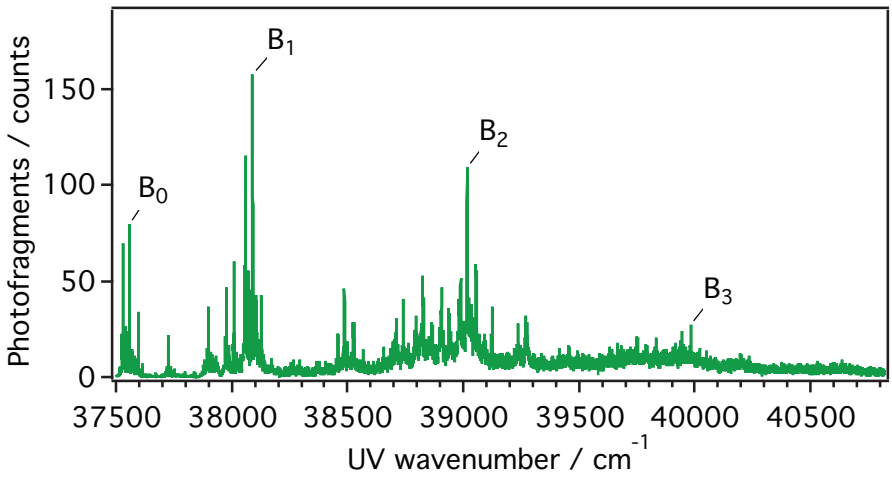


Figure 3.18. The UV photofragment spectrum of $AcFA_5K\text{-}H^+$, recorded monitoring the loss of neutral phenylalanine side-chain m/z=601. The UV peak $B_0$ (37555.3 $cm^{-1}$) is the band origin for conformer B. $B_1$ (38086.4 $cm^{-1}$), $B_2$ (39015.4 $cm^{-1}$), $B_3$ (39980.8 $cm^{-1}$) mark the vibronic transitions to different vibrationally excited levels of conformer B in $S_1$ state.

When the IR OPO probes the molecules 5 ns after the UV laser pumps the $B_0$ transition, the infrared spectrum is sharp and represents the molecules in the $S_1$ electronic state (Figure 3.19a). However, as the energy of the UV photon increases (Figure 3.19b-d), i.e. pumping the transitions $B_1$, $B_2$, and $B_3$, the infrared spectra recorded 5 ns after the UV excitation become broader. Moreover, the most strongly hydrogen bonded NH stretches shift blue upon the increase of the vibrational energy in the $S_1$ state (dashed arrows in Figure 3.19). The vibrational energy in the $S_1$ state redistributes *via* IVR before the fragmentation takes place, and this might result in the broadening of the spectrum. It can also be that the intersystem crossing to the triplet state increases at higher vibrational levels of the $S_1$ state, and as a result the infrared spectra presented in Figure 3.19b-d are the superposition of the spectra from the singlet and vibrationally excited triplet state. However, the experiment presented below ruled out the latter possibility.

We measure the singlet and the "average" triplet state lifetimes of $AcFA_5K\text{-}H^+$ excited to different vibrational levels of the $S_1$ state, analogously to what is described in Section 3.4.6. We probe the UV pre-excited molecules with the IR OPO fixed at 3391 $cm^{-1}$, which is a band that we attribute to a vibrational mode in the triplet state. Figure 3.20 depicts the enhancement of the phenylalanine side-chain loss fragment intensity for $AcFA_5K\text{-}H^+$ as a function of the UV-IR time delay for different excess vibrational energies. The initial rise time ~80 ns is similar in all the curves and is determined by the total lifetime of the $S_1$ state (see Section 3.4.6). The total deactivation rate of the $S_1$ state ($k_s$) is the sum of the rate of the intersystem crossing ($k_{ISC}$),

internal conversion ($k_{IC}$) and fluorescence ($k_r$). The fact that $k_s$ does not change with excess vibrational energy might be either caused by a very low rate of the intersystem crossing $k_{ISC} << k_{IC} + k_r$ or a negligible dependence of the intersystem crossing rate on the additional vibrational energy in this range of energies. In section 3.4.14 we estimated the rate of the intersystem crossing in a smaller peptide AcFAK-$H^+$ and found that it is just slightly smaller than the total rate of deactivation $k_s$. Because the total deactivation rate of the $S_1$ states of both AcFAK-$H^+$ and $AcFA_5K$-$H^+$ are similar to the total deactivation rate in toluene, we think that the rate of the intersystem crossing in those molecules is determined by the chromophore and should be comparable, suggesting that $k_{ISC}$ in $AcFA_5K$-$H^+$ can not be much slower than the rate of internal conversion and fluorescence. On the other hand, the intersystem crossing rate might easily stay constant over the range of the vibrational energies used in our experiment (<2500 $cm^{-1}$). We would expect the intersystem crossing rate to be dependent on the vibrations of the chromophore. However, in such a large molecule as $AcFA_5K$-$H^+$ the vibrational energy is quickly redistributed through IVR and the relative portion of this energy localized in the chromophore's vibrations is very low. Thus it can be, that in order to detect any change in the singlet state lifetime we have to introduce much more vibrational energy into the molecule.

The other explanation why the intersystem crossing rate might stay constant over the excess vibrational energy range used in our experiment is an existence of a higher energy triplet state, $T_2$, closer in energy to $S_1$ than $T_1$ state. Fischer et al. analyzed the effect of the vibrational energy excess in the $S_1$ state on the rate of the intersystem crossing (ISC) in several isolated molecules and showed that it depends on the energy difference between the singlet and the triplet states.[71] In naphthalene, for the large $S_1$-$T_1$ gap of 9600 $cm^{-1}$, the ISC rate increases exponentially with a high increase of vibrational energy in $S_1$ (>8000 $cm^{-1}$) and linearly with a low increase of vibrational energy.[71] However, for the small $S_1$-$T_3$ gap of 1400 $cm^{-1}$, the rate constant stays almost constant, provided the transition goes directly *via* spin-orbit coupling.[71] Ultrafast $S_1$-$T_2$ intersystem crossing followed by internal conversion to $T_1$ was observed in benzene.[72] Thus, it is also possible that the intersystem crossing happens first to the higher excited triplet state lying slightly below $S_1$ (for example $T_2$) and then relaxes to the lowest triplet state.

At longer time delays after the UV excitation ( > 1 μs) the enhancement of the side-chain loss fragment is lower for the vibrationally excited $S_1$ state compared with the case when the UV laser excites the zero vibrational level. The additional vibrational energy pumped into the system appears to reduce the lifetime of the triplet state in agreement with the vibrational energy dependence of alkylbenzene triplet lifetimes summarized by Lohmannsroben.[57] When $AcFA_5K$-

$H^+$ is initially excited above the band origin of the $S_1$ state, the triplet state obtains more vibrational energy after intersystem crossing and as a consequence has a shorter lifetime.

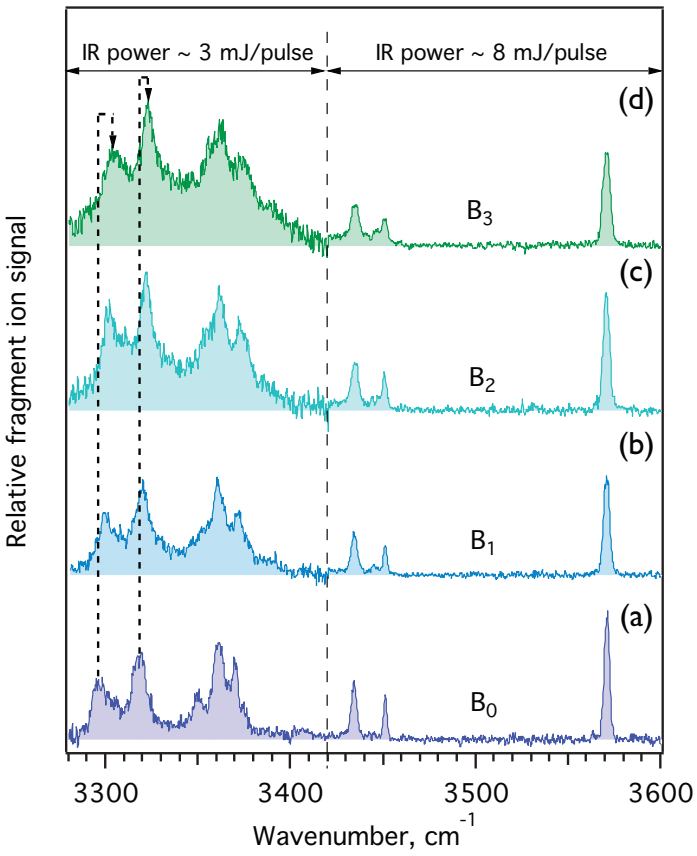


Figure 3.19. The infrared spectra of conformer B of $AcFA_5K\text{-}H^+$ recorded when the IR OPO probes the molecules 5 ns after the UV excitation. The UV laser excites different vibrational levels of the $S_1$ state: 37555.3 $cm^{-1}$ ($B_0$), 38086.4 $cm^{-1}$ ($B_1$), 39015.4 $cm^{-1}$ ($B_2$), 39980.8 $cm^{-1}$ ($B_3$)

## 3.4.8 Any prompt dissociation, causing $C_\alpha$-$C_\beta$ bond cleavage in $AcFA_5K\text{-}H^+$?

At this point, we would like to estimate whether along with intersystem crossing and internal conversion we have direct dissociation either from a πσ* state or *via* other prompt mechanisms, resulting in the $C_\alpha$-$C_\beta$ bond cleavage (analogs of mechanisms proposed in the groups of Jouvet and Dugourd for small protonated tyrosine-containing peptides).[10, 73] Indeed, we observe some side-chain loss fragmentation after the $AcFA_5K\text{-}H^+$ molecules are irradiated with the UV laser alone (see Figure 3.3 c). In Figure 3.21 we present the amount of the side-chain loss signal as a function of the UV laser pulse energy. The fragmentation is proportional to $I^n$, where I is the

intensity of the absorbed light, n is the number of absorbed photons. A least squares fit of the experimental data results in n = 2.07 ± 0.05, which means that the dissociation of the $C_\alpha$-$C_\beta$ bond with only the UV laser (see Figure 3.3 c) at the usual energy of 1.5 mJ/pulse used in our experiments results from two photon absorption. Any prompt dissociation mechanisms resulting in phenylalanine side-chain loss that require the absorption of one UV photon is less significant than the dissociation from the triplet state.

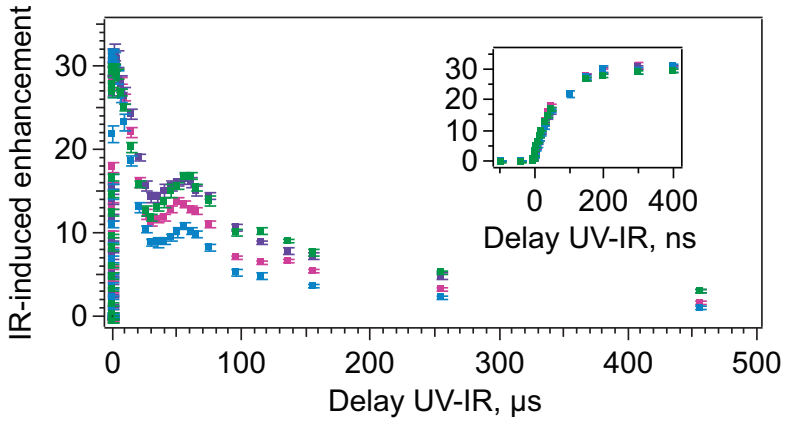


Figure 3.20 Infrared-induced enhancement of the chromophore side-chain loss fragment intensity for $AcFA_5K\text{-}H^+$ as a function of the UV-IR time delay at different amounts of vibrational energy in $S_1$ state. The UV laser excites different vibronic transitions of conformer B ( 37555.3 $cm^{-1}$ (violet), 38086.4 $cm^{-1}$ (green), 39015.4 $cm^{-1}$ (magenta), 39980.8 $cm^{-1}$ (light blue)), while the infrared OPO is fixed at 3391 $cm^{-1}$. We use the maximum infrared power available of 12 mJ/pulse to maximize the photofragmentation yield. The intensities are scaled to overlap at 400 ns for comparison. The inset shows the initial rise of the signal.

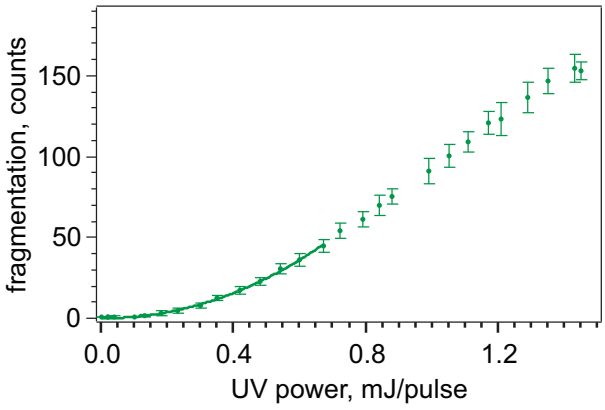


Figure 3.21 $AcFA_5K\text{-}H^+$ . The amount of the side-chain loss signal as a function of the UV laser pulse energy. The UV laser excites the band origin of conformer B. The low energy data is fit to the equation $f(x) = a \cdot x^n$. The resulting parameters are a = 104 ± 3, n = 2.07 ± 0.05.

The molecules that absorb only one UV photon still stay below the dissociation barrier after they experience intersystem crossing. In this case, subsequent absorption of IR radiation can

either increase the $S_1$-$T_1$ intersystem crossing rate (if the molecules are still in $S_1$) or promote these species above the dissociation threshold in the triplet state (Figure 3.3 d-e). With this knowledge, we try in the next section to develop a more quantitative picture of the barrier the $T_1$ species must overcome to dissociate. In doing so, we acknowledge that such measurements are complicated by the fact that we do not know the initial internal energy of the $T_1^{\dagger}$ species.

### 3.4.9 The barrier height in the triplet surface in $AcFA_5K\text{-}H^+$

If $AcFA_5K\text{-}H^+$ undergoes collisional cooling while on the triplet surface, there should be a time dependence to the total energy needed for dissociation. For $AcFA_5K\text{-}H^+$, we have already established that the $S_1$ lifetime is 79 ± 6 ns. Therefore, if the UV laser-IR OPO time delay is tuned to 600 ns, we can be sure that nearly all of the initially excited molecules have decayed to the triplet. While the vibrationally excited $T_1$ species experience a few collisions during this time, the delay is too short to allow complete vibrational cooling of the molecules.[74] One can determine how many photons are required for dissociation by fixing the IR OPO on the transition at 3391 $cm^{-1}$, which appears to be unique to the triplet state, and recording the infrared dissociation enhancement as a function of the IR OPO pulse energy. The quadratic dependence of the enhancement for energies below 3 mJ/pulse, shown in Figure 3.22a, clearly demonstrates that with a UV laser-IR OPO delay of 600 ns, the infrared dissociation enhancement is a two-photon process. The transition begins to saturate above 3 mJ/pulse, as evidenced by an inflection point in the enhancement curve, then asymptotically approaches a value around 3000%. This result supports the existence of a barrier on the triplet surface in accordance with our model and is consistent with what has been determined for phenylalanine derivatives.[20] Although it is evident that the dissociation barrier is above the $S_1$ band origin, we can provide only an upper limit of 6800 $cm^{-1}$ for its height. We always excite the molecules with the UV laser in the beginning of the trapping cycle, when there are still collisions with helium. It can happen that one IR photon is already enough to overcome the dissociation barrier, but because $AcFA_5K\text{-}H^+$ molecule has a large number of vibrational degrees of freedom, the dissociation rate may be slower than the cooling rate in the 22-pole ion trap such that the molecules cool again below the dissociation barrier. In this case the second infrared photon is necessary to increase the dissociation rate in order to detect photofragments on the timescale of our experiment.

To test this idea further, we can extend the UV laser-IR OPO time delay to 85 ms and once again measure the IR power dependence of the fragmentation signal. At this time delay, the vibrationally excited $T_1$ species clearly experience enough collisions to allow for vibrational

cooling. After IR excitation we leave the molecules 2 ms to dissociate in the 22-pole ion trap before we release them for detection, so that we would not have to account for the kinetic shift comparing the power dependence curves presented in Figure 3.22a and Figure 3.22b.[65, 66] Towards the end of the 100 ms trapping cycle the helium gas is mostly pumped away, and we have many fewer collisions, which greatly reduces the probability of the triplet state re-cooling during its dissociation timescale. We again fix the IR OPO on the transition corresponding to a band unique to the triplet state (3391 $cm^{-1}$) and record the enhancement of the side-chain loss fragment as a function of the infrared laser pulse energy (Figure 3.22b). The fit of the experimental data shows that at this long delay, one needs three photons to dissociate the molecule instead of two, providing evidence of cooling on the triplet surface. These results also allow us to place the limits for the total barrier height from the bottom of $T_1$ state to the dissociation threshold along the $C_\alpha$-$C_\beta$ bond in $AcFA_5K\text{-}H^+$ between 6782 $cm^{-1}$ and 10173 $cm^{-1}$. This is greater than the ~3500 $cm^{-1}$ (10 kcal/mol) derived from *ab initio* calculations made by Tseng *et al.* for phenylethylamine. However, we note that it is difficult to determine exact energetics of molecules this size due to the kinetic shift[65, 66] and our inability to monitor dissociation events that occur on a timescale longer than 100 ms.

These results also explain why in $AcFA_5K\text{-}H^+$ we do not observe an increase of fragmentation in the Amide I and Amide II spectral region by adding the IR OPO after the UV laser. The photon enegy in this spectral region is ~2 times smaller than in NH-stretch region and the infrared power of our IR OPO is lower (1–2 mJ/pulse). This power might be not sufficient to induce the absorption of the four photons that would be the minimum required for the molecule to dissociate.

### 3.4.10 Size dependence: $AcFAK\text{-}H^+$ *vs.* $AcFA_5K\text{-}H^+$.

We presented above the infrared power dependence for the dissociation of $AcFA_5K\text{-}H^+$ on the triplet surface and showed that it requires a minimum two 3391 $cm^{-1}$ photons. However, as the molecule gets smaller, its dissociation rate on the triplet surface would increase for the same amount of the total vibrational energy above the dissociation barrier. For example, in the smaller UV excited peptide $AcFAK\text{-}H^+$ we observe the enhancement of the side-chain loss fragment by adding the IR OPO in the amide I and amide II spectral regions (see Section 3.5.4). We can scan the energy of the IR photons down to 1550 $cm^{-1}$ and measure an infrared spectrum of the UV-excited species and still observe enhancement of the side-chain loss fragment, in contrast with the seven amino acid peptide $AcFA_5K\text{-}H^+$ where no enhancement was observed in this spectral

region under the same experimental conditions. This suggests that the energy difference between the dissociation barrier and the $S_1$ band origin in AcFAK-$H^+$ is less than 1550 $cm^{-1}$, provided the fragmentation is a one photon process, while in $AcFA_5K$-$H^+$ this difference seems to be larger (Section 3.4.9). However, it is possible that the barriers on the triplet surface are similar in both cases, but that $AcFA_5K$-$H^+$ requires a higher excess of the vibrational energy above the dissociation barrier to dissociate on the timescale of our experiment compared to AcFAK-$H^+$.

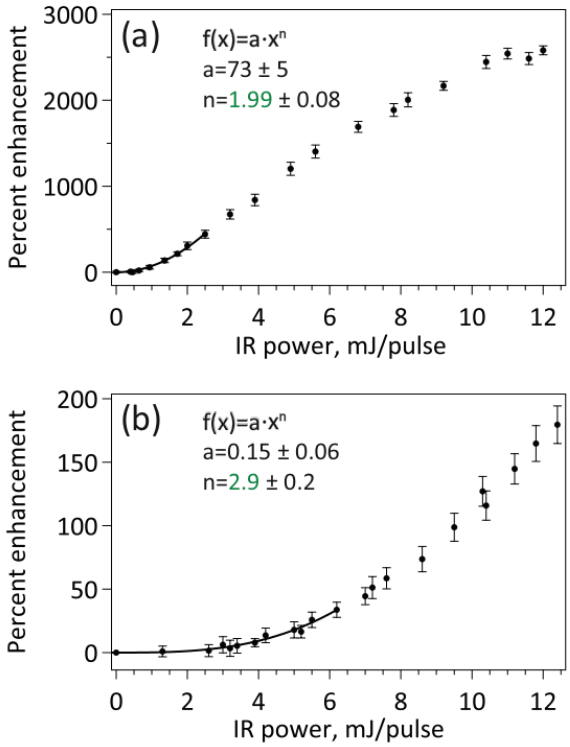


Figure 3.22 Infrared-induced enhancement of the phenylalanine side-chain loss fragment for $AcFA_5K$-$H^+$ when using UV-IR time delays of (a) 600 ns and (b) 85 ms as a function of infrared power. The UV laser excites the band origin of conformer B while the IR OPO probes at 3391 $cm^{-1}$. The fit parameters, shown above, reveal that fragmentation is a two photon process at short times but requires three photons at long times.

By fixing the IR OPO wavelength at 3397 $cm^{-1}$, corresponding to the phenylalanine NH stretch in the vibrationally excited triplet state (Figure 3.13), and the UV laser wavelength at the band origin of conformer A, we can record how the population in the triplet state changes with the increase of the delay between the UV and IR OPO lasers in AcFAK-$H^+$. Figure 3.23 shows that the maximum enhancement of the side-chain loss fragment in AcFAK-$H^+$ is ~2 times lower than in the larger peptide $AcFA_5K$-$H^+$ (Figure 3.17). Data in Figure 3.17 and in Figure 3.23 were recorded in the new cold octopole ion trap with the same experimental conditions such as pressure, delays, alignment, and UV laser power. The lower number of vibrational degrees of freedom in AcFAK-$H^+$ causes better fragmentation with the UV laser alone and hence lower enhancement by the IR photon.

The fit of the experimental data in Figure 3.23 with the Eqn. (3.5) from the kinetic model provides us with the singlet state lifetime 52 ± 3 ns and the "average" triplet decay time ~60 μs.

The singlet state lifetime in AcFAK-$H^+$ is thus ~1.5 times shorter than in $AcFA_5K$-$H^+$, which might be due to different interactions of the phenylalanine chromophore with the rest of the molecule. These same interactions probably cause the 71.3 $cm^{-1}$ difference between the positions of the band origins of conformer A of AcFAK-$H^+$ (37484.0 $cm^{-1}$) and conformer B of $AcFA_5K$-$H^+$ (37555.3 $cm^{-1}$) in the electronic spectrum. The "average" triplet state lifetime in AcFAK-$H^+$ from different vibrationally excited levels as the molecules cool down is ~1.7 times faster than in $AcFA_5K$-$H^+$. This means that the smaller molecule dissociates faster with the same excess of the vibrational energy on the triplet surface than a bigger one.

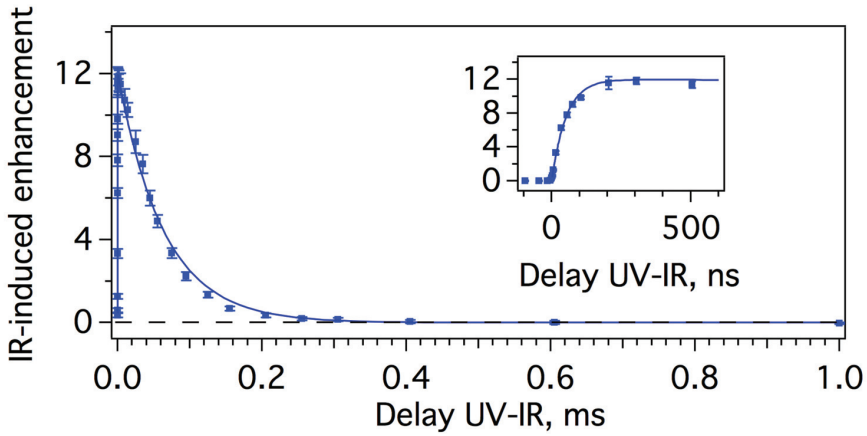


Figure 3.23 AcFAK-$H^+$. Data recorded in the new cold octopole trap. Enhancement of the side-chain loss fragment as a function of the delay between the UV and IR. UV excites the band origin of conformer A (37484 $cm^{-1}$), 8 ms after the helium pulse. IR probes the phenylalanine NH stretch in the vibrationally excited triplet state (3397 $cm^{-1}$, 13 mJ/pulse). We show the exponential fit from the Eqn. (3.5) that provides us with the time constants $\tau_S$=52 ± 3 ns and $\tau_T$=64 ± 2 μs.

When we probe with the IR OPO the NH stretch at 3418 $cm^{-1}$ in AcFAK-$H^+$ (Figure 3.24), we obtain the same decay time as when we excite the phenylalanine NH stretch of a vibrationally excited triplet state (3397 $cm^{-1}$) (Figure 3.23). While in the latter case the signal decays to zero around 300 μs after the UV excitation, in the former case we observe a constant enhancement of the side-chain loss fragmentation up to several tens of milliseconds after the UV excitation. This constant enhancement after 300 μs most probably is due to the longer lifetime of the cold triplet that we cannot measure on the time scale of our experiments.

In both the seven amino acid peptide, $AcFA_5K$-$H^+$,[38] and the three amino acid peptide, AcFAK-$H^+$ (Figure 4.1), the lowest transitions in the electronic spectrum are close to the band origin of protonated phenylalanine (37520.9 $cm^{-1}$),[75] indicating that the aromatic ring is relatively free and its electronic structure is similar to that of toluene. Either the height of the

dissociation barrier in $T_1$ relative to the $S_1$ band origin is lower in the smaller molecule or the dissociation rate is faster due to smaller number of vibrational degrees of freedom.

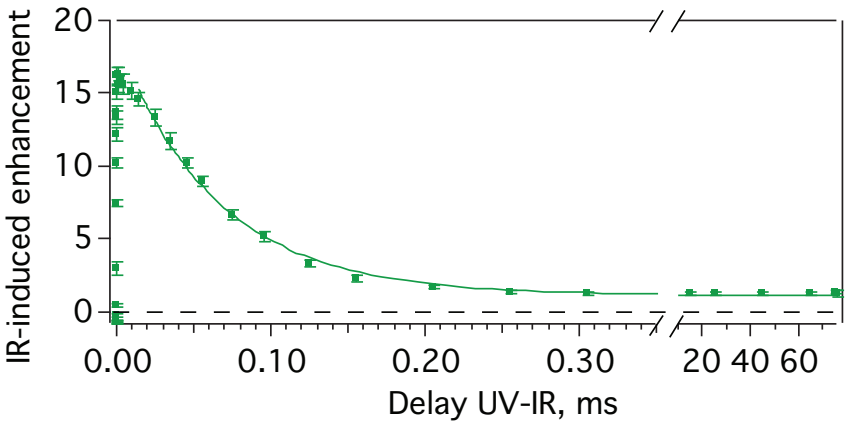


Figure 3.24 AcFAK-$H^+$. Data recorded in the new cold octopole trap. Enhancement of the side-chain loss fragment as a function of the delay between UV and IR. UV excites the band origin of conformer A (37484 $cm^{-1}$), 8 ms after the helium pulse. IR probes the NH stretch that we can still observe after cooling the vibrationally excited triplet state (3418.1 $cm^{-1}$, 13 mJ/pulse). The single exponential fit provides us with the time constant $\tau_T$=65 ± 2 μs.

## 3.4.11 Infrared spectra of the vibrationally deactivating triplet state $AcFA_5K$-$H^+$

We have already presented the time evolution of the transient IR spectra of $AcFA_5K$-$H^+$ (Conformer B) in Figure 3.9 at low infrared power. We have also shown that dissociation from the vibrationally excited triplet is a two-photon process, and that dissociation from the vibrationally deactivated triplet state is a three-photon process. When the IR power is ~1 mJ/pulse (one photon regime), there is no enhancement of the side-chain loss fragment at delays between UV excitation and IR OPO longer than several hundreds of microseconds. The power dependence data presented above provide evidence for collisional cooling of the $T_1$ species and imply that its infrared spectrum should evolve as a function of time. To verify this, we acquire infrared spectra of $AcFA_5K$-$H^+$ (conformer B) by scanning the IR OPO at different time delays after the UV excitation (Figure 3.25). The multiphoton nature of this experiment requires that maximum laser power be used, thus likely producing saturated spectra. Nevertheless, at a UV-IR time delay of 2 ms we record a sharper spectrum, which strongly supports the idea of vibrational cooling on the triplet surface (the top trace Figure 3.25). In fact, the cooling happens on the timescale of 860 μs, because at longer delays the enhancement of the side-chain loss fragment

stays constant (Figure 3.15 and Figure 3.17). Moreover, the infrared spectrum, recorded at 65 ms delay between the UV excitation and the IR OPO probe (the top trace in Figure 3.26), looks almost identical to the one obtained at 2 ms delay between the lasers (the top trace in Figure 3.25). This observation allows us to conclude that we are probing molecules at the bottom of the triplet well. We roughly estimate the average collision frequency in the 22-pole ion trap to be 1-10 collisions/μs. Because the helium gas is continuously pumped out of the trap, the collision frequency is higher in the beginning of the trapping cycle, when we prepare the electronically excited molecules, and lower towards the end of the trapping cycle. A collision frequency of 5 collisions/μs, provides us with approximately 4300 collisions on the timescale of 860 μs, that seems a reasonable number to cool down the molecules in the vibrationally excited triplet state.[74]

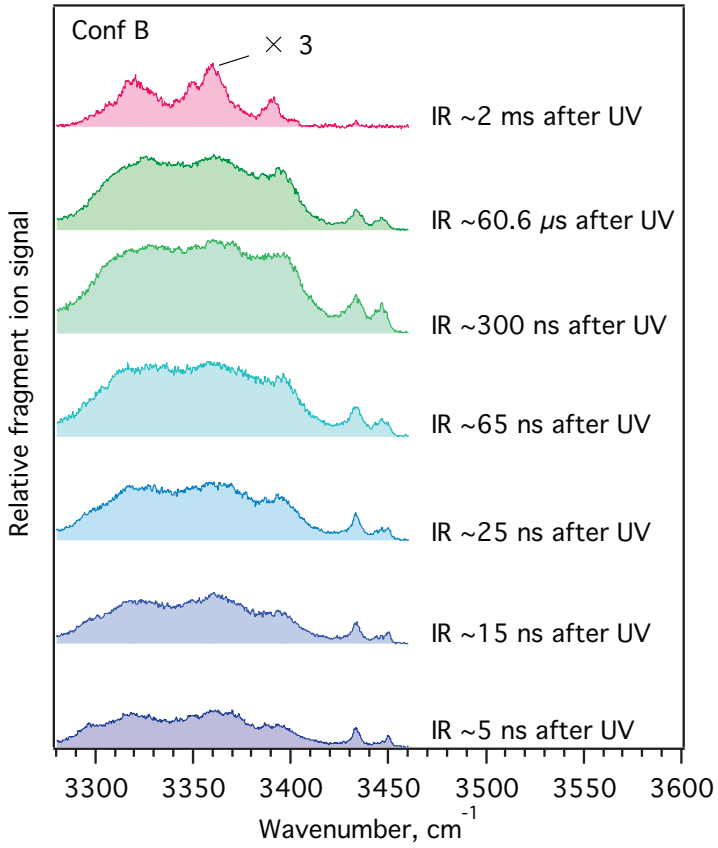


Figure 3.25. IR spectra of the UV excited $AcFA_5K\text{-}H^+$ for different delays between the UV and IR lasers with the UV wavenumber fixed at 37555.3 $cm^{-1}$. The IR power is ~9 mJ/pulse.

Figure 3.26 presents on one graph the comparison between the vibrational spectrum of conformer B of $AcFA_5K\text{-}H^+$ in its ground electronic state ($S_0$), its first electronically excited state ($S_1$), its vibrationally excited triplet state ($T_1^\dagger$), and its vibrationally deactivated triplet state ($T_1$).

The spectrum of vibrationally deactivated triplet state seems to resemble the ground state spectrum of conformer B. It seems reasonable to suggest, that the IR band at 3391 $cm^{-1}$ might be the $Phe^{1}$ NH-stretch that shifts to the red from 3402 $cm^{-1}$ in the ground state and to the blue from 3369 $cm^{-1}$ in the $S_1$ electronically excited state of conformer B. However, we have not yet confirmed this assignment by performing experiments with $^{15}N$ isotopically labeled phenylalanine.

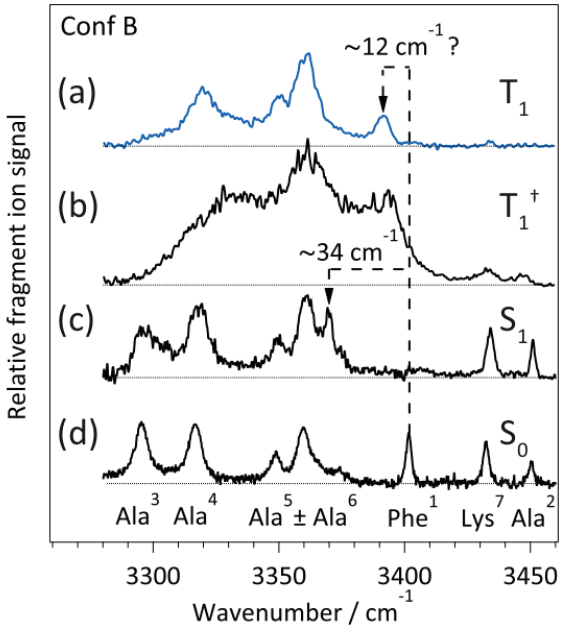


Figure 3.26. Infrared spectra of UV-excited $AcFA_5K\text{-}H^+$ (conformer B) recorded using UV-IR time delays of (a) 65 ms, (b) 600 ns, and (c) 5 ns. In (d), the IR OPO interrogates the ions 150 ns before the UV laser.

Interestingly, the spectrum acquired using a 85 ms time delay remains the same regardless of which conformer (A, B, C, or D) is initially excited with the UV laser (Figure 3.27). This means that the spectrum in Figure 3.26a could contain contributions from multiple conformers that are trapped during the cooling process on the triplet surface. If there are several local minima on the triplet surface, we might observe the contribution from different conformations that populate those local minima. Unfortunately, we do not have the ability to verify this spectroscopically using only one IR OPO. We can, however, take the analysis one step further using DFT calculations to determine to which extent various structures contribute to the non-conformer specific spectrum of the triplet state.

### 3.4.12 DFT calculations of the lowest triplet states of $AcFA_5K\text{-}H^+$

To find out which conformations contribute most to the non-conformer specific infrared spectrum of the triplet state, we decide to calculate the structures and the corresponding triplet state infrared spectra for four conformers (A, B, C, and D) of $AcFA_5K\text{-}H^+$. As a starting geometry we use the ground-state structures determined in a previous report using isotopic substitution and theoretical calculations.[33] We perform similar density functional theory calculations (UB3LYP/6-31G**) to those in the previous work and find four minimum energy structures for the triplet species, the infrared spectra of which are presented in Figure 3.28. We have to note here, that though the calculated spectra of the ground state conformations[33] show the right order of the spectroscopic transitions, the calculated frequencies do not match the measured values particularly well. Especially, in conformer B and A the calculated frequencies of $Ala^3$, $Ala^4$, $Ala^5$, and $Ala^6$ are all ~8–20 $cm^{-1}$ shifted to blue compared with the experiment. This might result in the similar errors for those frequencies in the triplet state configuration.

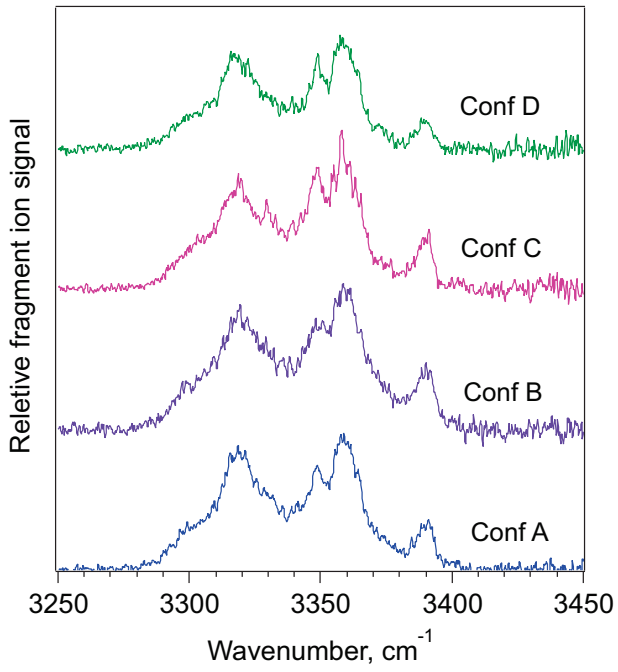


Figure 3.27. IR spectra of different UV excited conformers of $AcFA_5K\text{-}H^+$. IR OPO probes the molecules 85 ms after the UV excitation. The power of IR OPO is ~9 mJ/pulse at 3300 $cm^{-1}$ and in the region 3400–3450 $cm^{-1}$ it drops to ~4 mJ/pulse.

In Figure 3.28 we compare calculated spectra of the lowest triplet states of the conformers A, B, C, and D with the non-conformer selective infrared spectrum presented in Figure 3.26a. By comparing the relative energies of the triplet states we find that the most stable is the triplet state of conformer D, the next lowest in energy is the triplet state of conformer B, followed by C and A. Conformers D and B appear to be the most stable conformers in the ground state molecule as well, based on DFT calculations.[33] However, population transfer experiments in $AcFA_5K\text{-}H^+$ revealed higher population of conformer B than that of conformer D.[76]

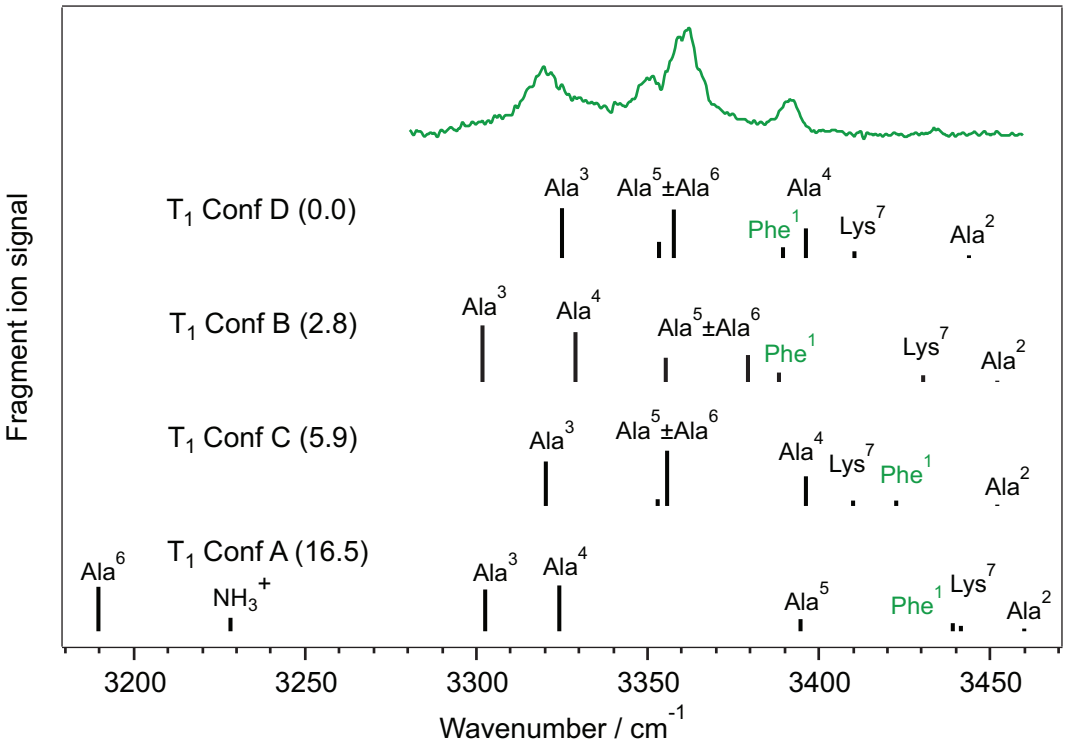


Figure 3.28. The black stick spectra are the calculated spectra of the lowest triplet state of conformers A, B, C, and D with their relative zero-point-corrected energy in kJ/mol. In green we present the experimental spectrum recorded 65 ms after the UV excitation of either of the conformers (A, B, C or D).

In Section 3.4.11 we made a tentative assignment of a new band appearing in the spectrum of the vibrationally deactivated triplet state at 3391 $cm^{-1}$ to phenylalanine NH stretch vibration. Indeed, the experimental spectrum of the "cold" triplet state (Figure 3.29b green trace) seems to resemble the experimental spectrum of the ground state of conformer B (Figure 3.29b black trace). Our calculations show that the change of the spin of the electron in conformer B does not considerably perturb the overall structure of the molecule. Similar to what we observed in the electronically excited singlet state (Figure 3.26 violet trace), the phenylalanine NH stretch forms

a stronger hydrogen bond with the π cloud of the chromophore, and as a result it shifts ~14 $cm^{-1}$ to the red, causing the main difference between the calculated spectra of the $S_0$ and $T_1$ state of conformer B (Figure 3.29a). Thus, the infrared band appearing in the experimental infrared spectrum of the cold triplet state at 3391 $cm^{-1}$ might correspond to phenylalanine NH stretch of the triplet state of conformer B. However, though the $Ala^4$, $Ala^5$, $Ala^6$, and $Lys^7$ NH stretch vibrations in the calculated spectrum of conformer B also line up with the infrared transitions in the experimental spectrum recorded at long delay (65 ms) after the UV excitation, the $Ala^3$ NH stretch that should appear around 3301 $cm^{-1}$ has a very low relative intensity. That means that the experimental infrared spectrum recorded at long delay should have a contribution from the other conformers that lack an infrared transition at ~3301 $cm^{-1}$.

Such a candidate could be a triplet state of conformer D, the calculated spectrum of which is presented in Figure 3.29c. According to the calculations, the slight change of the electron density in the triplet state of conformer D causes ~7 $cm^{-1}$ of red shift of the $Ala^3$ NH stretch, ~13 $cm^{-1}$ of red shift of the $Phe^1$ NH stretch and a stronger coupling between $Ala^5$ and $Ala^6$ NH stretches compared with the ground state (Figure 3.29c). Those infrared transitions that overlap in the triplet states of conformers B and D appear as the most intense in the experimental infrared spectrum recorded at long delay (65 ms) after the UV excitation (Figure 3.29d).

In the calculated infrared spectra of the triplet states of conformers C and A (Figure 3.28) we observe several transitions that do not match the experimental spectrum (Figure 3.28 green trace). Also the energies of the triplet states of conformers A and C are higher then the energies of the triplet states of conformers B and D, which under the conditions of slow collisional cooling in our trap would result in a lower population of these states.

At long delays after the UV excitation (>2 ms) all conformers undergo intersystem crossing to a mixture of the triplet states that after cooling mainly represents the triplet state of conformers B and D. These two conformers (B and D) have lower triplet state energies than the other two conformers (A and C). The energy gap between the first excited singlet state (measured to be 37551 $cm^{-1}$) and the lowest triplet state (calculated to be 28390 $cm^{-1}$) of conformer D is 9161 $cm^{-1}$. This value is similar to previous measurements of the $S_1$ - $T_1$ energy gap in toluene: 8400 $cm^{-1}$ derived from oxygen perturbed $S_0$ - $T_1$ absorption spectra,[77] and ~8100 $cm^{-1}$ derived from electron-energy loss spectra.[78] This is slightly higher than our estimation for this gap based on infrared power dependence (< 6800 $cm^{-1}$, see Section 3.4.9). We noted in Section 3.4.9, that the slow dissociation rate of a molecule as large as $AcFA_5K\text{-}H^+$ might be the reason why the estimation of the $S_1$-$T_1$ energy gap using the infrared power dependence is imprecise. It could

happen that upon an absorption of one IR photon 600 ns after the UV excitation (the time when we record 2-photon IR power dependence), the vibrationally activated molecules undergo collisions with cold helium, which bring them back below the dissociation barrier during the time required for its statistical dissociation on the triplet surface. Then, in order to dissociate, the molecules would have to absorb the second infrared photon, which would increase the dissociation rate. However, at 85 ms after the UV excitation (the time when we record 3-photon IR power dependence), the residual helium is mostly pumped away and the collisional cooling is much less efficient. We can also neglect the radiative cooling on the timescale of several ms, based on the work of Andersen et al.[79] This would result in the $S_1$-$T_1$ energy gap to lie between 6800 $cm^{-1}$ and 10200 $cm^{-1}$, which is close to the value based on DFT calculations.

### 3.4.13 Infrared spectra of the vibrationally deactivating triplet state AcFAK-$H^+$

The cooling process changes the spectrum of the triplet state more drastically in AcFAK-$H^+$ than in $AcFA_5K$-$H^+$. The time evolution of the infrared spectrum of the electronically excited conformer A of AcFAK-$H^+$, recorded at high IR OPO fluence, is depicted in Figure 3.30. At the power of IR OPO ~ 9 mJ/pulse the spectrum of the first electronically excited state of conformer A is clearly saturated (lower trace in Figure 3.30) compared to the spectrum recorded using the lower IR OPO power (lower trace in Figure 3.12, left side). The OH stretch is ~8.7 $cm^{-1}$ wide and has a dip in the middle corresponding to the wavenumber of the OH stretch in the ground state of conformer A. The infrared band at 3419 $cm^{-1}$, corresponding to the lysine NH stretch (Figure 4.7a), is also much lower in intensity compared to the unsaturated $S_1$ state spectrum (lower trace in Figure 3.12, left side). We mark the positions of both OH stretch and lysine NH stretch with the dashed vertical lines in Figure 3.30. The second trace from the bottom of the Figure 3.30 represents the vibrationally activated triplet state of AcFAK-$H^+$ with four infrared transitions in the NH stretch region (the band at 3397 $cm^{-1}$ corresponds to the phenylalanine NH stretch (Figure 3.13)). As the delay after the UV excitation increases, the molecules in the vibrationally excited triplet state cool down and the spectrum becomes sharper. However, after 500 μs instead of four infrared transitions, we start observing only two – 3419 and 3567 $cm^{-1}$. The OH stretch becomes artificially sharp – 2.1 $cm^{-1}$ compared with 4 $cm^{-1}$ that we measure in the unsaturated spectrum of the first electronically excited state (lower trace in Figure 3.12, left side). This suggests that we monitor the transition from the two-photon process to the three/four-

photon process, and observe only those infrared transitions that have the highest absorption cross sections.

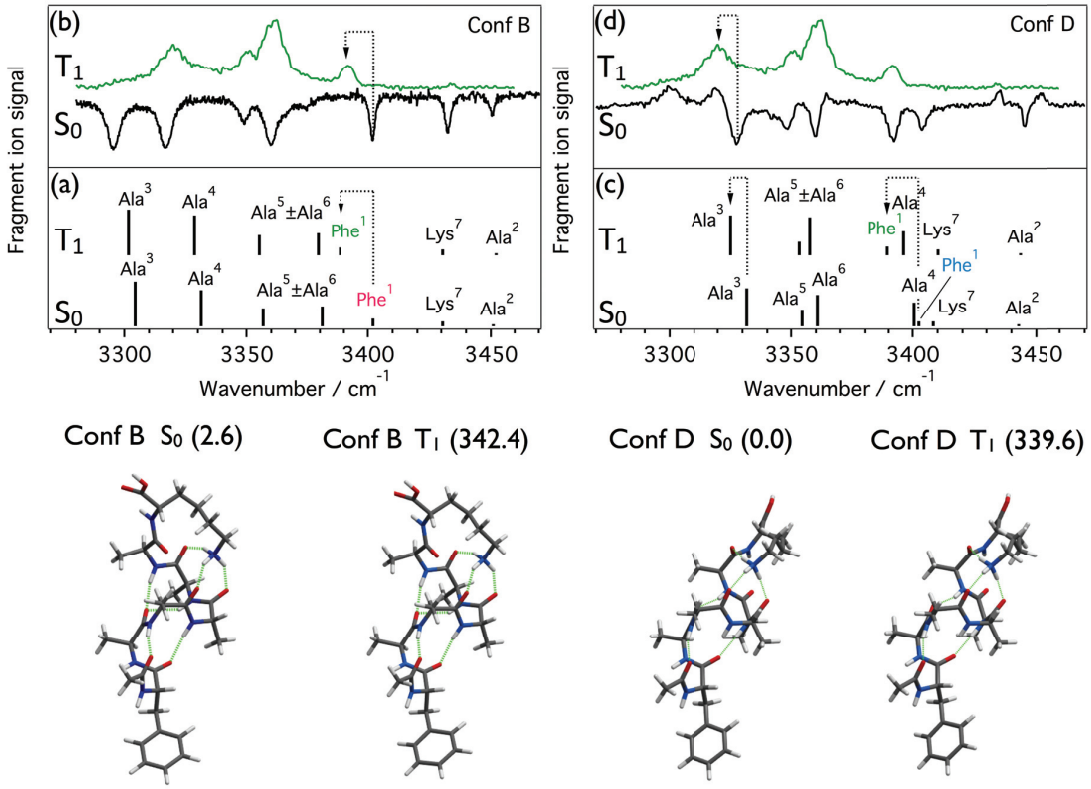


Figure 3.29. The UV laser excites the band origin of conformer B (37555 $cm^{-1}$) or conformer D (37551.4 $cm^{-1}$) of $AcFA_5K\text{-}H^+$. (a) The calculated ground state spectrum of conformer B from ref. [33] vs. the spectrum of the lowest triplet state of conformer B calculated at the DFT UB3LYP/6-31G** level of theory. (b) The experimental ground state spectrum of conformer B (in black) vs the experimental spectrum recorded 65 ms after the UV excitation (in green). (c) The calculated ground state spectrum of conformer D from ref. [33] vs. the spectrum of the lowest triplet state of conformer D calculated at the DFT UB3LYP/6-31G** level of theory. (d) The experimental ground state spectrum of conformer D (in black) vs the experimental spectrum recorded 65 ms after the UV excitation (in green). For each calculated spectrum we present the structures below, with their zero-point energy corrected relative energies in kJ/mol. The calcualted harmonic frequencies are scaled by a factor 0.952.

## 3.4.14 Triplet state quantum yield in AcFAK-$H^+$

We can excite with the UV laser the band origin of the conformer A of AcFAK-$H^+$ and tune the IR OPO wavelength to 1700.1 $cm^{-1}$ (the most intense peak in the fingerprint region, 5 ns after the UV excitation (Figure 3.31)). This allows us to measure the time for the $S_1$- $T_1^\dagger$ transition and

the "average" decay of the triplet state, recording the enhancement of the side-chain loss fragment as a function of the delay between the UV laser and the IR OPO. Because this spectroscopic band appears in the infrared spectrum of both $S_1$ and $T_1^{\dagger}$ states, the signal that we probe reflects the sum of populations in those states and allows us to determine not only the lifetime of the singlet state ($\tau_S$) and the "average" deactivation time of the triplet state ($\tau_T$), but also the time for the intersystem crossing ($\tau_{ISC}$). According to the simplified kinetic model, described in Section 3.4.6, the total population that we probe is the sum of Eqn. (3.3) and (3.4):

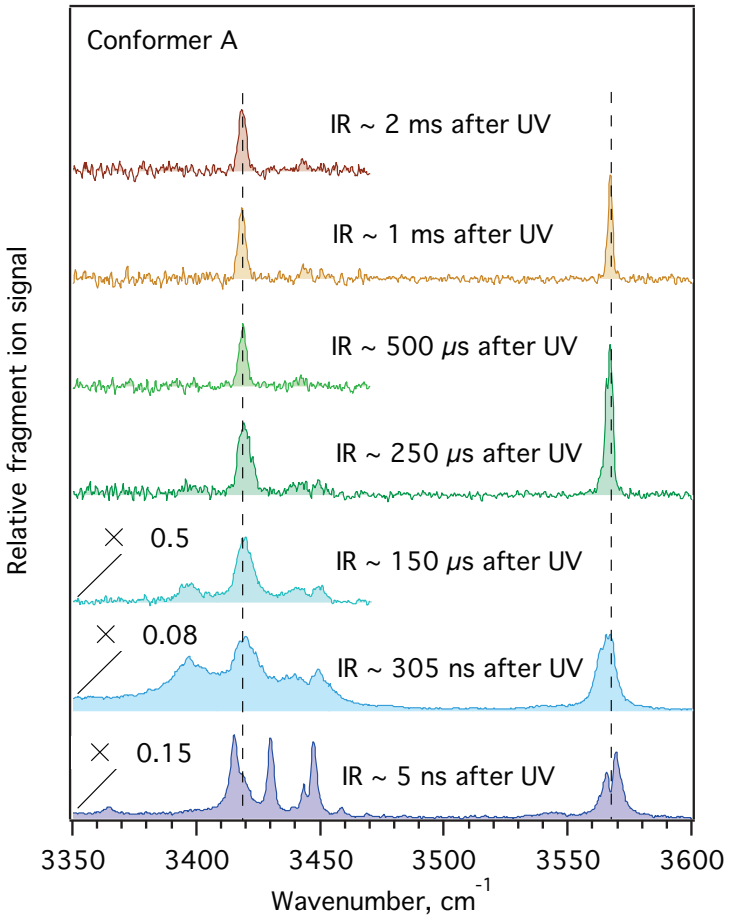


Figure 3.30 IR spectra of the UV excited AcFAK-$H^+$ for different delays between the UV and IR lasers with the UV wavenumber fixed at 37484.0 $cm^{-1}$. The IR power is ~9 mJ/pulse. The spectra were recorded in the new cold octopole ion trap.

$$[S_1] + [T_1^{\dagger}] = \frac{[S_1]_0 k_{ISC}}{k_T - k_S}\left((1 + \frac{k_T - k_S}{k_{ISC}})exp^{-k_S t} - exp^{-k_T t}\right) \tag{3.7}$$

Rewriting the same formula in terms of the lifetimes results in:

$$[S_1] + [T_1^\dagger] = \frac{[S_1]_0 \tau_T \tau_S}{\tau_{ISC}(\tau_S - \tau_T)}((1 + \frac{\tau_{ISC}(\tau_S - \tau_T)}{\tau_T \tau_S})exp^{-t/\tau_S} - exp^{-t/\tau_T}) \quad (3.8)$$

In Table 3.1 we present the values of $\tau_S$, $\tau_{ISC}, \tau_T$, obtained by performing the double exponential fit of the experimental data in Figure 3.31 with the Eqn. (3.8).

| | |
|---|---|
| $\tau_S$ | ~ 80 ns |
| $\tau_{ISC}$ | ~ 140 ns |
| $\tau_T$ | ~ 30 µs |

Table 3.1 The lifetimes of AcFAK-$H^+$ derived from the fit of the experimental data from Figure 3.31 with Eqn. (3.8). $\tau_S$ - the lifetime of the $S_1$ state, $\tau_{ISC}$ - the time for the intersystem crossing, $\tau_T$ - the time of the deactivation of the vibrationally excited triplet state, averaged over different vibrationally excited levels as the molecules cool.

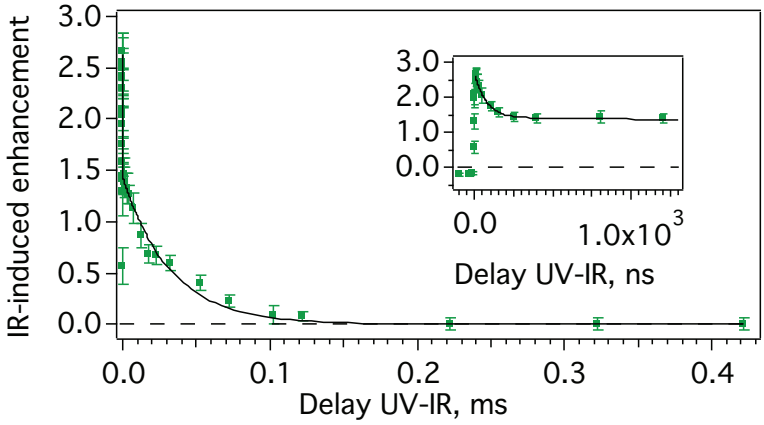


Figure 3.31 AcFAK-$H^+$. Data recorded in the 22-pole ion trap. Percent of the enhancement of the side-chain loss fragment as a function of the delay between UV laser and IR OPO. The UV laser excites the band origin of conformer A (37484.0 $cm^{-1}$). IR probes the C=O stretch that we observe both in the $S_1$ and $T_1^\dagger$ states (1700.1 $cm^{-1}$, 1.3 mJ/pulse). The double exponential fit with the Eqn. (3.8) provides the time constants $\tau_{ISC}$=140 ± 10 ns, $\tau_S$=75 ± 7 ns and $\tau_T$=33 ± 2 µs. In the inlet we show the zoom of the initial decay of the signal.

The determination of $\tau_{ISC}$ allows us to calculate the quantum yield for the intersystem crossing in AcFAK-$H^+$ that we found to be 0.54 ± 0.06

$$Q_T = \frac{\tau_S}{\tau_{ISC}} \tag{3.9}$$

Together with fluorescence, these channels account for the main deactivation pathways in the electronically excited AcFAK-$H^+$, similar to what have been observed in jet-cooled toluene.[64]

The initial decay, representing the singlet state lifetime, is 23 ns longer than measured in the 3 micron region (Figure 3.23). We think that the measurement of the lifetime of the singlet state might be convoluted by the wavelength of the probing IR OPO. We observe the dissociation of the UV excited molecules after they absorb IR OPO light and hence after we increase their total vibrational energy. After absorbing light in 6 micron region the intersystem crossing rate to the triplet state might be slower compared to the case when the molecules absorb the light in 3 micron region. So it is possible that 75 ± 7 ns is the lowest limit on the singlet state lifetime for conformer A of AcFAK-$H^+$. In order to check this idea, one would have to excite the AcFAK-$H^+$ to higher vibrational levels of the $S_1$ state and measure the singlet state lifetime, similar to what we have done for the larger molecule $AcFA_5K$-$H^+$ in Section 3.4.7. Though we did not observe any vibrational excess energy dependence on the intersystem rate constant in $AcFA_5K$-$H^+$ (Section 3.4.7), the smaller number of vibrational degrees of freedom in AcFAK-$H^+$ would result in a higher amount of the vibrational energy to be concentrated in the vibrational modes of the chromophore, which might change the spin-orbit coupling.

The "average" triplet decay time probed with the IR OPO in the fingerprint region at 1700.1 $cm^{-1}$ (Figure 3.32) is ~ 2 times faster than when the IR OPO wavelength is fixed at 3396.6 $cm^{-1}$ (Figure 3.23) or 3418.1 $cm^{-1}$ (Figure 3.24). This is not surprising taking into account the cooling of the molecules in the triplet state. The energy of one photon in the fingerprint region is ~2 times lower than in the NH stretch region, which means that for the same barrier height the molecules would need to absorb twice as many photons to dissociate. We have shown on the example of the seven amino-acid molecule, that upon cooling the molecules start to require three infrared photons of energy 3391 $cm^{-1}$ instead of two in order to dissociate. A similar process might take place in AcFAK-$H^+$, and because of the smaller energy of the photon in 6 micron region, we stop seeing the dissociation earlier than when we probe the molecules in 3 micron region. Thus this is not a good measure for the triplet state lifetime.

### 3.4.15 Summary of the fragmentation mechanism going through the triplet state

Thus far, we have presented a variety of data aimed at revealing the mechanistic details of UV photofragmentation in phenylalanine- and tyrosine-containing protonated peptides. Before proceeding, it is useful to summarize what we can say about the process. The absorption of a UV photon corresponding to the 0-0 vibronic transition promotes the species from the $S_0$ state to the lowest vibrational level of the $S_1$ state. If one or a couple of IR photons are absorbed shortly after the UV excitation (within ~5 ns), we record sharp features corresponding to the conformer specific IR spectra of the $S_1$ state. The dominant fragmentation channel enhanced by the absorption of the IR laser light is the loss of phenylalanine/tyrosine side-chain. This is most likely due to the fact that absorption of the IR photons by a species in the $S_1$ state increases the rate of intersystem crossing to the triplet state with sufficient energy to overcome the dissociation barrier along the $C_\alpha$-$C_\beta$ bond (Figure 3.4).

When the IR laser probes the UV pre-excited molecules at intermediate times (300 ns > t > 5 ns in case of $AcFA_5K\text{-}H^+$ and AcFAK-$H^+$, 30 ns > t > 5 ns in the case of $AcYA_5K\text{-}H^+$) we see gradually melting sharp features and the transformation into a new broader structure (Figure 3.9, Figure 3.12 and Figure 3.14). Because the time evolution of these spectra matches so well with the fluorescence lifetimes of the UV-excited chromophores, we likely observe the dynamical changes that different conformers undergo upon the intersystem crossing to the triplet state. At even longer delays (>1 ms after the UV excitation) the UV pre-excited molecules vibrationally deactivate on the triplet surface in collisions with residual cold helium. This increases the triplet state lifetime for phenylalanine-containing molecules up to more than 100 ms.

## 3.5 Alternative fragmentation models

### 3.5.1 Model based on the electronic absorption of a single aromatic amino acid.

The mechanism of photoinduced $C_\alpha$-$C_\beta$ bond cleavage in a single protonated aromatic amino acid was extensively studied in the group of Jouvet and co-workers.[4, 7, 10] The experiments with protonated tryptophan, in which ionic and neutral photofragments are detected simultaneously,

revealed two pathways for the $C_\alpha$-$C_\beta$ bond rupture, a slow one on a microsecond time scale and a fast one on a nanosecond time scale.[4] The left side of Figure 3.32 illustrates the slow process, which consists of two steps. First, the UV laser promotes light-induced electron transfer from the aromatic ring to the ammonium group that leads to fast hydrogen loss. In the second step, the newly formed radical cation slowly dissociates by breakage of the $C_\alpha$-$C_\beta$ bond. *Ab initio* calculations[6, 80] attribute the H-loss channel to a direct coupling between the locally excited ππ* state with a repulsive, low-lying πσ* state that dissociates along the NH bond of the amino group. This fragmentation channel is less accessible in the case of protonated tyrosine, because its dissociative πσ* configuration is higher in energy. In contrast to tryptophan, the H-loss channel was not observed for tyrosine, suggesting the presence of a different dissociation mechanism.

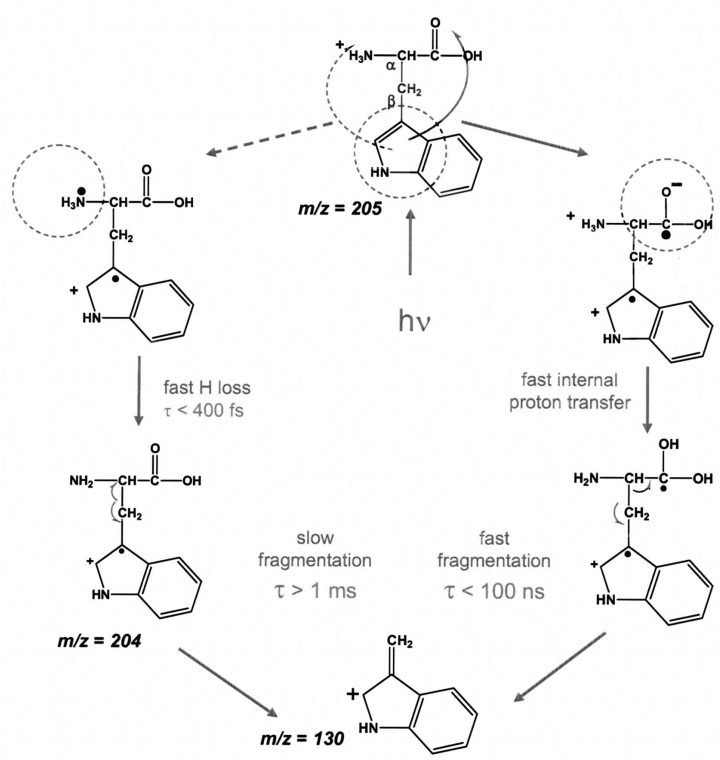


Figure 3.32 Scheme of the two mechanisms for $C_\alpha$-$C_\beta$ bond cleavage in tryptophan. Right side: the excited state mechanism, through proton transfer toward the carboxy group. Left side: The two-step mechanism. Slow dissociation of the radical cation subsequent to the H loss. Taken from the reference [7].

The second dissociation pathway, presented on the right side of Figure 3.32, involves electron transfer from the aromatic ring to the oxygen of the carboxy group upon UV laser excitation with subsequent fast proton transfer from the $NH_3^+$ group toward the C=O of the carboxy group. This

results in the formation of biradical cation that dissociates *via* $C_\alpha$-$C_\beta$ bond cleavage within 100 ns.[7] The comparative study of the fragmentation of protonated tyramine and tryptamine, (which correspond to decarboxylated tyrosine and tryptophan, respectively), showed slower fragmentation in the case of tryptamine and no fragmentation *via* $C_\alpha$-$C_\beta$ bond cleavage in the case of tyramine. This suggests that the presence of the carboxylic group is crucial for the fast fragmentation.

In IRLAPS experiments with protonated Phe previously done in our group, fast $C_\alpha$-$C_\beta$ bond rupture was observed (<100 ns after UV excitation).[40] Experiments with protonated phenethylamine (i.e., decarboxylated Phe) revealed no cleavage of the $C_\alpha$-$C_\beta$ bond. This confirmed the role of the COOH group in the dissociation mechanism after UV excitation, but according to the fast dissociation pathway model,[7] electron transfer to the COOH group leads to the formation of a short-lived biradical cation. In the larger peptides investigated with the IRLAPS technique after UV laser excitation, the intermediate lives at least 65 ms (Figure 3.17).

The role of the charge transfer on C=O was confirmed in the fragmentation study of the small tyrosine containing protonated peptides.[10] The authors observed the $C_\alpha$-$C_\beta$ bond breakage only when tyrosine was located on the N-terminus, for example in YG-$H^+$ and YA-$H^+$, but in the peptide GYG-$H^+$ another bond breaks, resulting in z-type fragmentation. However, we observe $C_\alpha$-$C_\beta$ bond breakage in a helical molecule $AcYA_5K$-$H^+$, where the charge is on lysine side-chain, far from the chromophore.

According to the fast mechanism of neutral side-chain loss proposed by Kumar et al.,[11] preventing proton transfer from $NH_3^+$ group after electronic excitation should inhibit fragmentation *via* $C_\alpha$-$C_\beta$ bond cleavage. In an IRLAPS experiment, the peptide $AcFA_5K$-$H^+$ was substituted with 18-crown-6-ether in order to block the charge.[40] It turned out that under UV only excitation without $CO_2$ laser assistance there were no fragments corresponding to the $C_\alpha$-$C_\beta$ bond cleavage, whereas after UV-$CO_2$ laser excitation this fragmentation channel was observed, in contrast to the expectation. This means that the charge doesn't play an active role in the formation of an intermediate state from which the $CO_2$ laser promotes dissociation.

The model might explain the dissociation of protonated phenylalanine and other single aromatic amino acids. However, for the larger peptides, charge seems not to be actively involved in the dissociation mechanism and the model doesn't explain the fact that $C_\alpha$-$C_\beta$ bond cleavage occurs at long times after electronic excitation.

## 3.5.2 The effect of the charge proximity on the fragmentation dynamics of $AcFA_5K\text{-}H^+$ *vs.* $AcA_5FK\text{-}H^+$

We would like to check if the proximity of the charge to the chromophore affects the fragmentation dynamics in a seven amino-acid peptide. For that purpose we decided to perform UV-IR double resonance spectroscopy on $AcA_5FK\text{-}H^+$ molecule, in which the phenylalanine chromophore is moved from the N terminus towards the C terminus compared with $AcFA_5K\text{-}H^+$. In this position the phenylalanine chromophore is closer to the protonated lysine side-chain and the interaction with the charge is stronger. The evidence for the stronger $\pi\text{-}NH_3^+$ interaction comes from ~100 $cm^{-1}$ red shift of the band origin in the electronic spectrum of $AcA_5FK\text{-}H^+$ [40] compared with $AcFA_5K\text{-}H^+$.[38]

Guidi performed IR-UV double resonance spectroscopy on different transitions in the electronic spectrum of $AcA_5FK\text{-}H^+$ and identified two distinct conformers, labeled as A and B, the ground state spectra of which are presented in Figure 3.33 (negative-going black spectra).[40] Based on DFT calculations, she made the assignment of the infrared transitions of conformer B and suggested a helical structure. Unfortunately, the calculated spectrum for conformer A did not match the experimental spectrum and the structure of this conformer stays unknown.[40]

By exciting with the UV laser a single conformer of $AcA_5FK\text{-}H^+$ and adding the IR OPO ~5 ns later, we observe an increase in the side-chain loss fragment (m/z=601) as in $AcFA_5K\text{-}H^+$ (see Figure 3.5), provided the wavelength of the IR OPO is in resonance with the vibrational transition in the electronically excited molecule. In Figure 3.33 (positive-going colored spectra) we present the spectra of $S_1$ state of conformer A and B of $AcA_5FK\text{-}H^+$, recorded by monitoring the side-chain loss fragments as a function of the IR OPO wavelength. Both spectra are sharp and closely resemble the ground state spectra for the relative conformer.

The $S_1$ state of conformer A of $AcA_5FK\text{-}H^+$ in the NH stretch region closely resembles the spectrum of the ground state. Probably in this conformer the aromatic ring interacts with the ammonium group of the lysine side-chain and upon electronic excitation does not perturb the other NH stretch vibrations.

In the $S_1$ state of conformer B of $AcA_5FK\text{-}H^+$, the lysine NH stretch (3394.8 $cm^{-1}$) shifts 15 $cm^{-1}$ to the red compared with its position in the ground state (3409.8 $cm^{-1}$), in contrast with the $S_1$ state of $AcFA_5K\text{-}H^+$ where in different conformers mainly the phenylalanine NH stretch changes its position relative to the ground state. This implies that in conformer B of $AcA_5FK\text{-}H^+$

the aromatic ring should be positioned in such a way that upon UV excitation it affects the lysine NH and does not affect the phenylalanine NH, which would strongly depend on the folded geometry. To test the assignment of the spectroscopic transitions based on the DFT calculations, it would be desirable to record the ground state spectrum of conformer B of $AcA_5FK\text{-}H^+$ with $^{15}N$ isotopic substitution on lysine NH. The spectra of the $S_1$ state reveal the local structural changes in the close proximity to the chromophore and can serve as an additional constraint to test the calculated structures.

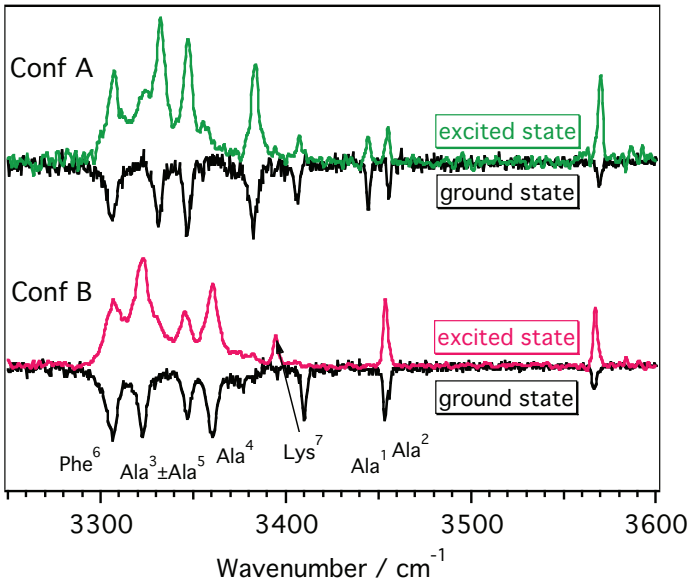


Figure 3.33 $AcA_5FK\text{-}H^+$. In black: the spectrum of the ground state of conformer A and conformer B and the assignment of the spectroscopic transitions based on DFT calculations from the ref. [40]. In color: the spectrum of the $S_1$ state of conformer A and conformer B, recorded by detecting the increase of the side-chain loss fragment as a function of the IR OPO wavenumber, when the IR OPO probes the molecules 5 ns after the UV excitation. The UV laser excites the band origin of conformer A (37434.3 $cm^{-1}$) and conformer B (37448.3 $cm^{-1}$), respectively.

When we increase the delay between the UV laser and the IR OPO, we can probe the time evolution of the infrared spectra as the $S_1$ state deactivates. In Figure 3.34 we present the infrared spectrum of conformer A and B of $AcA_5FK\text{-}H^+$ at different delays after the UV excitation that are longer than 5 ns. The initially sharp structures "melt", and on a time scale ~200 ns the infrared spectrum of both conformers becomes almost undistinguishable. Similar fragmentation pattern and the time scales for the evolution of the infrared spectra in the electronically excited $AcA_5FK\text{-}H^+$ and $AcFA_5K\text{-}H^+$ lead us to believe that the chromophore-charge interaction does

not play an essential role in the photofragmentation resulting in side-chain loss in larger protonated peptides.

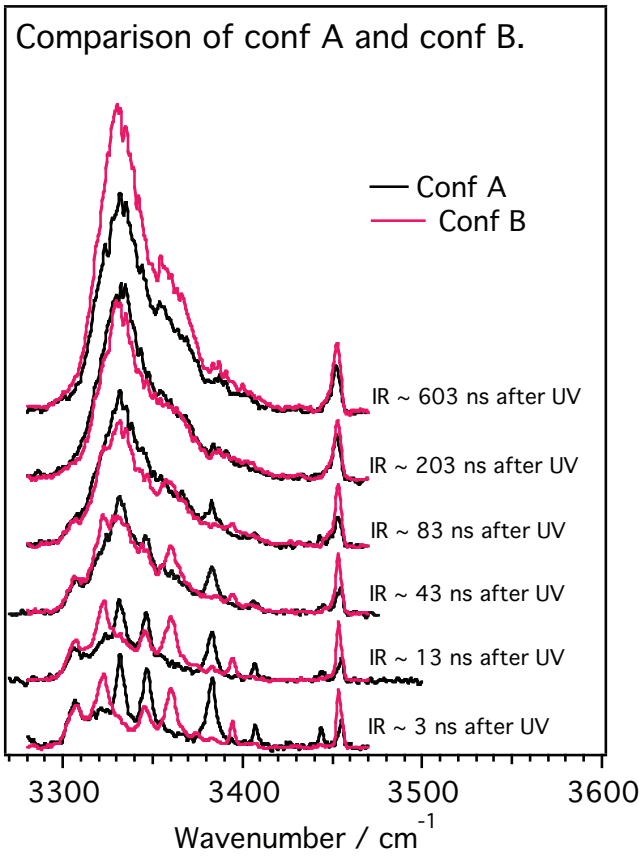


Figure 3.34 IR spectra of the UV-excited $AcA_5FK\text{-}H^+$ for different delays between the UV and IR lasers with the UV wavenumber fixed at the band origin of conformer A (black) or conformer B (red).

## 3.5.3 Biradical formation through the electron driven proton transfer (EDPT) mechanism

The biradical formation model was derived from studies of the excited states of hydrogen-bonded systems by Sobolewski and co-workers.[13] In proteins in the ground electronic state, hydrogen bonds are formed between CO and NH groups of the backbone, and this plays an essential role in determining their three-dimensional structure and photophysics. Excited electronic states of polyatomic molecules have open shell configurations and require the exploration of high-dimensional potential energy surfaces over wide regions, which renders their calculations challenging. In 2009, the electron driven proton transfer deactivation mechanism after UV excitation was established for the one of the low energy conformers of Gly-Phe-Ala peptide by *ab initio* calculations.[15]

According to this model in the first step the UV laser transfers population from the ground electronic state of the peptide to the lowest electronically excited ππ* state of the phenyl ring. One of the locally excited states ($^1$LE) lies slightly lower in energy than the ππ* state, which causes radiationless relaxation from the ππ* state to the $^1$LE state through a conical intersection. There exists also an optically dark charge transfer state (CT) that has a conical intersection with both the $^1$LE state and the ground electronic state $S_0$ at its minimum geometry. Population of the CT state involves transfer of the electron from the hydrogen-bonded NH group to the CO group along the intramolecular hydrogen bond. The high polarity of the CT state provides the driving force for the proton transfer following the electron. Afterwards, the electron is transferred back through the CT-$S_0$ conical intersection and the proton follows, closing the photophysical cycle. The large energy gradients and small mass of the proton ensure that the rate of this process is fast. The electronic energy is converted by the passage through three conical intersections into vibrational energy of the ground state on the timescale of a few fs.[13] This EDPT mechanism is schematically presented in a potential energy diagram in Figure 3.35.

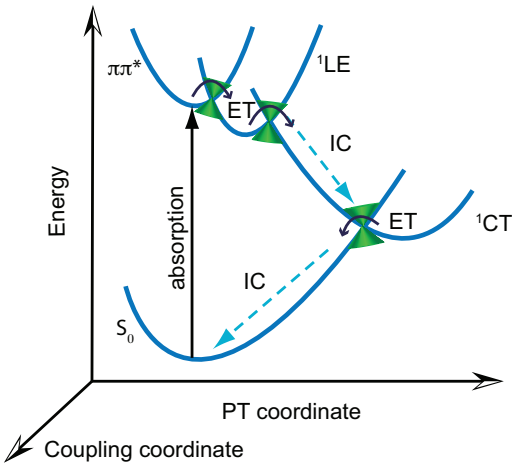


Figure 3.35 Schematic representation of the EDPT process in intramolecularly hydrogen-bonded systems. Abbreviations: LE, locally excited state; CT, charge transfer state; ET, electron transfer; IC, internal conversion.

In the Dugourd group[81] the dynamics of a neutral tryptophan radical formed from a doubly-deprotonated five amino acid peptide *via* double electron detachment was studied. The pump-probe experiments revealed that under UV excitation the Trp radical is promptly formed in less than 100 ns due to the loss of the electron and is stable for several milliseconds, so that it can be isolated and irradiated with a visible laser. The visible photofragmentation spectrum of the

radical Trp ions shows good agreement with the calculated absorption spectrum that indicates that the rest of the peptide has a weak influence on the optical properties of the radical.[81]

If the photoexcitation mechanism in the protonated aromatic peptides is similar to the mechanism in deprotonated peptides, the observation of the chromophore radical by means of visible spectroscopy should be possible in these cases as well. The use of a visible laser instead of a $CO_2$ laser led to the same fragmentation pattern as in the IRLAPS experiments, where an enhancement of the signal due to $C_\alpha$-$C_\beta$ bond rupture was observed.[40] These results support both assumptions that the UV laser induces the formation of a biradical as an intermediate, in which the $C_\alpha$-$C_\beta$ bond is the weakest bond, and that the molecules undergo intersystem crossing to the triplet state. If a biradical is formed, according to the model of Sobolewski and Domcke for the UV excited-state deactivation of the Gly-Phe-Ala peptide,[15] it should be short lived. This contradicts the observations made for larger protonated peptides in our group[40] as well as in the deprotonation experiments in the group of Dugourd.[81] A possible reason for this could be the existence of another potential minimum in the CT state (Figure 3.35) corresponding to the stable biradical that could live for several milliseconds and in which the $C_\alpha$-$C_\beta$ bond is the weakest.

Sobolewski performed *ab initio* calculations on the Ac-Phe-$(Ala)_2$ –NMe peptide[40] to see if the stable biradical can be formed in peptides larger than Gly-Phe-Ala. Because the model involves EDPT along the hydrogen bond between the CO of the acetylated group of Phe and the NH group of the first $^1$Ala in the sequence, it can be extended to larger peptides with further aminoacids on the C-terminal side.

Figure 3.36 represents the results of the calculations performed by Sobolewski.[40] In this model the absorption of a UV photon populates the $\pi\pi^*$ state of the phenyl ring that relaxes to the low-lying $^1$LE state, as in the case of Gly-Phe-Ala peptide.[15] In addition, there is a low-lying charge transfer state (CT) that has a conical intersection with the $^1$LE state and that is populated *via* electron transfer to the CO group of the acetylated part of Phe from the NH group of the $^1$Ala along the intramolecular hydrogen bond. The transfer of the electron induces the proton transfer to the CO group of the acetylated part of Phe, resulting in a COH---N hydrogen bond in a closed biradical. Such a closed biradical should be a short-lived species because it can easily relax to the ground electronic state through a conical intersection involving the back-reaction of a proton transfer on a fs timescale. However, after electron driven proton transfer (EDPT) the acetyl group also has enough energy to rotate and then stabilize *via* IVR without the formation of a COH---N hydrogen bond. The resulting product is an open biradical and can live for a long time because direct access to the conical intersection with the ground electronic state is prohibited.

The weakest bond of the open biradical is the $C_\alpha$-$C_\beta$ bond. The additional absorption of energy from a $CO_2$ laser or a visible laser would break the $C_\alpha$-$C_\beta$ bond, thus promoting fragmentation through this dissociation channel.

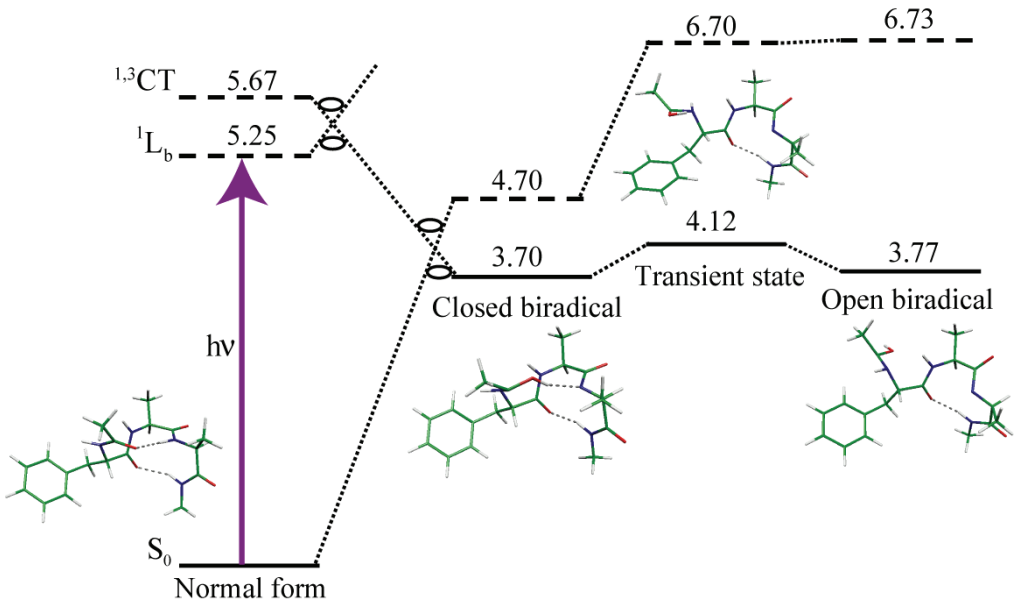


Figure 3.36. Photophysical scheme of the Ac-Phe-$(Ala)_2$–NMe peptide determined by excited-state ab initio calculations. Numbers denote energy in eV related to the ground state. Solid lines denote states in optimized geometry. Dashed lines denote vertical energy levels calculated at a given geometry. Dotted lines show the adiabatic correlations between the states [82] (Taken from M. Guidi [40]).

This model can describe the dissociation mechanism for the class of peptides in which the internal rotation is hindered by a single hydrogen bond. Breakage of the hydrogen bond due to the EDPT mechanism would leave the acetyl group free to rotate, which would lead to the dissipation of the energy and prevent the formation of the short-lived, closed biradical. However, the IRLAPS method was also successfully implemented to increase the dissociation yield of protonated peptides with multiple hydrogen bonds where it is hard to identify the moiety free to rotate after EDPT. These molecules are bradykinin,[46] which forms a salt-bridge in a gas phase,[83] and cyclic gramicidin S that forms ß-sheets in solution.[84] In this case one can argue that after EDPT along one of the multiple hydrogen bonds, the released energy is rapidly transferred to the vibrations (*via* IVR) or is used for conformational isomerization so that the broken hydrogen bond cannot be reformed. Whereas in the protected peptides the conformational change can be identified by the rotation of the protecting group, calculations of the biradical need to be performed for each molecule in order to identify the relevant conformations in the case of non-protected peptides.

### 3.5.4 Is there a proton transfer after the UV excitation in AcFAK-$H^+$?

If there was a biradical formation after the UV excitation it would involve a proton transfer from NH to C=O resulting in the formation of C-OH. If the structure that we probe by addition of an IR photon is a biradical, the IR spectrum in the fingerprint region would change considerably compared to the ground state, i.e. we would see the disappearance of one of the C=O bands and appearance of the C-OH band. Because we do not observe an increase of the fragmentation yield in the UV pre-excited $AcFA_5K\text{-}H^+$ when we subsequently excite its C=O chromophores, we chose the AcFAK-$H^+$ molecule to test the behavior of C=O stretch vibrations.

In the ground state spectrum of both conformers, instead of four well separated C=O stretch vibrations we see five infrared bands in the spectral region 1600 – 1800 $cm^{-1}$. Probably in conformer A the most intense infrared band at 1700 $cm^{-1}$ consists out of two overlapping vibrations (Figure 3.37b), which are separated in conformer B: 1695.4 $cm^{-1}$ and 1705.4 $cm^{-1}$ (Figure 3.37d). According to our calculations of the ground state structures, amide chromophores of the acetyl group, phenylalanine, and alanine interact with the charged amine of the lysine side-chain (Figure 4.7). Because of this interaction, coupling occurs between different C=O and $NH_3^+$ lysine group vibrations, and we cannot assign the peaks in the measured infrared spectrum to single amino acids (more details in Section 4.2.3).

In the first electronically excited-state spectra, presented in Figure 3.37a,c, no considerable changes occur compared to the ground state. In conformer A, the maximum of the band at 1700 $cm^{-1}$ in the ground state might be shifted to 1699 $cm^{-1}$ in the $S_1$ state (Figure 3.37a), but with our current resolution we can not be absolutely sure about this. In conformer B, the shift of the spectroscopic band occurring at 1705.4 $cm^{-1}$ in the ground state is more pronounced. It appears at 1702.6 $cm^{-1}$ in the $S_1$ state with the same shoulder at 1695.4 $cm^{-1}$ (Figure 3.37c). It might be that in the UV excited conformer A and conformer B of AcFAK-$H^+$ the infrared bands at 1699 $cm^{-1}$ and 1702.6 $cm^{-1}$ respectively correspond to acetyl or phenylalanine C=O, because they are the ones that should be most affected by the UV excitation. The other infrared transitions in the fingerprint region do not change upon the electronic excitation.

In Figure 3.38 we can observe how the shape and the intensity of the excited-state infrared bands in the fingerprint region change upon the increase of the delay between the UV laser and the IR OPO. All of the bands become broader, similar to what we saw in the NH-stretch

spectroscopic region (Figure 3.12), but the integral intensity does not increase as considerably. In conformer A at ~305 ns after the UV excitation the spectroscopic band at 1699 $cm^{-1}$, which we attributed to the acetyl or phenylalanine C=O, diminishes in intensity, but a new band arises at 1702.6 $cm^{-1}$ that has exactly the same frequency as in the electronically excited state of conformer B. Another spectroscopic band at 1632 $cm^{-1}$ in the $S_1$ state of conformer A shifts to approximately 1621 $cm^{-1}$, but this transition is most probably involves the NH bending vibrations.

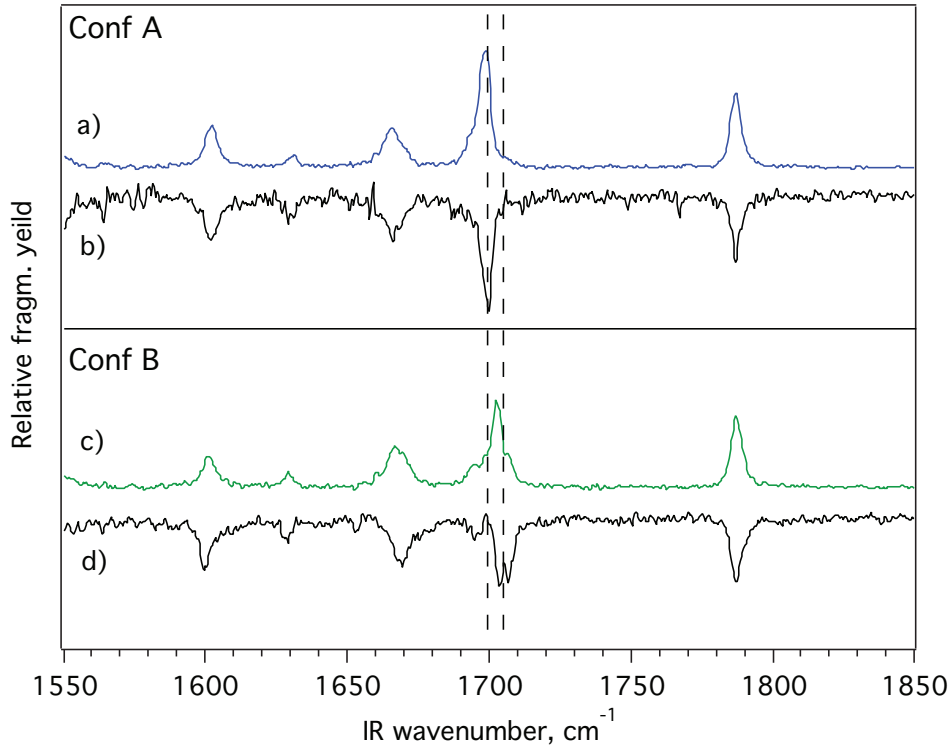


Figure 3.37 The $S_1$ state infrared spectrum of conformer A (a) and conformer B (c) *vs.* the ground state infrared spectrum of conformer A (b) and conformer B (d). The UV laser wavenumber is fixed at the conformer's band origin.

After 300 ns the infrared spectra for conformer A and conformer B of AcFAK-$H^+$ become almost undistinguishable (Figure 3.39). At this delay and at longer times after the UV pre-excitation the spectrum looks like a superposition of the $S_1$ spectra for both conformations with the decrease in the intensity of the acetyl/phenylalanine C=O. The integral intensity does not decrease upon the conversion, which suggests that none of the C=O stretches disappear from the spectrum.

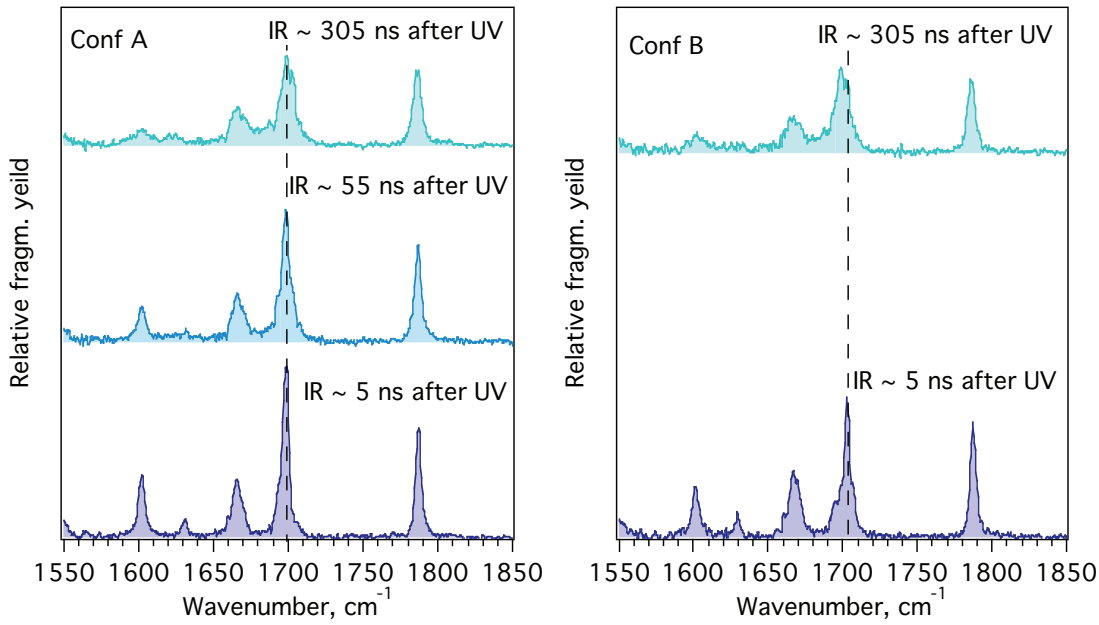


Figure 3.38 IR spectra in the fingerprint region of the UV-excited AcFAK-$H^+$ for different delays between the UV and IR lasers. The UV wavenumber is fixed at 37484.0 $cm^{-1}$ (conformer A) and at 37532.2 $cm^{-1}$ (conformer B). The spectra are all recorded at the same IR power.

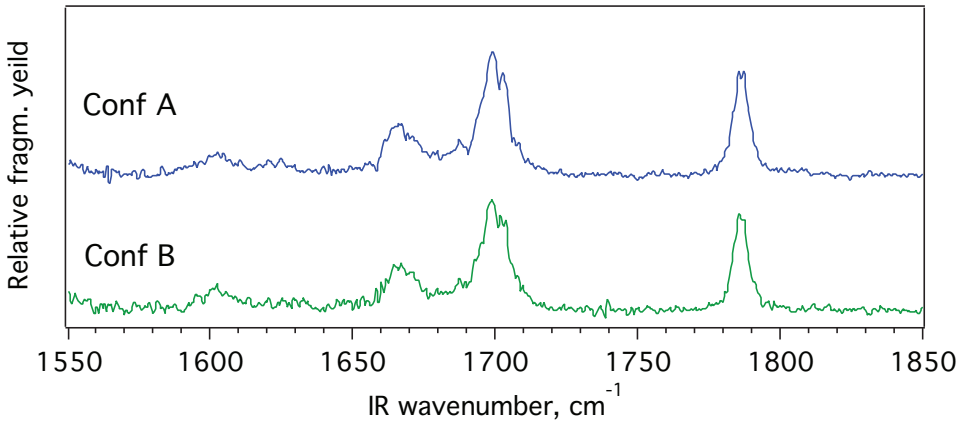


Figure 3.39 IR spectrum of the electronically excited AcFAK-$H^+$ in the fingerprint spectral region. The IR OPO probes the molecules 300 ns after the UV excitation. The UV wavenumber is fixed at 37484.0 $cm^{-1}$ (conformer A) and at 37532.2 $cm^{-1}$ (conformer B).

If the proton transfer takes place, it should proceed along the hydrogen bond between a C=O and an NH. In Figure 3.12 we can see that amide NH stretches do not form strong hydrogen bonds, because they are situated in the spectral region 3350–3470 $cm^{-1}$, which is what we would associate with a relatively free NH stretch band. According to our calculations, presented in

Figure 4.7, the carbonyls form hydrogen bonds with the $NH_3^+$ group of the lysine side-chain, and in order to confirm the absence of the proton transfer we should also monitor how the frequencies of $NH_3^+$ group change upon the deactivation of the UV-excited AcFAK-$H^+$. In Figure 3.40 we present the time evolution of the infrared spectrum of the UV-excited AcFAK-$H^+$ as a function of the delay between the UV laser and the IR OPO in the spectroscopic region of the $NH_3^+$ stretch vibrations. We observe that the integral intensity of the infrared transitions is conserved between the spectrum of the $S_1$ state (5 ns delay between the UV laser and the IR OPO) and 305 ns after the UV excitation.

These results, together with the data from 6 micron region, contradict the idea of a proton transfer directly after the UV excitation to form a biradical species and support the model involving the intersystem crossing to the triplet state. However, we cannot exclude the role of the proton transfer on the triplet surface. A proton transfer could occur after the molecules undergo intersystem crossing to the triplet state to actually induce the cleavage of the $C_\alpha$-$C_\beta$ bond.

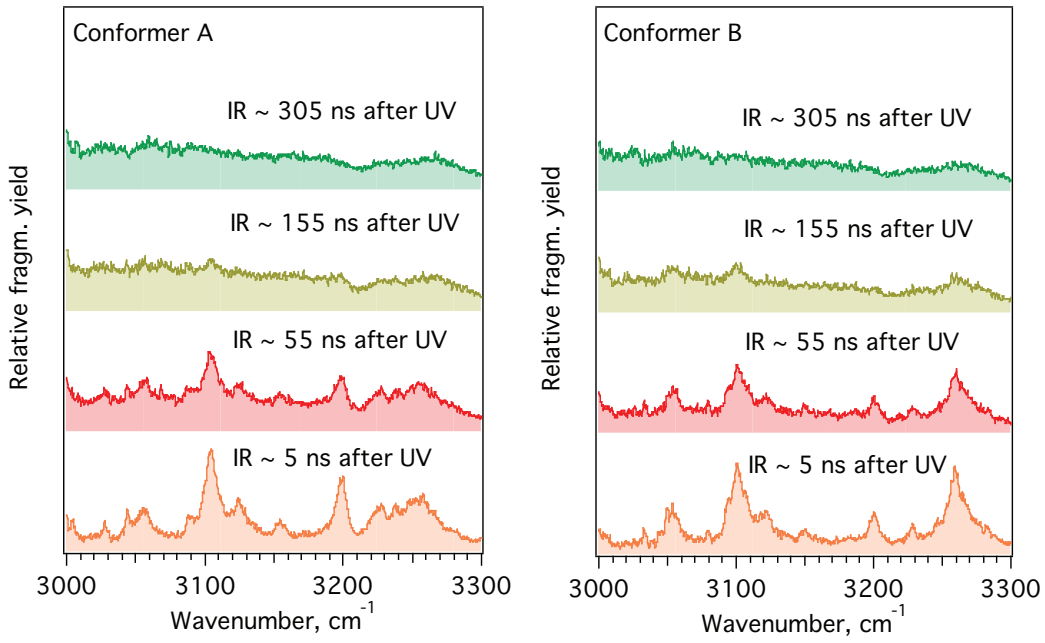


Figure 3.40 IR spectra in the $NH_3^+$ spectroscopic region of the UV excited AcFAK-$H^+$ for different delays between the UV and IR lasers. The UV wavenumber is fixed at 37484.0 $cm^{-1}$ (conformer A) and at 37532.2 $cm^{-1}$ (conformer B). The spectra are all recorded at the same IR power.

# 3.6 Conclusions

## 3.6.1 Summary of the mechanism

We conclude that after UV excitation of phenylalanine/tyrosine-containing peptides in the gas phase at low temperatures (10K), a considerable fraction of the molecules undergoes intersystem crossing into the triplet state. Subsequent absorption of ≥ 2 IR photons from an IR OPO or multiphoton excitation with a $CO_2$ laser results mainly in the increase of the fragmentation yield *via* $C_\alpha$-$C_\beta$ bond cleavage. Because the $C_\alpha$-$C_\beta$ bond is not the weakest bond in the ground state molecule, we rule out the possibility that it occurs after internal conversion to $S_0$. The cleavage of this particular bond in the case of the phenylalanine-containing protonated peptides $AcFA_5K$-$H^+$, $AcA_5FK$-$H^+$, and AcFAK-$H^+$, occurs even when the IR OPO interrogates the molecules 85 ms after the UV excitation, which is much longer than the lifetime of the electronically excited singlet state. The observation of long (but different) lifetimes for UV-excited protonated phenylalanine- and tyrosine-containing peptides suggests that the cleavage of $C_\alpha$-$C_\beta$ bond occurs from the triplet state with a barrier to dissociation. To test this idea we implemented a UV-IR double resonance spectroscopic technique in which the effect of the infrared absorption by UV-excited molecules is detected as an increase of the fragmentation yield. Promptly (5 ns) after UV excitation of a particular conformer, the IR spectrum of $AcFA_5K$-$H^+$ and AcFAK-$H^+$ is sharp and resembles that of the same conformer in the ground state apart from a small red shift of the NH stretches in closest proximity to the chromophore. We attribute this spectrum to the molecule in the $S_1$ state. A few hundred ns after UV excitation, all conformers give rise to the same IR spectrum, which is broader and has IR bands at different frequencies than the corresponding ground state conformers. We attribute this new spectrum to the vibrationally excited triplet state $T_1$. When the phenylalanine chromophore is substituted by tyrosine, we observe analogous small red shifts of the bands close to the chromophore in the $S_1$ state. However, the broadening of the spectrum occurs ~10 times faster than in the phenylalanine-containing peptides, and we see no enhancement of the fragmentation 100 μs after the UV excitation. The lifetime that we measure for the $S_1$ state of $AcFA_5K$-$H^+$, AcFAK-$H^+$, and $AcYA_5K$-$H^+$ is ~80 ns, ~50-80 ns and ~6 ns, respectively, which is consistent with the $S_1$ state lifetimes for neutral phenylalanine/tyrosine analogs. However, the triplet state lifetimes we determine are much longer than those reported in literature for toluene and phenol in supersonic jet expansion experiments.[58, 64] We attribute this difference to the size of the molecules and collisional cooling of the initially created vibrationally hot triplet state. The evidence for cooling

in collisions with the residual helium in our trap, which is maintained at 4 K, is the change of the infrared dissociation laser power dependence from a two-photon process to a three-photon process. Furthermore, the infrared spectrum recorded just after intersystem crossing (600 ns delay after the UV excitation) is considerably broader than the one recorded at delays longer than 1 ms. The vibrationally deactivated triplet state spectrum is the same for different initially excited conformers, and according to our DFT calculations, mainly consists of the two lowest energy conformers.

This mechanism might occur not only in the peptides studied as part of this work, but also in a number of other protonated peptides[40, 43-45] and the small protein ubiquitin.[46] In each case, infrared excitation of molecules first excited to the $S_1$ state increases fragmentation *via* $C_\alpha$-$C_\beta$ bond cleavage, although this has yet to be confirmed for ubiquitin (due to low resolution of the quadrupole mass filter).[46]

## 3.6.2 Implication for photofragment spectroscopy

The results of these studies have important implications for the extension of photofragment spectroscopy to larger biomolecular ions. Jouvet and co-workers pointed out the importance of fast charge transfer to CO to induce the chromophore side-chain loss fragmentation in small tyrosine-containing protonated peptides.[10] We do not observe fast proton transfer to CO in AcFAK-$H^+$, and we see similar photofragment dynamics in $AcFA_5K$-$H^+$ and $AcA_5FK$-$H^+$, suggesting that the charge is not involved in the initial deactivation of the $S_1$ state. We believe that in the case of large protonated peptides the mechanism of side-chain loss after UV excitation is different from that proposed by Jouvet and it involves the initial population of the triplet state.

Intersystem crossing to the triplet state subsequent to $S_0$-$S_1$ excitation seems to be affected by the local environment of the aromatic ring rather than the conformation of the entire biomolecule. Because the $C_\alpha$-$C_\beta$ bond seems to be particularly weakened in the triplet state of aromatic chromophores, the application of infrared laser-assisted photofragment spectroscopy to increase the fragmentation yield[44] should work for phenylalanine- or tyrosine-containing molecules of much larger size than if the fragmentation process proceeded mainly *via* internal conversion to the ground state.[17] Indeed, the recent application of this approach to molecules as large as ubiquitin[46] bear this out.

### 3.6.3 Implication for protein photostability

Our results may have implications for understanding the photostability of proteins in living cells. Depending on their conformation, some proteins may fragment directly from the charge transfer[10] and other dissociative states[85] or undergo internal conversion to the ground state upon the UV excitation, as proposed by Malis et al.[17] and Domcke and Sobolewski,[19] but at least some will be trapped in triplet states. Triplet states are long-lived and as a result could participate in destructive chemical processes. They can transfer energy to produce singlet oxygen and subsequently other radicals, causing DNA and protein damage.[86] Though our results suggest that peptides containing phenylalanine and tyrosine chromophores are not intrinsically photostable, nature has various protection mechanisms against UV photodamage. First, the phenylalanine chromophore absorption maximum is around 250 nm, which is at a wavelength that is very effectively absorbed by the ozone layer, so that only a small portion of the radiation reaches the surface of Earth. Second, the energy can transfer from the higher energy chromophores phenylalanine and tyrosine to tryptophan and cystine, reducing the population of the harmful triplet states by energy dissipation. Third, various UV filters, for example, kynurenin in the eye lens[1] and melanin in the skin,[87] absorb UV radiation and protect proteins against photooxidative damage.

### 3.6.4 Implication for protein dynamics in the gas phase

Using UV-IR double resonance photofragmentation, we can selectively break the chromophore's $C_\alpha$-$C_\beta$ bond. If our mechanism is right and the dissociation happens from the triplet state, one can study the long time dynamics of proteins in the gas phase, monitoring phosphorescence or the side-chain loss photofragments.

In solvated proteins with multiple chromophores, triplet states can be deactivated through triplet-triplet energy transfer.[88] In the gas phase, triplet-triplet energy transfer might result in a different amount of the side-chain loss fragments, depending on the relative position of the chromophores in the protein. Upon excitation of the tyrosine band origin, which is much lower in energy than the absorption of the phenylalanine residue, Guidi observed along with the tyrosine some phenylalanine side-chain loss fragment in $AcYA_4FK\text{-}H^+$.[40] While Förster resonance energy transfer or singlet-singlet energy transfer can not take place, the triplet state of phenylalanine chromophore is lower in energy than the singlet state of tyrosine chromophore and the triplet-triplet energy transfer is allowed. The distance between the chromophores will

determine the efficiency of the triplet-triplet energy transfer and will provide additional structural information when studying folded and unfolded peptides in the gas phase.

# References


[1] M. J. Davies and R. J. W. Truscott, J. Photochem. Photobiol. B **63**, 114 (2001).

[2] H. K. Muller and G. M. Woods, in *Radiation Proteomics: The Effects of Ionizing and Non-Ionizing Radiation on Cells and Tissues*, edited by D. Leszczynski (Springer, New York, 2013), Vol. 990, p. 111.

[3] M. J. Davies, BBA-Proteins Proteom. **1703**, 93 (2005).

[4] V. Lepere, B. Lucas, M. Barat, J. A. Fayeton, V. J. Picard, C. Jouvet, P. Carcabal, I. Nielsen, C. Dedonder-Lardeux, G. Gregoire, and A. Fujii, J. Chem. Phys. **127**, 134313 (2007).

[5] H. Kang, C. Jouvet, C. Dedonder-Lardeux, S. Martrenchard, G. Gregoire, C. Desfrancois, J. P. Schermann, M. Barat, and J. A. Fayeton, Phys. Chem. Chem. Phys. **7**, 394 (2005).

[6] G. Gregoire, C. Jouvet, C. Dedonder, and A. L. Sobolewski, J. Am. Chem. Soc. **129**, 6223 (2007).

[7] B. Lucas, M. Barat, J. A. Fayeton, M. Perot, C. Jouvet, G. Gregoire, and S. B. Nielsen, J. Chem. Phys. **128**, 164302 (2008).

[8] U. Kadhane, M. Perot, B. Lucas, M. Barat, J. A. Fayeton, C. Jouvet, A. Ehlerding, M. B. S. Kirketerp, S. B. Nielsen, J. A. Wyer, and H. Zettergren, Chem. Phys. Lett. **480**, 57 (2009).

[9] M. Perot, B. Lucas, M. Barat, J. A. Fayeton, and C. Jouvet, J. Phys. Chem. A **114**, 3147 (2010).

[10] C. Dehon, S. Soorkia, M. Pedrazzani, C. Jouvet, M. Barat, J. A. Fayeton, and B. Lucas, Phys. Chem. Chem. Phys. **15**, 8779 (2013).

[11] S. S. Kumar, B. Lucas, S. Soorkia, M. Barat, and J. A. Fayeton, Phys. Chem. Chem. Phys. **14**, 10225 (2012).

[12] A. L. Sobolewski and W. Domcke, ChemPhysChem **7**, 561 (2006).

[13] A. L. Sobolewski and W. G. Domcke, J. Phys. Chem. A **111**, 11725 (2007).

[14] D. Shemesh, C. Haettig, and W. Domcke, Chem. Phys. Lett. **482**, 38 (2009).

[15] D. Shemesh, A. L. Sobolewski, and W. Domcke, J. Am. Chem. Soc. **131**, 1374 (2009).

[16] D. Shemesh and W. Domcke, ChemPhysChem **12**, 1833 (2011).

[17] M. Malis, Y. Loquais, E. Gloaguen, H. S. Biswal, F. Piuzzi, B. Tardivel, V. Brenner, M. Broquier, C. Jouvet, M. Mons, N. Doslic, and I. Ljubic, J. Am. Chem. Soc. **134**, 20340 (2012).

[18] M. Malis, Y. Loquais, E. Gloaguen, C. Jouvet, V. Brenner, M. Mons, I. Ljubic, and N. Doslic, Phys. Chem. Chem. Phys. **16**, 2285 (2014).

[19] W. Domcke and A. L. Sobolewski, Nature chemistry **5**, 257 (2013).

[20] C. M. Tseng, M. F. Lin, Y. L. Yang, Y. C. Ho, C. K. Ni, and J. L. Chang, Phys. Chem. Chem. Phys. **12**, 4989 (2010).

[21] M. F. Lin, C. M. Tzeng, Y. A. Dyakov, and C. K. Ni, J. Chem. Phys. **126** (2007).

[22] P. Debye and J. O. Edwards, Science **116**, 143 (1952).

[23] A. L. Kwiram and J. B. A. Ross, Annu. Rev. Biophys. Bioeng. **11**, 223 (1982).

[24] J. Vanderkooi, D. Calhoun, and S. Englander, Science **236**, 568 (1987).

[25] S. Papp and J. M. Vanderkooi, Photochem. Photobiol. **49**, 775 (1989).

[26] G. B. Strambini, B. A. Kerwin, B. D. Mason, and M. Gonnelli, Photochem. Photobiol. **80**, 462 (2004).

[27] A. Kowalska-Baron, M. Chan, K. Galecki, and S. Wysocki, Spectrochim. Acta Part A **98**, 282 (2012).

[28] K. W. Rousslang, P. J. Reid, D. M. Holloway, D. R. Haynes, J. Dragavon, and J. B. A. Ross, J. Protein Chem. **21**, 547 (2002).

[29] D. V. Bent and E. Hayon, J. Am. Chem. Soc. **97**, 2606 (1975).

[30] J. L. King and T. H. Jukes, Science **164**, 788 (1969).

[31] H.-D. Belitz, W. Grosch, and P. Schieberle, *Food Chemistry* (Springer, 2009).

[32] T. R. Rizzo, J. A. Stearns, and O. V. Boyarkin, Int. Rev. Phys. Chem. **28**, 481 (2009).

[33] J. A. Stearns, C. Seaiby, O. V. Boyarkin, and T. R. Rizzo, Phys. Chem. Chem. Phys. **11**, 125 (2009).

[34] N. S. Nagornova, M. Guglielmi, M. Doemer, I. Tavernelli, U. Rothlisberger, T. R. Rizzo, and O. V. Boyarkin, Angew. Chem., Int. Ed. **50**, 5383 (2011).

[35] N. S. Nagornova, T. R. Rizzo, and O. V. Boyarkin, J. Am. Chem. Soc. **132**, 4040 (2010).

[36] L. L. Griffin and D. J. Mcadoo, J. Am. Soc. Mass. Spectr. **4**, 11 (1993).

[37] N. S. Nagornova, T. R. Rizzo, and O. V. Boyarkin, Angew. Chem., Int. Ed. **52**, 6002 (2013).

[38] J. A. Stearns, O. V. Boyarkin, and T. R. Rizzo, J. Am. Chem. Soc. **129**, 13820 (2007).

[39] J. A. Stearns, O. V. Boyarkin, and T. R. Rizzo, CHIMIA **62**, 240 (2008).

[40] M. Guidi, Ph. D. thesis, EPFL, Lausanne, 2010.

[41] J. S. Brodbelt and J. J. Wilson, Mass Spectrom. Rev. **28**, 390 (2009).

[42] D. Ortiz, P. Martin-Gago, A. Riera, K. Song, J. Y. Salpin, and R. Spezia, Int. J. Mass Spec. **335**, 33 (2013).

[43] G. Papadopoulos, A. Svendsen, O. V. Boyarkin, and T. R. Rizzo, Faraday Discuss. **150**, 243 (2011).

[44] M. Guidi, U. J. Lorenz, G. Papadopoulos, O. V. Boyarkin, and T. R. Rizzo, J. Phys. Chem. A **113**, 797 (2009).

[45] N. Nagornova, Ph. D. thesis, EPFL, Lausanne, 2011.

[46] G. Papadopoulos, Ph. D. thesis, EPFL, Lausanne, 2012.

[47] S. J. Martinez, J. C. Alfano, and D. H. Levy, J. Mol. Spectrosc. **158**, 82 (1993).

[48] C.-L. Huang, J.-C. Jiang, Y. T. Lee, and C.-K. Ni, J. Chem. Phys. **117**, 7034 (2002).

[49] C.-M. Tseng, Y. T. Lee, C.-K. Ni, and J.-L. Chang, J. Phys. Chem. A **111**, 6674 (2007).

[50] B. C. Dian, A. Longarte, and T. S. Zwier, J. Chem. Phys. **118**, 2696 (2003).

[51] N. M. Kidwell, D. N. Mehta-Hurt, J. A. Korn, E. L. Sibert, and T. S. Zwier, J. Chem. Phys. **140** (2014).

[52] T. Ebata, C. Minejima, and N. Mikami, J. Phys. Chem. A **106**, 11070 (2002).

[53] T. Ebata, N. Mizuochi, T. Watanabe, and N. Mikami, J. Phys. Chem. **100**, 546 (1996).

[54] C. Minejima, T. Ebata, and N. Mikami, Phys. Chem. Chem. Phys. **4**, 1537 (2002).

[55] D. Lin-Vien, N. B. Colthup, W. G. Fateley, and J. G. Grasselli, *The handbook of Infrared and Raman Characteristic Frequencies of Organic Molecules* (Academic press, San Diego, 1991).

[56] H. D. Bist, J. C. D. Brand, and D. R. Williams, J. Mol. Spectrosc. **24**, 413 (1967).

[57] H. G. Lohmannsroben, K. Luther, and M. Stuke, J. Phys. Chem. **91**, 3499 (1987).

[58] A. Sur and P. M. Johnson, J. Chem. Phys. **84**, 1206 (1986).

[59] G. A. Pino, A. N. Oldani, E. Marceca, M. Fujii, S. I. Ishiuchi, M. Miyazaki, M. Broquier, C. Dedonder, and C. Jouvet, J. Chem. Phys. **133** (2010).

[60] G. M. Roberts, A. S. Chatterley, J. D. Young, and V. G. Stavros, J. Phys. Chem. Lett. **3**, 348 (2012).

[61] C. G. Hickman, J. R. Gascooke, and W. D. Lawrance, J. Chem. Phys. **104**, 4887 (1996).

[62] T. Hashimoto, Y. Takasu, Y. Yamada, and T. Ebata, Chem. Phys. Lett. **421**, 227 (2006).

[63] Y. H. Lee, J. W. Jung, B. Kim, P. Butz, L. C. Snoek, R. T. Kroemer, and J. P. Simons, J. Phys. Chem. A **108**, 69 (2004).

[64] T. G. Dietz, M. A. Duncan, and R. E. Smalley, J. Chem. Phys. **76**, 1227 (1982).

[65] C. Lifshitz, Eur. Mass Spectrom. **8**, 85 (2002).

[66] S. M. Gordon and N. W. Reid, Int. J. Mass Spec. Ion Phys. **18**, 379 (1975).

[67] J. H. Moore, C. C. Davis, M. A. Coplan, and S. C. Greer, *Building Scientific Apparatus, 4th Edition* (Cambridge University Press, 2009).

[68] W. Kauzmann, *Kinetic theory of gases* (Courier Dover Publications, United States, 2012).

[69] A. A. Rehms and P. R. Callis, Chem. Phys. Lett. **208**, 276 (1993).

[70] P. R. Callis, in *Topics in Flourescence Spectroscopy*, edited by J. R. Lakowicz (Kluwer Academic Publishers, 2002), Vol. 5, p. p.27.

[71] S. Fischer, E. W. Schlag, and S. Schneider, Chem. Phys. Lett. **11**, 583 (1971).

[72] D. S. N. Parker, R. S. Minns, T. J. Penfold, G. A. Worth, and H. H. Fielding, Chem. Phys. Lett. **469**, 43 (2009).

[73] G. Aravind, B. Klaerke, J. Rajput, Y. Toker, L. H. Andersen, A. V. Bochenkova, R. Antoine, J. Lemoine, A. Racaud, and P. Dugourd, J. Chem. Phys. **136** (2012).

[74] R. Wester, J. Phys. B-At. Mol. Opt. **42** (2009).

[75] J. A. Stearns, S. Mercier, C. Seaiby, M. Guidi, O. V. Boyarkin, and T. R. Rizzo, J. Am. Chem. Soc. **129**, 11814 (2007).

[76] C. Seaiby, Ph. D. thesis, EPFL, Lausanne, 2011.

[77] J. Metcalfe, M. G. Rockley, and D. Phillips, J. Chem. Soc. Faraday Trans. 2 **70**, 1660 (1974).

[78] P. Swiderek, M. Michaud, and L. Sanche, J. Chem. Phys. **105**, 6724 (1996).

[79] J. U. Andersen, H. Cederquist, J. S. Forster, B. A. Huber, P. Hvelplund, J. Jensen, B. Liu, B. Manil, L. Maunoury, S. Brøndsted Nielsen, U. V. Pedersen, H. T. Schmidt, S. Tomita, and H. Zettergren, Eur. Phys. J. D **25**, 139 (2003).

[80] G. Gregoire, C. Jouvet, C. Dedonder, and A. L. Sobolewski, Chem. Phys. **324**, 398 (2006).

[81] L. Joly, R. Antoine, A. R. Allouche, and P. Dugourd, J. Am. Chem. Soc. **130**, 13832 (2008).

[82] A. L. Sobolewski, private communication (2009).

[83] P. D. Schnier, W. D. Price, R. A. Jockusch, and E. R. Williams, J. Am. Chem. Soc. **118**, 7178 (1996).

[84] E. M. Krauss and S. I. Chan, J. Am. Chem. Soc. **104**, 6953 (1982).

[85] T. Tabarin, R. Antoine, M. Broyer, and P. Dugourd, Rapid Commun. Mass Spectrom. **19**, 2883 (2005).

[86] B. A. Kerwin and R. L. Remmele, J. Pharm. Sci. **96**, 1468 (2007).

[87] M. Brenner and V. J. Hearing, Photochem. Photobiol. **84**, 539 (2008).

[88] W. R. L. J. B. Alexander Ross, Kenneth W. Rousslang, Hermann R. Wyssbrod, in *Topics in Fluorescence Spectroscopy*, edited by J. R. Lakowicz (Kluwer Academic Publishers, 2002), Vol. 3, p. 16.

# Chapter 4

# Strong anharmonic effects in the vibrational spectra of the electronically excited AcFAK-$H^+$

In this chapter we present the conformer-specific ground state infrared spectra of AcFAK-$H^+$ along with the corresponding structures, calculated using a combination of classical and quantum mechanical methods. For one of the conformers of AcFAK-$H^+$ we observe a low-frequency (12.6 $cm^{-1}$) harmonic vibrational progression in the electronic spectrum. The infrared spectra recorded by exciting different electronic transitions from this progression show up to six combination bands that arise from anharmonic coupling between this low-frequency motion and the phenylalanine/alanine NH stretch vibration. The wavenumber of the 12.6 $cm^{-1}$ vibration decreases to 11.8 $cm^{-1}$ or increases to 13.6 $cm^{-1}$ upon excitation of alanine or phenylalanine NH stretch, respectively. We describe the abnormal intensities of the combination bands by purely mechanical anharmonicity (with a quartic Taylor expansion for the potential energy surface) and the model of two displaced and distorted harmonic oscillators. In the end, we discuss which conformational changes result in the appearance of the combination bands in the infrared spectrum.

## 4.1 Introduction

Vibrational spectra in the harmonic approximation are described by the 3N - 6 normal modes. However in reality, additional bands often arise in the vibrational spectra that cannot be accounted by this approach and are due to anharmonic effects.[1, 2] There are two types of anharmonicity that leads to the appearance of combination bands, resonances, and overtones in the vibrational spectra: mechanical and electrical. The first arises from the anharmonicity in the

potential energy surface and the second is due to the presence of higher order terms in the Taylor expansion for the dipole moment function.[2]

Anharmonic effects are commonly observed in most small molecules[2] and they are fully described in, for example, HCN and $H_2CO$.[3] McCoy and co-workers stressed the role of both mechanical and electrical anharmonicities on the intensities of overtone and combination bands in hydrated halides[4, 5] and the intensity of the "association band" in hydronium ion complexes.[6] In water, vibrational energy transfer is faster than predicted by dipole-dipole interactions (the through-space interaction) and possibly occurs through anharmonic couplings of the hydrogen bonds (the through-bond interaction).[7, 8] Ishii et *al.* accounted for both types of anharmonicity in describing the coupling between the OH stretch vibration and the low frequency vibration in quinizarin, which is the model system to study vibrational energy transfer in biologically relevant hydrogen-bonded systems.[9] Recent theoretical work on the spectral intensities of vibrational transitions in water and formaldehyde suggests to truncate the Taylor expansion for the potential energy surface at the fourth level term and the dipole moment operator at the second term to predict the intensities for two quanta transitions.[1] Mechanical anharmonicity dominates for the states where the coupling between the vibrational states is strong.[1]

We present to our knowledge the first experimental example of strong mechanical anharmonicity in a biological molecule, AcFAK-$H^+$. The protonated tripeptide AcFAK-$H^+$ is a starting motif for peptide helix formation. In this chapter we show how the excitation of one amide NH stretch vibration reduces the frequency of a low-frequency molecular vibration involving the entire molecule, while excitation of another NH stretch vibration increases the frequency of this same molecular vibration. These effects arise from the coupling of the phenylalanine side-chain rotation with phenylalanine/alanine NH stretches in the electronically excited state. Ebata et al. observed mode-dependent anharmonic coupling between the OH stretch and various intermolecular vibrations in the $S_1$ state of jet-cooled phenol-$H_2O$ and phenol-$CH_3OH$ clusters.[10] In phenol-$H_2O$ the combination band between the OH stretch and the intermolecular stretching vibration is red-shifted relative to the OH stretch fundamental, and the combination band arising from the anharmonic coupling between the OH stretch and the wagging vibration is blue-shifted in the $S_1$ state. However, they did not excite the clusters to different vibrational levels of the $S_1$ state to see vibrational progressions of the combination bands. Johnson and co-workers observed low frequency vibrational progressions in the ground state infrared spectrum of $CH_3NO_2^- \cdot H_2O$ and $CH_3CO_2^- \cdot H_2O$ complexes.[11] They described the appearance of closely spaced bands to the red of the OH stretch fundamental through the

coupling between the OH stretch and the water rocking vibration. The excitation of the OH stretch causes a shift in the effective potential for the water rocking motion and leads to an increased intensity of the combination bands.[11, 12] Analyzing only the ground state spectrum, the authors could not account for possible frequency changes for the water rocking vibration upon the excitation of the OH stretch. Doi and Mikami observed a five-member progression in the OH stretch region for phenol-$NH_3$ complex, but they did not discuss the nature of those bands in detail.[13] We present a series of the ground state vibrational spectra of AcFAK-$H^+$ as well as excited state vibrational spectra for several vibrational levels of the first electronically excited state. We observe low-frequency progressions of up to six combination bands with a spacing that depends on which NH stretch is excited. The change in spacing accounts for the difference in the oscillator force constant in the harmonic potential for the low frequency vibration upon NH stretch excitation. In this chapter we provide a theoretical explanation for the dramatically enhanced intensities of the combination bands and present the conformational changes that account for the coupling between slow and fast vibrations in AcFAK-$H^+$.

# 4.2 Results

## 4.2.1 Electronic spectrum

Figure 4.1 presents the UV photofragmentation spectrum of AcFAK-$H^+$ recorded by counting the number of phenylalanine side-chain loss fragments as a function of excitation wavelength. We identified at least two different ground state conformations for this molecule, marked as A and B. Most of the vibronic transitions correspond to conformer A and only one intense UV peak at 37532.2 $cm^{-1}$ is due to the presence of conformer B. Conformer A exhibits a beautiful harmonic vibronic progression with a spacing of 12.6 $cm^{-1}$. Associated with this vibronic progression we identified the hot band at 37470.8 $cm^{-1}$ ($A_{10}$), the band origin at 37484.0 $cm^{-1}$ ($A_{00}$) and vibronic transitions to levels with up to 4 quanta of a low frequency vibration in the electronically excited state. The band origin of conformer A is only 36.9 $cm^{-1}$ red-shifted from that of protonated phenylalanine,[14] and the band origin of conformer B is 11.3 $cm^{-1}$ blue-shifted, indicating that the π-cloud of the phenylalanine aromatic ring is probably not involved in a strong interaction with $NH_3^+$ in both of the conformers.

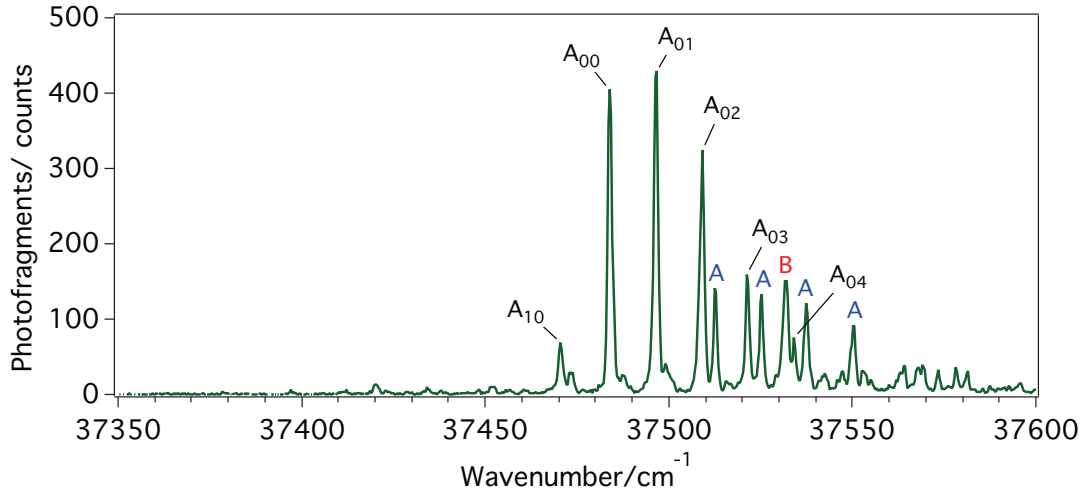


Figure 4.1 The UV photofragmentation spectrum of AcFAK-$H^+$, recorded monitoring the phenylalanine side-chain loss fragment as the function of UV wavenumber. We label the UV transitions corresponding to different conformers as A and B. The indices for the first vibronic progression of conformer A (in black) show the vibrational quantum number in the ground state and the electronically excited state, respectively.

## 4.2.2 Ground state infrared spectra of conformer A and conformer B

Using IR/UV double resonance spectroscopy (Figure 2.6) for each of the UV bands in the vibronic progression of conformer A, we record the same IR spectrum, presented in Figure 4.2a. The position of phenylalanine NH stretch is determined by $^{15}N$ isotopic substitution on the phenylalanine residue (see Figure 4.2b). Upon $^{15}N$ isotopic substitution, the phenylalanine NH-stretch shifts ~ 7.8 $cm^{-1}$ to the red (from 3443.9 $cm^{-1}$ to 3436.1 $cm^{-1}$). A small band that we see in AcFAK-$H^+$ at 3457.5 $cm^{-1}$ appears also red-shifted in the ground state spectrum of conformer A in the isotopically substituted molecule (AcF*AK-$H^+$), forming a shoulder at 3449.7 $cm^{-1}$. This small band, 13.6 $cm^{-1}$ to the blue from the phenylalanine NH stretch, can be a combination band. The other two IR transitions at 3417.1 $cm^{-1}$ and 3451.7 $cm^{-1}$ correspond to lysine and alanine NH stretches, but we do not know which one is which.

When the UV laser excites the electronic transition of conformer B at 37532.2 $cm^{-1}$, the infrared spectrum is different (Figure 4.2c). The position of the phenylalanine NH stretch was also determined by $^{15}N$ isotopic substitution on phenylalanine residue (see Figure 4.2d). The IR

band at 3403.9 $cm^{-1}$ in AcFAK-$H^+$ shifts ~ 7.8 $cm^{-1}$ to the red upon isotopic substitution (3396.1 $cm^{-1}$). The transitions 3416.5 $cm^{-1}$ and 3451.7 $cm^{-1}$ also correspond to lysine or alanine NH stretches and have similar values to conformer A.

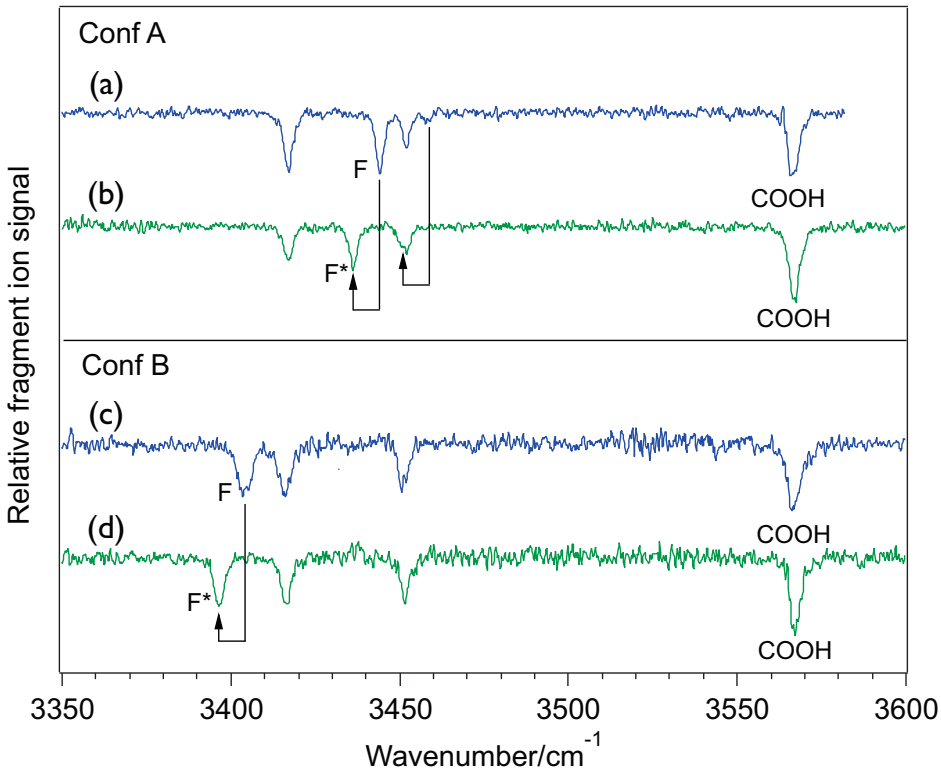


Figure 4.2. The ground state infrared spectrum of conformer A and B of AcFAK-$H^+$ (a and c respectively) compared with the ground state infrared spectrum of conformer A and B of AcF*AK-$H^+$ (b and d respectively), where F* is $^{15}N$ isotopically substituted phenylalanine. The UV laser excites the band origin of conformer A (37484.0 $cm^{-1}$) or conformer B (37532.2 $cm^{-1}$). The labels in the figure: F - phenylalanine NH stretch, F* - $^{15}N$ isotopically labeled phenylalanine NH stretch, COOH – carboxylic acid stretch. The arrows show which spectroscopic transitions change upon isotopic substitution.

The ground state IR spectra for conformers A and B in the fingerprint region are presented in Figure 4.3. For both conformers instead of four well separated C=O stretch vibrations we observe more infrared bands. The transitions around 1670 $cm^{-1}$, 1700 $cm^{-1}$, and 1790 $cm^{-1}$ are due to C=O stretch vibrations and the spectroscopic transitions at 1600 $cm^{-1}$ and 1630 $cm^{-1}$ are most probably caused by vibrations of the $NH_3^+$ lysine group or other NH bending modes. Also it seems that in conformer A the most intense infrared band at 1700 $cm^{-1}$ consists of two overlapping vibrations that separate in conformer B (1695.4 $cm^{-1}$ and 1705.4 $cm^{-1}$). Due to water

absorption in the air, the power of the IR beam in IR/UV depletion experiments sometimes drops. After IR power normalization, an artificial peak arose at 1653.0 $cm^{-1}$ and a sharp dip appeared at 1699.0 $cm^{-1}$ in the IR spectrum of conformer B, which we ignore in further analysis.

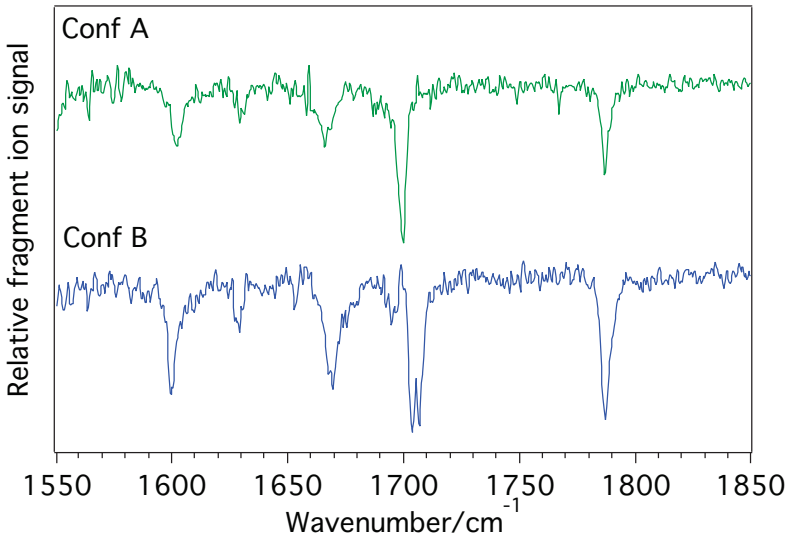


Figure 4.3. The ground state infrared spectra of conformer A (green trace) and B (blue trace) of AcFAK-$H^+$ in a fingerprint spectral region. The UV laser excites the band origin of conformer A (37484.0 $cm^{-1}$) or conformer B (37532.2 $cm^{-1}$).

### 4.2.3 Structures of the ground state of conformer A and conformer B

The theoretical approach used to calculate the ground state structures of conformers A and B of AcFAK-$H^+$ is described in detail in Chapter 2, Section 2.3.1.1. Using this method, where the preliminary conformational search is performed with the MMFF94 force field and then refined at DFT B3LYP /6-31+G** level of theory, we found several structures (see Figure 4.4). The two lowest energy structures (I and II) exhibit hydrogen bonds between the $NH_3^+$ group of the lysine side-chain and the carbonyl of the acetyl group and those of phenylalanine and alanine. These two structures differ mainly by the rotation of the phenyl side-chain. A similar pattern of interactions occurs in longer alanine peptides and initiates helix formation.[15] Structures III and IV, which also differ from each other by the rotation of the phenyl ring around $C_\alpha$-$C_\beta$ bond, lie somewhat higher in energy. They favor the interaction between the ammonium group and the three carbonyls as in structures I and II, but they have a different orientation of COOH group,

which flips 180° and breaks the hydrogen bond between the lysine amide NH and the carboxylic C=O. The last two structures V and VI differ from III and IV respectively in that instead of three NHs of the lysine ammonium group only two interact with carbonyls (of the acetyl group and the alanine), liberating the carbonyl of phenylalanine.

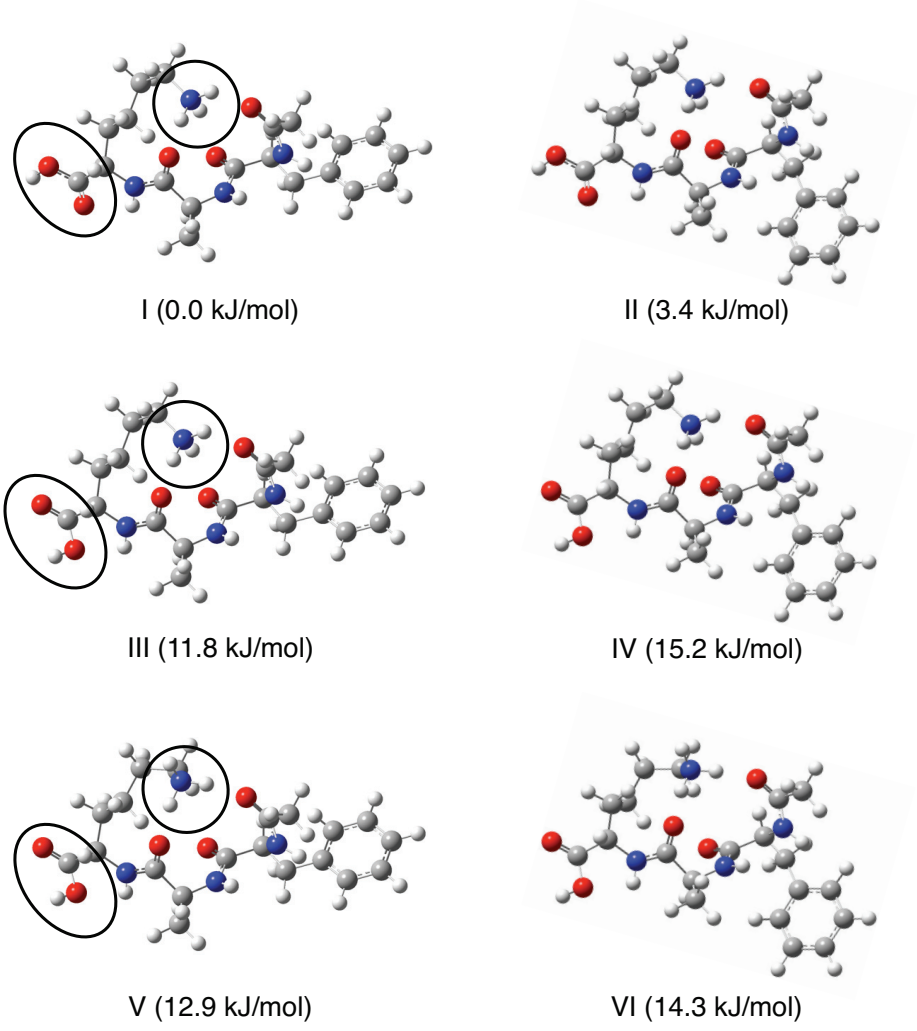


Figure 4.4 Lowest energy structures calculated using B3LYP/6-31+G** level of theory. The relative energies are corrected for zero-point energies.

The other favorable interaction, which is common among the structures from the protein data bank, is the cation-π interaction between the charged side-chain of lysine or arginine and an aromatic side-chain of phenylalanine, tyrosine or tryptophan.[16, 17] A similar cation-π interaction is responsible for the turn structure observed in the $H^+$AlaTyr dipeptide.[18] Using the MMFF94 force field, we generated a few conformations of AcFAK-$H^+$ in which the $NH_3^+$ group of lysine interacts with the π system of the aromatic side-chain. However, after re-optimization at the DFT

B3LYP /6-31+G** level of theory, those conformations appeared at least 20 kJ/mol higher in energy than the most stable conformer I (Figure 4.4), suggesting that in AcFAK-$H^+$ cation-π interaction is unfavorable.

Figure 4.5 presents the comparison between the experimental and calculated vibrational spectra (using the B3LYP/6-31+G** level of theory) for the lowest energy structures. All frequencies are scaled by a factor 0.987 in the fingerprint region and a factor 0.952 in the NH stretch region to account for anharmonicities. The factor 0.987 was chosen for the best match with the experimental data and the factor 0.952 was chosen based on the previous work on protonated helical peptides.[15]

In the 1650 – 1720 $cm^{-1}$ spectral region, it is difficult to assign the vibrational transitions to single carbonyls, because the strong NH---C=O interaction with the lysine ammonium group causes coupling between the individual C=O vibrations. The C-terminal carboxylic acid C=O vibration is isolated and appears in the experimental spectrum at 1787 $cm^{-1}$. The calculated infrared spectrum I seems to match the experimental spectrum of conformer B and the calculated spectrum II - the one of conformer A in the fingerprint region (Figure 4.5). All the other structures give rise to a higher wavenumber for the COOH vibration due to the lack of hydrogen bond between the carboxylic acid C=O and the lysine amide NH. In contrast to the work of Bakker et al.,[19] our calculations showed that carboxyl C=O stretching vibration is very sensitive to hydrogen bonding and can be used to determine the structure.

In the NH stretch region, however, the calculated spectra do not match the experiment as well. The vibrational spectra of structures I and II reproduce the right order of the NH stretch vibrations in conformer A, but the wavenumbers of the phenylalanine and the lysine NH stretches are red-shifted compared with the experiment (Figure 4.5). This is probably a result of a strong carbonyl – $NH_3^+$ hydrogen bond formations, which would shift the NH wavenumbers of the same amide group. The vibrational spectra of structures III and IV in the NH stretch region seem to match the experimental spectrum of conformer B fairly well. However, the blue shift of the lysine NH stretch in spectrum III and IV compared with the spectrum I and II happens at the expense of the blue shift of the carboxylic acid C=O, because of the loss of a hydrogen bond between these groups due to the rotation of COOH.

It is clear that none of the calculated spectra accounts for the experimental spectra of AcFAK-$H^+$ perfectly. There might be several reasons for this:

- Not extensive enough conformational search in the Monte Carlo method

- The failure of the force fields to estimate the energies
- The failure of DFT to find the minimum energy geometries
- The failure of DFT to estimate the strength of dispersive and Van der Waals interactions.

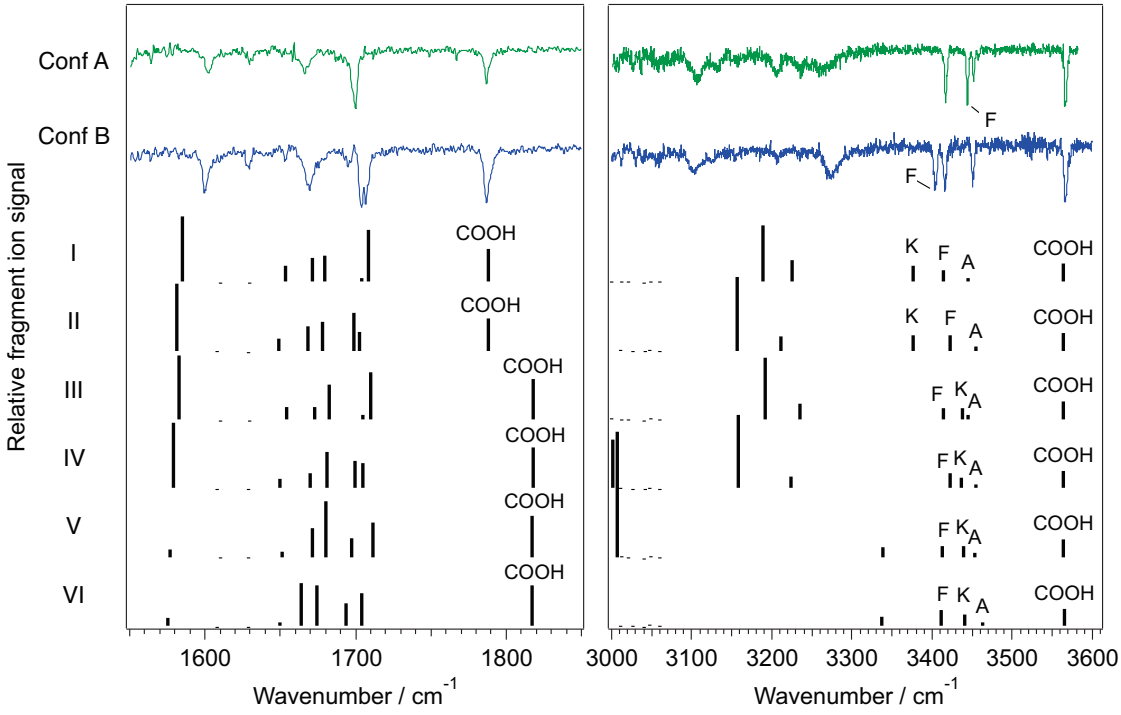


Figure 4.5 The experimental ground state infrared spectra of conformer A (green) and B (blue) of AcFAK-$H^+$ in comparison with the calculated spectra of structures I-VI presented in Figure 4.4. Labels K, F and A stand for lysine, phenylalanine and alanine NH stretch vibrations. COOH stands for the vibration of either the OH or the C=O group of the C-terminal carboxylic acid.

Before proceeding with more extensive conformational search, we decided to put some constrains on the possible structures based on our experimental data. First, the band origin of both conformers A and B is close to that of bare, protonated phenylalanine,[14] suggesting that the electronic structure of the chromophore is not highly perturbed and the interaction of the aromatic ring with the charge is weak. This discards the conformations that have the direct interaction of the charge with the π cloud of the phenylalanine side-chain . Second, upon electronic excitation, in conformer B mainly the phenylalanine NH shifts to the red, whereas in conformer A, along with the shift of the phenylalanine NH stretch we observe ~5 $cm^{-1}$ red shift of the band appearing in the ground state spectrum at 3451.7 $cm^{-1}$ (Figure 4.2 a,c and Figure 4.8

a,c). To be affected by the electronic excitation, it is likely that the bond associated with the vibrational band at 3451.7 $cm^{-1}$ is closer to the aromatic ring of the chromophore in conformer A than in conformer B. Moreover, we have noticed that the pattern of NH stretch vibrations in the experimental spectrum of conformers A and B of AcFAK-$H^+$ is reminiscent of the vibrational bands in conformers A and B of the helical, seven-amino acid peptide $AcFA_5K$-$H^+$. In Table 4.1 we list the positions of phenylalanine, alanine, and lysine NH stretches for conformers A and B of $AcFA_5K$-$H^+$ [15] compared with the spectroscopic bands in the ground state spectra of conformer A and B of a AcFAK-$H^+$.

| | Phe NH, $cm^{-1}$ | Ala NH, $cm^{-1}$ | Lys NH, $cm^{-1}$ |
|---|---|---|---|
| $AcFA_5K$-$H^+$ conformer A | 3447 | 3453 | 3432 |
| AcFAK-$H^+$ conformer A | 3444.1 | 3451.7/3417.1 | 3417.1/3451.7 |
| $AcFA_5K$-$H^+$ conformer B | 3402 | 3450 | 3432 |
| AcFAK-$H^+$ conformer B | 3403.9 | 3450.7/3416.5 | 3416.5/3450.7 |

Table 4.1 The position of some NH stretches in the ground state infrared spectra of conformers A and B of $AcFA_5K$-$H^+$ [15] compared to the positions of the NH stretches in the ground state infrared spectra of conformers A and B of AcFAK-$H^+$. For AcFAK-$H^+$ we do not know which band corresponds to alanine NH stretch and which corresponds to lysine NH stretch.

The phenylalanine NH in conformer B of AcFAK-$H^+$ forms a stronger π-hydrogen bond than it does in conformer A, resulting in a red shift of NH stretch frequency in conformer B (Figure 4.2). This only significant difference between the ground state infrared spectra of these conformers can result from different orientation of the phenylalanine side-chain, similar to what Stearns et *al.* observed in the conformers A and B of the helical molecule $AcFA_5K$-$H^+$.[15] In conformer A of AcFAK-$H^+$, the phenylalanine side-chain might be located just under the alanine and phenylalanine NHs and in conformer B it turns away from the alanine NH and forms a stronger hydrogen bond with the phenylalanine NH. Thus the infrared band appearing in the infrared spectrum of conformers A and B of AcFAK-$H^+$ at around 3451 $cm^{-1}$ should correspond to the alanine NH stretch. The amide NH stretches below 3400 $cm^{-1}$ usually belong to the NH groups that form strong hydrogen bonds, and in our case they might correspond to the vibrations of the NHs from the $NH_3^+$ group of the lysine side-chain .

By analogy with the helical peptide $AcFA_5K$-$H^+$ and with the other experimental constraints, we can confine our conformational search to two conformations that differ by the rotation of the phenylalanine ring around the $C_\alpha$-$C_\beta$ bond and in which lysine side-chain is not involved in a

cation-π interaction. With this analysis in mind, it seems strange that the calculated vibrational spectrum in the NH stretch region does not reflect any significant difference between the two lowest energy structures I and II (Figure 4.5). We expect the phenylalanine NH stretch vibration to be more pronouncedly red-shifted in the spectrum of conformer I compared with the spectrum of conformer II due to a stronger NH-π interaction. While the B3LYP method with 6-31G** basis set described well the geometries and the frequencies of different conformers of the seven-amino acid helical peptide $AcFA_5K\text{-}H^+$,[15] in some cases it underestimates the weak Van der Waals and dispersion interactions.

To test this, we decided to re-optimize the geometries of structures I and II using M05-2X/6-31G** level of theory with tight convergence criteria and ultrafine grid and then calculate the vibrational frequencies using B3LYP/6-31G** (the theoretical method is described in Chapter 2, Section 2.3.1.2). The results of the calculation are presented in Figure 4.6. The main difference between the structures optimized with the B3LYP functional and those re-optimized with the M05-2X functional is the $C_\alpha C_\beta C_\gamma$ dihedral angle of phenylalanine side-chain. In structure $I_{m052X}$ this angle is 111.5 degrees while in structure $I_{B3LYP}$ this angle is 113.2 degrees. Such a position of the chromophore results in a stronger NH-π interaction of the phenylalanine NH with the aromatic ring in conformer $I_{m052X}$ than in conformer $I_{B3LYP}$, which causes the red-shift of the phenylalanine NH stretch. In conformer $II_{m052X}$, on the other hand, this type of interaction is weaker than in $II_{B3LYP}$, resulting in the blue-shift of the phenylalanine NH stretch. The simulated vibrational spectra of the structures $I_{m052X}$ and $II_{m052X}$ better describe the experimental spectra of conformers B and A of AcFAK-$H^+$ respectively, however, the lysine NH stretch frequency is still too much red-shifted, which might be due to a different isomeric form of the lysine side-chain.

After we found a functional that describes well the dispersion interaction between the phenylalanine NH and the aromatic ring, we proceeded with a more extensive conformational search (the theoretical method is described in Chapter 2, Section 2.3.1.3). Because the MMFF94 force field, which we utilized initially, is mainly optimized for organic compounds,[20, 21] we decide to perform the MonteCarlo conformational search using the optimized potentials for liquid simulations (OPLS) force field[22, 23] with the improved parameterization for proteins.[24] The OPLS force field is also successfully applied to identify cation-π interactions within the protein database,[16] and indeed we obtained a lot of structures in which the cationic lysine side-chain interacts with the π-cloud of phenylalanine. However, after the geometry optimization of the 60 lowest energy structures (generated with the force field) in Gaussian 09[25] using M05-2X[26, 27]/6-

31G**, we found that the structures with the cation-π interaction are more than 20 kJ/mol higher in energy than the other structures in which the charged lysine side-chain interacts with carbonyls. The relative energies calculated using the force field and the DFT methods differ a lot. The second lowest energy structure optimized with the OPLS force field is the global minimum after optimization with the DFT M05-2X/6-31G** level of theory, and the 39$^{th}$ – the second lowest energy structure after optimization with the DFT M05-2X/6-31G**. These geometries were re-optimized again at the M05-2X/6-31++G** level with tight convergence criteria and ultrafine grid, and their vibrational frequencies were calculated at the same level of theory. The resulting vibrational spectra along with the corresponding structures are presented in Figure 4.7. They well reproduce the experimental data in both the 3 micron and 6 micron spectral regions. The main difference between the structures $I_{m052X}$ and $II_{m052X}$ (appearing ~ 8.4 kJ/mol higher in energy) (Figure 4.6) and those assigned for conformer B and A (Figure 4.7) respectively is a slightly different fold of the lysine side-chain.

In conclusion, we found two structures corresponding to conformer A and B of AcFAK-$H^+$ (Figure 4.7). Conformer A has the lowest energy at this level of theory, and conformer B lies 1.8 kJ/mol higher in energy. The structures represent the starting motif for the formation of an α-helix, and this type of interaction is about 20 kJ/mol more favorable than the cation-π interaction. The structures of conformer A and B differ by the rotation of the aromatic chromophore around the $C_\alpha$-$C_\beta$ bond. In conformer B the phenylalanine NH forms a slightly stronger hydrogen bond with the π cloud of the phenyl ring than in conformer A. The lowest frequency vibration (15.9 $cm^{-1}$) in the ground state of conformer A corresponds to the movement of the molecule involving mainly the phenylalanine chromophore side-chain rotation around the $C_\alpha$-$C_\beta$ bond. We think that the same motion is responsible for the 12.6 $cm^{-1}$ vibrational progression in the electronically excited state of AcFAK-$H^+$ (Figure 4.1). We also show that AcFAK-$H^+$ is a good model system to test the performance of different DFT functionals. The B3LYP density functional fails to describe the dispersive interactions, while the M05-2X density functional yields reliable geometries in which the NH-π interaction is well described.

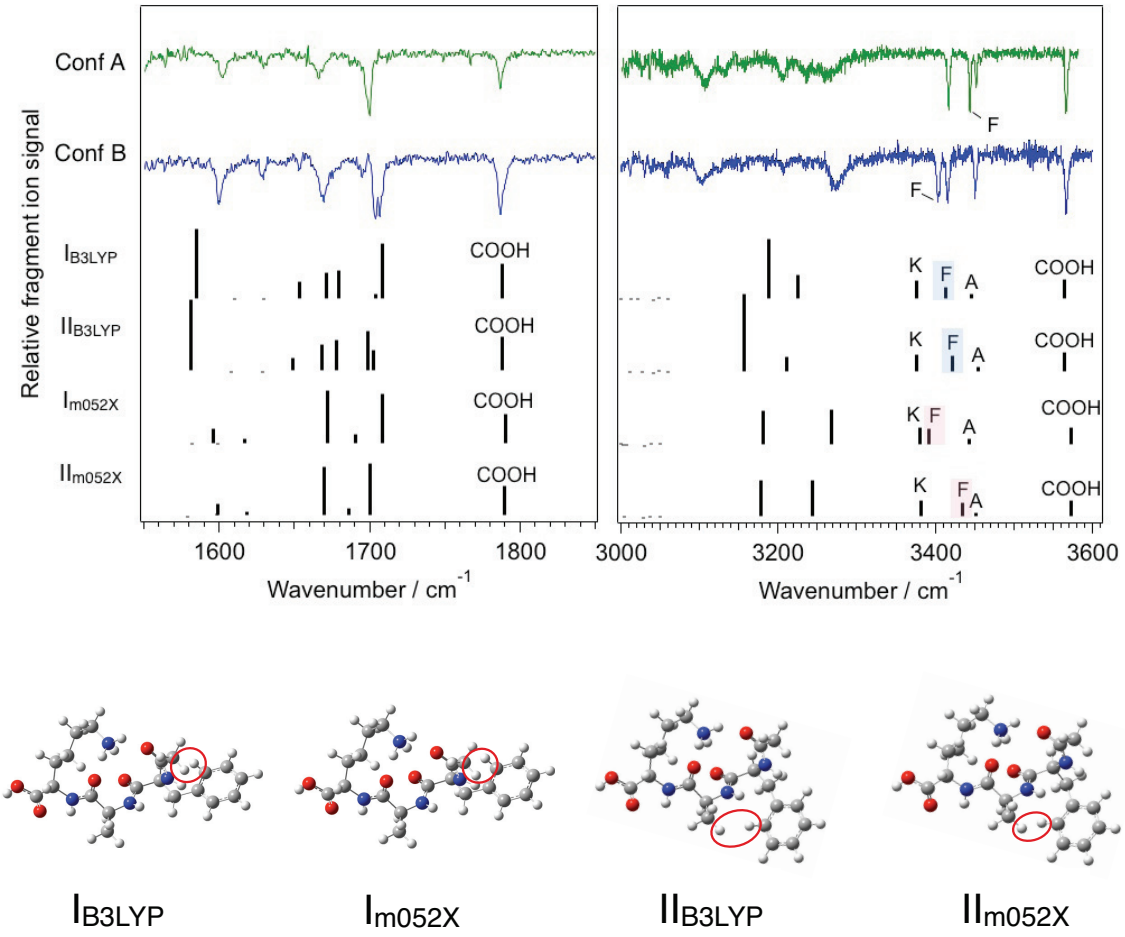


Figure 4.6 The experimental ground state infrared spectra of conformer A (green) and B (blue) of AcFAK-$H^+$ in comparison with the calculated spectra of the corresponding structures $I_{B3LYP}$, $II_{B3LYP}$, $I_{M052X}$, and $II_{M052X}$. Structures $I_{B3LYP}$ and $II_{B3LYP}$ are calculated using B3LYP functional (I and II in Figure 4.4). Structures $I_{M052X}$ and $II_{M052X}$ were calculated by geometry re-optimization of $I_{B3LYP}$ and $II_{B3LYP}$ with M05-2X functional. The harmonic frequencies are calculated for all of the structures using B3LYP/6-31G** level of theory. The scale factor in the fingerprint region is 0.987 and 0.94, in the NH stretch region – 0.952 and 0.955 for the structures optimized with B3LYP and M05-2X respectively. Labels K, F and A stand for lysine, phenylalanine and alanine NH stretch vibrations. COOH stands for the vibration of either the OH or the C=O group of the C-terminal carboxylic acid.

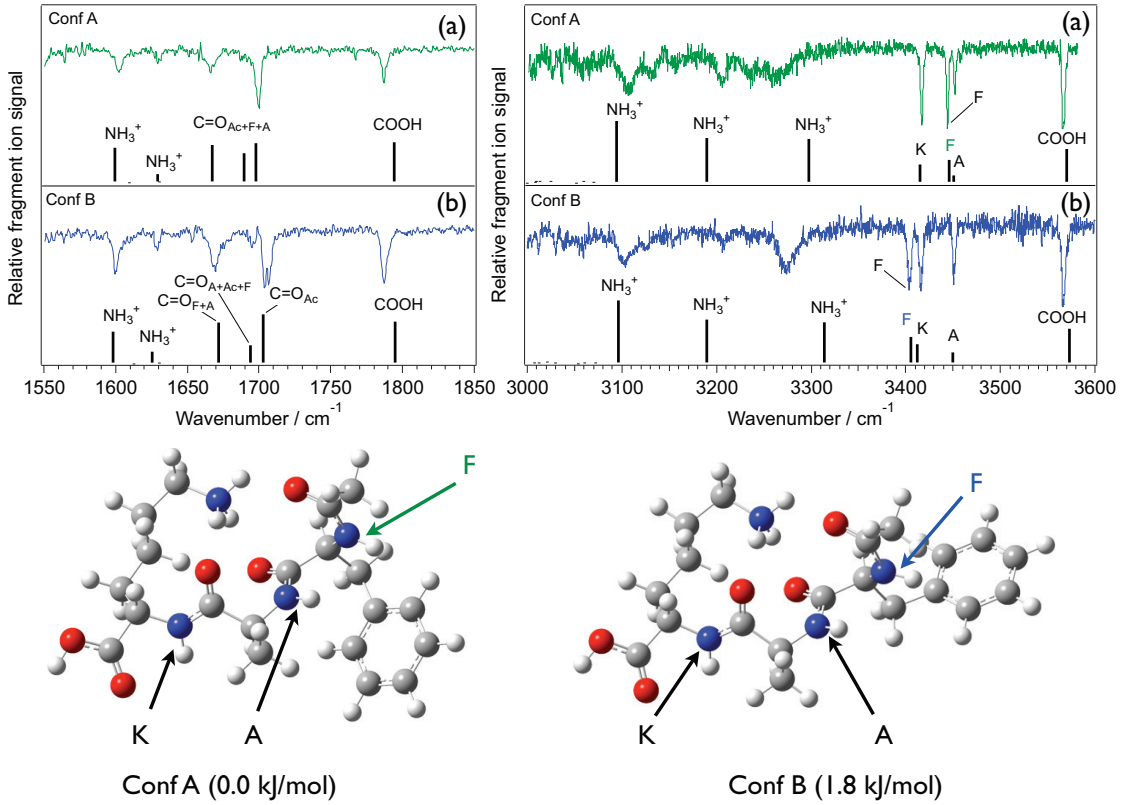


Figure 4.7 Comparison between the experimental and calculated infrared spectra of conformer A (a) and conformer B (b) of AcFAK-$H^+$. Calculations are performed at the M05-2X/6-31++G** level of theory with tight convergence criteria and ultrafine grid. We use a scale factor 0.937 in amide I and amide II spectral region and a scale factor 0.959 in NH stretch spectral region in the calculated spectrum. We mark the positions of lysine, phenylalanine, alanine NH stretches with the labels K, F, and A respectively. The corresponding structures are presented underneath the spectra with their relative energies corrected for zero-point energy.

## 4.2.4 Infrared spectra of conformers A and B in their first excited electronic state ($S_1$)

When the molecules absorb IR light before the UV laser promotes them to the electronically excited state, ground state infrared spectra are recorded. We can invert the order of the two lasers. If initially the UV laser pre-excites the molecules and then the IR OPO promptly (~5 ns) interrogates them, we record conformer-selective infrared spectra of the electronically excited molecules. This is possible because the lifetime of the $S_1$ state for this molecule appears to be longer than 5 ns and absorption of the IR light by the electronically excited molecule leads to the increase the side-chain loss photofragment yield. The fragmentation mechanism and the

evidence that we probe the $S_1$ state has been presented in Chapter 3. Figure 4.8a presents the infrared spectrum of conformer A in the $S_1$ state, recorded as a gain in the photofragmentation yield when the IR OPO is scanned across a vibrational transition. The position of the phenylalanine NH stretch is determined with $^{15}N$ isotopic substitution (Figure 4.8b). Curiously, three infrared bands shift 8 $cm^{-1}$ upon isotopic substitution (Figure 4.8 b), which means that all of them are associated with the phenylalanine NH. The spacing between them is 13.6 $cm^{-1}$, the same as in the ground state infrared spectrum (Figure 4.2 a-b). However, compared to the ground state, instead of one NH stretch and a combination band, we observe one NH stretch and two additional bands.

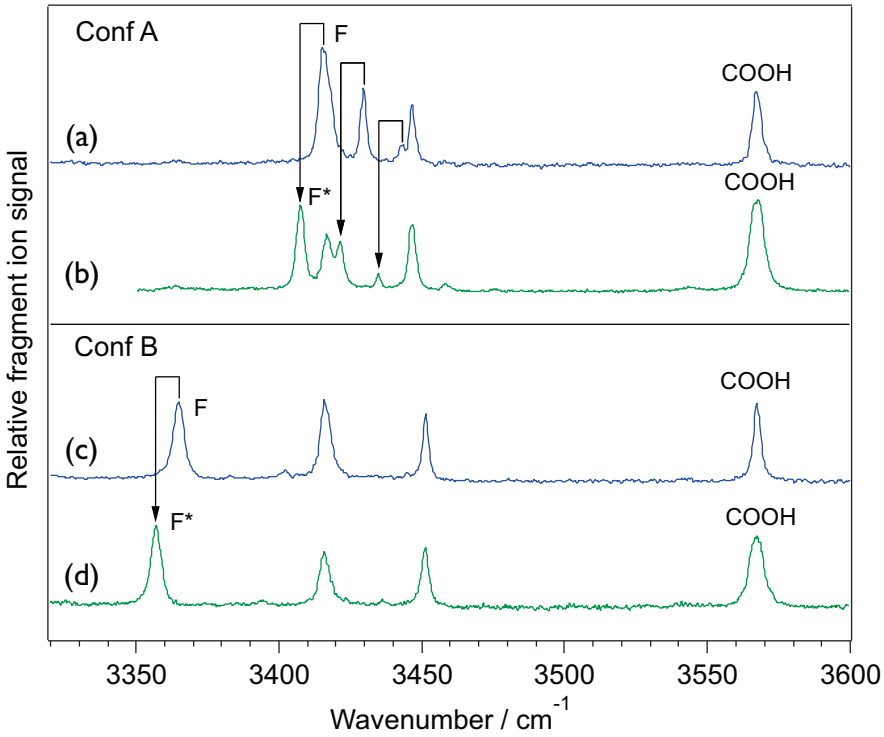


Figure 4.8. The infrared spectrum of $S_1$ state of conformer A and B of AcFAK-$H^+$ (a and c respectively) compared with the infrared spectrum of $S_1$ state of conformer A and B of AcF*AK-$H^+$ (b and d respectively), where F* is $^{15}N$ isotopically substituted phenylalanine. The UV laser excites the band origin of conformer A (37484.0 $cm^{-1}$) or conformer B (37532.2 $cm^{-1}$). The IR OPO is scanned ~ 5 ns after the UV excitation. The power of the IR OPO is adjusted to avoid saturation.

The excited state infrared spectrum of conformer B looks simpler than that of conformer A. When we excite the band origin of conformer B with the UV laser (37532.2 $cm^{-1}$), no additional intense spectroscopic bands appear in the spectrum (Figure 4.8c). Only the phenylalanine NH

stretch shifts 39 $cm^{-1}$ to the red compared with the ground state spectrum (Figure 4.2c). To verify our assumption that the spectroscopic band at 3365 $cm^{-1}$ corresponds to the phenylalanine NH stretch, we label it with $^{15}N$ and record the infrared spectrum again (Figure 4.8d). Only one band appears 8 $cm^{-1}$ red-shifted compared with the infrared spectrum of the unlabeled peptide, which is due to the phenylalanine NH stretch vibration with a different reduced mass.

In the electronically excited state, the phenylalanine NH stretch (3414.9 $cm^{-1}$ in conformer A and 3365 $cm^{-1}$ in conformer B) is 29 $cm^{-1}$ red-shifted from its position in the ground state for conformer A and 39 $cm^{-1}$ for conformer B. The stronger effect of the electronic excitation on the frequency of the phenylalanine NH in conformer B led us to consider also a stronger interaction of the phenylalanine NH with the π cloud of the phenyl ring, which is also evidenced from the DFT calculations (Figure 4.7). Moreover, in the electronically excited state of conformer A, the alanine NH stretch is ~ 5 $cm^{-1}$ red-shifted from its position in the ground state spectrum whereas in the conformer B the alanine NH stretch vibration is not effected by the electronic excitation. The electronic excitation of the aromatic chromophore results in the perturbation of only those modes involving atoms in the closest proximity to the expanded electronic cloud.

### 4.2.5 Infrared spectra of different vibrational levels of $S_1$ state of conformer A: combination bands

The infrared spectra of the molecules excited to different vibrational levels in the $S_1$ state, starting from the band origin and ending with the excitation of up to 4 vibrational quanta (12.6 $cm^{-1}$ each) above the band origin, are presented in Figure 4.9. Because in AcF*AK-$H^+$, where F* is the $^{15}N$ substituted phenylalanine amino acid, NH stretches are better separated from the alanine and the lysine vibrations, we present the spectra for AcF*AK-$H^+$ in Figure 4.9. By comparing all the spectra with those for the non-isotopically substituted molecule, the positions of the IR bands corresponding to phenylalanine NH are determined (blue dots in Figure 4.9). Instead of one, we observe several bands separated by 13.6 $cm^{-1}$. As the UV laser excites higher vibrational levels of the electronically excited state, more F* combination bands appear. With one additional vibrational quantum in the electronic excitation, the F* NH stretch and each F* combination band shift 1 $cm^{-1}$ to blue. Moreover, the intensities of the IR transitions in the electronically excited AcF*AK-$H^+$ vary for different UV wavelengths from the vibronic progression in the electronic spectrum (Figure 4.1). For example, the IR band at 3407.3 $cm^{-1}$, which is the most intense when the UV laser excites the band origin (Figure 4.9 a), completely

disappears from the IR spectrum when the UV laser excites 3 or 4 quanta of 12.6 $cm^{-1}$ (Figure 4.9 d-e) vibration in the electronically excited state.

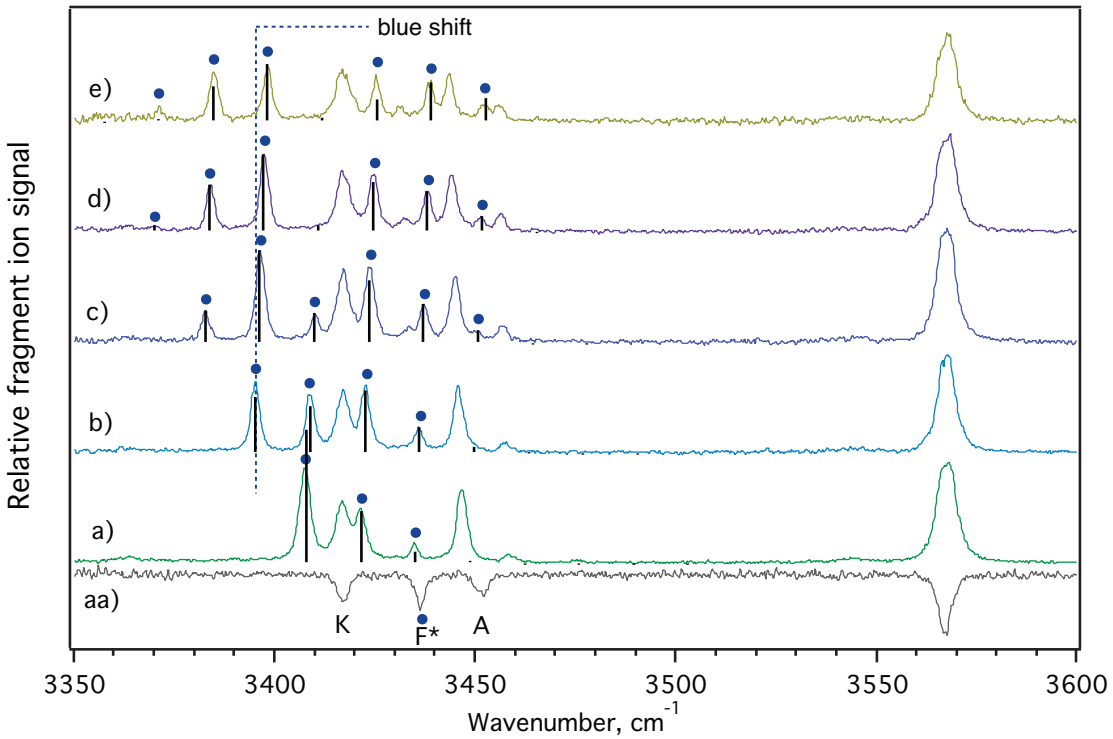


Figure 4.9 AcF*AK, F* $^{15}N$ isotopically substituted phenylalanine. aa) ground state spectrum of conformer A. a-e) Excited state IR spectrum of conformer A recorded when the IR OPO probes the molecules ~ 5 ns after the UV excitation. The UV laser excites the 0-0 band origin at 37484.0 $cm^{-1}$ (a), vibronic transition 0-1 at 37496.7 $cm^{-1}$ (b), vibronic transition 0-2 at 37509.4 $cm^{-1}$ (c), vibronic transition 0-3 at 37521.8 $cm^{-1}$ (d), vibronic transition 0-4 at 37534.5 $cm^{-1}$ (e). Blue dots show the position of phenylalanine NH. Vertical line shows that for each vibrational quantum in UV all the bands associated with the phenylalanine NH shift 1 $cm^{-1}$ to blue. Black stick spectra represent the intensities of the transitions, calculated using the Franck Condon model.

The lysine NH stretch (3417.1 $cm^{-1}$ in the ground state spectrum (Figure 4.9aa)) appears in all electronically excited state infrared spectra at the same position no matter how many vibrational levels are excited. However, the alanine NH stretch (3451.7 $cm^{-1}$ in the ground state spectrum (Figure 4.9aa)) shifts to the red upon the electronic excitation and appears at 3446.7 $cm^{-1}$ (Figure 4.9a). The other small band at 3458.1 $cm^{-1}$ (Figure 4.9a) appears to be a combination band of 3446.7 $cm^{-1}$, because it does not shift upon the $^{15}N$ substitution on the phenylalanine amino acid. The electronic excitation is local to the phenylalanine chromophore and perturbs only the vibrations in its closest proximity. In the structure that we assign to conformer A of AcFAK-$H^+$

(Figure 4.7), both the alanine and phenylalanine NHs are localized above the phenyl ring and are likely to be affected by the electronic excitation of the π cloud. In Figure 4.10 we mark with red triangles the positions of the alanine NH stretch and its combination bands. The assignment of the transitions is based on the spacing between the bands that do not shift upon the $^{15}N$ isotopic substation on the phenylalanine. The separation between the combination bands is 11.8 $cm^{-1}$ and it stays constant when the UV laser excites different members of the vibrational progression. However, all of the bands marked with red triangles move 0.7 $cm^{-1}$ to the red for each additional vibrational quantum in the electronically excited state (look at the red dashed line in Figure 4.10).

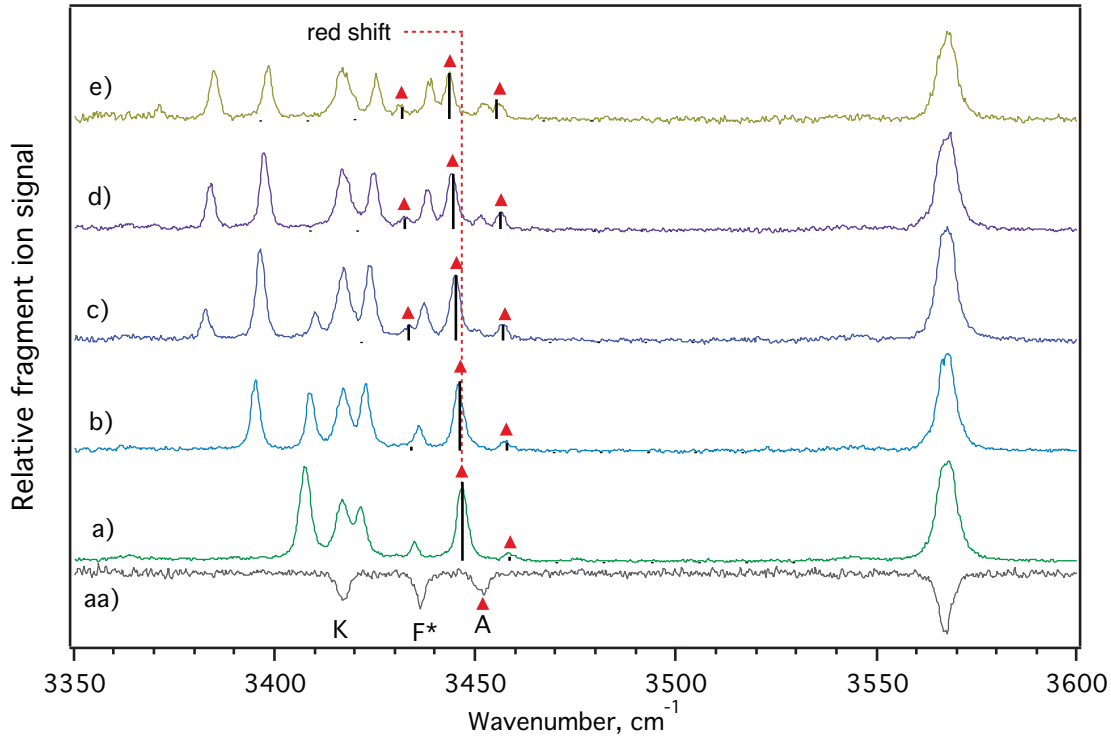


Figure 4.10 AcF*AK, F* $^{15}N$ isotopically substituted phenylalanine. aa) ground state spectrum of conformer A. a-e) Excited state IR spectrum of conformer A recorded when the IR OPO probes the molecules ~ 5 ns after the UV excitation. The UV laser excites the 0-0 band origin at 37484.0 $cm^{-1}$ (a), vibronic transition 0-1 at 37496.7 $cm^{-1}$ (b), vibronic transition 0-2 at 37509.4 $cm^{-1}$ (c), vibronic transition 0-3 at 37521.8 $cm^{-1}$ (d), vibronic transition 0-4 at 37534.5 $cm^{-1}$ (e). Red triangles show the position of alanine NH stretch and corresponding combination bands. Vertical line shows that for each vibrational quantum in UV all the bands related to alanine (lysine) NH shift 0.7 $cm^{-1}$ to red. Black stick spectra represent the intensities of the transitions, calculated using the Franck Condon model.

# 4.3 Discussion

## 4.3.1 Previous observations of the Franck Condon like progressions in IR spectra

Johnson and coworkers observed a strong anharmonic coupling between the OH stretch and the low frequency motion in mid-IR argon predissociation spectra of $CH_3NO_2^-\cdot H_2O$ and $CH_3CO_2^-\cdot H_2O$ complexes.[11] The authors recorded a Franck Condon like progression of closely spaced spectroscopic bands several hundred wavenumbers below the calculated OH fundamentals. They addressed the question of this spectral complexity in a qualitative manner. The OH is more strongly bound to the ion in the vibrationally excited state than in the ground state, which causes a shift in the equilibrium distance for the excitation of the water rocking motion. This displacement of the effective potential for the water rocking motion results in a Franck Condon like progression built on top of the OH transition.[11] Later Myshakin and al. showed mathematically that an adiabatic model involving the OH stretch and an intramolecular rock vibration is enough to describe the observed combination band intensities in a near quantitative manner.[12] While such a one-dimensional anharmonic potential fairly well describes the spectral intensities in the ground state spectrum, this model does not account for the possible change of the rocking motion frequency upon the OH stretch excitation.

We apply a similar model to analyze the progressions of combination bands in our IR spectra of electronically excited conformer A of AcFAK-$H^+$. We will introduce into this model both the shift of the harmonic PES and the change of the oscillator force constant. The truncation of the Taylor expansion for the PES at the forth order term allows us to account for the frequency change due to the coupling between the NH stretch and the low frequency vibration of the molecule.

## 4.3.2 Schematic model explaining the appearance of the combination bands and their shifts

Figure 4.11 schematically explains the appearance of the phenylalanine combination bands through the coupling between the phenylalanine NH stretch and a low frequency vibration of the entire molecule. The 12.6 $cm^{-1}$ harmonic vibrational progression that we see in the UV spectrum (Figure 4.1) is due to the excitation of different quanta of the low frequency vibration in the $S_1$

state of the molecule. The additional excitation of one quantum of F NH stretch perturbs the structure of the molecule such as the frequency of this low frequency motion changes to 13.6 $cm^{-1}$. In fact, the vibration at 12.6 $cm^{-1}$ is ~ 251 times slower than the NH stretch frequency, and we can use an adiabatic model to describe the slow motion of the molecule in the average potential created by the fast NH stretch motion. In Figure 4.11 we show how four phenylalanine combination bands appear when exciting with the UV light the transition at 37496.6 $cm^{-1}$, which involves 1 quantum of 12.6 $cm^{-1}$ vibration in the first electronically excited state (Figure 4.9b). The blue curves represent the potential energy for the low frequency vibration when 0 or 1 quantum of the phenylalanine NH stretch is excited. In the case of 0 quanta of the NH stretch, the frequency for the low frequency vibration is 12.6 $cm^{-1}$; in the case of 1 quantum, the frequency is 13.6 $cm^{-1}$. The most red-shifted IR band in Figure 4.9b (3394.7 $cm^{-1}$) arises from the loss of 1 quantum of the low frequency vibration ($\nu_{lf}$) and the excitation of 1 quantum of phenylalanine NH stretch ($\nu_{NH}$). The next IR band at 3408.3 $cm^{-1}$ comes from the transition that involves only the excitation of 1 quantum of phenylalanine NH without the loss of 1 quantum of the low frequency vibration and so on. However, upon the excitation of the NH stretch, the width of the potential changes and now the lowest frequency vibration is 1 $cm^{-1}$ higher. This explains why the phenylalanine NH stretch fundamental that appears at 3407.3 $cm^{-1}$ when the UV laser excites the zero vibrational level of the $S_1$ state (Figure 4.9a) shifts 1 $cm^{-1}$ to blue when the UV laser excites the first vibrational level of the $S_1$ state (Figure 4.9b). The same applies to the other combination bands at 3421.9 $cm^{-1}$ and 3435.5 $cm^{-1}$ that arise from the simultaneous excitation of 1 quantum of phenylalanine NH and 2 or 3 quanta of the low frequency vibration, respectively.

We can use the same scheme illustrated in Figure 4.11 to explain the appearance and the shift of the alanine NH stretch and its combination bands. The difference between the excitation of the phenylalanine NH stretch and the alanine NH stretch is that it changes the vibrations of the UV excited molecule differently. The former increases the wavenumber of the slowest vibration from 12.6 $cm^{-1}$ to 13.6 $cm^{-1}$ and the latter decreases the wavenumber of the slowest vibration form 12.6 $cm^{-1}$ to 11.8 $cm^{-1}$. The decrease of the wavenumber results in the red-shift of the alanine NH stretch and its combination bands upon UV excitation of the higher vibrational levels of the $S_1$ state from the 12.6 $cm^{-1}$ vibrational progression.

While this schematic very precisely describes the positions of the combination bands for the UV excited AcF*AK-$H^+$, one might be surprised why the combination bands are so intense in the IR spectra and why the intensities vary for the different number of vibrational quanta in the low frequency vibration of the $S_1$ state (Figure 4.9a-e and Figure 4.10a-e). For example, the

phenylalanine NH stretch fundamental (3407.3 $cm^{-1}$) dominates in intensity the combination bands when the UV laser excites the band origin of the $S_1$ state (Figure 4.9a). It decreases in intensity as the UV laser excites 1 or 2 vibrational quanta of 12.6 $cm^{-1}$ harmonic vibration in the $S_1$ state (Figure 4.9b-c), until it completely disappears from the IR spectrum for the UV transitions that involve 3 and 4 quanta of $v_{lf}$ (Figure 4.9d-e).

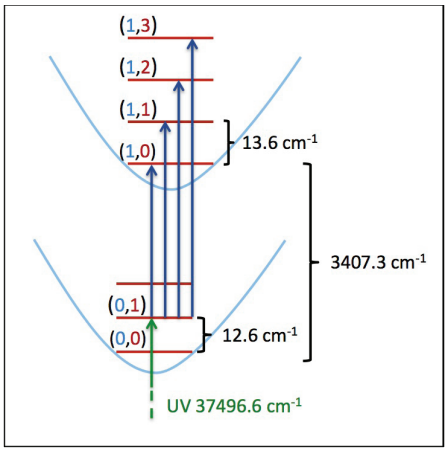


Figure 4.11. The schematic representation of the phenylalanine NH stretch combination bands in the IR spectrum of the electronically excited AcF*AK-$H^+$. Phenylalanine NH stretch in the $S_1$ electronically excited state has a frequency 3407.3 $cm^{-1}$ (see Figure 4.9a). The blue curve shows the potential energy for the low frequency vibration that changes upon the excitation of one quantum of phenylalanine NH stretch so that the frequency for the low frequency vibration changes from 12.6 $cm^{-1}$ to 13.6 $cm^{-1}$. The green arrow shows an example of the UV excitation of the first electronically excited state and 1 quantum of 12.6 $cm^{-1}$ vibration (Figure 4.1 band 0-1). The shortest blue arrow shows the excitation of 1 quantum of Phe NH stretch and the loss of 1 quantum of the low frequency vibration (IR band at 3394.7 $cm^{-1}$ in Figure 4.9b). The other blue arrows from left to right represent the IR transitions that involve excitation of 1 quantum of Phe NH stretch together with 1, 2, and 3 quanta of the low frequency vibration respectively (IR bands at 3408.3 $cm^{-1}$, 3421.9 $cm^{-1}$ and 3435.5 $cm^{-1}$ on Figure 4.9b). The numbers in brackets represent how many quanta of NH stretch (in blue) and low frequency vibration (in red) are excited.

## 4.3.3 Calculation of the combination band intensities using the model of two displaced and distorted harmonic oscillators

Such an intensity distribution is reminiscent of Franck-Condon progressions, for example that observed by Rizzo et al. in the fluorescence spectrum of jet-cooled tryptophan.[28, 29] In that case, the electronic excitation involves a geometry change along the vibrational coordinate. In our

case, the vibrational excitation of the high frequency vibration involves the change in the geometry along the coordinate for the low frequency vibration.

We decided to simulate the distribution of intensities using a simple adiabatic model, where the coordinates for the low frequency vibration are separated from the NH stretch vibration. Two harmonic oscillators that are displaced along the coordinate for the low frequency vibration and have different vibrational frequencies can serve as a good approximation. In the initial state, the vibrational frequency corresponds to the frequency of the progression of conformer A in the electronic spectrum ($w_0$) (see Figure 4.1). In the final state, after the excitation of one quantum of the phenylalanine or alanine NH stretch, the frequency changes ($w_1$). In 2005 Chang derived an analytical formula to calculate the overlap integral between the wave functions in the case of two displaced and distorted harmonic oscillators.[30] The Franck-Condon factor for the transition between $|\nu\rangle$ and $|\nu'\rangle$ states can be calculated by

$$|\langle\nu|\nu'\rangle|^2 = \left(\frac{Ae^{-S}}{2^{\nu+\nu'}\nu!\,\nu'!}\right)\cdot\left[\sum_{i=0}^{\nu}\sum_{j=0}^{\nu'}\frac{\nu!}{(\nu-i)!\,i!}\frac{\nu'!}{(\nu'-j)!\,j!}H_{\nu-i}(b)H_{\nu'-j}(b')\left(2\sqrt{\alpha}\right)^i\left(2\sqrt{\alpha'}\right)^j I(K)\right]^2 \quad (4.1)$$

The coefficients in this formula are the following:

$$A = \frac{2\sqrt{\alpha\alpha'}}{\alpha+\alpha'} \quad (4.2)$$

$$S = \frac{\alpha\alpha' d^2}{\alpha+\alpha'} \quad (4.3)$$

$$b = -\frac{\alpha'\sqrt{\alpha}d}{\alpha+\alpha'};\ b' = \frac{\alpha\sqrt{\alpha'}d}{\alpha+\alpha'} \quad (4.4)$$

$$I(K) = \begin{cases} 0\ if\ i+j\ is\ odd \\ \dfrac{(2K-1)!!}{(\alpha+\alpha')^K}\ if\ i+j\ even \end{cases};\ K = \frac{i+j}{2} \quad (4.5)$$

$$\alpha = \frac{w}{\hbar};\ \alpha' = \frac{w'}{\hbar} \quad (4.6)$$

$H_\nu(x)$ – the Hermite polynomial

d – the displacement between the two oscillators

$w$ – the angular frequency of the oscillator in $|\nu\rangle$ state

$w'$ – the angular frequency of the oscillator in $|\nu'\rangle$ state

$\hbar = 1.054 \cdot 10^{-34}\left[\frac{m^2 kg}{s}\right]$ – the reduced Planck's constant

The parameters $\alpha$ and $\alpha'$ have the units [$m^{-2}$] in the international system of units SI. For this reason the vibrational frequencies for the initial ($w_0$) and final ($w_1$) states that we measure in the experiment in [$cm^{-1}$] have to be converted into the angular frequency of the oscillator

$$\alpha = \frac{w_0[cm^{-1}] \cdot c\left[\frac{cm}{s}\right] \cdot M[kg] \cdot 2\pi}{\hbar\left[\frac{m^2 kg}{s}\right]} \tag{4.7}$$

$$\alpha' = \frac{w_1[cm^{-1}] \cdot c\left[\frac{cm}{s}\right] \cdot M[kg] \cdot 2\pi}{\hbar\left[\frac{m^2 kg}{s}\right]} \tag{4.8}$$

where

M – the reduced mass of the harmonic oscillator

c – the speed of light

The standard deviation between the theoretically calculated Franck-Condon factors and the experimental intensities can be calculated using the Eqn. (4.9)

$$\Delta FC = \sqrt{\sum_{\nu=0}^{4}\sum_{\nu'=0}^{8}(f \cdot Theor|\langle\nu|\nu'\rangle|^2 - Exp|\langle\nu|\nu'\rangle|^2)^2} \tag{4.9}$$

where

$Theor|\langle\nu|\nu'\rangle|^2$– the theoretical value calculated using the Eqn. (4.1)

$Exp|\langle\nu|\nu'\rangle|^2$ – the experimental intensities of the transitions between $|\nu\rangle$ and $|\nu'\rangle$ states , where $\nu$ defines the number of the vibrational quanta in the initial state and $\nu'$ defines the number of the vibrational quanta in the final state after the excitation of the phenylalanine/alanine NH stretch

f – the scale factor

To find the least squares fit of the experimental intensities we wrote a program in Mathematica 9[31] that minimizes Eqn. (4.9) as a function of three parameters: reduced mass (M), the shift of the equilibrium bond distance between the two harmonic oscillators (d), and the scale factor (f). There is no global minimum, because for every reduced mass a relative shift of the potential results in the same force constant. After this observation, we fixed the reduced mass at 70.6536 a.u., which corresponds to the vibration of the phenylalanine side-chain (91 a.u.) relative to the rest of the backbone (316 a.u.), and optimized two parameters d and f for excitation of the phenylalanine NH stretch or the alanine NH stretch.

The results of the fit when exciting the phenylalanine NH stretch or the alanine NH stretch are presented as a stick spectrum in Figure 4.9 and Figure 4.10 respectively, and the fit parameters are summarized in Table 4.2

| Te, $cm^{-1}$ | $w_0$, $cm^{-1}$ | $w_1$, $cm^{-1}$ | f | d, Å |
|---|---|---|---|---|
| 3407.9 | 12.6 | 13.58 | 3614.33 | 0.140 |
| 3446.7 | 12.6 | 11.8 | 1530.07 | 0.068 |

Table 4.2 The parameters used to fit the intensities of the combination bands. Te - the distance between the 0-0 vibrational levels of the harmonic potential curves corresponding to the excitation of the phenylalanine NH stretch or the alanine NH stretch, $w_0$ – is the frequency of the first harmonic oscillator, $w_1$ – the frequency of the second harmonic oscillator, f – is the scale factor, d – the shift of the equilibrium distance between the two harmonic potentials. Te, $w_0$, and $w_1$ are taken from the experiment and the parameters f and d are varied to find the optimal fit.

The phenylalanine NH stretch seems to be more strongly coupled to the low frequency vibration than the alanine NH stretch, because the equilibrium distance and the frequency change more when exciting phenylalanine than alanine. Also, the frequency of the slow vibration increases when we excite the phenylalanine NH and decreases when we excite the alanine NH, meaning that these two excitations change the oscillator force constant in opposite ways. According to the DFT calculations, the lowest frequency vibration in the ground state conformer A mainly involves the rotation of the aromatic ring around the $C_\alpha$-$C_\beta$ bond. In the $S_1$ state, the ring probably moves faster or slower depending on which NH stretch is excited. We find it amazing that the processes in the excited state of such a big molecule as AcFAK-$H^+$ can be so well described by a simple Franck-Condon approximation.

### 4.3.4 The theoretical model that justifies the separation of coordinates

The Born-Oppenheimer approximation is based on the large difference between the mass of the electron and the nuclei in a molecule. In the case of coupling between the NH stretch and the low frequency vibration, the reduced mass difference is approximately 70.6/0.9 ≈ 76 times, if we assume that the low frequency vibration involves the rocking motion of the UV excited chromophore around the $C_\alpha$-$C_\beta$ bond or any other relative movement of the chromophore side-chain and the rest of the molecule. The phenylalanine/alanine NH stretch can be quickly adjusted to the change of the geometry caused by a slow vibration of a molecule as a whole.

In the Schrödinger equation we can separate the normal coordinates for the NH stretch and the other vibration and solve the equation for the NH stretch in the static potential of the position of the chromophore. The phenylalanine NH stretch wave function parametrically depends on the coordinates for the normal mode of the low frequency vibration. The coupling between these vibrational modes can be treated as a small perturbation in the Hamiltonian.

We have shown in the previous section that in order to fit the experimental data, we have to have a shift of the equilibrium distance and the change in the frequency for the low frequency vibration upon the absorption of the one quantum of phenylalanine/alanine NH stretch. In order to fulfill both conditions we include several coupling terms in the Hamiltonian for the joint system:

$$H = \frac{p_{NH}^2}{2} + \frac{p_l^2}{2} + \frac{\omega_{NH}^2}{2} Q_{NH}^2 + \frac{\omega_l^2}{2} Q_l^2 + \lambda {Q_{NH}}^2 Q_l + \lambda' {Q_l}^2 Q_{NH} + \beta {Q_{NH}}^2 {Q_l}^2$$

where

$Q_{\mathrm{NH}}$ – the normal mode coordinate for the phenylalanine/alanine NH stretch

$Q_{\mathrm{l}}$ – the normal mode coordinate for low frequency vibration

$\omega_{NH}$ – the frequency of the NH stretch vibration

$\omega_l$ –the frequency of the low frequency vibration

$\lambda$, $\lambda'$ – the coupling constants for the first order of the perturbation theory

$\beta$ – the coupling constant for the second order term of the perturbation theory

Using the same principle as in the Born-Oppenheimer approximation that $\omega_{NH}>>\omega_l$ and first treating $Q_l$ as a fixed parameter, we can write the Hamiltonian for the NH stretch

$$H_{NH} = \frac{p_{NH}^2}{2} + \frac{\omega_{NH}^2}{2} Q_{NH}^2 + \lambda {Q_{NH}}^2 Q_l + \lambda' {Q_l}^2 Q_{NH} + \beta {Q_{NH}}^2 {Q_l}^2$$

Through first and second order in $Q_l$ the frequency of the associated vibration will be

$$H_{NH} = \frac{p_{NH}^2}{2} + \frac{{\omega'_{NH}}^2}{2} Q_{NH}^2 + \lambda' {Q_l}^2 Q_{NH}$$

$$\omega'_{NH} = \omega_{NH} + \frac{\lambda Q_l + \beta {Q_l}^2}{\omega_{NH}}$$

The term $\lambda' {Q_l}^2 Q_{NH}$ results in the shift of the potential, but it does not affect the frequency, as can be seen from the formula below

$$H_{NH} = \frac{p_{NH}^2}{2} + \frac{{\omega'_{NH}}^2}{2} Q_{NH}^2 + \lambda' {Q_l}^2 Q_{NH} = \frac{p_{NH}^2}{2} + \frac{{\omega'_{NH}}^2}{2} Q_{NH}^2 + \lambda' {Q_l}^2 Q_{NH} + \frac{\lambda'^2 {Q_l}^4}{2{\omega'_{NH}}^2} - \frac{\lambda'^2 {Q_l}^4}{2{\omega'_{NH}}^2}$$

$$= \frac{p_{NH}^2}{2} + \frac{{\omega'_{NH}}^2}{2}\left(Q_{NH} + \frac{\lambda' {Q_l}^2}{{\omega'_{NH}}^2}\right)^2 - \frac{\lambda'^2 {Q_l}^4}{2{\omega'_{NH}}^2}$$

In this approximation the energy of the system will be

$$E_{NH}(n) = \hbar\omega'_{NH}(n+1) - \frac{\lambda'^2 {Q_l}^4}{2{\omega'_{NH}}^2}$$

and the energy for the excitation of one quantum of the NH stretch corrected by the zero-point energy will be

$$E_{NH}(1) = \hbar\omega'_{NH}$$

Then the Hamiltonian for the low frequency vibration can be written as following

$$H_l = \frac{p_l^2}{2} + \frac{\omega_l^2}{2} Q_l^2 + \hbar\omega'_{NH}$$

$$H_l = \frac{p_l^2}{2} + \frac{\omega_l^2}{2} Q_l^2 + \hbar\omega_{NH} + \frac{\hbar(\lambda Q_l + \beta {Q_l}^2)}{\omega_{NH}}$$

$$H_l = \frac{p_l^2}{2} + \frac{\omega_l'^2}{2}\left(Q_l + \frac{\hbar\lambda}{\omega_l'^2 \omega_{NH}}\right)^2 + \hbar\omega_{NH} - \frac{\hbar^2\lambda^2}{2\omega_l'^2 \omega_{NH}^2}$$

where in the first order approximation the frequency for the slow vibration is

$$\omega_l' = \omega_l + \frac{\hbar\beta}{\omega_l\omega_{NH}}$$

Apart from the frequency change, we get the displacement of the potential energy curve minimum relative to the ground state

$$d = \frac{\hbar\lambda}{\omega_l'^2\omega_{NH}}$$

The wave functions of the low frequency vibration upon excitation of one quantum of NH stretch vibration can be described as those of a harmonic oscillator with a different frequency $\omega_l'$. Now with the same assumptions that allow us to separate the coordinates for the NH stretch vibration and a low frequency vibration, we can derive the intensities of the spectroscopic transitions between different states. The probability of the spectroscopic transition between two states with zero quanta of NH stretch and 1 quantum of NH stretch is determined by the equation

$$P_{01} = \iint \psi_0(r,R)\mu(r,R)\psi_1^*(r,R)drdR$$

$\mu$ is the transition dipole moment

$\psi$ is a vibrational wavefunction in the first electronically excited state

The NH stretch vibration wave function depends on the coordinate of the low frequency vibration as a parameter, and the total vibrational wave function can be written as

$$\psi(r,R) = \varphi(r,R)\cdot\chi(R)$$

where $\varphi(r,R)$ is the vibrational wave function that depends on the coordinates of the NH vibration (r) and the coordinates of the low frequency vibration as a parameter (R), and $\chi(R)$ is the vibrational wave function that depends only on the coordinates for the low frequency vibration (R). We can also divide the dipole moment into a part that depends on the coordinates of the NH vibration $\mu_{NH}(r)$ and a part that depends on the coordinates of the low frequency vibration $\mu_l(R)$

$$\mu(r,R) = \sum_i q_i r_i + \sum_j q_j R_j = \mu_{NH}(r) + \mu_l(R)$$

Then the probability of 0-1 transition would be

$$P_{01} = \iint \varphi_0(r,R) \cdot \chi_0(R) \cdot \mu(r,R) \cdot \varphi_1^*(r,R) \cdot \chi_1^*(R) dr dR$$

$$= \left[ \iint [\varphi_0(r,R) \cdot \mu_{NH}(r) \cdot \varphi_1^*(r,R) dr] \cdot \chi_0(R) \cdot \chi_1^*(R) dR \right]$$

$$+ \left[ \iint [\varphi_0(r,R) \cdot \varphi_1^*(r,R) dr] \cdot \chi_0(R) \cdot \mu_l(R) \cdot \chi_1^*(R) dR \right]$$

The second term is zero, because the wave functions are orthogonal $\varphi_0(r,R) \cdot \varphi_1^*(r,R) dr = \delta_{01}$ and only the first term is responsible for the selection rules.

We can introduce the NH stretch vibrational transition moment that depends on the coordinate of the low frequency vibration R

$$\mu_{vib}(R) = \int \varphi_0(r,R) \cdot \mu_{NH}(r) \cdot \varphi_1^*(r,R) dr$$

In the adiabatic approximation, the dependence of the NH stretch vibrational transition moment on the parameter R is very weak, so that it can be replaced by an average value

$$\mu_{vib}(R) \simeq \mu_{vib}(\bar{R})$$

$$P_{01} \simeq \mu_{vib}(\bar{R}) \cdot \int \chi_0(R) \cdot \chi_1^*(R) dR$$

The intensity of the NH stretch combination bands would be thus determined by the overlap of the wave function of the low frequency vibration between the state with zero quanta in the NH stretch vibration and the one with one quantum in the NH stretch vibration. This is an analog of the Franck-Condon factor.

$$I_{01} \simeq \left(\mu_{vib}(\bar{R})\right)^2 \cdot \left( \int \chi_0(R) \cdot \chi_1^*(R) dR \right)^2$$

When there is no coupling between the high and low frequency vibrations, i.e. no shift of the potential energy for the low frequency vibration upon the excitation of the NH stretch, the overlap integral would be zero and no combinational bands would appear in the infrared spectrum.

### 4.3.5 We observe the combination bands in conformer A, but not in conformer B

In conformer A (Figure 4.7), the phenylalanine and alanine backbone NHs are positioned directly above the phenylalanine side-chain, pointing towards the center of the aromatic ring. Thus, excitation of one of these NH stretches perturbs the local environment of the chromophore. Unfortunately, the DFT calculations are not precise enough to predict the exact frequencies of the slow motions in the molecule. According to the DFT calculations the lowest frequency vibration in the ground state of conformer A is 15.9 $cm^{-1}$, and it is mainly due to the rotation of the phenylalanine side-chain around the $C_\alpha$-$C_\beta$ bond. If the low frequency vibration observed in the electronically excited state of conformer A (12.6 $cm^{-1}$) also involves this rotation, the excitation of phenylalanine/alanine NH stretch would definitely perturb the electron density around the chromophore and affect the frequency of this vibration. Interestingly, the excitation of the phenylalanine NH stretch increases the frequency (13.6 $cm^{-1}$), whereas the excitation of the alanine NH stretch decreases the frequency of the slow motion of the molecule (11.8 $cm^{-1}$). Probably, the excitation of phenylalanine NH stretch extends the first turn of the helix, weakening the hydrogen bonding between the lysine $NH_3^+$ group and carbonyls, facilitating the low frequency motion of the molecule. The excitation of the alanine NH stretch, on the other hand, might stiffen the helical turn by stronger hydrogen bonding, resulting in the red-shift of frequency of the slow vibration involving the phenyl ring.

However, there is no such a low frequency progression in the UV spectrum for the conformer B of AcFAK-$H^+$ (Figure 4.1), and we do not observe combination bands in the infrared spectrum. A very subtle change in conformation such as a small rotation of the phenylalanine aromatic ring changes the dipole interactions and breaks the coupling between the phenylalanine/alanine NH stretch vibration and the low frequency vibration in the molecule. Probably, a stronger phenylalanine NH – $\pi$ cloud interaction in conformer B inhibits the rotation of the aromatic ring that is responsible for the low frequency vibration observed in conformer A.

### 4.3.6 IR power saturation in the infrared spectrum of the electronically excited AcF*AK-$H^+$

At high infrared power in the vibrational spectrum of the electronically excited conformer A of AcF*AK-$H^+$ (Figure 4.12b) we observe depletion at the positions corresponding to the

transitions from the ground state of the same conformer (Figure 4.12a). Figure 4.12b-d depicts how the infrared spectrum of the electronically excited conformer A changes as the power of the IR OPO decreases. At low infrared power (Figure 4.12d) the depletion disappears and the infrared transitions become sharper. Usually, power broadening results only in the broadening of the spectroscopic bands, but not in dips in the spectrum. If upon the multiphoton infrared absorption in the $S_1$ state, the branching ratio between the dissociation *via* the $C_\alpha$-$C_\beta$ bond and other fragmentation channels changes, the dips in the infrared spectrum could appear, but at the wavenumbers corresponding to the infrared spectrum of the $S_1$ state, not the ground state. The dips also could not result from the time overlap between the UV and IR laser pulses, because we still observe them in the spectrum, recorded at high infrared power at the delay 20 ns between the IR OPO and the UV laser. While we can not explain this experimental effect, one has to be careful to properly adjust the power of the infrared laser when recording the spectra of the electronically excited states using UV-IR double resonance photofragment spectroscopy to avoid the confusion from appearing of multiple splitting bands.

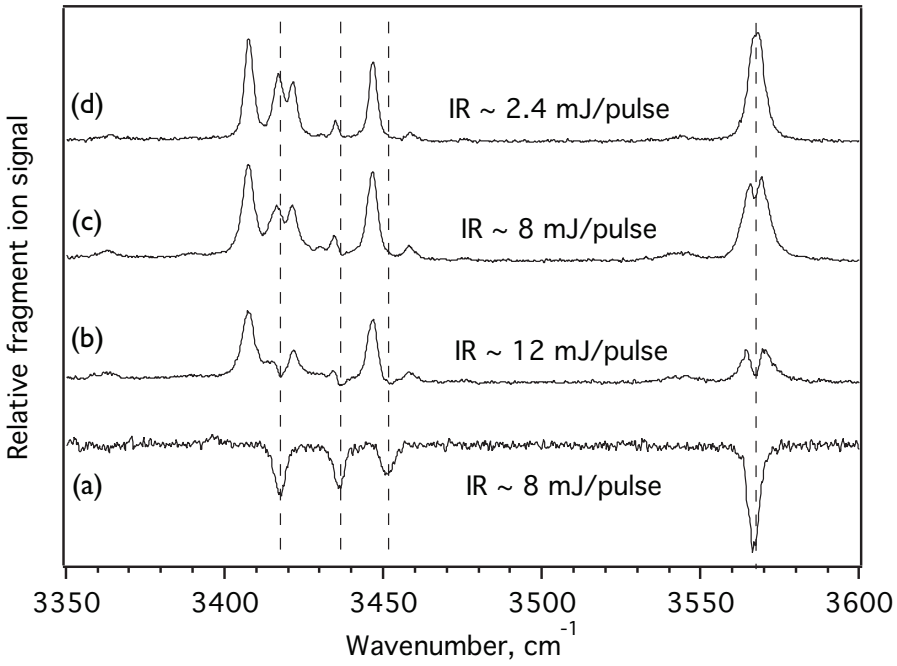


Figure 4.12. The infrared power saturation in the electronically excited state of AcF*AK-$H^+$ (F* N15 isotopically substituted F). The UV laser excites the band origin of conformer A. a. The ground state spectrum of conformer A recorded when the IR OPO probes the molecules 150 ns before the UV excitation. b-d. The $S_1$ state infrared spectrum of conformer A recorded using UV-IR double resonance photofragment technique at different infrared power. The IR OPO probes the molecules 5 ns after the UV excitation.

## 4.4 Conclusions

In this chapter we have presented conformer-specific ground and excited state infrared spectra of AcFAK-$H^+$. By performing IR-UV double resonance spectroscopy on different peaks in the electronic spectrum, we identified two major conformers A and B. DFT calculations revealed two stable structures that favor the hydrogen bond formation between the lysine ammonium and three carbonyls, forming a motif similar to the one that initiates a helix. Interestingly, all the structures with $NH_3^+ - \pi$ cloud type of interaction are higher in energy, and the calculated spectra for these structures do not match the experimental data. We also showed that the M052X/6-31G** level of theory takes better account of the dispersion interaction and better optimizes the geometry than the B3LYP/6-31G**. The two structures corresponding to conformer A and B are similar. The main and almost only difference is the rotation of the phenylalanine side-chain around the $C_\alpha$-$C_\beta$ bond. However, this slight conformational change results in a completely different behavior in the electronically excited state.

When the IR OPO probes the molecules ~5 ns after the UV excitation, we record conformer specific infrared spectra of the $S_1$ state by monitoring the gain in fragmentation (*via* the $C_\alpha$-$C_\beta$ bond rupture). In the $S_1$ state of conformer B, the phenylalanine NH shifts to the red relative to its position in the ground state spectrum. In the $S_1$ state of conformer A, both the phenylalanine and the alanine NH stretches experience the red-shift. The local character of the UV excitation dictates that the bands that shift are close to the chromophore. The infrared spectra of the electronically excited molecules thus pose additional constraints for our conformational search and greatly facilitate it. Moreover, by exciting with the UV laser different vibrational levels of the $S_1$ state in conformer A, we observe vibrational progressions in the infrared spectra that correspond to combination bands of phenylalanine/alanine NHs. The absorption of one quantum of the phenylalanine/alanine NH stretch vibration results in a geometrical change of conformer A along the coordinate for the low frequency vibration, involving the rotation of the chromophore side-chain. We model the distribution of the combination band intensities by constructing harmonic potentials for the low frequency vibration and optimizing the shifts and shapes of those potentials depending on which NH stretch is excited. The excitation of the phenylalanine NH stretch increases the frequency of the low frequency vibration, and the excitation of the alanine NH stretch decreases. We further theoretically describe the appearance of the combination bands by means of purely mechanical anharmonicity (with a quartic Taylor expansion for the potential energy surface).

A very slight change in conformation can result in the coupling of the vibrations and the appearance of the progressions of combination bands in the IR spectrum of the electronically excited state. This change is a slight rotation of the aromatic chromophore around the $C_\alpha$-$C_\beta$ bond. In conformer A the interaction of the aromatic ring with the phenylalanine/alanine NH is weak. However, in conformer B, the phenylalanine NH forms a stronger hydrogen bond with the $\pi$ cloud of the chromophore, which prohibits the low frequency motion observed in conformer A and breaks the coupling. Though the AcFAK-$H^+$ molecule is big, a simple adiabatic approximation describes the combination band intensities amazingly well. If one observes the progressions of the combination bands in the electronically excited state, they would most probably be local to the NH stretches in the closest proximity to the chromophore.

# References


1 S. Banik and M. D. Prasad, Theor. Chem. Acc. **131** (2012).

2 G. Herzberg, *Molecular spectra and molecular structure. II. Infrared and Raman spectra of polyatomic molecules* (Van Nostrand, 1939).

3 A. B. McCoy and E. L. Sibert, J. Chem. Phys. **95**, 3488 (1991).

4 J. R. Roscioli, E. G. Diken, M. A. Johnson, S. Horvath, and A. B. McCoy, J. Phys. Chem. A **110**, 4943 (2006).

5 S. Horvath, A. B. McCoy, B. M. Elliott, G. H. Weddle, J. R. Roscioli, and M. A. Johnson, J. Phys. Chem. A **114**, 1556 (2010).

6 A. B. McCoy, T. L. Guasco, C. M. Leavitt, S. G. Olesen, and M. A. Johnson, Phys. Chem. Chem. Phys. **14**, 7205 (2012).

7 M. L. Cowan, B. D. Bruner, N. Huse, J. R. Dwyer, B. Chugh, E. T. J. Nibbering, T. Elsaesser, and R. J. D. Miller, Nature **434**, 199 (2005).

8 S. Woutersen and H. J. Bakker, Nature **402**, 507 (1999).

9 K. Ishii, S. Takeuchi, and T. Tahara, J. Chem. Phys. **131** (2009).

10 T. Ebata, K. Nagao, and N. Mikami, Chem. Phys. **231**, 199 (1998).

11 W. H. Robertson, E. A. Price, J. M. Weber, J. W. Shin, G. H. Weddle, and M. A. Johnson, J. Phys. Chem. A **107**, 6527 (2003).

12 E. M. Myshakin, K. D. Jordan, E. L. Sibert, and M. A. Johnson, J. Chem. Phys. **119**, 10138 (2003).

13 A. Doi and N. Mikami, J. Chem. Phys. **129** (2008).

14 J. A. Stearns, S. Mercier, C. Seaiby, M. Guidi, O. V. Boyarkin, and T. R. Rizzo, J. Am. Chem. Soc. **129**, 11814 (2007).

15 J. A. Stearns, C. Seaiby, O. V. Boyarkin, and T. R. Rizzo, Phys. Chem. Chem. Phys. **11**, 125 (2009).

16 J. P. Gallivan and D. A. Dougherty, Proc. Natl. Acad. Sci. U.S.A. **96**, 9459 (1999).

17 D. A. Dougherty, Science **271**, 163 (1996).

18 J. A. Stearns, M. Guidi, O. V. Boyarkin, and T. R. Rizzo, J. Chem. Phys. **127** (2007).

19 J. M. Bakker, C. Plutzer, I. Hunig, T. Haber, I. Compagnon, G. von Helden, G. Meijer, and K. Kleinermanns, ChemPhysChem **6**, 120 (2005).

20 T. A. Halgren, J. Comput. Chem. **20**, 730 (1999).

21 T. A. Halgren, J. Comput. Chem. **17**, 490 (1996).

[22] W. L. Jorgensen, D. S. Maxwell, and J. TiradoRives, J. Am. Chem. Soc. **118**, 11225 (1996).

[23] G. Kaminski, E. M. Duffy, T. Matsui, and W. L. Jorgensen, J. Phys. Chem. **98**, 13077 (1994).

[24] G. A. Kaminski, R. A. Friesner, J. Tirado-Rives, and W. L. Jorgensen, J. Phys. Chem. B **105**, 6474 (2001).

[25] M. J. Frisch, G. W. Trucks, H. B. Schlegel, G. E. Scuseria, M. A. Robb, J. R. Cheeseman, G. Scalmani, V. Barone, B. Mennucci, G. A. Petersson, H. Nakatsuji, M. Caricato, X. Li, H. P. Hratchian, A. F. Izmaylov, J. Bloino, G. Zheng, J. L. Sonnenberg, M. Hada, M. Ehara, K. Toyota, R. Fukuda, J. Hasegawa, M. Ishida, T. Nakajima, Y. Honda, O. Kitao, H. Nakai, T. Vreven, J. A. Montgomery, J. E. Peralta, F. Ogliaro, M. Bearpark, J. J. Heyd, E. Brothers, K. N. Kudin, V. N. Staroverov, R. Kobayashi, J. Normand, K. Raghavachari, A. Rendell, J. C. Burant, S. S. Iyengar, J. Tomasi, M. Cossi, N. Rega, J. M. Millam, M. Klene, J. E. Knox, J. B. Cross, V. Bakken, C. Adamo, J. Jaramillo, R. Gomperts, R. E. Stratmann, O. Yazyev, A. J. Austin, R. Cammi, C. Pomelli, J. W. Ochterski, R. L. Martin, K. Morokuma, V. G. Zakrzewski, G. A. Voth, P. Salvador, J. J. Dannenberg, S. Dapprich, A. D. Daniels, Farkas, J. B. Foresman, J. V. Ortiz, J. Cioslowski, and D. J. Fox, *Gaussian 09, Revision B.01* (Gaussian, Inc., Wallingford CT, 2009).

[26] Y. Zhao, N. E. Schultz, and D. G. Truhlar, J. Chem. Theory Comput. **2**, 364 (2006).

[27] C. T. Lee, W. T. Yang, and R. G. Parr, Phys. Rev. B **37**, 785 (1988).

[28] T. R. Rizzo, Y. D. Park, L. A. Peteanu, and D. H. Levy, J. Chem. Phys. **84**, 2534 (1986).

[29] T. R. Rizzo, Y. D. Park, and D. H. Levy, J. Chem. Phys. **85**, 6945 (1986).

[30] J. L. Chang, J. Mol. Spectrosc. **232**, 102 (2005).

[31] Mathematica, version 9.0, (Wolfram Research, Inc., Champaign, Illinois, 2012).

# Chapter 5

# IR-UV spectroscopy for the assessment of the amide I spectroscopic maps

This chapter describes the application of cold ion spectroscopy to test the accuracy of the DFT calculations and to access amide I spectroscopic maps. We will present infrared spectra in the amide I and II spectroscopic region for a single conformation of the helical peptide $AcFA_5K\text{-}H^+$ and its singly and doubly $^{13}C$-labeled variants. Single $^{13}C$ labeling reduces the amide I frequency by ~40 $cm^{-1}$ and permits decoupling labeled and unlabeled amide chromophores for better characterization of individual frequencies. Double $^{13}C$ labeling decouples the pair of labeled amides from others and permits the characterization of the coupling within this pair. First we will compare the infrared spectra to the DFT calculations at the B3LYP/6-31G** level of theory and then use the results of the DFT calculations to assess the spectroscopic maps developed by the Skinner group for the deuterated and $^{13}C^{18}O$ labeled peptides. We find these maps to be accurate to within a few $cm^{-1}$ for both frequencies and couplings with larger errors only for the terminal amides. Joshua Carr and Santanu Roy from Prof. Skinner's group performed all the calculations presented in this chapter.

Note that in this chapter we use the word "chromophore" referring to C=O group that acts as an infrared absorber. In the previous chapters we referred to UV chromophores, such as phenylalanine or tyrosine.

## 5.1 Introduction

The amide I spectroscopic region (C=O stretching vibrations) is widely used to determine protein structure and dynamics in solution and in lipid environments.[1-4] The amide I mode is highly sensitive to the secondary structure of the proteins, such as α-helices and β-sheets. Proteins in an α-helical conformation typically give rise to the amide I band in the range 1650-

1658 $cm^{-1}$,[5, 6] and two bands around 1633 $cm^{-1}$ and 1677 $cm^{-1}$ are usually attributed to β-sheet formation.[7] With the advances in 2D-IR spectroscopy, the dynamics of peptides in their native environment can be probed with picosecond resolution through the time and conformational dependence of the amide I couplings.[8, 9] However, the interpretation of the experimental infrared spectra is challenging and requires the development of suitable theoretical methods.

At room temperature the line shape of the amide I band usually contains multiple contributions from different conformers with diverse C=O stretch frequencies influenced by intramolecular couplings. These conformers interconvert on a variety of timescales and they also interact with the solvent molecules, resulting in a broad amide I band with a complex shape.

To decompose the shape of the amide I spectral line, several researchers proposed to employ so-called spectroscopic "maps" that use parameterized force fields in classical molecular dynamics to predict the frequency shifts, amide I transition dipoles, and vibrational couplings as a function of the peptide geometry.[10-19] The main advantage of the spectroscopic maps over electronic-structure calculations[20-26] is their much lower computational cost that allows the simulation of spectra for hundreds of chromophores over hundreds of nanoseconds. The methods based on classical force fields can be applied to much larger systems and allow the incorporation of dynamical effects.

The spectroscopic maps that we would like to evaluate are those developed and implemented by the Skinner group.[15, 27-29] These maps were parameterized to reproduce the experimental amide I line shape of a model peptide N-methylacetamide (NMAD) in $D_2O$, dimethylsulfoxide (DMSO), and chloroform. To do so, first a molecular dynamics simulation is performed, and then the infrared spectrum is calculated for each of the conformations using parameterized maps. The experiment and theory rarely agree perfectly, and it is unclear in which of these steps the errors arise: are they mainly due to erroneous generation of conformers in molecular dynamics (MD) simulation or inaccuracies of the spectroscopic maps themselves? To assess the spectroscopic maps independently of the MD simulation, we decided to examine a single conformer of a model peptide $AcFA_5K\text{-}H^+$, the amide I spectrum of which we record using IR-UV double resonance spectroscopy. This approach was inspired by the work of Buchanan et al., in which the authors use gas phase infrared spectra to determine local mode frequencies and inter-mode couplings.[30, 31]

The spectroscopic maps use several parameters to describe the local-mode frequencies and the couplings between different amides. We can address the question of the local-mode frequencies

by recording amide I spectra for $^{13}C$ singly isotopic labeled isotopomers of $AcFA_5K\text{-}H^+$. The $^{13}C$ isotopic labeling reduces the frequency of the labeled amide chromophore by ~40 $cm^{-1}$, which diminishes the effect of coupling between labeled and unlabeled amides and allows its better frequency characterization.[32-35] We also record the infrared spectra of $^{13}C$ double isotopically labeled isotopomers of $AcFA_5K\text{-}H^+$ to evaluate the coupling within different pairs of amides. In this case, the labeled pair is decoupled from the other modes, and we deduce the coupling by comparing the spectroscopic shifts to the results for single labels.

It would have been desirable to compare the results from the spectroscopic maps directly to the experiment, but those maps were parameterized for deuterated peptides (because most of NMR experiments are performed in $D_2O$) and $^{13}C^{18}O$ isotopic labels (for even better decoupling of the labeled and unlabeled amides). Moreover, we did not test all possible combinations of $^{13}C$ labels experimentally.

The structure of the conformer for which we recorded the amide I spectra was previously assigned by comparing NH stretch experimental spectra with the calculated using DFT at B3LYP/6-31G** level of theory.[36] Joshua Carr and Santanu Roy performed DFT calculation in the amide I region and observed an excellent agreement with the experiment, which allowed us to compare the results from the spectroscopic maps to those from the DFT calculations performed for deuterated peptide and its $^{13}C^{18}O$ singly and doubly labeled isotopomers. This method allows to characterize the reliability of the spectroscopic maps in a more direct manner than has been achieved previously.[29]

# 5.2 Methods

## 5.2.1 Experimental details

The $AcFA_5K$ peptides were synthesized using solid phase Fmoc chemistry on an Applied Biosystems 433A synthesizer and purified by high-performance liquid chromatography. For the synthesis of the singly and doubly isotopically labeled samples, we used carbon-13 substituted L-alanine of 99% isotopic purity (CortecNet).

First, we measure an electronic spectrum of the cold, protonated peptide ions by recording the photofragment ion signal as a function of the UV laser wavelength. Since isotopic labeling doesn't change the electronic properties of the chromophore, electronic spectra for the unlabeled,

singly and doubly $^{13}$C-labeled $AcFA_5K\text{-}H^+$ appear identical to that reported previously for unlabeled $AcFA_5K\text{-}H^+$ (Figure 3.1).[37] Secondly, we record ground state conformer-specific vibrational spectra of the cold ions using IR-UV double resonance spectroscopy, schematically depicted in Figure 2.6. In this chapter we mainly focus on the infrared spectra of the ground state molecules in the amide I and amide II spectral region.

## 5.2.2 Previous DFT calculations

Previously, Stearns et *al.* performed DFT calculations to determine the lowest energy conformations of $AcFA_5K\text{-}H^+$, which were validated using the infrared spectra of the cold ions in the NH-stretch region.[36] The initial conformational search was done in MacroModel[38] using the AMBER force field,[39] and the most favorable structures were further optimized in Gaussian 03[40] at the B3LYP/6-31**[41, 42] level of theory. The vibrational frequencies were calculated for the 21 most stable conformations and scaled by a factor of 0.952 for comparison to the NH stretch band frequencies. (Note that this factor is different from the one used below for comparison of amide I frequencies.)

The structure assigned to conformer B of $AcFA_5K\text{-}H^+$ is a helix with the $C_{10}$-$C_{10}$-$C_{10}$-$C_{13}$ hydrogen-bonding pattern and *g*- orientation of the phenylalanine side-chain.[36] This conformer gives the highest photofragmetnation signal in the UV spectrum, and that is why we chose it for our studies. Figure 5.1 depicts the structure of conformer B with the labels showing seven amide chromophores.

## 5.2.3 DFT calculation of amide I IR spectra

Joshua Carr and Santanu Roy from Skinner's group performed the DFT calculations of the relevant conformer of $AcFA_5K\text{-}H^+$ in Gaussian 09.[43] Both the minimum energy geometry optimization and the harmonic frequencies analysis were performed at the B3LYP/6-31G** level of theory for the following isotope conditions:

- Unlabeled (with $^1$H, $^{12}$C, and $^{16}$O)
- Single and double $^{13}$C-labeled at the experimental positions
- D-labeled at all amide groups and the lysine amine group, and both unlabeled and $^{13}C^{18}O$-labeled at the backbone amide groups for all single and double labels.

They used the first two isotopic conditions to compare the DFT results with the experiment. The DFT calculations for the last isotopic conditions served for the direct comparison with the

results from the spectroscopic maps. The details of these theoretical methods can be found elsewhere and won't be discussed in this chapter.[44] Typically all the harmonic frequencies from the DFT calculations are too high and require proper scale factors that differ for different levels of theory.[45] The scale factor used in this work is 0.970751. It was chosen in such a way that the wavenumber of the strongest theoretical peak of the unlabeled peptide (labeled "3" in Figure 5.2) matches that of the strongest peak in the experimental spectrum.

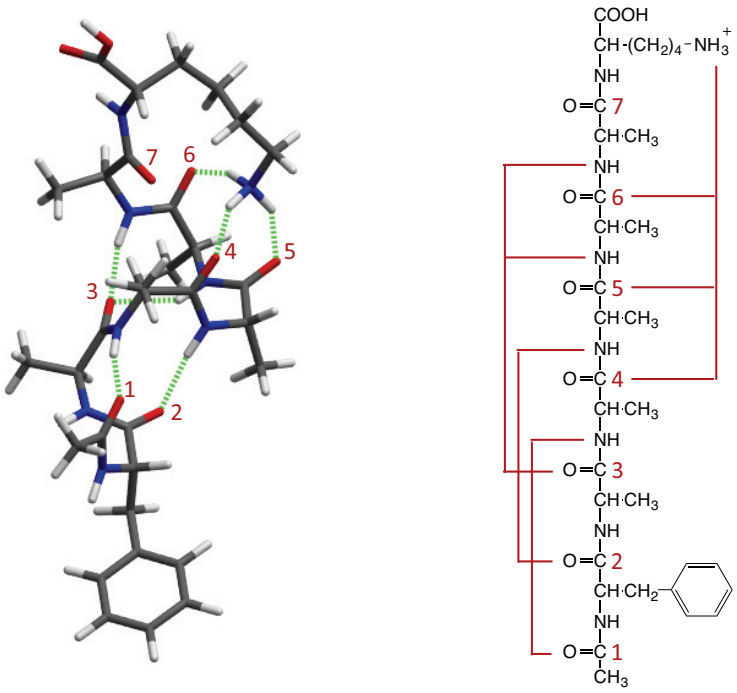


Figure 5.1 (Left) Conformer B of $AcFA_5K\text{-}H^+$ studied in this chapter with the labels showing seven amide chromophores. (Right) Diagram of the molecular structure, with the red lines showing hydrogen bonds between amide and amine chromophores.

## 5.3 Infrared spectrum of unlabeled $AcFA_5K\text{-}H^+$

The spectrum in the amide I and amide II spectral regions for four unlabeled conformers of $AcFA_5K\text{-}H^+$ was first recorded by Seaiby.[46] We repeated the experiment for conformer B of $AcFA_5K\text{-}H^+$ and compared the experimental infrared spectrum with the DFT calculated (Figure 5.2). The DFT and experimental results agree very well: frequencies are accurate within 1 $cm^{-1}$ and the intensities reasonably reproduce the experimental values. Very low intensity line "R", appearing in the calculated spectrum at 1611 $cm^{-1}$, corresponds to phenyl ring-breathing mode.

Line "B", appearing at 1638 $cm^{-1}$, corresponds to a bending mode of the lysine $NH_3^+$. The spectroscopic bands below 1600 $cm^{-1}$ are due to different amide bending modes and a band appearing in the experimental infrared spectrum at 1789 $cm^{-1}$ is the carboxylic acid amide I mode. The other lines are from amide I modes that are labeled 1-7 according to the local mode (see labels in Figure 5.1) that mainly contributes to the normal mode.

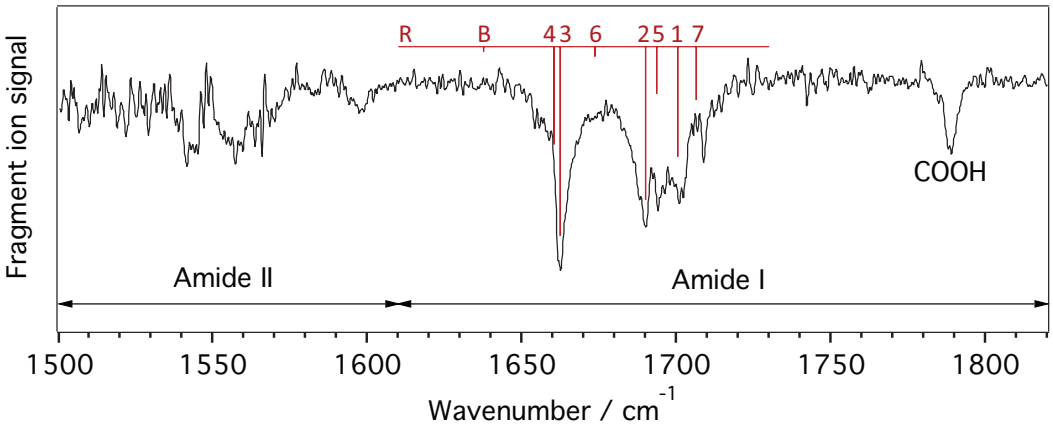


Figure 5.2 Experimental (black) and DFT (red) spectra for unlabeled conformer B of $AcFA_5K\text{-}H^+$. DFT lines are labeled according to the dominant contributor to the mode. The labels 1-7 correspond to the amide I chromophores, labeled as in Figure 5.1. "B" indicates a lysine ammonia bending mode, "R" indicates a phenyl ring-breathing mode, COOH indicates carboxylic acid amide I mode.

## 5.4 Infrared spectra of singly and doubly $^{13}C$-labeled $AcFA_5K\text{-}H^+$

In the conformer B of the helical molecule $AcFA_5K\text{-}H^+$ amides form a strong hydrogen bonding network that makes the helix an ideal candidate for the study of the coupling strength between different amide I modes. In Figure 5.3 we present DFT and experimental infrared spectra for conformer B with single $^{13}C$ labels at different amide I positions, specified with numbers in Figure 5.1.

For a harmonic oscillator the frequency of the vibration (w) is described as follows:

$$\omega = \frac{1}{2\pi}\sqrt{\frac{k}{\mu}} \tag{5.1}$$

where k is the force constant and μ is the reduced mass. The reduced mass changes upon isotopic substitution that results in a frequency change

$$\omega_2 = \omega_1 \cdot \sqrt{\frac{\mu_1}{\mu_2}} \tag{5.2}$$

$\omega_1$- the frequency of $^{12}C=^{16}O$ vibration, $\omega_2$- the frequency of $^{13}C=^{16}O$ vibration, $\mu_1$- the reduced mass for $^{12}C=^{16}O$ vibration (6.857), $\mu_2$- the reduced mass for $^{13}C=^{16}O$ vibration (7.1724)

$$\omega_2 = \omega_1 \cdot 0.9777 \tag{5.3}$$

If the amide I local modes were uncoupled from the other amide I modes, we would expect only the labeled mode to shift (for example, a band at 1700 $cm^{-1}$ should shift ~ 38 $cm^{-1}$ to the red). However, because of the coupling between different local modes, we observe several shifts corresponding to the other chromophores. With the single $^{13}C$ label, an amide I local mode isolates at least partially from the rest of the amide I modes, allowing the DFT to treat it as an isolated chromophore and to reproduce the changes in the frequencies of the other amide I local modes upon shifting this frequency.[47-49] In general, the DFT calculated frequencies well reproduce the experimental spectra presented in Figure 5.3. We observe the greatest errors for the lysine $NH_3^+$ bending mode and the $^{13}C$ labeled mode 6, which is strongly coupled to the bend. This is not surprising, since the anharmonicity of the NH bending modes and amide I modes is not the same and the use of a single scale factor does not account for this difference.[45]

In Figure 5.4 we compare DFT and experimental infrared spectra for conformer B of $AcFA_5K\text{-}H^+$ with double $^{13}C$ labels at different amide I positions, specified with numbers in Figure 5.1. The C=O at the position 3 forms a strong hydrogen bond with the NHs of amide 5 and 6, resulting in a red shift of this C=O (Figure 5.2). Also amide I chromophores 5 and 6 interact with each other and with the lysine $NH_3^+$ group. As we mention in the introduction for this chapter, the double labels allow one to a good extent to isolate a pair of the labeled amides from the other amide modes and to study the coupling within this pair.[29, 48, 50] The double $^{13}C$ labels at positions 5 and 6 allow us to determine the nearest-neighbor coupling and the double $^{13}C$ labels at positions 3 and 5, and 3 and 6 let us to determine non-nearest neighbor (transition-dipole) couplings. The agreement between the DFT results and the experiment is again very good, with slight errors observed for the predictions of frequencies for local modes 5 and 6, which couple to the bend, and the bending mode itself. By looking at the Figure 5.2, Figure 5.3, and Figure 5.4, we can conclude that DFT calculations at the B3LYP/6-31G** level of theory accurately describe the system we study and can be used to evaluate the spectroscopic maps.

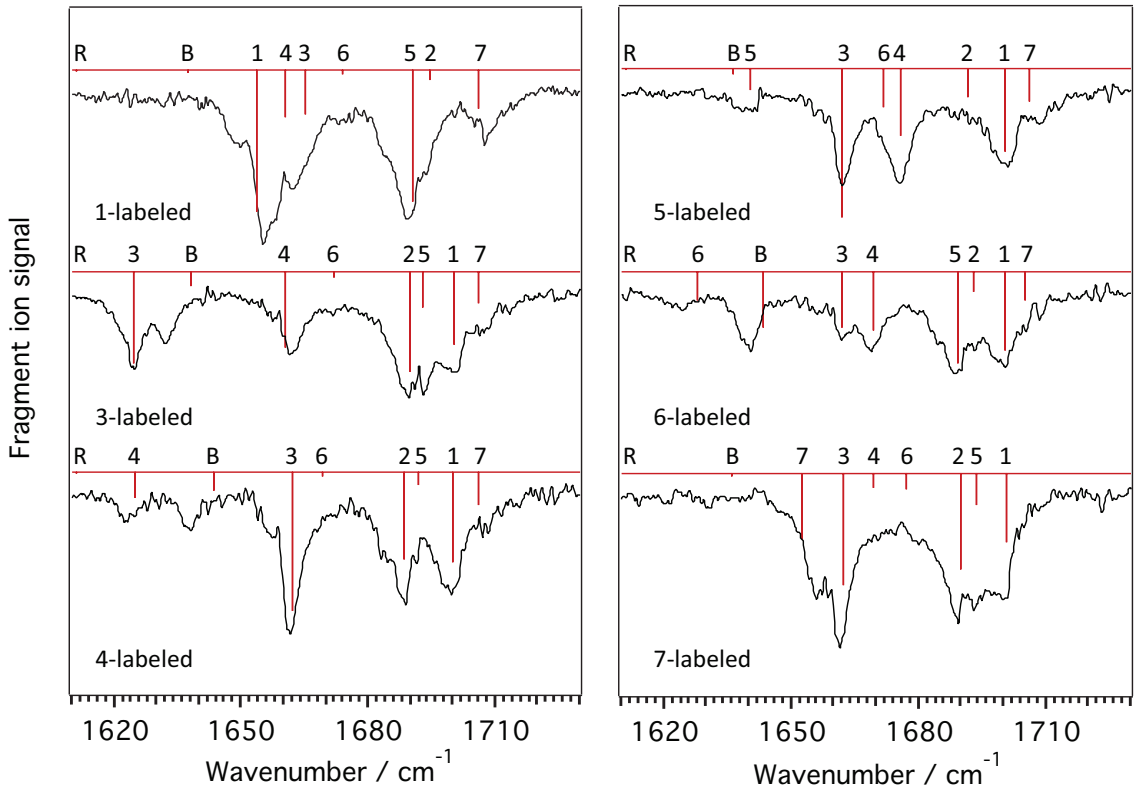


Figure 5.3 Experimental (black) and DFT (red) spectra for singly $^{13}$C-labeled conformer B of $AcFA_5K$-$H^+$. DFT lines are labeled according to the dominant contributor to the mode. The labels 1-7 correspond to the $^{13}$C-labeled amide I modes (numbered as in Figure 5.1). "B" indicates a lysine ammonia bending mode, "R" indicates a phenyl ring-breathing mode.

## 5.5 Assessment of the spectroscopic maps

The DFT calculations for the unlabeled, singly and doubly $^{13}$C-labeled peptides agree very well with the experiment. This allows us to use a similar DFT method on deuterated and $^{13}C^{18}O$-labeled peptides, the conditions for which the spectroscopic maps are developed, and compare the results to the ingredients of the spectroscopic maps. The Hamiltonian for the amide I vibrations has diagonal elements (the local-mode frequencies) and off-diagonal elements (the couplings between pairs of local modes). These matrix elements constitute the ingredients of the maps that Joshua Carr and Santanu Roy from Skinner's group evaluated using various methods.[15]

Table 5.1 compares the frequencies for $^{13}C^{18}O$-labeled and deuterated (at backbone amides and lysine amine) conformer B of $AcFA_5K$-$H^+$, calculated using DFT at the B3LYP/6-31G**

level of theory and the spectroscopic maps. The mean unsigned error is 3.5 $cm^{-1}$, and the mean signed error is -1.8 $cm^{-1}$. The frequencies of the terminal chromophores 1 and 7 (labeled as in Figure 5.1) result in the greatest errors, and if they are excluded, the mean unsigned error is 1.8 $cm^{-1}$, and the mean signed error is 0.6 $cm^{-1}$. Taking into the account the 35 $cm^{-1}$ frequency variation among different amide I modes, these errors are relatively small. However, the fact that the terminal residues frequencies are described less well, suggests that they ought to be parameterized separately.

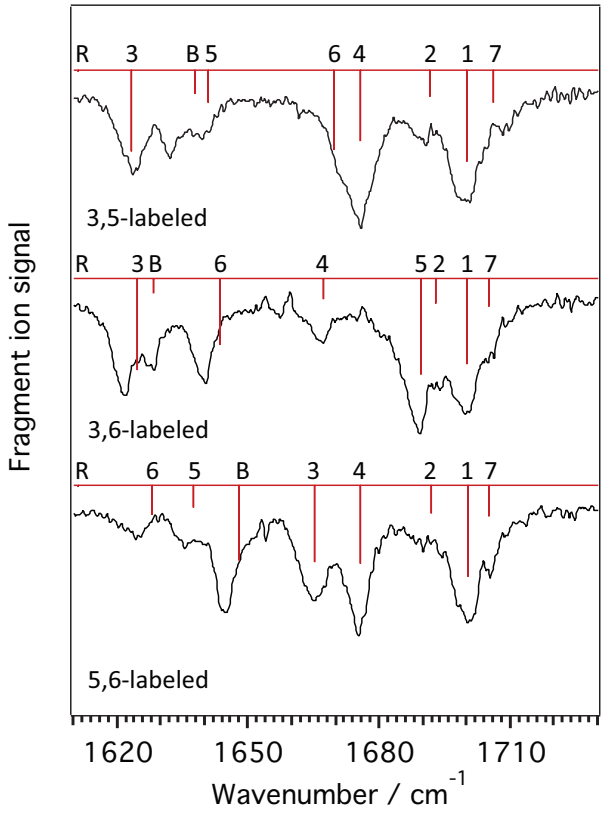


Figure 5.4 Experimental (black) and DFT (red) spectra for doubly $^{13}C$-labeled conformer B of $AcFA_5K$-$H^+$. DFT lines are labeled according to the dominant contributor to the mode. The labels 1-7 correspond to the $^{13}C$-labeled amide I modes (numbered as in Figure 5.1). "B" indicates a lysine ammonia bending mode, "R" indicates a phenyl ring-breathing mode.

In table 5.2 we present the couplings between the nearest neighbor chromophores. The map values come from the nearest-neighbor coupling map.[51] The mean unsigned error is 1.7 $cm^{-1}$ and the mean signed error is -0.4 $cm^{-1}$.

In table 5.3 we show the couplings for all other chromophore pairs (non-nearest neighbor couplings). The map values are calculated using a transition-dipole scheme developed earlier by Torii and Tasumi.[52] The mean unsigned error is 0.9 $cm^{-1}$, and the mean signed error is -0.4 $cm^{-1}$.

| Labeled chromophore | DFT frequency ($cm^{-1}$) | Map frequency ($cm^{-1}$) |
|---|---|---|
| 1 | 1618.1 | 1607.2 |
| 2 | 1615.1 | 1612.8 |
| 3 | 1589.0 | 1591.2 |
| 4 | 1590.4 | 1593.9 |
| 5 | 1601.2 | 1601.5 |
| 6 | 1586.5 | 1585.7 |
| 7 | 1621.4 | 1616.7 |

Table 5.1 Comparison of $^{13}C^{18}O$-labeled frequencies between DFT (B3LYP/6-31G**) and the spectroscopic map. The chromophores are labeled as in Figure 5.1.

| Labeled chromophore | DFT coupling ($cm^{-1}$) | Map coupling ($cm^{-1}$) |
|---|---|---|
| 1,2 | 1.3 | 2.5 |
| 2,3 | 0.0 | 0.9 |
| 3,4 | 0.9 | -1.0 |
| 4,5 | 5.9 | 4.2 |
| 5,6 | 6.2 | 7.9 |
| 6,7 | 7.3 | 4.5 |

Table 5.2 Comparison of nearest-neighbor couplings between DFT (B3LYP/6-31G**) and the spectroscopic map. The chromophores are labeled as in Figure 5.1.

## 5.6 Conclusions

Cold ion spectroscopy with $^{13}C$ single and double isotopic labeling have proved to be a useful tool in assessing the newly developed spectroscopic maps. This method also permits to determine the coupling strength between different amide chromophores in biological molecules. The DFT calculations performed by the Skinner group very well reproduce the couplings between different amide I modes and can be used to compare directly with the calculations from the spectroscopic maps. This comparison results in an accuracy of the spectroscopic maps within a few $cm^{-1}$ for both the frequencies and the couplings.

The frequency map works better for the chromophores in the middle of the chain than for the terminal chromophores 1 and 7 (labeled as in Figure 5.1). This can be due to a cancellation of

errors between the N-side and C-side nearest neighbor frequency shifts. It is probably worth parameterizing the terminal residues separately to improve the performance of the spectroscopic maps. The couplings, however, are very well described with the existing parameterization, especially when using the transition dipole scheme (for the non-nearest-neighbors couplings).

| Labeled chromophores | DFT coupling ($cm^{-1}$) | Map coupling ($cm^{-1}$) |
|---|---|---|
| 1,3 | -5.3 | -4.6 |
| 1,4 | -0.5 | -2.7 |
| 1,5 | -0.5 | -0.8 |
| 1,6 | -1.2 | -0.4 |
| 1,7 | 1.2 | 1.0 |
| 2,4 | -4.3 | -3.9 |
| 2,5 | 0.0 | -2.6 |
| 2,6 | 0.9 | -0.5 |
| 2,7 | -0.9 | 0.5 |
| 3,5 | -3.5 | -3.2 |
| 3,6 | -5.3 | -6.4 |
| 3,7 | 1.9 | 0.0 |
| 4,6 | 2.7 | 2.8 |
| 4,5 | 5.0 | 5.6 |
| 5,7 | -1.4 | -1.3 |

Table 5.3 Comparison of non-nearest neighbor (transition-dipole) couplings between DFT (B3LYP/6-31G**) and the spectroscopic map. The chromophores are labeled as in Figure 5.1.

# 5.7 Additional effects of the $^{13}C$ labeling in the experimental infrared spectrum of $AcFA_5K\text{-}H^+$

## 5.7.1 Amide II region for the structure elucidation

In addition to amide I bands, the amide II region, which is a combination of CN stretch and NH bend vibrations, has proved to be useful for distinction between α-helical and $3_{10}$-helical structures[53] using vibrational circular dichroism. In the case of linear infrared spectroscopy, the amide II region is usually not very informative for structure determinations. However, one can see that upon $^{13}C$ isotopic substitution at positions 4, 5, and 6 (Figure 5.1) the spectroscopic band that was at 1542 $cm^{-1}$ in the spectrum for the unlabeled peptide shifts ~4 $cm^{-1}$ to the red and appears at 1538 $cm^{-1}$ (Figure 5.5). Most probably this band corresponds to the lysine $NH_3^+$

bending mode. Amide I chromophores 4, 5, and 6 form hydrogen bonds with the lysine $NH_3^+$ and are coupled to it. The amide II spectroscopic region can be thus useful to determine which amide chromophores interact with the charged lysine or arginine side chains or charged N-terminus.

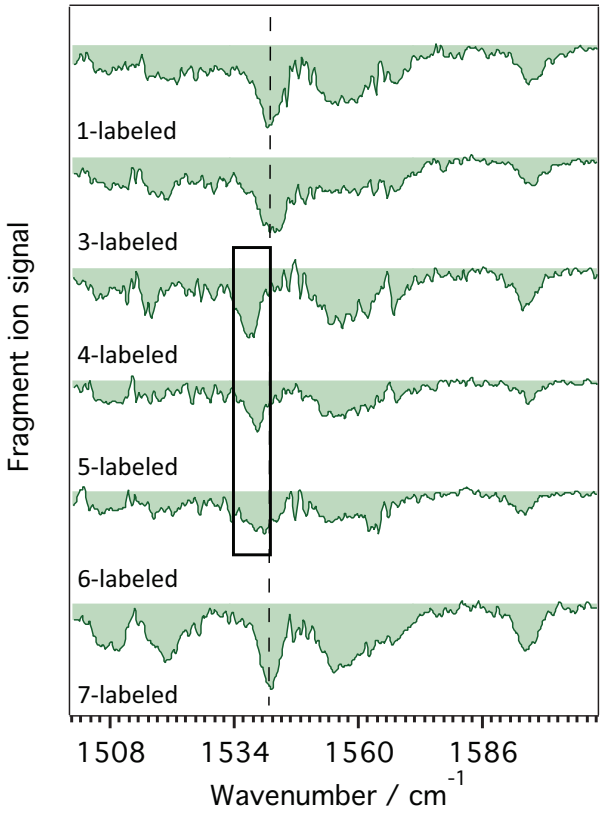


Figure 5.5 Experimental infrared spectra in amide II spectral region for singly $^{13}$C-labeled conformer B of $AcFA_5K\text{-}H^+$. The labels 1-7 correspond to the $^{13}$C-labeled amide I modes (numbered as in Figure 5.1).

## 5.7.2 Effect of $^{13}$C isotopic labeling on the NH frequency

In the Section 5.4 we discussed how the $^{13}$C isotopic labeling on different amide I modes affects the lysine $NH_3^+$ bending mode. It would have been even more desirable to link different amide I chromophores with the NHs to which they form hydrogen bonds. We decided to check the effect of $^{13}$C isotopic substitution on the NH stretch frequency. The C=O of the acetyl group (labeled as "1" in Figure 5.1) forms a hydrogen bond with the NH of the first alanine ($Ala^3$). Also this C=O is a part of the amide group with the NH of phenylalanine ($Phe^1$), which shifts to the red upon the electronic excitation. To check simultaneously if the $^{13}$C isotopic labeling changes the response of the phenylalanine NH stretch ($Phe^1$) to the electronic excitation of the

phenylalanine aromatic ring and the frequency of the NH stretch vibration it is hydrogen bonded to, we decided to record the spectrum of the electronically excited conformer B $^{13}$C-labeled at position 1 (labeled as in Figure 5.1). The results are presented in Figure 5.6.

We observed no frequency shift of the NH stretch vibrations upon $^{13}$C isotope substitution at the amide I of the acetyl. Neither Ala$^3$ nor Phe$^1$ changed in frequency, which means that we cannot use $^{13}$C isotope labeling to link hydrogen bonded amide groups.

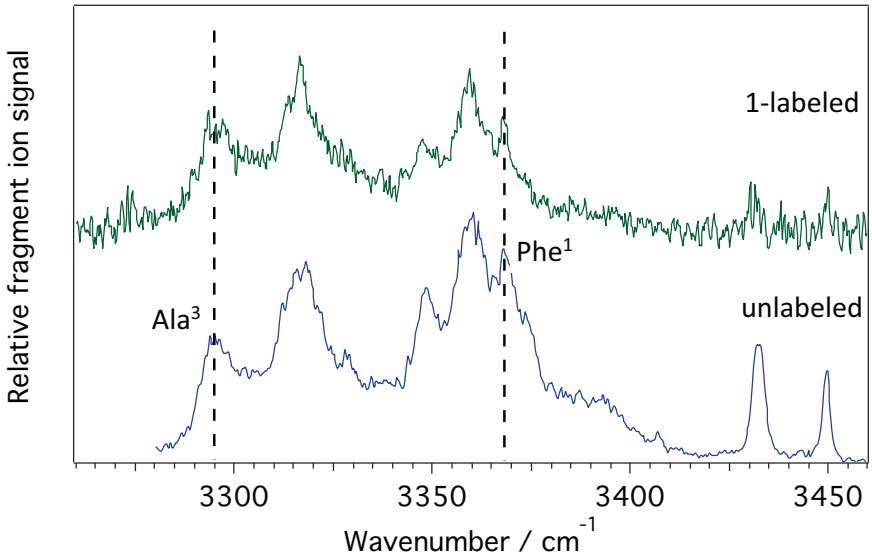


Figure 5.6 The infrared spectrum of the electronically excited conformer B of $AcFA_5K\text{-}H^+$, unlabeled (blue) and $^{13}$C-labeled at position 1 (green) (labeled as in Figure 5.1). The UV laser excites the band origin of conformer B (37555.3 cm$^{-1}$). The IR OPO probes the molecules 10 ns after the UV excitation. The infrared power is lower in the spectral region 3400-3460 cm$^{-1}$ in the 1-labeled spectrum than in the unlabeled.

# References


[1] A. Barth and C. Zscherp, Q. Rev. Biophys. **35**, 369 (2002).

[2] H. Torii and M. Tasumi, J. Chem. Phys. **96**, 3379 (1992).

[3] S. Krimm and J. Bandekar, Adv. Protein Chem. **38**, 181 (1986).

[4] M.-P. Gaigeot, Phys. Chem. Chem. Phys. **12**, 3336 (2010).

[5] P. I. Haris and D. Chapman, Trends Biochem. Sci. **17**, 328 (1992).

[6] W. K. Surewicz, H. H. Mantsch, and D. Chapman, Biochem. **32**, 389 (1993).

[7] D. Du, Y. Zhu, C.-Y. Huang, and F. Gai, Proc. Natl. Acad. Sci. U.S.A. **101**, 15915 (2004).

[8] S. Gnanakaran and R. M. Hochstrasser, J. Am. Chem. Soc. **123**, 12886 (2001).

[9] S. Woutersen and P. Hamm, J. Phys. Chem. B **104**, 11316 (2000).

[10] P. Bour and T. A. Keiderling, J. Chem. Phys. **119**, 11253 (2003).

[11] S. Ham, J. H. Kim, H. Lee, and M. H. Cho, J. Chem. Phys. **118**, 3491 (2003).

[12] J. R. Schmidt, S. A. Corcelli, and J. L. Skinner, J. Chem. Phys. **121**, 8887 (2004).

[13] T. L. Jansen and J. Knoester, J. Chem. Phys. **124** (2006).

[14] Y. S. Lin, J. M. Shorb, P. Mukherjee, M. T. Zanni, and J. L. Skinner, J. Phys. Chem. B **113**, 592 (2009).

[15] L. Wang, C. T. Middleton, M. T. Zanni, and J. L. Skinner, J. Phys. Chem. B **115**, 3713 (2011).

[16] M. Reppert and A. Tokmakoff, J. Chem. Phys. **138** (2013).

[17] K. C. Cai, T. T. Su, S. Lin, and R. H. Zheng, Spectrochim. Acta Part A **117**, 548 (2014).

[18] T. Hayashi, W. Zhuang, and S. Mukamel, J. Phys. Chem. A **109**, 9747 (2005).

[19] S. Roy, J. Lessing, G. Meisl, Z. Ganim, A. Tokmakoff, J. Knoester, and T. L. C. Jansen, J. Chem. Phys. **135** (2011).

[20] M. P. Gaigeot, R. Vuilleumier, M. Sprik, and D. Borgis, J. Chem. Theory Comput. **1**, 772 (2005).

[21] J. Jeon, S. Yang, J. H. Choi, and M. Cho, Accounts Chem. Res. **42**, 1280 (2009).

[22] R. Viswanathan and J. J. Dannenberg, J. Phys. Chem. B **112**, 5199 (2008).

[23] J. H. Choi and M. Cho, Chem. Phys. **361**, 168 (2009).

[24] I. Daidone, M. Aschi, L. Zanetti-Polzi, A. Di Nola, and A. Amadei, Chem. Phys. Lett. **488**, 213 (2010).

[25] W. R. W. Welch, J. Kubelka, and T. A. Keiderling, J. Phys. Chem. B **117**, 10343 (2013).

[26] S. Yang and M. Cho, J. Chem. Phys. **131** (2009).

[27] L. Wang, C. T. Middleton, S. Singh, A. S. Reddy, A. M. Woys, D. B. Strasfeld, P. Marek, D. P. Raleigh, J. J. de Pablo, M. T. Zanni, and J. L. Skinner, J. Am. Chem. Soc. **133**, 16062 (2011).

[28] L. Wang and J. L. Skinner, J. Phys. Chem. B **116**, 9627 (2012).

[29] A. M. Woys, A. M. Almeida, L. Wang, C. C. Chiu, M. McGovern, J. J. de Pablo, J. L. Skinner, S. H. Gellman, and M. T. Zanni, J. Am. Chem. Soc. **134**, 19118 (2012).

[30] E. G. Buchanan, W. H. James Iii, A. Gutberlet, J. C. Dean, L. Guo, S. H. Gellman, and T. S. Zwier, Faraday Discuss. **150**, 209 (2011).

[31] E. G. Buchanan, W. H. James, S. H. Choi, L. Guo, S. H. Gellman, C. W. Müller, and T. S. Zwier, J. Chem. Phys. **137** (2012).

[32] P. Bour and T. A. Keiderling, J. Phys. Chem. B **109**, 5348 (2005).

[33] R. Huang, V. Setnicka, M. A. Etienne, J. Kim, J. Kubelka, R. P. Hammer, and T. A. Keiderling, J. Am. Chem. Soc. **129**, 13592 (2007).

[34] S. D. Moran, A. M. Woys, L. E. Buchanan, E. Bixby, S. M. Decatur, and M. T. Zanni, Proc. Natl. Acad. Sci. U.S.A. **109**, 3329 (2012).

[35] S. D. Moran, S. M. Decatur, and M. T. Zanni, J. Am. Chem. Soc. **134**, 18410 (2012).

[36] J. A. Stearns, C. Seaiby, O. V. Boyarkin, and T. R. Rizzo, Phys. Chem. Chem. Phys. **11**, 125 (2009).

[37] J. A. Stearns, O. V. Boyarkin, and T. R. Rizzo, J. Am. Chem. Soc. **129**, 13820 (2007).

[38] MacroModel, version 9.1, (Schrödinger, LLC, New York, 2005).

[39] W. D. Cornell, P. Cieplak, C. I. Bayly, I. R. Gould, K. M. Merz, D. M. Ferguson, D. C. Spellmeyer, T. Fox, J. W. Caldwell, and P. A. Kollman, J. Am. Chem. Soc. **117**, 5179 (1995).

[40] M. J. Frisch, G. W. Trucks, H. B. Schlegel, G. E. Scuseria, M. A. Robb, J. R. Cheeseman, J. J. A. Montgomery, T. Vreven, K. N. Kudin, J. C. Burant, J. M. Millam, S. S. Iyengar, J. Tomasi, V. Barone, B. Mennucci, M. Cossi, G. Scalmani, N. Rega, G. A. Petersson, H. Nakatsuji, M. Hada, M. Ehara, K. Toyota, R. Fukuda, J. Hasegawa, M. Ishida, T. Nakajima, Y. Honda, O. Kitao, H. Nakai, M. Klene, X. Li, J. E. Knox, H. P. Hratchian, J. B. Cross, and C. A. V. Bakken, J. Jaramillo, R. Gomperts, R. E. Stratmann, O. Yazyev, A. J. Austin, R. Cammi, C. Pomelli, J. W. Ochterski, P. Y. Ayala, K. Morokuma, G. A. Voth, P. Salvador, J. J. Dannenberg, V. G. Zakrzewski, S. Dapprich, A. D. Daniels, M. C. Strain, O. Farkas, D. K. Malick, A. D. Rabuck, K. Raghavachari, J. B. Foresman, J. V. Ortiz, Q. Cui, A. G. Baboul, S. Clifford, J. Cioslowski, B. B.

Stefanov, G. Liu, A. Liashenko, P. Piskorz, I. Komaromi, R. L. Martin, D. J. Fox, T. Keith, M. A. Al-Laham, C. Y. Peng, A. Nanayakkara, M. Challacombe, P. M. W. Gill, B. Johnson, W. Chen, M. W. Wong, C. Gonzalez, and J. A. Pople, *Gaussian 03, Revision D.01* (Gaussian, Inc., Pittsburgh, PA, 2004).

[41] A. D. Becke, J. Chem. Phys. **98**, 5648 (1993).

[42] P. C. Hariharan and J. A. Pople, Theor. Chim. Acta **28**, 213 (1973).

[43] M. J. Frisch, G. W. Trucks, H. B. Schlegel, G. E. Scuseria, M. A. Robb, J. R. Cheeseman, G. Scalmani, V. Barone, B. Mennucci, G. A. Petersson, H. Nakatsuji, M. Caricato, X. Li, H. P. Hratchian, A. F. Izmaylov, J. Bloino, G. Zheng, J. L. Sonnenberg, M. Hada, M. Ehara, K. Toyota, R. Fukuda, J. Hasegawa, M. Ishida, T. Nakajima, Y. Honda, O. Kitao, H. Nakai, T. Vreven, J. A. Montgomery, J. E. Peralta, F. Ogliaro, M. Bearpark, J. J. Heyd, E. Brothers, K. N. Kudin, V. N. Staroverov, R. Kobayashi, J. Normand, K. Raghavachari, A. Rendell, J. C. Burant, S. S. Iyengar, J. Tomasi, M. Cossi, N. Rega, J. M. Millam, M. Klene, J. E. Knox, J. B. Cross, V. Bakken, C. Adamo, J. Jaramillo, R. Gomperts, R. E. Stratmann, O. Yazyev, A. J. Austin, R. Cammi, C. Pomelli, J. W. Ochterski, R. L. Martin, K. Morokuma, V. G. Zakrzewski, G. A. Voth, P. Salvador, J. J. Dannenberg, S. Dapprich, A. D. Daniels, Farkas, J. B. Foresman, J. V. Ortiz, J. Cioslowski, and D. J. Fox, *Gaussian 09, Revision B.01* (Gaussian, Inc., Wallingford CT, 2009).

[44] J. K. Carr, A. V. Zabuga, S. Roy, T. R. Rizzo, and J. L. Skinner, J. Chem. Phys. **140** (2014).

[45] Y. Bouteiller, J. C. Gillet, G. Gregoire, and J. P. Schermann, J. Phys. Chem. A **112**, 11656 (2008).

[46] C. Seaiby, Ph. D. thesis, EPFL, Lausanne, 2011.

[47] C. Fang and R. M. Hochstrasser, J. Phys. Chem. B **109**, 18652 (2005).

[48] J. Torres, A. Kukol, J. M. Goodman, and I. T. Arkin, Biopolymers **59**, 396 (2001).

[49] J. Torres, P. D. Adams, and I. T. Arkin, J. Mol. Biol. **300**, 677 (2000).

[50] C. Fang, J. Wang, A. K. Charnley, W. Barber-Armstrong, A. B. Smith, S. M. Decatur, and R. M. Hochstrasser, Chem. Phys. Lett. **382**, 586 (2003).

[51] T. l. C. Jansen, A. G. Dijkstra, T. M. Watson, J. D. Hirst, and J. Knoester, J. Chem. Phys. **125** (2006).

[52] H. Torii and M. Tasumi, J. Raman Spectrosc. **29**, 81 (1998).

[53] J. Kubelka, R. Silva, and T. A. Keiderling, J. Am. Chem. Soc. **124**, 5325 (2002).

# Chapter 6

# Conclusions and perspectives

When phenylalanine- or tyrosine-containing peptides absorb a UV photon, an electronically excited state is prepared. In this study, we address the question of what happens to this energy after UV absorption. It is known that once excitation occurs, a portion of the excited molecules will fragment if the energy is transferred to vibrational degrees of freedom through internal conversion.[1-3] In this case one might expect to observe cleavage of the weakest bonds in the molecule, which are typically backbone cleavages. However, by exciting the UV excited molecules further with an infrared laser, we observe that the dominant fragment results from side-chain loss due to the cleavage of the $C_\alpha$-$C_\beta$ bond, which cannot be explained by statistical fragmentation from the ground state.

We propose that prior to fragmentation some fraction of the UV-excited molecules undergoes intersystem crossing to the triplet state with a small barrier towards the dissociation along the $C_\alpha$-$C_\beta$ bond (similar to what Tseng et al. proposed for the dissociation of neutral phenylalanine[4]). To test the model, we employ a UV-IR double resonance spectroscopic technique that along with the vibrational cooling allows us to record conformer-selective infrared spectra of $S_1$ state for several protonated peptides. These infrared spectra indicate that initially, UV excitation perturbs only the oscillators local to the UV chromophore. These spectra also pose additional constraints on the structure of the lowest energy conformers and facilitate the conformational search using quantum mechanical calculations. By increasing the delay after the UV excitation, we monitor the energy flow within different vibrational modes in the molecule and how this yields almost the same infrared spectra for different initially excited conformers. The dynamical change in phenylalanine-containing peptides happens in ~80 ns and for tyrosine-containing molecule in ~7 ns, which is consistent with the singlet state lifetimes of their simplest chromophore analogs – toluene and phenol.[5, 6] At longer delays after the UV excitation we observe cooling of the species on the triplet surface that is evidenced by sharpening of the infrared spectra and the change of the number of photons required for dissociation. In a small phenylalanine-containing peptide we estimated the triplet state quantum yield to be ~50%, suggesting that triplet states might play an

important role in peptide deactivation. In the case of phenylalanine-containing peptides the triplet state lifetime is longer than the timescale of our experiments (>100 ms). However, the experiments were performed at extremely cold temperatures (10 K), which might result in a longer triplet state lifetime than under biological conditions at room temperature.

We also explore other fragmentation models proposed for small model peptides containing phenylalanine or tyrosine chromophores. Fast fragmentation (<20 ns) from the electronically excited state that involves proton transfer to C=O[7] or fragmentation after the formation of an open biradical,[8] both seem not to apply to the systems we study in this work. Infrared spectra in the amide I spectral region revealed the absence of proton transfer to any of the C=O groups, and experiments on molecules with the charge in closer proximity to the UV chromophore did not change considerably the dynamics we observe.

Additionally, we discovered an interesting phenomenon of coupling in the electronically excited state between fast and slow vibrations in AcFAK-$H^+$ molecule. This coupling, arising from mechanical anharmonicity, results in up to a six member vibrational progression in the infrared spectra of the electronically excited state. These couplings are conformer dependent. In the conformer where two NHs are located above the phenylalanine aromatic ring, their excitation alters the frequency of the ring rotation around the $C_\alpha$-$C_\beta$ bond, slowing it down or speeding it up. In the other conformer, the aromatic ring forms a stronger NH–$\pi$ hydrogen bond with one of the NHs, which partially hinders the rotation of the aromatic ring around the $C_\alpha$-$C_\beta$ bond and breaks the coupling.

Finally, we combine IR-UV double resonance spectroscopy with the $^{13}C$ isotopic labeling and DFT calculations to assess spectroscopic maps, which are used to model protein's conformations in solution. Our experimental ground state infrared spectra allow one to evaluate the coupling between different amide groups and to assess the quality of the spectroscopic maps independently from the molecular dynamics simulations.

The results of the current work have several important implications. First, we observe that significant electronically excited state population goes to the triplet state. Triplet states are reactive unless they are efficiently quenched. It suggests that phenylalanine- and tyrosine-containing peptides are not intrinsically photostable, but their photostability in the living cells is driven by successful deactivation of the triplet species, for example, through the energy transfer to other chromophores or through oxygen quenching. Because the $C_\alpha$-$C_\beta$ bond seems to be particularly weakened in the triplet state of aromatic chromophores, the application of infrared laser-assisted photofragment spectroscopy (IRLAPS) to increase the fragmentation yield[9] should

work for phenylalanine- or tyrosine-containing molecules of much larger size than if the fragmentation process proceeded mainly *via* internal conversion to the ground state. The recent application of the IRLAPS technique to a protein as large as ubiquitin seems to support our findings.[10]

The results obtained in this thesis suggest several new avenues of research. The fact that we observe specific fragmentation from the triplet state opens new ways to study dynamics in the gas phase by monitoring triplet-triplet or singlet-singlet energy transfer using native chromophores. Singlet-singlet Forster energy transfer is mediated by dipolar coupling and occurs through space with $1/r^6$ distance dependence. Triplet-triplet energy transfer requires the exchange of two electrons and is restricted to small distances (Dexter mechanism). Triplet-triplet energy transfer is used to study protein folding dynamics in solution.[11-13] Usually the triplet-triplet energy transfer is observed in condensed phases by means of fluorescence/phosphorescence[14, 15] or triplet-triplet absorption.[11-13, 16, 17] In the gas phase one could perhaps monitor triplet-triplet energy transfer using photofragment detection. If the side-chain loss is a specific fragment from the triplet surface, one could use native chromophores in the protein to monitor its folding dynamics in the gas phase by counting the number of side-chain loss fragments. Guidi showed that in $AcYA_4FK\text{-}H^+$, no matter which chromophore she excited with the UV laser, she observed the same ratio of the phenylalanine and tyrosine side-chain loss fragments.[8] The singlet-singlet energy transfer from tyrosine to phenylalanine cannot take place, because the tyrosine $S_1$ band origin is lower in energy than in phenylalanine. Even if the triplet state of phenylalanine lies higher in energy than the triplet state of tyrosine, there can be energy transfer from the highly excited vibrational levels of the tyrosine triplet state to the triplet state of phenylalanine. In double chromophore molecules one could use tyrosine as a donor and phenylalanine as an acceptor. If the UV laser excites the tyrosine band origin the infrared OPO could probe the position of the tyrosine OH stretch that has a different frequency in the triplet state that in the ground state. By monitoring the phenylalanine side-chain loss increase with the addition of the IR OPO, one could measure the triplet-triplet energy transfer rate. Alternatively, one could excite the phenylalanine chromophore and monitor triplet-triplet energy transfer to the tyrosine. Because the lifetime of the phenylalanine triplet state is longer than that of tyrosine, we might observe an increase of the triplet state lifetime in $AcYA_4FK\text{-}H^+$ compared with the molecule containing only tyrosine chromophore $AcYA_5K\text{-}H^+$. One could vary the distance between the donor and acceptor by adding more alanine residues into the chain and measure the efficiency of the triplet-triplet energy transfer by observing the change in the triplet state lifetime and in the relative intensities of tyrosine and phenylalanine side-chain loss photofragments. Additionally,

one could measure the conformer dependent triplet-triplet energy transfer, because one can selectively excite single conformations in the gas phase.

The fact that one could measure the singlet state lifetimes by detecting the side-chain loss photofragments (Chapter 3, Section 3.4.6) allows studying the singlet-singlet energy transfer in the gas phase. Phenylalanine-to-tyrosine singlet energy transfer was detected in the Archaebacterium histone-like protein in solution by its emission spectrum.[18] In the fluorescence of tyrosine residues two components were found: a fast one (3.9 ns) and a slower one (12.1) ns. The fast component is the fluorescence from the tyrosine residues that were excited directly and the slow component is the de-excitation of those tyrosine residues that were excited *via* energy transfer from phenylalanine. When the energy transfer rate is relatively slow, the radiative lifetime of the acceptor would reflect the depopulation time of the donor chromophore. When all of the tyrosine chromophores were enzymatically removed from the molecule, the lifetime of phenylalanine excited state was increased up to 22.5 ns. In Ac-Phe-Tyr-$NH_2$ after the excitation of phenylalanine only the short lifetime fluorescence was observed from the tyrosine.[18] When the distance between the chromophores is small, the rate of energy transfer is faster and the efficiency is higher. For example, in molecules containing phenylalanine and tyrosine chromophores, one can excite the phenylalanine chromophore and observe the loss of the tyrosine side-chain. The singlet lifetime for tyrosine should contain two components: one from the direct excitation of the tyrosine residue (the tyrosine singlet state is lower in energy than that of phenylalanine), and the other due to the energy transfer from phenylalanine.

While we propose these new scientific directions, due to time limitations we were not able to perform the experiments suggested above. We leave the new PhD students to enjoy future discoveries!

# References


[1] D. Shemesh, A. L. Sobolewski, and W. Domcke, J. Am. Chem. Soc. **131**, 1374 (2009).

[2] W. Domcke and A. L. Sobolewski, Nature chemistry **5**, 257 (2013).

[3] M. Malis, Y. Loquais, E. Gloaguen, H. S. Biswal, F. Piuzzi, B. Tardivel, V. Brenner, M. Broquier, C. Jouvet, M. Mons, N. Doslic, and I. Ljubic, J. Am. Chem. Soc. **134**, 20340 (2012).

[4] C. M. Tseng, M. F. Lin, Y. L. Yang, Y. C. Ho, C. K. Ni, and J. L. Chang, Phys. Chem. Chem. Phys. **12**, 4989 (2010).

[5] T. G. Dietz, M. A. Duncan, and R. E. Smalley, J. Chem. Phys. **76**, 1227 (1982).

[6] A. Sur and P. M. Johnson, J. Chem. Phys. **84**, 1206 (1986).

[7] C. Dehon, S. Soorkia, M. Pedrazzani, C. Jouvet, M. Barat, J. A. Fayeton, and B. Lucas, Phys. Chem. Chem. Phys. **15**, 8779 (2013).

[8] M. Guidi, Ph. D. thesis, EPFL, Lausanne, 2010.

[9] M. Guidi, U. J. Lorenz, G. Papadopoulos, O. V. Boyarkin, and T. R. Rizzo, J. Phys. Chem. A **113**, 797 (2009).

[10] G. Papadopoulos, Ph. D. thesis, EPFL, Lausanne, 2012.

[11] O. Bieri, J. Wirz, B. Hellrung, M. Schutkowski, M. Drewello, and T. Kiefhaber, Proc. Natl. Acad. Sci. U.S.A. **96**, 9597 (1999).

[12] A. Reiner, J. Pept. Sci. **17**, 413 (2011).

[13] B. Fierz, A. Reiner, and T. Kiefhaber, Proc. Natl. Acad. Sci. U.S.A. **106**, 1057 (2009).

[14] G. A. Zalesskaya, V. T. Pavlova, D. L. Yakovlev, E. G. Sambor, and N. N. Belyi, Opt. Spectrosc. **93**, 848 (2002).

[15] W. G. McGimpsey, L. Chen, R. Carraway, and W. N. Samaniego, J. Phys. Chem. A **103**, 6082 (1999).

[16] G. Basu, D. Anglos, and A. Kuki, Biochem. **32**, 3067 (1993).

[17] G. L. Closs, P. Piotrowiak, J. M. Macinnis, and G. R. Fleming, J. Am. Chem. Soc. **110**, 2652 (1988).

[18] D. G. Searcy, T. Montenaygarestier, C. Helene, T. Montenaygarestier, J. S. Sun, and D. G. Searcy, Biochem. **28**, 9058 (1989).

# Acknowledgements

There are a lot of people that contributed to my research and personality. This thesis would not be complete without a thank you note to my friends and colleagues. If you are reading this section, you are most likely one of them.

First of all, I would like to express gratitude to my university supervisors from Saint-Petersburg, S. Y. Tolstyakov and N. A. Timofeev, who helped me to find this position at EPFL and who introduced me to science.

Importantly, I would like to thank Thomas Rizzo for accepting me to the LCPM group and giving me his guidance during all these years. His personal wisdom, understanding, and encouragement helped me a lot. You have a brilliant lab, Tom!

I'd also like to say thank you to my thesis committee members Timothy Zwier, Christophe Jouvet, Jacques-Edouard Moser, and Sandrine Gerber for very interesting discussions and evaluation of my thesis.

In the beginning of my PhD, I got a lot of technical and scientific advice from Oleg Boyarkin, Tobias Wassermann, Ulrich Lorenz, Georgios Papadopoulos, and Maxim Grechko. Sharing the office with Caroline Seaiby, Natalia Nagornova, Irina Konistyapina, and chatting with different LCPM members during their coffee breaks were both fun and constructive.

I want to thank Marta Perez and Vladimir Kopysov for our discussions about the DFT calculations; Yoshiya Inokuchi and Marcel Drabbels for talks about quantum mechanics and vibrational couplings; Josh Carr, Santanu Roy, and Jim Skinner for our joint project described in Chapter 5; and Ryan Julian, Evan Williams, and Maria Demireva for various interesting experiments that are not part of this thesis. I liked optimizing the ion signal with our summer student, Solène Oberli – hope she will also get her PhD soon. A special thanks goes to Frédéric Rosu, who introduced me to the mysterious world of DNA and Belgian food. It was such a pleasure to work together. I also want to thank Maxim Kazansky for cheering me up during hard times in the lab.

I am so happy that Oleg Aseev started his bio projects and moved to work on the same machine. Thanks for teaching me how to love “Mathematica” and for all your help in the lab. I want to acknowledge our great postdocs Antoine Masson and Mike Kamrath for being available for any questions. Especially, I’d like to thank Mike Kamrath and Oleg Boyarkin for endless discussions about the fragmentation mechanisms!

I admire Lucy Voronina for being so energetic, and creating a wonderful atmosphere in the lab and outside of it.

I spent a lot of nice time hiking with Nils Brauer, Xiaohang Zhang, Li Chen and my other colleagues. I enjoyed LCPM lunches where Reiner Beck was talking about technologies, and Morten Hundt, Hirokazu Ueta, Maarten Van Reijzen, Helen Chadwick, Jörn Werdecker, Chiara Masellis, Aleksandr Pereverzev, Valeriu Scutelnic, Andrew Bonnar, Andreas Osterwalder… were eating.

Particularly, I want to say thank you to Marianne Dang for being the greatest secretary in the world. I owe you so much!

Usually people say that the period of writing the thesis is the hardest, but Alex managed to make it so easy and enjoyable for me. It is still a mystery how you came into my life and gave me all this strength. You know, I would not be able to finish the thesis without you…

And finally, I want to thank my family - my mom and dad, my sister and her husband, and my grandparents. They were supporting me from the first until the last day of my PhD, and I dedicate this thesis to them.

# Curriculum Vitae

## Education

2010–2014 Ph.D. in Physical Chemistry, Ecole Polytechnique Fédérale de Lausanne, Switzerland
Laboratory of Molecular Physical Chemistry, Prof. T. R. Rizzo

Title: Dynamics of UV-excited, protonated peptides in the gas phase

2007–2010 MSc. in Physics with honors, Saint Petersburg State University, Russia
Specialization in Plasma Chemistry and Physics with Prof. N. A. Timofeev and Dr. S. Y. Tolstyakov

Title: Near-infrared plasma spectroscopy in support of optical diagnostics development for ITER

2003–2007 BSc. in Physics with honors, Saint Petersburg State University, Russia

## Languages

Russian (native), English (fluent), French (upper intermediate), German (beginner)

## Publications

1. S. Y. Tolstyakov, E. E. Mukhin, M. M. Kochergin, G. S. Kurskiev, V. V. Semenov, A. G. Razdobarin, K. A. Podushnikova, **A. V. Zabuga**, V. S. Lisitsa, M. G. Levashova, V. A. Soukhanovskii, M. Beurskens, S. Brezinsek, A. Meigs, P. Andrew, M. T. Globus, N. Team, and J. E. T. Team, *"Near-infrared plasma spectroscopy in support of divertor Thomson scattering diagnostics development for ITER"*, J. Phys. Conf. Series, 14th International Symposium on Laser-Aided Plasma Diagnostics **227** (2010)

2. J. K. Carr, **A. V. Zabuga**, S. Roy, T. R. Rizzo, and J. L. Skinner, *"Assessment of amide I spectroscopic maps for a gas-phase peptide using IR-UV double-resonance spectroscopy and density functional theory calculations"*, J. Chem. Phys. **140** (2014).

3. **A. V. Zabuga**, M. Z. Kamrath, O. V. Boyarkin, and T. R. Rizzo, *"Fragmentation mechanism of UV-excited peptides in the gas phase"*, J. Chem. Phys. (2014), accepted.